UNIVERSITY
OF LATVIA

FACULTY OF PHYSICS, MATHEMATICS AND OPTOMETRY

INSTITUTE OF NUMERICAL MODELLING

Valters Dzelme

ELECTROMAGNETICALLY DRIVEN LIQUID METAL FLOWS WITH STRONG FREE SURFACE DYNAMICS

DOCTORAL THESIS

Submitted for the degree of PhD in Physics
Subfield of Fluid Mechanics

Riga 2024

Work on the thesis was carried out at the Institute of Numerical Modelling, Faculty of Physics, Mathematics and Optometry, University of Latvia from 2017 to 2023.

The thesis contains an introduction, 5 chapters, conclusions, outlook and a list of references.

Form of the thesis: dissertation in the field of physics, subfield of fluid mechanics.

Thesis supervisor: *Dr. phys.* **Andris Jakovičs**, leading researcher, Institute of Numerical Modelling, University of Latvia

Reviewers:
1. *Dr. phys.* **Ilmārs Grants**, University of Latvia, Latvia
2. *Dr. ing.* **Bernard Nacke**, Leibniz University of Hannover, Germany
3. *Dr.* **Michele Forzan**, University of Padua, Italy

The thesis will be defended at the public session of the Promotion Council of Physics and Astronomy, University of Latvia, at 15:00 on 12th of January, 2024. The thesis and the summary are available at the Library of the University of Latvia, Kalpaka blvd. 4.

The author of the thesis participated in the project No. 8.2.2.0/20/I/006 “Strengthening the capacity of the UL PhD programme in the new doctoral model” at the University of Latvia.

Promotion Council of Physics and Astronomy, University of Latvia

chairman: _____ /*Dr. phys.* **Andrejs Cēbers**/

secretary: _____ /**Sintija Siliņa**/

Abstract

In many metallurgical processes, such as electromagnetic (EM) melting and stirring, and continuous casting, controlling the motion of the free surface of liquid metal is crucial to maintaining stability of the process and ensuring high quality of the final product. The thesis focuses on developing numerical models using open-source software for simulation of liquid metal flows with pronounced free surface motion driven by different configurations of magnetic field. Different approximations are tested to find the most adequate options to simulate the variety of MHD systems. In addition to numerical verification, three experimental setups are built to validate the models.

Experiments reveal interesting free surface dynamics depending on geometry and EM field frequency and strength, ranging from relatively stable deformation and fluctuations with direct (DC) or low-frequency alternating current (AC) injection and with traveling magnetic field, to diverse surface dynamics and parametric instabilities in high-frequency AC field. These effects were succesfully captured by the numerical models, providing an insight into the physical mechanisms.

Some of the aspects from the laboratory setups are potentially relevant to the direct strip casting (DSC) process, where liquid metal is poured onto an intensively-cooled moving belt where it solidifies into a thin sheet. Possible solutions, using EM fields, to several stability issues in DSC, such as backflow and free surface oscillations, are investigated numerically. Static magnetic field was found to efficiently stabilize the free surface, resulting in uniform strip thickness profile. The backflow problem can be solved using AC field of an inductor placed near the backflow area, however, compromising the stability downstream. Combining static and high-frequency field results in completely stable casting process.

Contents

List of Figures

Introduction

Motivation

Electric and magnetic fields are widely used in modern metallurgy and material processing to heat, melt, mix, transport and control solid and liquid metals. In many technological processes, such as cold crucible melting, electromagnetic (EM) stirring and continuous casting, quality of the final product can be improved by optimizing different process parameters, such as magnetic field magnitude, frequency and configuration. In some cases, instabilities of the free surface and bulk flow occur, which can have detrimental effect on the stability of the whole process. Therefore, it is important to study physical phenomena present in the processes, how they interact and affect the outcome.

Numerical modelling is a powerful tool to study physical processes in almost any detail. However, complex processes involving different coupled effects, such as fluid flow and EM field, often require many simplifications and approximations for numerical solutions to be feasible. Depending on specific applications, different levels of simplifications are acceptable. Moreover, apart from numerical verification, the simplified models may require experimental validation.

The thesis focuses on liquid metals in static and time-varying electric and magnetic fields, which is a topic of liquid metal magnetohydrodynamics (MHD). In particular, EM-driven free surface dynamics and instabilities are considered in different laboratory-scale systems, such as electrically-induced vortical flows, rotating permanent magnet stirrers and thin liquid metal drops and pools in transverse high-frequency magnetic field. In addition, a novel technological process - direct strip casting with electromagnetic flow control - is also investigated. This process combines several of the phenomena present in the laboratory setups - turbulence, heat transfer, magnetic slip, electromagnetic induction, free surface deformation and instabilities. Possible solutions to several stability issues in the casting process are explored numerically.

Goal and tasks

The goal of the thesis is to develop numerical models in open-source software for simulating technologically important EM-driven liquid metal flows with free surface. The following tasks are formulated:

1. Develop, implement and test mathematical models and numerical approximations for simulating liquid metal MHD in different systems.

2. Prepare and conduct laboratory experiments to study liquid metal flows with pronounced free surface dynamics induced by different configurations of magnetic field, as well as validate the numerical models.

3. Using the developed, verified and validated models, study EM-driven free surface dynamics and instabilities in the laboratory setups.

4. Study numerically a complex industrial process - direct metal strip casting with EM flow control.

Theses

- In case of low magnetic Reynolds number, the $\vec{v} \times \vec{B}$ term in relevant numerical models can be considered in a simplified way as a correction to the induced current, which can significantly reduce simulation time of coupled electromagnetics - fluid dynamics processes.
- Free surface dynamics of thin liquid metal layers in AC magnetic field depend strongly on layer's dimensions (thickness or diameter) and field strength - stable surface deformation at smaller thickness or diameter and weaker field transitions into distinct waves and oscillations at larger dimensions and stronger field. For given dimensions, this transition can be spontaneous depending on the rate of increase of magnetic field.
- Given optimal magnetic field magnitudes, the direct strip casting process can be fully stabilized by combining AC and DC field.

Novelty and author's contribution

Complex numerical models were developed using free open-source software Elmer, OpenFOAM and EOF-Library. The models were used to efficiently simulate liquid metal flows with strong free surface deformation induced by different electromagnetic excitations, ranging from direct current injection to traveling magnetic field and high-frequency induction. Corresponding experimental setups were created, which not only allowed validating the models, but also revealed interesting free surface dynamics and instabilities which have not been reported before.

Original solutions to known stability issues in the novel direct strip casting process were demonstrated numerically, which can potentially contribute to significant improvements of the casting process.

The author has developed and tested all of the numerical models, performed all simulations and analysed all simulation results, prepared and conducted all experiments, and processed and analysed all experimental results, with a couple of exceptions. Aleksandrs Jegorovs processed images from the experiments of stirring by rotating permanent magnets. Mihails Birjukovs helped preparing code for processing images from the experiments with thin melt layers in AC field.

The author is the main author of 8 and a co-author of one publication about the thesis topic, and a co-author of two papers closely related to the topic (all publications are listed below). The author has participated in numerous scientific conferences (listed below).

The author was the advisor of one bachelor's thesis in 2020 on simulation of liquid metal flow induced by rotating permanent magnets, created and taught a master's level course about modelling of multiphysical processes in 2020, as well as prepared materials and supervised workshops in two PhD schools in 2019 and 2021.

Approbation of results

Publications

The author of the thesis has published 9 papers about the thesis topic and 2 closely related to the topic:

[A.1] A. Jegorovs, **V. Dzelme**, A. Jakovičs. Experimental validation of liquid metal MHD numerical models. *Magnetohydrodynamics*, Vol. 58, pp. 409-416, 2022

[A.2] **V. Dzelme**, A. Jakovičs, E. Baake. Dynamics of liquid metal layer in transverse AC magnetic field. *Magnetohydrodynamics*, Vol. 58, pp. 141-149, 2022

[A.3] **V. Dzelme**, A. Jegorovs, A. Jakovičs. Liquid metal free surface dynamics in rotating permanent magnet stirrer. *IOP Conference Series: Materials Science and Engineering*, Vol. 950, art. no. 012018, 2020

[A.4] **V. Dzelme**, A. Jakovičs, E. Baake. Liquid metal free surface deformation in electrically induced vortical flow. *Magnetohydrodynamics*, Vol. 56, pp. 67-74, 2020

[A.5] **V. Dzelme**, A. Jakovičs, I. Bucenieks. Numerical modelling of liquid metal electromagnetic pump with rotating permanent magnets. *IOP Conference Series: Materials Science and Engineering*, Vol. 424, art. no. 012046, 2018

[A.6] **V. Dzelme**, A. Jakovičs, J. Venčels, D. Köppen, E. Baake. Numerical and experimental study of liquid metal stirring by rotating permanent magnets. *IOP Conference Series: Materials Science and Engineering*, Vol. 424, art. no. 012047, 2018

[A.7] **V. Dzelme**, A. Jakovičs, A. Chudnovsky, E. Baake. Simulation of electrically induced vortical flows. *IOP Conference Series: Materials Science and Engineering, Vol. 424, art. no. 012083*, 2018

[A.8] **V. Dzelme**, A. Jakovičs, I. Bucenieks. Numerical modelling of a real rotating permanent magnet based electromagnetic induction pump. *Magnetohydrodynamics*, Vol. 53, pp. 731-738, 2017

[A.9] **V. Dzelme**, M. Ščepanskis, V. Geža, A. Jakovičs, M. Sarma. Modelling of liquid metal stirring induced by four counter-rotating permanent magnets. *Magnetohydrodynamics*, Vol. 52, pp. 461-470, 2016

[A.10] M. Birjukovs, **V. Dzelme**, A. Jakovičs, K. Thomsen, P. Trtik. Phase boundary dynamics of bubble flow in a thick liquid metal layer under an applied magnetic field. *Physical Review Fluids*, Vol. 5, art. no. 061601, 2020

[A.11] M. Birjukovs, **V. Dzelme**, A. Jakovičs, K. Thomsen, P. Trtik. Argon bubble flow in liquid gallium in external magnetic field. *International Journal of Applied Electromagnetics and Mechanics*, Vol. 63, pp. S51-S57, 2020

Conferences

The author has presented the following papers in international scientific conferences:

[C.1] **V. Dzelme**, A. Jakovičs, E. Baake. Dynamics of liquid metal surface in AC magnetic field. *Heating by Electromagnetic Sources*, Padua, Italy, May 9-12, 2023

[C.2] **V. Dzelme**, A. Jakovičs. Simulation of direct strip casting with electromagnetic flow control. *12th PAMIR International Conference*, Krakow, Poland, July 4-8, 2022

[C.3] A. Jegorovs, **V. Dzelme**, A. Jakovičs. Experimental validation of MHD numerical simulations. *12th PAMIR International Conference*, Krakow, Poland, July 4-8, 2022

[C.4] **V. Dzelme**, A. Jakovičs, E. Baake, Liquid metal layer dynamics in transverse alternating magnetic field. *UIE Congress*, Pilsen, Czech Republic, September 1-3, 2021

[C.5] **V. Dzelme**, A. Jakovičs, Simulation of direct metal strip casting, *Electromagnetic Processing of Materials*, Riga, Latvia, June 13-17, 2021

[C.6] **V. Dzelme**, A. Jakovičs, E. Baake, Electromagnetic forming of a liquid metal layer. *Electromagnetic Processing of Materials*, Riga, Latvia, June 13-17, 2021

[C.7] **V. Dzelme**, A. Jakovičs, E. Baake, Thin liquid metal layer instability in AC magnetic field. *11th International PAMIR Conference*, Reims, France, July 1-5, 2019

[C.8] **V. Dzelme**, A. Jakovičs, E. Baake. Electrically induced liquid metal free surface dynamics. *Heating by Electromagnetic Sources*, Padua, Italy, May 22-24, 2019

[C.9] **V. Dzelme**, A. Jakovičs, E. Baake. Simulation of electrically induced vortical flows. *Electromagnetic Processing of Materials*, Awaji, Japan, October 14-18, 2018

[C.10] **V. Dzelme**, A. Jakovičs, I. Bucenieks. Numerical modelling of liquid metal electromagnetic pump with rotating permanent magnets. *Electromagnetic Processing of Materials*, Awaji, Japan, October 14-18, 2018

[C.11] **V. Dzelme**, A. Jakovičs, J. Venčels, D. Köppen and E. Baake. Numerical and experimental study of liquid metal stirring by rotating permanent magnets. *Electromagnetic Processing of Materials*, Awaji, Japan, October 14-18, 2018

[C.12] **V. Dzelme**, M. Sarma, A. Jakovičs, K. Thomsen, Modelling of rotating permanent magnet induced liquid metal stirring. *Modelling for Material Processing*, Riga, Latvia, September 21-22, 2017

[C.13] **V. Dzelme**, M. Ščepanskis, M. Sarma, P. Vontobel, P. Trtik, K. Thomsen, A. Jakovičs, T. Beinerts, Numerical and neutron radiography investigation of liquid metal flow. *UIE Congress*, Hannover, Germany, June 6-9, 2017

1 Literature review

In this chapter, literature relevant to liquid metal MHD is reviewed. Section 1.1 gives an overview of MHD-related phenomena occurring in practical applications. Section 1.2 reviews general aspects and the most important studies of electromagnetically-driven free surface dynamics. Section 1.3 presents a review of relevant numerical modelling approaches. Typical experimental techniques are reviewed in section 1.4.

1.1 Liquid metal MHD in applications

The interaction of electric and magnetic fields with electrically conducting fluids manifests in many different ways. A wide variety of phenomena can be observed depending on electromagnetic field magnitude and frequency, fluid properties, presence of different phases, as well as geometrical conditions. Electrically conducting fluids are typically plasma, electrolytes and liquid metals. Plasma is ionized gas and is characterised by low density and compressibility. Electrical conductivity of plasmas depends on density and degree of ionization. Electrolytes are weakly electrically conducting liquids containing charged particles. An example of an electrolyte is salt water, which contains H^+, Cl^- and other ions. Liquid metals are characterised by incompressibility and high electrical and thermal conductivities. In contact with air or water, liquid metals have high surface tensions coefficient, e.g. 0.7 N/m for gallium at 30°C [1].

High thermal and electrical conductivities of metals are widely used in modern metallurgy and material processing to heat, melt, mix, transport and control solid and liquid metals. The main interactions in all of those processes are Joule heat and Lorentz force. Joule heat is generated in a material through which electric current passes. The current can be induced in two ways - direct injection via electrodes or via electromagnetic induction due to time-varying magnetic fields. Direct injection can be direct (DC) or alternating current (AC). Induction by time-varying magnetic fields can be produced by either AC wires/inductors or by moving/rotating permanent magnets.

Direct current injection is used, for example, in electric arc furnaces [2][3] and welding [4][5]. Note that in typical arc furnaces the main melting power is not the Joule heat dissipated directly in the metal. The hot arc provides most of the energy through strong convection and radiation.[6] However, in many cases, when modelling physical processes in the melt, the arc can be ignored or considered in a simplified fashion to take into account its effect on the melt (for example, the arc can be approximated as a solid cylinder [3]). Arcs and plasmas are not considered in the thesis.

When metal is liquid, the injected current flowing through the melt pool interacts with its own magnetic field resulting in Lorentz force. In many cases, the current distribution in the liquid metal is non-uniform, such as when diverging from a small electrode through the melt pool. The non-uniform current distribution leads to non-conservative Lorentz force (curl of which is not zero) and melt stirring. The recirculating flow in these cases is called electrically induced vortical flow (EVF).[7]

A classical example of EVF is a hemi-spherical melt pool. Electric current is injected

from a small top electrode and diverges through the liquid metal into the hemi-spherical wall. Such radial current causes azimuthal magnetic field and the resulting Lorentz force drives a poloidal flow.[7] For other geometries or electrode configurations the flow patterns can be different.

By applying external magnetic field, different EVF patterns can be achieved. In the hemi-spherical point-electrode case, with axial field, melt swirl is induced [8]; with horizontal field, the flow pattern changes to a double-vortex in horizontal plane [9]. The swirl can actually develop spontaneously without applying any external fields.[10] It has been found that EVFs can be sensitive to any stray magnetic fields, such as that of the Earth or surrounding electrical equipment [11]. Further description and analysis of EVFs is given in [8]. Theoretical treatment of many different EVFs can be found in [7].

Motion of the free surface is usually not considered when studying EVFs. Free surface in most typical geometrical and electrode configurations has very small deformation, such as some small deflection around the small top electrode in the hemi-spherical case.[12] However, this is not always the case. In this work, a special configuration of EVF was built in which notable free surface deformation can be achieved - a cylindrical container with current passing through the melt between a small bottom electrode and the cylindrical wall of the container. This will be described in the experimental work section, as well as presented in the results section.

Another notable application of direct current injection is in liquid metal conduction pumps, where current is passed between two electrodes through a channel with liquid metal. To create Lorentz force in the channel direction, external magnetic field is applied perpendicular to the current and the channel. The conduction pumps are essentially the opposite of MHD generators, in which, instead of using injected current and external field to generate flow, a flow of electrically conducting fluid through an applied field is used to generate electric current.[8]

Many industrial applications use EM induction. The basic mechanism is described by the Faraday's law that relates a time-varying magnetic field to an induced electromotive force (EMF). The EMF drives electric current in conductors. EM induction enables contactless processing. A classical example is induction heating [13] and melting [14][15] where high-frequency magnetic field induces eddy currents that produce Joule heat in conductors.

Conductors in AC magnetic field experience skin-effect - magnetic field and induced currents concentrate near the surface in a skin layer with thickness $\delta = \frac{1}{\sqrt{\sigma \mu_0 \pi f}}$, where f - field frequency, σ - electrical conductivity, μ_0 - vacuum permeability. For a specific material, this means that one can control effective heating depth by changing magnetic field frequency. This is important in induction surface hardening [16][17], where thin surface layer of a workpiece is heated for a short period to initiate phase transition.

Additional effect is that the induced currents interact with magnetic field resulting in Lorentz force. In typical induction melting equipment, such as cold crucible, where molten metal is contained in a cylindrical crucible surrounded by inductor windings, the induced Lorentz force causes a recirculating bulk flow [10]. This is often beneficial because the

turbulent bulk flow homogenizes the temperature distribution and helps mixing additives and inclusions [18], as well as can promote grain refinement during solidification [19]. Different types and configurations of magnetic field can be used to optimize the melting and mixing processes.

Traveling magnetic field (TMF) can be used to stir or transport liquid metal. TMF can be generated by either phase-shifted AC windings [20] or rotating permanent magnets [21][22]. A well-known example of an MHD pump with permanent magnets where channel is wound around a rotating block with permanent magnets with alternating poles [23], often arranged in a Halbach array to increase the strength of magnetic field. The liquid metal in the channel is then driven in the direction of the rotating block.

In continuous casting, EM brakes with static or traveling magnetic field can be used to control and stabilize liquid metal flow to improve cast product quality.[24][25][26] Active research is taking place with the direct strip casting (DSC) [27] or horizontal single belt casting (HSBC) process [28], which is a novel technique to cast near-net-shape thin metal strips. Since the belt casting process will be studied in the thesis, the process is discussed in more detail separately in section 1.1.1.

Strong emphasis in the thesis is on EM-driven free surface dynamics. Section 1.2 reviews the most important results of free surface dynamics and instabilities driven by low and high frequency magnetic fields.

1.1.1 Direct strip casting

The belt casting process is developed by multiple research groups, mainly in Canada (McGill Metals Processing Centre) and Germany (TU Clausthal), under the names of Horizontal Single Belt Casting (HSBC) and Direct Strip Casting (DSC), respectively. For simplicity, the DSC abbreviation is used throughout the thesis. A thorough review of the belt casting and similar technologies can be found in [29][30].

In the DSC process, liquid metal is poured onto a moving belt, which is intensively cooled from the bottom and goes through an area of inert gas atmosphere to protect the cast alloy from oxidation and contamination. The liquid metal gradually solidifies, and the solid strip is continuously pulled away with the moving belt for further processing and coiling. Typical cast materials are steel [27] or aluminium alloys [31], although this process can be used for other metals, such as magnesium [32]. The melt is contained on the belt by copper blocks on both sides that move together with the belt.[27] In a related technology, Twin Roll Casting, the use of electromagnetic dam has been reported for containment of the liquid metal.[33] Perhaps, similar approach could be also applied to the belt casting.

One possible configuration of the belt casting equipment is shown in Fig. 1.1.1. Laboratory-based research casters are usually relatively small, e.g. belt width of 75 mm [34] or 160 mm [32]. The first commercial belt casting plant for steel was launched in Germany in 2012.[35] The cast strips are 1 m wide and 15 mm thick, pulled at around 24 m/min.[36] For comparison, older technologies, such as Thin Slab Casting [37], allow casting 50-60 mm thick strips at 5 m/min [38], which requires considerably more secondary

rolling and processing.

There are several stability issues in the belt casting process. One is in the zone where liquid metal initially contacts the moving belt. Upon impact onto the belt, liquid metal can flow not only in the direction of the belt movement but also into the small gap between the belt and the bottom of the refractory.[39] If the melt starts solidifying inside the gap, it can damage the equipment. A stable meniscus at the entrance of the gap can form if the gap height is below 1 mm.[40] However, it may depend on the physical properties of the melt and other factors. There have been efforts to minimize this backflow by creating an inclined refractory [31], which reduces the impact of liquid metal onto the belt. As will be shown in the results of the thesis, AC or traveling magnetic field can be used to limit this backflow.

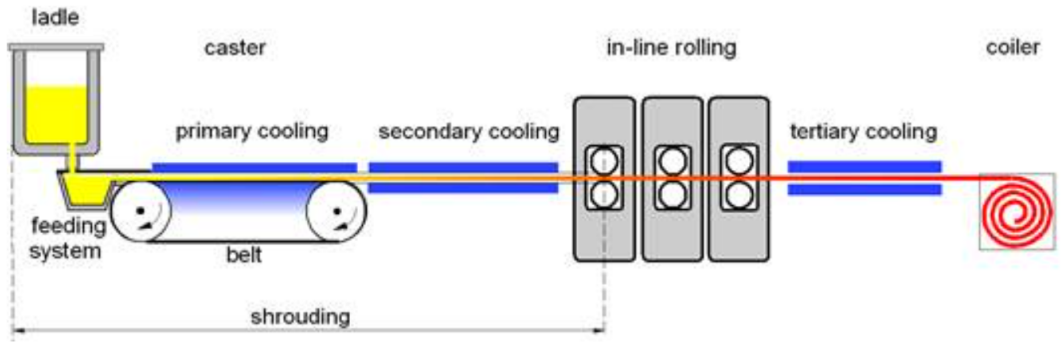

Fig. 1.1.1. Scheme of a direct strip casting equipment.[41]

Another problem in DSC is related to the synchronicity of the melt and belt speeds and free surface motion. Non-uniform flow speeds and free surface oscillations in the zone before the metal is fully solidified can affect the final strip thickness profile. There are different ways of controlling liquid metal flow and free surface shape. One option reported for strip casting is blowing argon jets against the liquid metal to ensure uniform layer distribution across the belt.[27] Another option is to use EM interaction. For example, the use of TMF to modify the flow has already been reported for DSC.[27] Since using EM technologies in the DSC process has not been reported in much detail, it will be investigated numerically in the thesis.

Since the DSC process is relatively new, a lot of research is required to understand the underlying processes and their dependence on different parameters, and eventually optimizing the process for widespread use. A part of the thesis is devoted to simulating this process with and without electromagnetic interaction.

1.2 Free surface dynamics

In many applications, all or part of the liquid metal is in contact with a gas phase, such as air or argon, or a significantly lighter liquid, such as water or some acid solution. That part of the surface is considered to be free surface. A wide variety of free surface effects have been observed experimentally, depending on surface size and shape, oxidation level, magnetic field strength and frequency, material properties, temperature and other factors.

There are different ways of categorizing the effects. Since the thesis deals with EM-driven cases (in contrast to otherwise-driven flows affected by magnetic field, such as Hartmann flow), two main groups can be distinguished - low- and high-frequency magnetic field. Transition from low to high frequency is not sharp, combined effects may be present in the medium range. Also, both types can be employed at the same time, for example, combining AC and DC in induction melting and stirring [42].

The division of free surface effects by frequency f of the driving magnetic field, firstly, means that we are separating the cases by magnetic field penetration or skin depth δ. Roughly, low frequency means that $\delta \gg L$, where L - characteristic size of the system (e.g. melt pool radius or thickness) and high is $\delta \ll L$. For example, at 50 Hz in liquid gallium $\delta = 37$ mm and at 1000 Hz $\delta = 8.3$ mm. To generalize the influence of skin depth relative to the system size, dimensionless frequency is introduced as $S = \frac{L^2}{\delta^2}$. Dimensionless frequency is often used to compare the magnitudes of primary and secondary magnetic field. This is briefly discussed in the theory section.

Skin depth determines how sensitive the EM field is to changes of free surface shape. In case of high frequency, the coupling is strong - induced Lorentz force concentrates near the surface and even small surface perturbations influence EM field distribution. This aspect is very important when it comes to numerical modelling, because this leads to strongly coupled EM and fluid dynamics equations, which, with a segregated coupling approach, means frequent recalculation of EM fields and long simulation times. This modelling aspect is further described in the modelling section.

Skin depth is only one of motivations to separate low and high frequency cases. The other reason is related to fluid's response to time-dependent forcing. As will be shown in the theory section, sinusoidal Lorentz force can be decomposed into a constant time-averaged and time-dependent parts. In case of EM forcing with low frequency, the fluid will be directly affected by the time-dependent force. If the frequency is equal or close to the natural frequencies, resonance with strong oscillations can develop. Note that the constant time-averaged part can't generally be completely ignored, since flow velocity is present in both parts.

In high-frequency cases, the flow is driven mainly by the time-average force. Moreover, the frequency can be too high for the oscillating part to directly induce free surface oscillations. It has been shown experimentally that free surface waves generated by AC magnetic field are negligible when the field frequency is above 10 Hz.[43] It does not mean that the free surface would not oscillate above 10 Hz, only that directly induced (directly related to the field frequency) oscillations would be small. The following subsections separately review low and high frequency cases.

1.2.1 Low-frequency magnetic field

As already mentioned above, time-dependent Lorentz force can be decomposed into the time-averaged and oscillating parts. In case of low frequency, the oscillating part, which has double the frequency of the applied field, is responsible for many free surface behaviors predicted theoretically and observed experimentally. Low-frequency electromagnetic

excitation can be not only single-phase sinusoidal, but also pulsed [44], consisting of a high base frequency and low pulsing frequency. Theoretical analysis of free surface waves in a cylindrical tank with liquid metal driven by low-frequency magnetic field was reported in [45], predicting both axisymmetric waves and asymmetric modes due to parametric instability. The instability occurs at some combinations of the frequency and strength of the applied magnetic field. This was confirmed experimentally in [43] for liquid 200 mm diameter mercury pool in 2-20 Hz magnetic field, identifying four regimes - axisymmetric standing waves, appearance of azimuthal waves together with concentric waves, large azimuthal waves without concentric waves and, finally, chaotic motion of the free surface. While in most industrial applications surface waves would be unwanted, this could be beneficial for melt purification [46][47], as surface waves mean larger surface area through which impurities can evaporate.

If the liquid metal volume is small and it is supported only from the bottom, i.e. a case of semi-levitation, low-frequency magnetic field can induce many different shapes and oscillations of the free surface. An experimental study is reported in [46], where liquid mercury drops up to 106 mm in diameter are subjected to transverse AC magnetic field up to 0.3 T from 1 to 10 Hz. Depending on frequency and field strength, axisymmetric, non-axisymmetric azimuthal and irregular oscillations with pinching have been observed. Some regular azimuthal oscillations of mode number 4, 5 and 6 have been attributed the nickname "starfish" [48] due to obvious appearance. Note that axisymmetric oscillations are at a frequency equal to the force (double that of magnetic field), while non-axisymmetric oscillations at higher field strengths are at the frequency of magnetic field (half that of the force). This is a characteristic of parametric excitations.[49][50][46]

The mechanism of transition between different oscillation regimes is not completely clear. Most probably, the transition is triggered by a small perturbation of the free surface, which is further enhanced by the pinching effect of magnetic field.[46] Internal flow distribution could play a role in causing those perturbations, based on observations in water models [51], which may induce the transition. Numerical modelling could potentially provide explanations, but no detailed simulations have been reported.

Low-frequency cases, as they are described above, will not be considered in the thesis. However, low-frequency excitation will be used in the case of liquid metal stirring by rotating permanent magnets.

1.2.2 High-frequency magnetic field

In high-frequency cases, the potential part of Lorentz force dominates over the rotational part, meaning that Lorentz force is directly influencing the free surface, instead of through the flow and dynamic pressure. Classical examples are semi-levitation [15] and full levitation [52], where high-frequency field is used to support liquid metal volumes. The oscillating part has no direct influence on the fluid flow and surface dynamics. However, it has been shown that the time-averaged force can have a destabilizing effect, inducing waves on the free surface of liquid metal.[53][54]

Most studies of thin melt layers in high-frequency AC field consider circular drops or

pools. A liquid gallium drop with initial diameter $d = 60$ mm in $f = 13$ kHz magnetic field was studied experimentally in [55], noting the transition from axisymmetric squeezing to interesting azimuthal pinch-type instabilities with increasing magnetic field. It was also found that surface oxidation can significantly affect the drop shapes, with also C and H-shape forms developing, and that the melt can sometimes stick to the vessel surfaces, making the drop deformations nearly static. Similar shapes were observed for semi-levitated $d = 60$ mm liquid nickel-based alloy in cold-crucible furnace [56].

Liquid Pb-Bi alloy in 4 kHz magnetic field was studied experimentally and analytically in [57]. Using an electrotechnical model, it was shown analytically that the C shape of the drop observed experimentally at $B_0 = 28$ mT corresponds to a stable energy minimum. The same group also used boundary integral method in [58] to simulate edge deformation of a conducting disk in the limit of infinite frequency, attributing the experimental observations to the equilibrium of pressures.

The studies mentioned above didn't control oxidation of the free surface. Circular liquid Galinstan drop covered with HCl solution to prevent oxidation was studied experimentally in [59], finding axisymmetric squeezing and azimuthal waves of different modes m depending on hydrodynamic and magnetic Bond numbers. A thorough experimental and numerical investigation of circular liquid Galinstan drops in 7.8 kHz AC field is reported in [60]. The authors studied both free drops, as well as larger drops filling the whole container (free surface touching side walls). They observed different oscillations, drop rotations and instabilities. Drop rotation has been attributed to both helicity of the inductor coil and asymmetry of the drop shapes, although it is not easy to distinguish real rotation from traveling azimuthal waves without knowing the bulk flow distribution. When the surface is oxidized, the drop shapes can become increasingly complex. Similar shapes were observed in [57][58]. The oxide film actually adheres to walls, making the deformed drop shapes almost static.

The observed surface instabilities are in qualitative agreement to linear stability theory for an infinitely conducting thin sheet [61][62]. The theoretical analysis attributes the pinching instability mechanism to redistribution of induced current and magnetic field in perturbations of the edge. Interestingly, a related effect has been reported for electrode induction melting for inert gas atomization [63], where ridges or lamellae along the perimeter of the cylindrical electrode develop during the melting process. It was shown numerically that it is due to the redistribution of induced current in perturbations of the surface leading to uneven Joule heat distribution.

Evidently, most studies are concerned with axisymmetric setups, although other configurations might be relevant in some applications. A different configuration - vertical annular Galinstan layer under a ring-like inductor producing 20 to 50 kHz magnetic field, was studied experimentally in [64]. With increasing magnetic field strength, initial capillary surface waves develop into static surface deformations, eventually leading to pinching instability above some critical magnetic field. In the thesis, one of the cases considers thin horizontal liquid metal layer in a rectangular container subjected to transverse AC magnetic field, which has not been studied neither experimentally nor numerically before.

The closest to such configuration is the theoretical analysis in [61], where the edge pinch instability is considered for an infinitely thin conducting half space.

Numerical studies of free surface dynamics and instabilities in high-frequency magnetic field are scarce. Numerical modelling here means solving numerically the full set of equations describing the physics, such as Maxwell's and Navier-Stokes equations, instead of numerical integration of a derived equation for specific oscillations. Most numerical studies are focused on practical applications, such as semi-levitation in cold crucible [65] and full levitation in different configurations [52][66]. In the thesis, numerical models are developed for thin liquid metal layers in AC magnetic field. This can potentially reveal more details about instability mechanisms and how they depend on different parameters.

1.3 Numerical modelling

There are many physical effects and processes taking place in liquid metal MHD: electromagnetic field, induction, fluid flow with free surface motion, heat transfer, solidification/melting and others. Generally, all of the aspects are coupled. Fluid flow can depend directly on heat transfer due to temperature-dependent physical properties of the fluid. In EM-driven flows, the flow and free surface motion depends on EM field distribution, which in turn depends on the fluid flow and surface shape. However, in a complex model involving many different effects, one must first make sure that each individual part of the model works as well as possible, before turning to coupled models. The following sections briefly review typical modelling approaches for effects relevant to liquid metal MHD with free surface.

1.3.1 General methods

The first step towards a robust numerical model is deciding on a suitable numerical framework, such as finite element (FEM) or finite volume method (FVM). The two mentioned are the most flexible regarding computational cell shapes and applicability to complex geometries [67]. Each of the methods can be fully utilized to solve all the physics - from electromagnetics to fluid flow and heat transfer. However, historical development of the methods has led to their specialization - FEM is now more efficiently applied to solid mechanics and electromagnetics problems, while FVM is more naturally implemented for fluid dynamics. It is only reasonable then to use the most suitable framework to model each underlying process of a multi-physical system. For example, electromagnetically driven liquid metal flow can be modelled in a segregated fashion - solving electromagnetics with FEM and fluid dynamics with FVM, each on its own numerical grid. Then the problem is achieving efficient coupling between the two methods.

The next step is deciding on mathematical models for adequate description of each physical process – electromagnetic field, fluid flow, turbulence, free surface changes etc. Electromagnetic field is typically simulated using potential formulation - Maxwell's equations are rewritten for electric scalar and magnetic vector potentials, including also Ohm's law and Lorentz force. The electromagnetic aspect of complex magnetohydrodynamics simulations is well established and requires little attention, apart from occasional neces-

sity to consider the influence of fluid velocity on magnetic field and force distribution in the form of $\vec{v} \times \vec{B}$ term in Ohm's law. This term can be considered by either adding it to EM simulation or, in the case of small magnetic Reynolds numbers, to fluid flow simulation as a correction to the Lorentz force [68][A.5][A.8], an approach that is also used in the thesis.

Simulation of turbulent fluid flow is a more difficult matter, with many researchers working in this field for decades. Adequate turbulence description requires special attention if heat exchange processes or free surface dynamics are important. Despite being popular in industry due to their easy implementation and simulation speed, drawbacks of eddy-viscosity turbulence models based on Reynolds averaging, such as the k-ε model [69], have been demonstrated for simulation of temperature distribution in induction crucible furnaces [14] and liquid metal free surface shape in EM levitation [66]. Applying more advanced and accurate turbulence models, such as Large Eddy Simulation (LES), provides results that more closely agree to experiments.

1.3.2 Free surface models

Studying free surface dynamics requires a good interface tracking or capturing algorithm. Deforming or moving mesh approach, based on the kinematic boundary condition on the surface (fluid particles cannot cross the surface), is the most accurate in the case of small surface deformations. In this approach, mesh nodes initially on the free surface follow it during the simulation. This method has been applied, for example, to study liquid metal flows with free surface driven by AC and DC EM field [70], implementing all equations into FEM framework. In the case of topological changes (drop separation, splashing etc.), this approach requires special treatment, making the numerical models rather complicated and expensive.

For liquid metal MHD with free surface, the models need to be as flexible as possible, as the melt volume can move rapidly and can assume virtually any shape depending on excitations. There are several free surface capturing methods for a fixed numerical mesh allowing topological changes of the interface. Particle methods, such as Marker-And-Cell (MAC) [71], are based on mass-less particles distributed throughout the fluid that are convected with the flow velocity. In two-phase flows, if one phase contains particles but the other not, the interface is then at numerical cells around which there are both empty and filled cells. The main disadvantage of particle methods is the memory requirements to store all the particle data.

A popular method similar to MAC but requiring much less memory is the Volume of Fluid (VOF) method [72], based on advection equation for volume fraction α:

$$\frac{\partial \alpha}{\partial t} + \nabla \cdot (\alpha \vec{v}) = 0, 0 \leq \alpha \leq 1 \tag{1.3.1}$$

$\alpha = 1$ for one fluid and $\alpha = 0$ for the other. The VOF model makes it possible to solve only one set of equations for all phases. Density and viscosity are then

$$\rho = \alpha \rho_1 + (1 - \alpha)\rho_2 \tag{1.3.2}$$

$$\mu = \alpha\rho_1 + (1-\alpha)\mu_2 \tag{1.3.3}$$

where indices 1 and 2 designate fluid 1 and 2, respectively. It does not matter which phase has $\alpha = 1$ and which $\alpha = 0$, as long as it is used consistently throughout the model. The volume fraction does not provide the interface directly but only a percentage of each fluid at each cell. With VOF, interface between the phases is represented implicitly by $0 < \alpha < 1$.

With liquid metals, it is very important to consider surface tension. The effect of surface tension is the tendency of fluid to minimize its free surface. This leads to added pressure in the liquid volume proportional to surface tension coefficient γ and local surface curvature κ. This surface tension pressure is normal to the surface and can be modelled as normal forces. Numerically, using the VOF method this is easily implemented using the Continuum Surface Force (CSF) method as an additional body force acting only at the surface (where $\nabla\alpha \neq 0$) [73]:

$$\vec{f_s} = \gamma\kappa\nabla\alpha \tag{1.3.4}$$

where $\kappa = -\nabla \cdot \vec{n}$, $\vec{n}$ - surface normal.

A disadvantage of the VOF method with the CSF model is the problem of spurious currents - unphysical acceleration of fluid at the interface cells where the volume fraction changes from 0 to 1.[74] This is because a discretized α field is not smooth along the interface cells and the resulting surface tension force has erroneous components. This effect is especially pronounced in surface tension dominated flows, like liquid metal flows. The problem can be partly solved by, for example, combining the VOF method with some other model which can provide more accurate surface normals and curvatures, such as the Level-Set method [75] or applying some smoothing to the α field during calculation of the curvature. A comprehensive review of different approaches to surface tension treatment with the VOF method is provided in [76].

Spurious currents are a problem only when surface tension is the dominant force, such as for static or slowly moving droplets and bubbles. In most cases considered in the thesis, Lorentz force or fluid inertia dominate, hence the spurious currents do not pose a problem in these calculations. An exception to some degree is the case with circular drops in transverse high-frequency magnetic field. In that case, spurious currents can cause the drops to oscillate in a very similar way as due to electromagnetic forces. Smoothing of the α field [77][78], which is used in the thesis, helps reducing these numerical effects. The implementation in OpenFOAM can be found in [79].

Since α field is not discontinuous, the phase boundary, where $0 < \alpha < 1$, is smeared over a number of cells, depending on applied discretization schemes. There are different approaches to treat the interface and to reduce numerical smearing with VOF. It can be either reconstructed geometrically, such as by piecewise linear interface calculation (PLIC) [80], or by using compression schemes to ensure a sharp interface [81]. Geometrical reconstruction is more accurate at the expense of higher computational cost [82][83]. Some studies report that no grid-convergence can be achieved with interface compression, for example, for a rising gas bubble [84]. However, the exact source of this is not clear and the accuracy and correctness of results should be assessed by other means, not just by

performing grid convergence. Both PLIC and interface compression are implemented in OpenFOAM. Due to cheaper computations, interface compression with volume fraction smoothing will be used in the thesis. For verification and validation, OpenFOAM simulations will be compated to simulations using other software, as well as to experiments.

Regarding free surface MHD problems, special care must be taken when applying electromagnetic forces to one of the phases (liquid metal). Since the volume fraction α is not completely discontinuous at the interface, i.e. there are numerical mesh cells where it is between 0 and 1, some portion of the gas phase can be unphysically accelerated [66][85]. This can be solved by multiplying the electromagnetic force by the volume fraction α every time-step of the simulations, as well as refining the mesh near the interface.

VOF method has been successfully applied to simulate many different two-phase flows with liquid metal, such as gas bubble flows [86][87][88], free surface waves [89][47], electromagnetic semi- and full levitation [52][66] and others.

1.3.3 Multiphysics coupling

The problem of coupling between electromagnetics and fluid flow has been addressed by many researchers in the past. The simplest approach of calculating liquid metal free surface shape in steady high-frequency magnetic field is by finding the balance between electromagnetic pressure, gravity and surface tension forces [90][14]. In such a case, effect of fluid flow on the surface shape is ignored. This is adequate for finding approximate steady shape of the free surface but cannot be used to study melt surface dynamics in time.

Adequate simulation of transient free surface dynamics requires solution of velocity in the melt volume, as well as the surface changes. Electromagnetics and fluid flow can be solved using separate numerical frameworks or programs that can then be coupled. Segregated coupling between two separate programs has been done recently in [66], where simulation of liquid metal electromagnetic levitation has been performed using external coupling between commercial packages ANSYS Emag (electromagnetic part) and Fluent (fluid flow part). The results are in a good agreement to experiments regarding free surface shape for different levitation installations. Additional result of [66] is the confirmation of the validity of VOF approach - simulated liquid metal free surface oscillations are in a good agreement to analytical calculations. A similar coupling between ANSYS Emag and Fluent is reported in [91] to simulate electroslag remelting process, giving excellent agreement to experiments for the melt pool profile.

The disadvantage of the segregated coupling described above is the simulation time – the external coupling between the two software packages is file-based, which means that in every iteration of data communication between the two programs files are written to hard drive, which is a slow process compared to data exchange within random access memory (RAM). Another drawback is the use of commercial software, which can be quite expensive.

The latest development in coupled liquid metal MHD simulations is the recently developed EOF-Library [92][93] which effectively couples open-source codes OpenFOAM [94]

and Elmer [95]. OpenFOAM is an FVM-based library and Elmer is a FEM-based software. The coupling library does not use writing to disk for data communication and therefore the simulations are considerably faster. Additional advantage is that all of these codes are free and open-source, which removes any license limitations and allows code modification to customize mathematical models. This library has already been applied to simulate liquid metal pumping or stirring by rotating permanent magnets [A.5][A.6][96], electromagnetic levitation [85], as well as low-frequency alternating magnetic field induced liquid metal free surface waves [97][47].

Due to their flexibility and customizability, OpenFOAM is used to simulate fluid dynamics and heat transfer, Elmer is used for electromagnetics, with EOF-Library facilitating coupling between the two softwares. A few custom mathematical models will be implemented in OpenFOAM to simulate solidification and melting and to enable more efficient simulation of coupled MHD problems.

1.4 Experimental methods

The main tool of research in the thesis is numerical modelling. However, experiments are usually required to validate the numerical models. This section review typical experimental methods used to study liquid metal flows and MHD.

Methods for flow measurement is an active field of research. This subsection presents the current trends in flow measurement in liquid metals. The main difficulty in measuring flow velocity in liquid metal is its opacity. Optical methods with particle tracing, such as Particle Image Velocimetry (PIV) [98], are not applicable.

Two most popular methods for measuring flow velocity in liquid metals are the Ultrasonic Doppler Velocimetry (UDV) [99] and the potential difference probe (often called Vives probe) [100]. A review of both methods can be found in [101][102]. UDV works on the principle of reflection of pulsed ultrasound signal from particles or any inhomogeneities in the liquid. The reflected signal or echo contains frequency shifts that relate to the velocity of the particles parallel to the direction of the ultrasound beam. Flow velocity is reconstructed from a correlation between consecutive bursts of ultrasound. UDV allows measuring velocity profile along the direction of the beam. Combining multiple probes in arrays allow mapping 3D velocity distribution [103]. The main disadvantages of UDV include the requirement for microparticles for reflecting the beam, limited use in high temperatures and spatial and temporal resolution.[102]

Vives probe consists of a small permanent magnet between small electrodes. Motion of electrically conducting fluid perpendicular to the magnetic field induces voltage between the electrodes. The voltage correlates to the flow velocity. Vives probe allows simultaneous measurement of two velocity components only at a point (or a small volume due to finite size of the probe), although with high sensitivity and high temporal resolution.[102] A major disadvantage of the Vives method is that the probe must be submerged in the melt, which may disturb the flow, as well as the limitation of temperature that has to be below the Curie point of the permanent magnet.

A more advanced non-contact velocity measurement technique, called Lorentz force

velocimetry (LFV) [104], involves measuring force exerted by the flow of electrically conducting fluid on a small magnet located close to the flow channel or vessel. The measurement system can be arranged as a single magnet (measuring force) or as multiple magnets on a rotating wheel (measuring torque). The force acting on the magnet is due to magnetic field of the eddy current induced in the liquid metal. The magnet must be weak enough not to disturb the flow. The force or torque is directly related to the flow velocity. An interesting modification of this method is a single rotating magnet, which is set into rotation by the torque from the moving conductor. The rotation rate of this single magnet, which correlates to the velocity of the conductor, is independent of the electrical conductivity of the conductor and the magnetization of the magnet, given that friction and other factors are negligible compared to the torque.[105] A disadvantage of LFV and similar methods is temperature limitations and that the correlation of force to flow velocity must be found for each setup individually, as it depends not only on the electrical conductivity, but also flow distribution.[106][104]

Further in the complexity list are tomography methods, such as X-ray [107] and neutron radiography [108][109]. Both methods require something in the melt for contrast, such as gas bubbles or tracer particles. If particles are to be used as flow tracers, they must be very small to follow the flow. The tracers must have density as close to that of the liquid metal as possible and they must have considerably higher radiation attenuation coefficient. Moreover, radiography resolution and other factors may dictate the size of the particles.[110][109] Furthermore, extracting flow velocity from radiography images can involve complicated image analysis.[111][108] Lastly, radiography methods require access to expensive facilities, which may not be readily available.

During development of the thesis, UDV was used to measure velocity in multiple setups. However, it proved to be difficult to achieve reliable results. This was due to limitations of the UDV method (poor signal quality), as well as limitations of the setups (relatively thin melt layers). Measuring flow velocity was not a priority in the thesis. Experiments were mainly done for validating numerical models. Since the main aspect is free surface dynamics, flow velocity was of secondary importance. It must be mentioned, however, that in some situations bulk flow velocity directly correlates to the deformation of the free surface. According to a large Weber number (flow inertia dominates over surface tension) in the case of stirring by rotating permanent magnets, the strong upwards flow is mostly responsible for deforming the surface. This means that flow velocity is implicitly represented by the surface deformation.

Studying free surface motion is usually easier than the bulk flow. Often, the free surface can be simply recorded using a digital camera. However, to allow quantitative measurements and analysis, more sophisticated methods can be used. Various configurations of laser scanning, such as projecting a line onto the surface [112][44], can be used in conjunction with some data processing to obtain the shape of the free surface.

In the thesis, for the experiment where free surface is agitated by a rotating permanent magnet, a simple technique with surface projections was employed. The surface motion was filmed using a backlight, which generated images of dark melt volume and bright

background. It was relatively easy to process such contrast images, finally obtaining quantitative data about the free surface dynamics. This is described in more detail in the experimental work section.

All experiments in the thesis are relatively simple regarding measurements. In most cases, simple recording of the free surface with a camera was sufficient to obtain enough information for validating the numerical models.

2 Theoretical background

This section provides a brief mathematical basis of the physical processes considered in the thesis - turbulent two-phase fluid flow with free surface, heat transfer with phase change, electromagnetics and the coupling between these effects. The following sections are devoted to each of these aspects.

2.1 Fluid dynamics

In most cases, liquid metal can be considered to be an incompressible Newtonian fluid. So can the other phase, gas or acid solution, typically present in the cases considered in the thesis. Fluid flow is described by the Navier-Stokes equations for incompressible fluid:

$$\frac{\partial \rho \vec{v}}{\partial t} + (\vec{v} \cdot \nabla)(\rho \vec{v}) = -\nabla p + \nabla \cdot (\mu(\nabla \vec{v} + \nabla \vec{v}^T)) + \vec{f}_V \tag{2.1.1}$$

$$\nabla \cdot \vec{v} = 0 \tag{2.1.2}$$

where ρ - density, p - pressure, $\vec{v}$ - flow velocity, μ - dynamic viscosity. $\vec{f}_V$ includes all volumetric forces. The main forces relevant in this work are gravity $\vec{f}_g = \rho \vec{g}$, Lorentz force $\vec{f}_L = \vec{j} \times \vec{B}$ and those arising from surface tension $\vec{f}_s$. Surface tension is generally a surface force, however, in the Volume of Fluid method, that is used in the thesis, it is defined as a volumetric force acting in the mesh cells where the interface is located (see section 1.3.2).

2.1.1 Turbulence

It is generally assumed that equation (2.1.1) fully describes turbulent flows. In that case, solution of this equation would give all information about the flow in question. Turbulent flow contains many different time and length scales, ranging from geometry scale down to dissipation scale. Complete numerical solution of a flow is called Direct Numerical Simulation (DNS), in which all flow structures are resolved, which means that the numerical grid must be fine enough to resolve every small detail down to the dissipation scale. In industrial applications and engineering, using DNS is unreasonable, firstly because Reynolds number in industrial flows can be very large, meaning that DNS is unfeasible even using supercomputers. Secondly, the smallest details may not be important in practical applications.

Considerably more affordable approach is the Large Eddy Simulation (LES), which directly resolves large-scale structures, while modelling the smallest scales. LES applies filtering to the Navier-Stokes equations, which essentially lead to decomposition of flow variable ϕ into the resolved part $\overline{\phi}$ and unresolved part ϕ', i.e. velocity $v = \overline{v} + v'$. Strictly mathematically, the filtering is different from the Reynolds decomposition detailed below, but the decomposed equations have a very similar form - Navier-Stokes equations for the resolved or filtered part, plus a new unknown term of the form $\tau_{ij} = -\overline{v_i v_j} + \overline{v}_i \overline{v}_j$ (i,j denote components). A popular way of dealing with the unresolved part to close the

model is to use the eddy-viscosity or Boussinesq hypothesis:

$$\tau_{ij} = -\overline{v_i v_j} + \overline{v}_i \overline{v}_j = 2\nu_t \left(\frac{\partial \overline{v}_i}{\partial x_j} + \frac{\partial \overline{v}_j}{\partial x_i} \right) - \frac{2}{3} k \delta_{ij} = 2\nu_t \overline{S_{ij}} - \frac{2}{3} k \delta_{ij} \tag{2.1.3}$$

where ν_t is eddy viscosity, δ_{ij} - Kronecker delta, S_{ij} - strain rate, $k = \frac{1}{2}(\overline{v}_i \overline{v}_i - \overline{v_i v_i})$ - turbulence kinetic energy. The problem is now calculating ν_t instead of the complicated term $\overline{v}_i \overline{v}_j - \overline{v_i v_j}$. There are many models to find ν_t, such as the classical Smagorinsky model [113], $\nu_t = (C_s \Delta)^2 \sqrt{2 S_{ij} S_{ij}}$, where C_s is a constant and Δ is the filter width (e.g. related to the size of the mesh element).

Much cheaper way of simulating turbulent flows is using Reynolds-Averaged Navier-Stokes (RANS) turbulence models. The main idea of this approach is decomposing instantaneous variables as $v = \overline{v} + v'$, where $\overline{v}$ is a time-averaged variable and v' is a fluctuation. Applying this to (2.1.1) and time-averaging, after some mathematical manipulations RANS equation is obtained. This new equation is just like (2.1.1) for time-averaged variables with a new term of the form $\overline{v'_i v'_j}$ called the Reynolds stress, where v_i and v_j are fluctuations of different velocity components and overbar means time-averaged. The problem is that this new term is a new unknown and so there are more unknowns than equations. Normally, the Boussinesq hypothesis is used:

$$-\overline{v'_i v'_j} = 2\nu_t \overline{S_{ij}} - \frac{2}{3} k \delta_{ij} \tag{2.1.4}$$

where $k = \frac{1}{2}\overline{v_i v_i}$ - turbulence kinetic energy. Now the unknown is the turbulent viscosity ν_t and it is calculated using turbulence models.

A typical RANS model used in industry is the k-ε [114], where k is turbulence kinetic energy and ε - turbulence dissipation rate. It assumes that $\overline{v'_i v'_i} = \overline{v'_j v'_j} = \overline{v'_k v'_k} = \frac{1}{3}k$. Additional equations for k and ε are solved and then the turbulent viscosity is calculated as $\nu_t = C_\mu k^2/\varepsilon$, $C_\mu = 0.09$ is a model constant. Another popular model is k-ω SST [115] which solves additional equations for k and ω (specific rate of dissipation). This model combines the advantages of k-ε model in free shear regions and standard k-ω model in near wall regions. Note that, while the basic idea of RANS models involve time-averaging, these models are often reformulated in time-dependent form as Unsteady RANS (URANS). This approach allows resolving some part of fluctuations [116] in time-dependent flows.

Somewhere between LES and RANS or URANS lies the Detached Eddy Simulation (DES) [117] approach. It combines RANS in regions of low spatial resolution (e.g. near walls where boundary layers are not resolved) and LES everywhere else. Many RANS models can be reformulated to be DES models, such as k-ω SST [117][118]. DES has been shown to give very good results compared to RANS and LES.[119]

Different turbulence models are suited for different flows, there is no one model that fits all cases. More theoretical background on turbulence modelling can be found in [120]. A thorough review of turbulence models is provided in [116]. In the thesis, where appropriate, the RANS k-ω SST (in axisymmetric or 2D models), LES or DES models (where resolving free surface fluctuations is important) are used. The use of specific models are mentioned in the corresponding descriptions of the numerical models.

2.2 Heat transfer

Thermal effects are considered in the model of direct strip casting. Heat transfer is modelled using the temperature equation with latent heat [121]:

$$\frac{\partial}{\partial t}\left(\rho c_p T\right) + \nabla \cdot \left(\rho c_p \vec{v} T\right) = \nabla \cdot \left(\kappa \nabla T\right) - L_T \left(\frac{\partial}{\partial t}(\rho\beta) + \nabla \cdot \left(\rho \vec{v} \beta\right)\right) + Q \tag{2.2.1}$$

where c_p - specific heat capacity, $\vec{v}$ - flow velocity, κ - thermal conductivity, L_T - latent heat of phase change, β - liquid fraction, Q - volumetric heat sources. Natural convection (thermal buoyancy) and thermal radiation are ignored. In the belt casting case, most of the heat losses are through the intensively-cooled belt, and so radiation plays a minor role. Also, since the melt layer is thin (order of 1 cm), buoyancy is negligible. Buoyancy in the gas phase might be notable, but the density of the gas is much smaller than that of the liquid metal, therefore it can be ignored in this case (gas flow does not affect the flow of liquid metal).

Volumetric heat source in the casting process is only from the Joule heat due to induced electric currents $\vec{j}$, $Q = \frac{|\vec{j}|^2}{\sigma}$, where σ - electric conductivity.

2.3 Electromagnetics

Electric and magnetic field is described by the Maxwell's equations (2.3.1)-(2.3.4), Ohm's law (2.3.5) and charge conservation (2.3.6):

$$\nabla \cdot \vec{E} = \frac{\rho_e}{\epsilon_0} \tag{2.3.1}$$

$$\nabla \cdot \vec{B} = 0 \tag{2.3.2}$$

$$\nabla \times \vec{E} = -\frac{\partial \vec{B}}{\partial t} \tag{2.3.3}$$

$$\nabla \times \vec{B} = \mu_0 \vec{j} + \frac{1}{c^2}\frac{\partial \vec{E}}{\partial t} \tag{2.3.4}$$

$$\vec{j} = \sigma\left(\vec{E} + \vec{v} \times \vec{B}\right) \tag{2.3.5}$$

$$\frac{\partial \rho_e}{\partial t} + \nabla \cdot \vec{j} = 0 \tag{2.3.6}$$

where $\vec{E}$ - electric field intensity, $\vec{B}$ - magnetic flux density, ρ_e - charge density, ϵ_0 - vacuum electric permittivity, μ_0 - vacuum permeability, $\vec{j}$ - current density, σ - electrical conductivity, $\vec{v}$ - velocity of electrically conducting fluid. Magnetic materials are not considered in the thesis.

Last term in (2.3.4) is called displacement current, which, in the case of liquid metal MHD can usually be neglected (this can be seen if one compares the magnitudes of the terms involved for some test case).

Charge density ρ_e is also irrelevant here. It is known that electric charges (free electrons) in metal redistribute to compensate external electric field. In alternating field case,

since relaxation time of electric charges $\tau = \epsilon_0/\sigma$ is much smaller than the EM field oscillation period, it can be assumed that in every time instant the charges have achieved equilibrium distribution.

Equations (2.3.1) and (2.3.2) are usually used as constraints when deriving equations that are solved numerically. In the numerical methods used in the thesis, the EM equations are not solved for $\vec{E}$ and $\vec{B}$ directly. Instead, $\vec{E}$ and $\vec{B}$ are rewritten using electric scalar potential ϕ and magnetic vector potential $\vec{A}$ [122]:

$$\vec{E} = -\nabla\phi - \frac{\partial \vec{A}}{\partial t} \tag{2.3.7}$$

$$\vec{B} = \nabla \times \vec{A} \tag{2.3.8}$$

To make the fields unique, some additional constraints for ϕ and $\vec{A}$ are needed. The most usual choice is to make $\phi \to 0$ at infinity and apply the Coulomb gauge $\nabla \cdot \vec{A} = 0$.[122] The equations for the numerical model are then:

$$\Delta\vec{A} = -\mu_0\vec{j} \tag{2.3.9}$$

$$\vec{j} = \sigma\left(-\nabla\phi - \frac{\partial \vec{A}}{\partial t} + \vec{v} \times \vec{B}\right) + \vec{j}_s \tag{2.3.10}$$

$$\nabla \cdot \vec{j} = 0 \tag{2.3.11}$$

where $\vec{j}_s$ are source currents (inductor current etc.). If the magnetic field is due to permanent magnets, $\vec{j}_s = \nabla \times \vec{M}$, where $\vec{M}$ is magnetization. In cases where the currents in liquid metal are due to induction (as opposed to direct injection), $\vec{j}_s$ in liquid metal are zero.

In the thesis, one of the processes is liquid metal stirring by rotating permanent magnets. In that case, the rotating magnet is a diametrically magnetized cylinder rotating about its axis. The rotation is modelled as time-dependent magnetization vector $\vec{M} = \vec{M}(t)$. A magnet with magnetization amplitude M_0 rotating around the Z axis can be described as:

$$\begin{cases} M_x = M_0 cos\,(\omega t) \\ M_y = M_0 sin\,(\omega t) \end{cases} \tag{2.3.12}$$

where $\omega = 2\pi f$, f - frequency.

Sinusoidally oscillating fields are often modelled in frequency domain using phasor notation to simplify calculations. For example, vector potential is written as $\vec{A} = \vec{A}_0 cos(\omega t) = Re\{\vec{A}_{0C}e^{i\omega t}\}$, where subscripts 0 and C denote amplitude and a complex field, respectively. In complex form, the time-dependent exponents drop out of equations, which are then solved for the amplitudes. The rotating magnetization in complex form is $M_{x,re} = M_0$, $M_{y,im} = M_0$.

There are two variables from EM that come into play in fluid dynamics and heat transfer - Lorentz force $\vec{f}_L$ and Joule heat q_{EM}.

$$\vec{f_L} = \vec{j} \times \vec{B} \tag{2.3.13}$$

$$q_{EM} = \frac{|\vec{j}|^2}{\sigma} \tag{2.3.14}$$

Using Maxwell's equations and vector calculus, $\vec{f_L}$ can be decomposed into potential (irrotational) and rotational parts:

$$\vec{f_L} = \vec{j} \times \vec{B} = -\frac{1}{2\mu_0}\nabla B^2 + \frac{1}{\mu_0}(\vec{B} \cdot \nabla)\vec{B} \tag{2.3.15}$$

The term $\frac{B^2}{2\mu_0}$ is sometimes called the magnetic pressure. As a potential force, the first term on the right in Eq. (2.3.15) is responsible for deforming the free surface. The rotational part, the last term in Eq. (2.3.15), drives fluid flow. If frequency f is high, such that skin depth $\delta = \frac{1}{\sqrt{\mu_0 \pi f \sigma}}$ is small, the potential part dominates. This is utilized, for example, in electromagnetic levitation [123][52], where EM forces support levitating liquid metal drops. Of course, in most practical applications, both potential and rotational parts co-exist. In simulations in the thesis, however, these parts are not considered separately. Lorentz force from EM simulations is simply as in Eq. (2.3.13).

When considering oscillating electric and magnetic field, say, $\vec{j} = \vec{j_0}cos(\omega t)$ and $\vec{B} = \vec{B_0}cos(\omega t + \phi_{em})$, where ϕ_{em} is phase, the Lorentz force can be decomposed into the time-average and oscillating part [124]:

$$\vec{f_L}(t) = \vec{j}(t) \times \vec{B}(t) = \vec{j_0} \times \vec{B_0}cos(\phi_{em}) + \vec{j_0} \times \vec{B_0}cos(2\omega t + \phi_{em}) \tag{2.3.16}$$

Notice that the force oscillates with double the frequency of current and magnetic field. As already discussed in section 1.2, in low-frequency cases, the oscillating part can directly influence the fluid. In high-frequency cases, the fluid may not respond to the oscillating part due to inertia.

In the low-frequency cases in the thesis (stirring by rotating permanent magnets), the time-averaged and oscillating parts are not considered separately. Lorentz force in those cases is simply $\vec{f_L}(t) = \vec{j}(t) \times \vec{B}(t)$. In high-frequency cases, however, the oscillating part is completely neglected.

2.4 Dimensionless parameters

The importance of different physical effects can be assessed using dimensionless parameters, which are obtained from non-dimensionalizing equations describing the processes. In fluid dynamics, there are several parameters relevant for free surface flows studied in this work. The first is the Reynolds number

$$Re = \frac{\rho U L}{\mu} \tag{2.4.1}$$

where U - velocity scale, L - characteristic size of the system. It basically determines whether the flow is laminar or turbulent. It is usually said that if $Re > 2000$ the flow is

turbulent. In liquid metal flows, since density is relatively high and viscosity low, Re can easily be above 10^4, so the flows are usually fully turbulent.

A ratio between fluid inertia and surface tension forces is called the Weber number

$$We = \frac{\rho U^2 L}{\gamma} \tag{2.4.2}$$

where γ - surface tension coefficient. This parameter is normally useful in studying formation of droplets and bubbles. We is relevant in this work. In the process of stirring by rotating permanent magnets, We characterizes how much the free surface deformation is influenced by the surface tension. If $We >> 1$, surface tension plays a minor role, and the surface deformation is mostly due to the bulk flow (dynamic pressure).

Another important parameter is the capillary number

$$Ca = \frac{\mu U}{\gamma} \tag{2.4.3}$$

describing relative effect of viscous and surface tension forces. Ca determines whether free surface oscillations are small linear capillary waves influenced mainly by surface tension or large nonlinear waves with breaking etc. determined by gravity or other forces.

If heat transfer processes are considered, several additional effects come into play. Prandtl number, independent of flow, describes a specific fluid - it is a ratio between momentum and thermal diffusivities:

$$Pr = \frac{c_p \mu}{\kappa} \tag{2.4.4}$$

Prandtl number basically determines relative thickness of viscous and thermal boundary layers. For liquid metals $Pr \sim 10^{-2}$, so that heat diffuses quicker than momentum and so the thermal boundary layer is much thicker than the velocity boundary layer.

Bond, or Eotvos, number is a ratio between gravitational and surface tension forces:

$$Bo = \frac{\Delta \rho g L^2}{\gamma} \tag{2.4.5}$$

where $\Delta\rho$ - density difference between two fluids, g - gravitational acceleration. For liquid metal volumes resting on solid surfaces, Bo characterizes the influence of surface tension on the shape of the liquid metal volume and how easily it can deform. Sometimes, a generalized Bond number is introduced as $Bo^* = Bo - Ca$ [125], which also takes into account viscous forces within the capillary number Ca. Since for liquid metals $Ca \ll 1$, $Bo^* \approx Bo$, and we can simply consider the regular Bo.

Several dimensionless numbers are used to analyse MHD flows. One of them is the ratio of advection and diffusion of magnetic field, called the magnetic Reynolds number

$$Re_m = \mu_0 \sigma U L \tag{2.4.6}$$

This parameter can be used to estimate the ratio between external (primary) magnetic field B_0 to the secondary (induced) field b due to fluid flow. Writing total magnetic

field as $\vec{B} = \vec{B}_0 - \vec{b}$ (the secondary field opposes the primary, hence the minus sign), and considering Eqs. (2.3.4) and (2.3.5) in magnitudes ($\nabla \sim \frac{1}{L}$), one can obtain the relationship between Re_m, $B_0 \sim |\vec{B}_0|$ and $b \sim |\vec{b}|$ as $b = \frac{Re_m}{1+Re_m} B_0$. If $Re_m << 1$, magnetic field induced by the conductive fluid flow is negligible, which can simplify numerical modelling since fluid velocity can be neglected in magnetic field simulation.

A purely electromagnetic parameter is the shielding factor or dimensionless frequency

$$R_\omega = \mu_0 \sigma \omega L^2 = \left(\frac{L}{\delta}\right)^2 \tag{2.4.7}$$

that basically is square of the ratio between characteristic length L (e.g., radius in axisymmetric cases) and electromagnetic field penetration depth δ at angular frequency ω. Analogously to Re_m, R_ω also relates secondary field to primary as $b = \frac{R_\omega}{1+R_\omega} B_0$ (b here is due to time-varying magnetic field instead of fluid flow). R_ω is used to analyse stirring efficiency in induction crucible furnaces - the characteristic velocity is nonlinearly dependent on R_ω with a saturation at some specific value.[126] Due to a wide range of frequencies considered in the thesis (from 1 to $\sim 10^3$ Hz), R_ω can also have very different values.

Hartmann number

$$Ha = BL\sqrt{\frac{\sigma}{\mu}} \tag{2.4.8}$$

where B - characteristic magnetic flux density magnitude, characterizes the ratio between electromagnetic and viscous forces. It is usually used in studying wall bounded electrically conductive liquid flows in magnetic field to estimate boundary layer thicknesses and velocity profiles.[8]

In free surface MHD flows, magnetic Bond number is a ratio between electromagnetic force f_L and surface tension:

$$B_m = \frac{L^2 f_L}{\gamma} \tag{2.4.9}$$

When analysing liquid metal free surface flows, f_L can be estimated differently, depending on magnetic field source and other considerations. Generally, $f_L \sim jB$, where j is induced current. Using Faraday's law, $j \sim \sigma f B L$, and $B_m = \frac{\sigma f B^2 L^3}{\gamma}$. When field source is an inductor with current I and number of windings per unit height N_i, $B_m = \frac{\sigma f (\mu_0 N_i I)^2 L^3}{\gamma}$. The formula using magnetic field instead of current may be more accurate in cases where the inductor has only a few windings, in which case the inductor leads have larger influence on the field. f_L can also be acquired from a numerical model as the characteristic EM force magnitude on the surface of liquid metal.

Many dimensionless parameters can be expressed as functions of others. One of such is the ratio between electromagnetic forces and fluid inertia, called the interaction parameter or Stuart number

$$N = \frac{B^2 L \sigma}{\rho U} = \frac{Ha^2}{Re} \tag{2.4.10}$$

This parameter appears in dimensionless Navier-Stokes equations as a coefficient to electromagnetic forces. Naturally, if $N << 1$, electromagnetic forces play a negligible role in

determining the flow, unless the main flow is driven by those forces (then the parameter has little significance).

All relevant dimensionless parameters and their ranges for liquid metal MHD with free surface are summarized in Table 2.4.1. Note that exact values can differ between studies depending on how characteristic sizes and other factors are considered. For example, characteristic size L can be taken as the diameter of the system or cube-root of the volume.

Table 2.4.1: Characteristic ranges of dimensionless parameters relevant to liquid metal MHD with free surface

Parameter name	**Formula**	**Range**
Reynolds number	$Re = \frac{\rho U L}{\mu}$	10^4 - 10^6
Weber number	$We = \frac{\rho U^2 L}{\gamma}$	10^{-3} - 10^2
Capillary number	$Ca = \frac{\mu U}{\gamma}$	10^{-5} - 10^{-3}
Prandtl number	$Pr = \frac{c_p \mu}{k}$	10^{-2} - 10^{-1}
Bond number	$Bo = \frac{\Delta \rho g L^2}{\gamma}$	1 - 10^2
Magnetic Reynolds number	$Re_m = \mu_0 \sigma U L$	10^{-3} - 10^0
Shielding factor	$R_\omega = \mu_0 \sigma \omega L^2$	10^{-3} - 10^3
Hartmann number	$Ha = BL\sqrt{\frac{\sigma}{\mu}}$	10^0 - 10^4
Magnetic Bond number	$B_m = \frac{\sigma f B^2 L^3}{\gamma}$	10^{-1} - 10^5
Interaction parameter	$N = \frac{B^2 L \sigma}{\rho U}$	10^{-4} - 10^4

3 Numerical models

This section presents the description of the developed numerical models. The main simulations are done using Elmer for EM, OpenFOAM for fluid flow, heat transfer, solidification, and EOF-Library for coupling the two programs. This combination will be referred to as EOF.

For verification purposes, EM equations were also implemented directly in OpenFOAM, which was applicable to some limited cases. More details are presented in section 3.2.

As an extra layer of verification of the coupled simulations of Elmer and OpenFOAM, a simple framework for coupling ANSYS CFX and Maxwell was also created. This is described in section 3.3.

The final numerical models, which will be used to study different liquid metal MHD cases, including the ones corresponding to the laboratory experiments, are described in section 3.7.

3.1 Elmer and OpenFOAM

Elmer is an open-source software for simulation of multiphysical problems using FEM.[95] It has capabilities for solid mechanics, acoustics, electromagnetics etc. It can also solve fluid flow, but being based on finite element method, it is not the best for that. Elmer can use structured and unstructured grids composed of triangular and quadrangular elements in 3D, and tetrahedrons, hexahedrons, prisms and pyramids in 3D. The built-in mesher, however, is too basic, and the meshes are mostly generated in external software, such as Salome or Gmsh. In the thesis, Elmer is used exclusively for electromagnetics.

OpenFOAM is an open-source C++ library for simulating different physical problems using FVM.[94] It is mainly used for fluid dynamics and heat transfer. OpenFOAM has only 3D capabilities. To simulate 2D and axisymmetric problems, planar or wedge meshes with one element thickness must be used with symmetry boundary conditions. OpenFOAM supports different types of elements, ranging from triangular to polyhedral. It has a built-in mesher, `blockMesh`, which can generate relatively simple hexahedral meshes. Alternatively, mesh can be generated in many other programs, as OpenFOAM can import many different formats. One of the benefits of OpenFOAM is a large user community, which means that a lot of information and help can be found online. In the thesis, OpenFOAM is used to simulate fluid dynamics with free surface, turbulence, heat transfer, solidification, as well as some parts of electromagnetics.

EOF-Library [92][93] enables efficient solution of liquid metal MHD using Elmer and OpenFOAM software. The library provides data exchange and interpolation between Elmer and OpenFOAM models. To solve specific problems using the EOF-Library, some programming on the OpenFOAM side is usually needed. First and foremost, some code must be included in OpenFOAM solvers to enable communication with Elmer. As part of this, specific coupling algorithms were implemented, i.e. how, what and when to exchange

between Elmer and OpenFOAM.

There are many coupling algorithms, each appropriate for specific cases. For example, the simplest coupling scheme is calculating EM fields only once and then proceeding with the fluid simulation. This approach may be appropriate for single-phase systems (liquid metal in a closed container, for instance) where flow velocity does not influence EM fields, i.e. where $\sigma\vec{v} \times \vec{B}$ is small compared to current density induced by oscillating magnetic field ($\sigma\frac{\partial\vec{A}}{\partial t}$) or direct injection. In two-phase cases with free surface, this simple approach can be valid for very limited systems depending on position of the surface relative to the Lorentz force distribution. If the induced currents and Lorentz force is concentrated far from the surface and the surface does not deform significantly, EM fields can be calculated only once for the initial free surface shape. This will be employed for simulating the electrovortical flow with free surface. More complex coupling schemes involve updating EM fields based on some criteria involving the conducting liquid region shape and location of the free surface, as well as flow velocity in case $\vec{v} \times \vec{B}$ is important.

The implementation of different coupling schemes is not a difficult task, but different schemes can lead to significantly different simulation times. It is always desirable to simplify numerical models, to reduce simulation time without significantly affecting accuracy. On the other hand, there may be situations where high accuracy is important and the simulation time is not the highest priority, so that the most accurate coupling scheme can be used. This can be the case is one wants to perform a very detailed study of some instability phenomena or simply wants to obtain some benchmark results against which simplified models can be tested.

3.2 MHD in OpenFOAM

For verification purposes, the possibility of solving some MHD problems in OpenFOAM alone was also investigated. Standard OpenFOAM comes with the `mhdFoam` solver for MHD problems. The drawback of it is that it solves the induction equation for magnetic flux density (instead of vector potential) and does not include electric current. This solver can be used to simulate, for example, Hartmann flow where a conducting fluid flow is influenced by external magnetic field. In the cases considered in the thesis, inductors or moving permanent magnets must be included, and induced currents must be calculated, which considerably complicates the models.

Since OpenFOAM is open-source, almost anything can be implemented with appropriate efforts. In this case, it is necessary to solve equations for EM and two-phase fluid flow. The fluid part is already well established in OpenFOAM. For electromagnetics, it was only necessary to implement a few equations - the Ampere's and Ohm's laws etc.

The inconvenient part here is that ideally one would need to simulate inductors/magnets and containers as solids. OpenFOAM has the so-called multi-region solver capabilities that provide a way of simulating both solid and liquid regions. The issue with these solvers is that data exchange between solids and fluids is through the boundaries between them. Such solvers are typically used for conjugate heat transfer where heat is indeed transferred between solids and fluids via boundaries. In electromagnetic cases,

magnetic field must be solved in the entire domain and penetrate the liquid metal, not be transferred to it as a boundary condition on the liquid metal surface, therefore the multi-region solvers are not applicable.

The not-so-universal solution to this is to simulate the whole domain with fluids and inductors/magnets as a fluid region. In such a case there is no problem with magnetic field penetrating liquid metal. But now the liquid metal can flow everywhere, even through the parts which in reality should be solid. This approach can be used in electromagnetic levitation cases, where liquid metal is supported by Lorentz force and surface tension, i.e. there are no container walls. The levitated droplet is repelled from the inductors, so it should not cross them and there would be no problem of the liquid unphysically going through "solids". The air flowing through the "illegal" zones is not a problem, as it is not electrically conducting and so does not interact with magnetic field.

To extend this approach to cases with liquid metal in containers, there is an option in OpenFOAM of setting boundary conditions on some cell faces inside the domain. This means that, in principle, the whole model can be considered as fluid region, like mentioned above, but with some internal walls that constrains the liquid metal like a container. This option does not work by default, since the magnetic field does not penetrate this internal boundary. This is due to the boundary condition for the magnetic vector potential. In OpenFOAM, each boundary in the model has a type (wall, symmetry plane etc.) and for each field boundary conditions must be set on each boundary. The internal boundary is a wall with no-slip and zero gradient condition for velocity and pressure, respectively. For magnetic field, though, this boundary must be ignored, since it should be transparent to magnetic field (like a glass or other non-magnetic and non-conducting container). Because this boundary has to act as a wall for velocity and pressure, its type cannot be changed to something else for magnetic field. The solution to this would be to create a new boundary condition for the wall type in OpenFOAM that simply ignores the boundary for a specified field (magnetic vector potential in this case).

Programming new boundary conditions is not a simple task and the development of full MHD capabilities in OpenFOAM is not the main goal of the work (the main simulation approach used in the thesis is to solve EM in Elmer and fluid flow in OpenFOAM), so it was decided not to go this route. Nevertheless, a general framework of simulating liquid metal MHD in OpenFOAM was still developed in the thesis, which can currently be applied to the levitation problem due to absence of container walls and the need for internal boundaries. This approach can possibly provide valuable data for verification of coupled Elmer/OpenFOAM simulations. The usefulness of such simulations comes mainly from the fact that solving everything in one software package should be more precise, since the coupling occurs every time-step and the errors of interpolation between different meshes do not exist (the mesh is the same for electromagnetics and fluid flow).

Let us focus on developing numerical models for EM levitation. EM equations were implemented in the incompressible two-phase solver `interFoam` that comes with default OpenFOAM package. Introducing magnetic vector potential $\vec{A}$ as $\vec{B} = \nabla \times \vec{A}$ and using the Coulomb's gauge $\nabla \cdot \vec{A} = 0$, Ampere's law is

$$\Delta\vec{A} = -\mu_0\vec{j} \tag{3.2.1}$$

where $\vec{j}$ is the total current density. Using Ohm's law $\vec{j} = \sigma\vec{E} = -\sigma\frac{\partial\vec{A}}{\partial t}$ (for induction by time-varying magnetic field, no external voltage is applied) and separating the source (inductor) currents $\vec{j}_0$ from the induced ones $\vec{j}_i$, equation (3.2.1) reads

$$\Delta\vec{A} = \mu_0\sigma\frac{\partial\vec{A}}{\partial t} + \mu_0\vec{j}_0 \tag{3.2.2}$$

Equation (3.2.2) is basically a Poisson's or diffusion equation for vector potential. Magnetic flux density and induced currents are then, respectively:

$$\vec{B} = \nabla \times \vec{A} \tag{3.2.3}$$

$$\vec{j}_i = -\sigma\frac{\partial\vec{A}}{\partial t} \tag{3.2.4}$$

To add equations (3.2.2), (3.2.3) and (3.2.4) in OpenFOAM, the following code must be included right before the solution of momentum equations:

```
while (pimple.correct())
{
    fvVectorMatrix AEqn
    (
        elcond*mu0*fvm::ddt(A) - fvm::laplacian(A)
     ==
        mu0*j0
    );

    AEqn.solve();
}

B = fvc::curl(A);
j = -elcond*fvc::ddt(A);
```

where `elcond` is electrical conductivity (the name `sigma` is reserved for surface tension coefficient). The `while` loop is for iterative solution of the equation. Lorentz force

$$\vec{f}_L = \vec{j}_i \times \vec{B} \tag{3.2.5}$$

or, in OpenFOAM code,

```
JxB = alpha1*(j^B);
```

is then included in the momentum equations as a source term. `alpha1` is volume fraction equal to 1 in liquid metal and 0 in gas phase.

In EM levitation, magnetic field source is sinusoidal inductor current

$$\vec{j}_0 = \vec{j}_{0A}cos(2\pi ft) \tag{3.2.6}$$

where f is frequency and index A designates amplitude.

Note here that OpenFOAM does not have complex-valued fields, so these equations must be solved as time-dependent with appropriate time-step to resolve the field oscillation period. This is certainly an issue for EM levitation, where the frequency is around 10

kHz. To resolve one sine period with 50 points, a time-step of 2 μs is required. Even though hydrodynamic simulation itself may sometimes require a small time-step to keep the Courant number below 1, such a strict requirement from EM simulation side can often increase simulation time considerably. One way to avoid this can be found by considering the EM field distribution in the liquid metal. The distribution is characterised by the penetration depth

$$\delta = \frac{1}{\sqrt{\mu_0 \pi f \sigma}}. \tag{3.2.7}$$

There are two non-constant parameters - frequency f and conductivity σ. These two basically determine the Lorentz force distribution. Increasing f and decreasing σ by some factor will give the same force density distribution. This was tested in a simple EM induction simulation and was found to be true. Therefore, the frequency can be decreased and the conductivity increased accordingly, to be able to use larger time-steps. This must be done with caution. The frequency must still be high enough for the fluid not to "feel" the force oscillations directly. As shown in [43] for liquid mercury in a cylindrical container with diameter 200 mm, directly induced free surface waves are negligible above 10 Hz. Generally, the threshold frequency depends on material properties, such as density, surface tension and viscosity, as well as size of the system relative to the skin depth. For the case of EM levitation, it was found from test simulations that reducing the frequency and increasing the conductivity by a factor of 100 is adequate.

3.3 ANSYS coupling

Numerical results can usually be verified either analytically, experimentally or numerically by other codes or methods. The main simulation tools of this work are free and open-source software. Established commercial packages can be useful for verification of both individual models (only fluid flow, for example) and coupled magnetohydrodynamics models.

Since we are dealing with coupled MHD processes, for verification purposes a simple coupling framework was developed where ANSYS Maxwell (EM part) exchanges data with ANSYS CFX (fluid dynamics part). Such a segregated approach was necessary because ANSYS has very limited MHD capabilities by default, e.g., MHD systems with inductors cannot be simulated in a single program.

This work deals with simulations of liquid metal MHD flows where free surface effects are important. In many such cases, two-way coupling between EM and fluid flow must be established, because magnetic field distribution depends on the shape of the melt and the melt shape conversely depends on the field (or Lorentz force) distribution. One representative example is EM levitation, where liquid metal volume is supported only by Lorentz force and surface tension. To correctly simulate this process, EM fields must be updated every time the liquid metal shape changes slightly, because otherwise the resulting Lorentz force may not be correct and the liquid would not be supported as it should be. Other examples where the coupling may not be so strong is cases where liquid metal is also supported by container walls or where the Lorentz force distribution does not influence the free surface shape greatly.

This section describes the coupling of commercial software ANSYS CFX, which solves fluid flow with free surface, and ANSYS Maxwell, which solves electromagnetics. ANSYS does not provide automatic data exchange and coupling between these two programs, therefore custom coupling scripts had to be created. The chosen programs can be run from the command line and controlled with scripts. ANSYS Maxwell uses IronPython, a variant of Python programming language, and CFX uses its own CFX Command Language (CCL).

To begin the coupling script development, one must first decide what problems will be solved and what data will be exchanged. Cases relevant to the thesis topic involve incompressible two-phase fluid flow and electromagnetics. Electromagnetic simulation needs information about the location of the conducting fluid and fluid dynamics simulation needs Lorentz force distribution. To make the coupling description and model development easier, let us now consider a particular problem - electromagnetic levitation of liquid metal drop, for which also literature data is available (both numerical and experimental). The coupling approach developed for this problem can later be adapted to other MHD problems.

The following sections provides more details about CFX, Maxwell and the coupling between them.

CFX

CFX consists of three sub-programs - CFX-Pre for preprocessing and case setup, CFX-Solver for numerical solution and CFD-Post for postprocessing. All CFX programs can be run from the command line and controlled using CFX Command Language (CCL) scripts. The CCL script development is made considerably easier by the possibility of recording all manual actions in the program. In other words, one can first manually set up the case, recording the actions and saving them as a CCL script. Then it is possible to repeat the process for different parameters by simply editing the recorded script, changing the necessary parameters and running CFX with it.

CFX-Pre prepares a `.def` file for CFX-Solver. The file contains the mesh and all case settings. If the case building was recorded in a script as mentioned above, then CFX-Pre can be run again with this script by running in the terminal

```
cfx5pre -batch case.pre
```

where `case.pre` is the script that contains all steps for CFX case. The case setup was fully automated by modifying the `.pre` script to parameterize some variables - mesh file, material properties, etc., which are read from a data file that user provides. In that case, the whole coupled simulation can be easily repeated for different parameters etc. The full `.pre` script is not included in the thesis because it really depends on specific case configuration. However, here is an excerpt from the file that reads in mesh and creates a material with relevant properties:

```
> gtmImport filename=mesh_file, \
type=IDEAS, units=m, genOpt=-n, specOpt=-n -f -l, \
nameStrategy= Assembly
```

```
> update

LIBRARY:
  &replace   MATERIAL: liquidmetal
    Coord Frame = Coord 0
    Material Group = User
    Object Origin = User
    Option = Pure Substance
    Thermodynamic State = Liquid
    PROPERTIES:
      Option = General Material
      DYNAMIC VISCOSITY:
        Dynamic Viscosity = melt_viscosity [Pa s]
        Option = Value
      END # DYNAMIC VISCOSITY:
      EQUATION OF STATE:
        Density = melt_density [kg m^-3]
        Molar Mass = 1.0 [kg kmol^-1]
        Option = Value
      END # EQUATION OF STATE:
    END # PROPERTIES:
  END # MATERIAL:liquidmetal
END # LIBRARY:
> update
```

The main coupling script that is described below modifies this `.pre` file and assigns the necessary parameters based on the user data. The result of running CFX-Pre is a `.def` file which is used by the CFX-Solver, which is called by the command

```
cfx5solve -def case.def -fullname results
```

where `case.def` is the solver input file from CFX-Pre and after the simulation a`results.res` file will be created containing all results of CFX. The `.res` file can be opened in CFD-Post for postprocessing. CFD-Post gives an option to save surfaces as STL files. When using the Volume of Fluid method for interface capturing, liquid is usually set volume fraction $\alpha = 1$ and the gas phase has $\alpha = 0$. The free surface is assumed at $\alpha = 0.5$. For 3D cases one would export the iso-surface $\alpha = 0.5$, cut a solid volume with it and send it to Maxwell as the conducting region. In 2D case considered here, one can create a surface based on $\alpha > 0.5$ and already use it as the conducting region.

CFD-Post allows one to record a `.cse` script. In this case the only actions are creating the necessary surface and exporting it as an STL file, as well as saving current volume fraction distribution that will be used to determine the next coupling time (this is described later). To repeat these steps during the coupled simulation when the melt shape changes, CFD-Post is called after CFX-Solver with the following command:

```
cfdpost -res results.res -batch export.cse
```

where `.cse` is the CFD-Post script. Again, the whole script is not included here as it depends on specific case, region names etc, but here is an example of exporting the STL file from CFD-Post:

```
PLANE:Plane 1
  Normal = 1 , 0 , 0
  Option = ZX Plane
  Plane Bound = None
  Plane Type = Slice
  Point = 0 [m], 0 [m], 0 [m]
```

```
  Point 1 = 0 [m], 0 [m], 0 [m]
  Point 2 = 1 [m], 0 [m], 0 [m]
  Point 3 = 0 [m], 1 [m], 0 [m]
END

CONTOUR: Contour 1
  Colour Scale = Linear
  Colour Variable = liquidmetal.Volume Fraction
  Colour Variable Boundary Values = Conservative
  Constant Contour Colour = Off
  Contour Range = Local
  Location List = /PLANE: Plane 1
  Number of Contours = 3
END

USER SURFACE: User Surface 1
  Contour Level = 3
  Contour Name = /CONTOUR: Contour 1
  Option = From Contour
END

EXPORT:
  Export Coord Frame = Global
  Export File = new_melt_stl_file
  Export Type = STL
  Include Header = On
  Location List = /USER SURFACE: User Surface 1
  Overwrite = On
  Precision = 8
  Spatial Variables = X,Y,Z
END
>export
```

where `new_melt_stl_file` is the path to the STL file which is determined by the case path. The CFD-Post script file is edited by the main coupling script at the start of simulation to assign the correct directory paths, file names etc.

To summarize, scripting from CFX side begins with manually creating the case, recording the actions and saving them to text files, and then one can repeat these actions using an external script which can edit these files to change parameters and run CFX-Solver and CFD-Post. The external script will be described later.

Maxwell

Working with Maxwell is relatively easier compared to CFX, because there are no sub-programs, at least they don't have to be run separately. Similarly to CFX, one must first manually create the model. Maxwell has the option to save the case building and solution process in a Python script. To repeat the simulation, one can simply run the following command:

```
ansysedt -features=beta -runscriptandexit scriptname.py projectname.aedt
```

where `scriptname.py` is the Maxwell case script and `projectname.aedt` is an empty Maxwell project file. This command opens Maxwell, executes everything in the script and closes Maxwell.

One slight issue with Maxwell is that the geometry import in STL format sometimes does not work very well. This can be solved by converting it to another format. This is

done using Salome software by running this command:

```
python3 salome-path -t convert.py
```

where `salome-path` is the path to the Salome executable and `convert.py` is a Salome script that imports the STL file from CFX and exports it to IGS format, which is better quality than STL.

A more fundamental problem with Maxwell is that it does not support including velocity distribution, only solid body motion. Therefore the CFX/Maxwell simulations will not consider cases where flow velocity must be included in EM simulation, e.g. cases of large magnetic Reynolds numbers. Another inconvenience is that permanent magnets cannot be included in frequency-domain simulations, a feature that is present in Elmer.

Coupling CFX and Maxwell

The previously mentioned CFX and Maxwell commands must be run sequentially and this process must be repeated for as long as necessary to reach steady state or some other condition. This can be achieved by an external script. In this case, it was a Python script that basically contains a loop within which CFX and Maxwell commands are called using the `subprocess.call()` function. For example, the CFX-Solver command written above is run in Python as

```
subprocess.call(['cfx5solve', '-def', 'case.def', '-fullname', 'results'])
```

The loop condition will determine how often the electromagnetic force is updated in the flow simulation. This condition should take into account melt shape changes. For example, typical condition used in coupled Elmer/OpenFOAM simulations is the maximum difference of volume fraction α between the current values and the ones used in previous EM calculation. Typically, if the change is $\Delta\alpha > 0.5$ in any mesh cell, then the electromagnetic field is updated and the new forces are sent to the flow simulation. A more primitive approach would be to simply set a constant coupling time interval, although it would be difficult to choose an appropriate interval.

The coupling loop condition was implemented based on the maximum volume fraction change. This was achieved by creating a new user variable in CFX as $\Delta\alpha = |\alpha - \alpha_{old}|$, where α_{old} is the previous volume fraction distribution (which is created in CFD-Post as mentioned in the CFX section). The simulation is interrupted if $\Delta\alpha > 0.5$ anywhere in the domain, EM fields are updated and flow simulation is resumed with new forces. In steady state situation, the melt is static and EM simulation is not repeated.

The case parameters are given in `data.py` file. These are used in case setup and simulations. The file contents for EM levitation case are

```
n_turns = 3
d_turn = 0.006
r_first_turn = 0.016
z_first_turn_b = -0.025
z_first_turn_t = 0.037
r_dist_turns = 0.007
z_dist_turns = 0.003
dist_ext = 0.15
```

```
current = 750
frequency = 9650

droplet_r = 0.012
droplet_z0 = 0.005

density = 2311
viscosity = 0.01
surface_tension = 0.94
el_cond = 3000000

melt_elem_size = 0.0005

max_iter = 10
max_rel_diff = 0.5
cpu_cores = 4
end_time = 100

restart = 0
```

where `restart` parameter determines if the simulation is restarted from a previous run or it's a new run. `restart = 0` means a new simulation. `melt_elem_size` is the element size to use in the liquid metal region. Scheme of the levitation model is shown in Fig. 3.3.1.

Mesh for CFX is made in Salome software at the start of simulation, although the script can be easily modified to use a mesh from another program. The EM mesh is made directly in Maxwell. The coupling is tested in section 3.6.

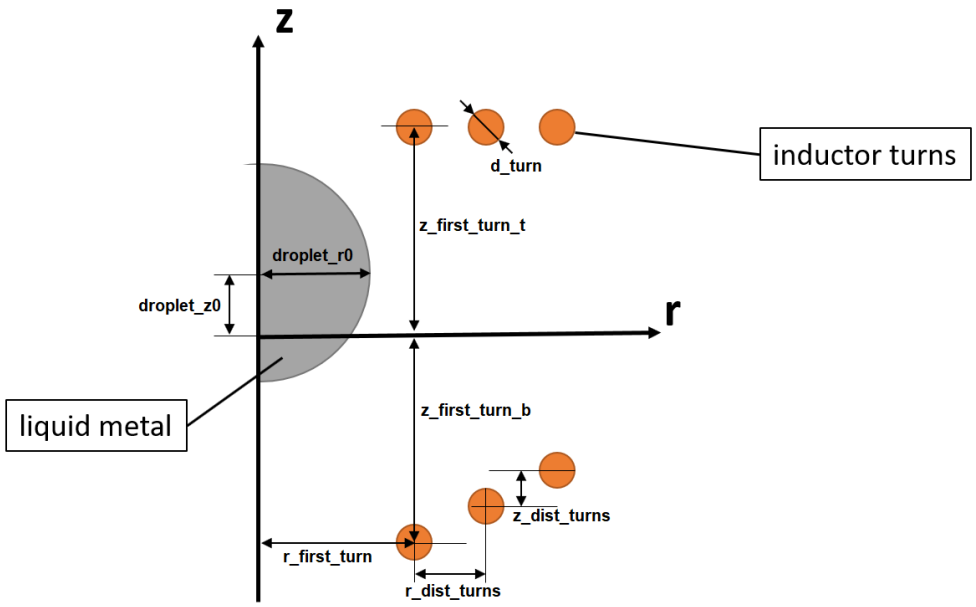

Fig. 3.3.1. Scheme of the EM levitation model.

3.4 Induced current approximation

As a generalization of the cases considered in the thesis, magnetic field can be viewed as consisting of three parts - the (external) primary field $\vec{B}_0$ created by magnets or current

wires, secondary field $\vec{B}_t$ due to the induced currents $-\sigma\frac{\partial\vec{A}}{\partial t}$ and another part $\vec{B}_v$ due to the $\sigma\vec{v}\times\vec{B}$ current:

$$\vec{B} = \vec{B}_0 + \vec{B}_t + \vec{B}_v \tag{3.4.1}$$

Now, imagine a situation where one simulates EM induction by some time-dependent magnetic field $\vec{B}(t) = \nabla\times\vec{A}(t)$ with $\phi = 0$ and ignores the contribution of flow velocity in calculation of total magnetic field. This leads to neglecting the $\vec{B}_v$ part. It may or may not be a good approximation, depending on the magnetic Reynolds number Re_m which describes the importance of the secondary field compared to primary. That is only one part of the problem. Even if $\vec{B}_v$ is very small and $\vec{v}\times\vec{B}$ can be dropped from calculation of magnetic field, the $\vec{v}\times\vec{B}$ term may still be very important to include in the Lorentz force $\vec{f_L} = \vec{j}\times\vec{B}$. In other words, the effect of $\sigma\vec{v}\times\vec{B}$ current may be ignored for $\vec{B}$ but it must be included in the total current $\vec{j}$.

Simulations can be simplified if $Re_m \ll 1$ - the flow velocity can be decoupled from the magnetic field. In other words, the $\vec{v}\times\vec{B}$ term can be neglected in Eq. (2.3.9). Since $\vec{j}$ would still include the velocity term, some correction to it must be applied for it to still obey charge conservation $\nabla\cdot\vec{j} = 0$.

The correction used here is based on the ϕ-formulation derived in [68]. In this formulation, the induced current density in the fluid is obtained by solving the equation for the electric scalar potential ϕ_v:

$$\nabla\cdot(\sigma\nabla\phi_v) = \nabla\cdot(\sigma\vec{v}\times\vec{B}) \tag{3.4.2}$$

where the subscript v is used to distinguish this potential from the externally applied one (in case of current injection etc.). Boundary conditions are needed for ϕ_v on the boundary of the conducting liquid. This is simply $\frac{\partial\phi_v}{\partial n} = 0$, so that current cannot leave the conductor. Perfectly conducting walls would be imposed by $\phi_v = 0$.

After solving Eq. (3.4.2), in a general case with an external potential ϕ and time varying magnetic field $\vec{A}(t)$:

$$\vec{j} = -\sigma\left(\nabla\phi_v - \frac{\partial\vec{A}}{\partial t} + \vec{v}\times\vec{B}\right) \tag{3.4.3}$$

where $\vec{B} = \vec{B}_0 + \vec{B}_t$ (without $\vec{B}_v$).

From the simulation point-of-view, this has several implications. For cases without external potential and without time-varying magnetic fields, this allows us to solve only fluid flow with an additional equation to obtain $\vec{j}$, and additional software to solve EM would not be needed. This can be very useful for simulating direct strip casting with static magnetic field - everything can be solved in OpenFOAM alone, which is several times faster than together with Elmer.

If external potential is also applied (but still no induction by time-varying fields), an external solver is needed to simulate magnetic field due to the directly injected current. This cannot be tackled in the fluid flow simulation because the space surrounding the

liquid metal must be considered to some extent. However, this still simplifies matters if this injected current does not change considerably throughout the simulation. This is the case, for example, in the electrovortical flow with free surface considered in the thesis. The simplification is that the EM simulation can be done only once at the beginning of the simulation.

For cases where also time-varying fields are present, this approach solves only part of the problem. The time-varying part must still be solved by an external EM solver. However, some simulation speed-up can be achieved by not transferring (and interpolating) velocity to the EM simulation. In case of coupled Elmer-OpenFOAM simulations, OpenFOAM then transfers to Elmer only electrical conductivity distribution and Elmer returns its part of current density and magnetic field and the Lorentz force in OpenFOAM is then:

$$\vec{f}_L = \vec{j} \times \vec{B} = \left(\vec{j}_{elmer} - \sigma \nabla \phi_v + \sigma \vec{v} \times \vec{B}\right) \times \vec{B} \tag{3.4.4}$$

where subscript *elmer* denotes the field imported from Elmer (that does not include the flow velocity term but includes all other).

A practical implementation of Eq. (3.4.2) is also described in [68]. To make the solution consistent and stable, σ and the $\sigma\vec{v} \times \vec{B}$ term are interpolated to cell faces (`fvc::interpolate()`) before solving Eq. (3.4.2). After the solution, total current density is reconstructed from cell faces to centroids using a volume-weighted interpolation. In OpenFOAM code, these steps are written as follows (`elcond` is σ, `U` is $\vec{v}$, `B` is $\vec{B}$, `pot` is ϕ_v):

```
//interpolate VxB to cell faces
surfaceScalarField VxBf = fvc::interpolate(elcond)*fvc::interpolate(U ^ B) & mesh.Sf();

//define the equation
fvScalarMatrix potEqn
(
  fvm::laplacian(fvc::interpolate(elcond),pot)
  ==
  fvc::div(VxBf)
);

//set reference potential and solve the equation
potEqn.setReference(potRefCell, potRefValue);
potEqn.solve();

//calculate total current density at cell faces
surfaceScalarField jf = -fvc::interpolate(elcond)*(fvc::snGrad(pot) * mesh.magSf()) + VxBf;

//calculate current density at face centers
surfaceVectorField jfc = jf * mesh.Cf();

//reconstruct total current density to cell centers
volVectorField jcorr = fvc::surfaceIntegrate(jfc) - (fvc::surfaceIntegrate(jf) * mesh.C());

//update current density distribution and boundary condition
jcorr.correctBoundaryConditions();
```

Note again that all of this applies only if $Re_m \ll 1$. In other cases, velocity cannot be decoupled from magnetic field. The approach presented here will be tested in section 3.6.

3.5 Liquid metal solidification

Many metallurgical processes involve solidification and melting of metals. In continuous casting, for example, liquid metal is usually poured into a cooled mold or onto a moving belt where it solidifies and is continuously pulled away for processing. To simulate such processes, at least two phases must be considered - liquid and solid metal. If some gas atmosphere is present and the metal surface is exposed to it, such as in the belt casting process, the gas phase must also be included in the model.

To simulate the belt casting, fluid flow with free surface, heat transfer and solidification must be considered. Without solidification, the problem is liquid metal flow with free surface and heat transfer, which one would normally simulate using a two-phase solver with the VOF method for free surface capturing. With solidification, it is still possible to use a two-phase solver by implementing a possibility for the liquid metal to also be in a solid state. It leads to a pseudo three-phase system where gas is always fluid but the other "fluid" can assume two states - liquid and solid. This considerably simplifies things because from the computational fluid dynamics standpoint the model still has only two phases - liquid metal and air, with liquid metal having some temperature-dependent properties to make it behave like solid below the melting point.

The solidification approach implemented here is based on the enthalpy-porosity method, such as described in [121]. This method is normally applied to simulate liquid/solid systems without gas phase. In a two-phase system with liquid and solid, the liquid fraction function β is introduced

$$\beta = \begin{cases} 0, & T < T_s \\ \frac{T-T_s}{T_l-T_s}, & T_s < T < T_l \\ 1, & T > T_l \end{cases} \tag{3.5.1}$$

where T_l and T_s are the liquidus and solidus temperatures. If $T_s = T_l$ (e.g. for pure metals),

$$\beta = \begin{cases} 0, & T < T_s \\ 1, & T > T_s \end{cases} \tag{3.5.2}$$

To make β smooth and differentiable, it can be redefined using the error function as

$$\beta_T = 0.5 \, \mathrm{erf}\left(a_T(T - T_s)\right) + 0.5 \tag{3.5.3}$$

where a_T is a steepness parameter that determines the range of temperatures over which β_T changes from 0 to 1 (the subscript T was added to later distinguish it from another function). Ideally, for metals, a_T tends to infinity, but numerically it can lead to instabilities. For $a_T = 20$ and $T_s = 300$ β_T is shown in Fig. 3.5.1 (left).

Now, the definition above is for a two-phase system with liquid and solid, without gas. In a three-phase system, gas is also present. The liquid fraction for gas must always be 1

and solidification should only occur in the liquid phase. Conveniently, using the volume fraction α that is 0 in gas and 1 in the other fluid (liquid and solid metal), the total liquid fraction can be written as

$$\beta = 1 + \alpha(\beta_T - 1) \tag{3.5.4}$$

Since the interface between gas and metal (both liquid and solid) described by α is centered at 0.5 and is not perfectly sharp, to have more control over behaviour of β near the metal-gas interface, α used in the definition (3.5.4) can be replaced by a function

$$\alpha \to \beta_\alpha = 0.5 \text{ erf}\,(b_T(\alpha - \alpha_0)) + 0.5 \tag{3.5.5}$$

where b_T is steepness coefficient and α_0 is the value where the function is centered. To summarize, the liquid fraction β determining solidification is now given by

$$\beta = 1 + (0.5 \text{ erf}\,(b_T(\alpha - \alpha_0)) + 0.5)(0.5 \text{ erf}\,(a_T(T - T_s)) + 0.5 - 1) \tag{3.5.6}$$

Finally, the liquid fraction is used in the momentum equation to make the liquid metal flow temperature-dependent. If $T < T_s$, the liquid metal must behave as if it is solid - either completely static or, in case of continuous casting, moving with the casting or pull speed. This is achieved by a momentum source term

$$\vec{f}_{solid} = A\frac{(1-\beta)^2}{\beta^3 + \epsilon}(\vec{v}_p - \vec{v}) \tag{3.5.7}$$

where A is the mushy zone constant (a large number, like 10^5) and ϵ is a small number (like 10^{-3}).

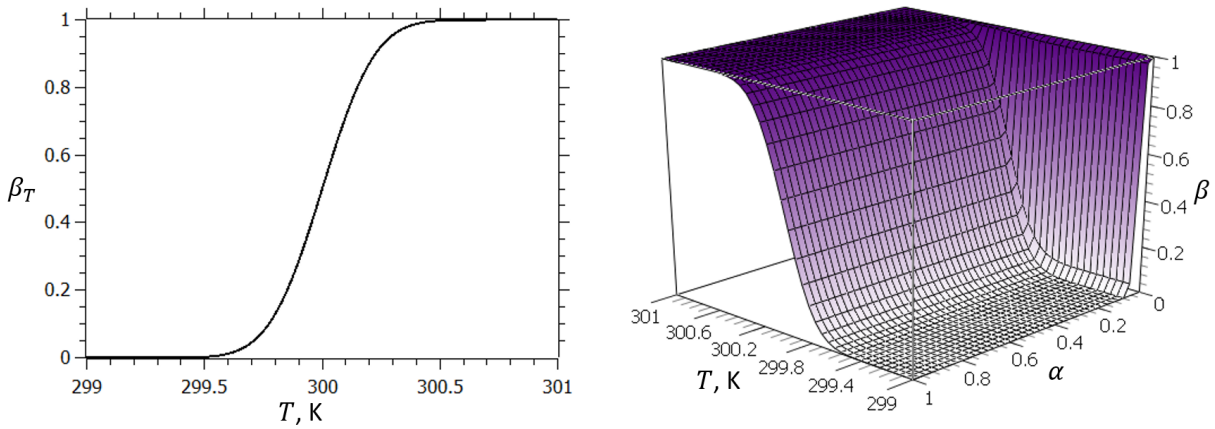

Fig. 3.5.1. Liquid fraction functions: (left) β_T with $a_T = 4$ and $T_s = 300$; (right) β with $\alpha_0 = 0.04$, $a_T = 20$, $b_T = 100$ and $T_s = 300$.

The reason for using the function (3.5.5) instead of α itself was that one may want to control how the solidified metal surface behaves when it is in direct contact with the gas

phase (for example, when the whole metal layer is solid in the belt casting case). That is, one may want to use $\alpha_0 < 0.5$ to avoid $\vec{f}_{solid}$ decreasing too rapidly near the surface to avoid unphysical smearing of solid metal surface.

The total liquid fraction β with $\alpha_0 = 0.04$, $a_T = 4$, $b_T = 100$ and $T_s = 300$ is shown in Fig. 3.5.1 (right). Notice the rapid change of β to 1 near $\alpha = 0$ (gas phase).

The phase-change term on the right side of heat equation (2.2.1) contains a time-derivative of liquid fraction β. To make the numerical model more robust, as explained in [121], this derivative can be expressed using the chain-rule as

$$\frac{\partial \beta_T}{\partial t} = \frac{\partial \beta_T}{\partial T}\frac{\partial T}{\partial t} \tag{3.5.8}$$

In OpenFOAM code, the heat equation (2.2.1) is then

```
fvScalarMatrix TEqn
(
    fvm::ddt(rhoCp,T) +
    fvm::div(rhoPhiCp,T)
    - fvm::laplacian(kappa, T)
    ==
    -rho*alpha1*L1*dbetadt*fvm::ddt(T)
    -rho*alpha1*L1*dbetadt*(U & fvc::grad(T))
    +Q
);
```

where `L1` is the latent heat of metal,`rho` is density, `U` is velocity, `dbetadt` is $\frac{\partial \beta_T}{\partial T}$, `kappa` is thermal conductivity, `rhoCp` is ρc_p, `Q` is volumetric heat source (e.g. Joule heat), `ddt()` is time-derivative, `grad()` is gradient, `&` is dot-product. The developed solidification model is tested in the results section.

3.6 Numerical model verification

This section is concerned with verification of numerical models of liquid metal free surface flows in electromagnetic field. These models include magnetic field, electric current, two-phase fluid flow with free surface. For the casting simulations, the model also includes solidification.

Verification means finding optimal parameters with which the models perform best and give the most accurate results. The accuracy basically means that the solution is stable and is independent of further improvements of the parameters. For example, one important aspect is numerical mesh. Usually, a very fine mesh is required to capture all important effects and features. To find the optimal mesh, grid independence study is usually performed in which one simulates the problem using successively finer meshes and analyzes the performance to accuracy ratio. In many cases, it may be that even a somewhat coarse mesh is good enough to capture the necessary effects, considering that a finer mesh can increase simulation time considerably.

Another aspect in verification is to find the optimal discretization schemes and methods. Generally, low order schemes are considered inaccurate and too diffusive. For example, upwind schemes used in fluid flow simulations are normally first-order accurate

and introduce numerical or false diffusivity. This is especially important in free surface flows when using the VOF method for interface capturing. First order discretization can lead to interface smearing and that is highly undesirable. Of course, performance of discretization schemes depends on the mesh element size and type and it can normally be said that the finer and more regular the mesh, the less the results depend on the schemes used.

A good way of verifying numerical models is comparing simulations using different programs or methods. Here, the main fluid flow simulations to be verified are done in OpenFOAM. ANSYS Fluent and CFX were selected as the commercial alternatives. Main electromagnetics tool is Elmer with ANSYS Maxwell as the commercial alternative. Commercial packages are often considered, if not more accurate, well established in their respective fields of application.

The following subsections are devoted to verification of different numerical aspects - EM induction, coupled MHD simulations, induced current approximations, different EM-HD coupling approximations, and liquid metal solidification.

3.6.1 Electromagnetics

Some aspects of EM simulations are tested in this section. EM simulations are relatively simple - there is no turbulence, no overwhelming number of discretization schemes to choose from. Nevertheless, there are some aspects that need to be checked to achieve the best solution. One is the mesh size or spatial resolution. The other is the domain size. The active zone with inductors, magnets, conductors etc. is surrounded by vacuum or air. The surrounding space is needed because magnetic field exists in the whole space. Finite size of the domain means that whatever boundary conditions is set on the outer boundary may affect the results in the active zone. This is important for cases where special asymptotic boundary conditions are not available. The influence of spatial resolution and domain size for a representative case - AC electromagnetic induction, is quantified below.

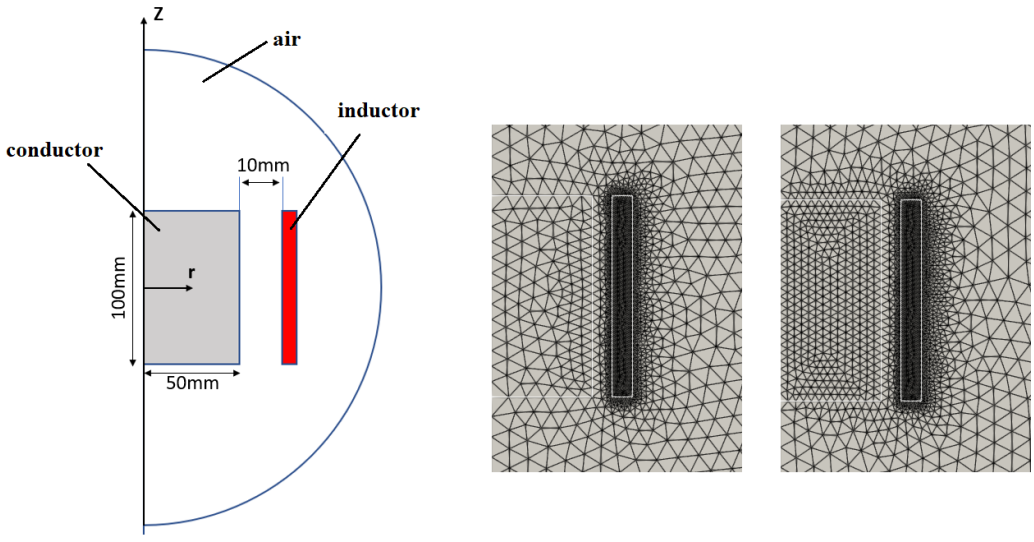

Fig. 3.6.1. Scheme of the induction model (left) and two mesh examples (center and right).

Fig. 3.6.1 shows the scheme of the test case. The model is axisymmetric. Outer radius of the inductor is $R_{ind} = 65$ mm. The external boundary is a semi-circle with radius R ranging from 100 mm to 1 m with boundary condition of magnetic vector potential $\vec{A} = 0$. The problem is solved in frequency domain.

Let us start with the domain size analysis. Domain size itself is relevant only in relation to the size of its parts, such as the outer radius of the inductor. Hence, the varied parameter here is the distance of the external boundary to the inductor, $\Delta R = R - R_{ind}$. A good measure to assess the results of simulations are some integral values. Here, a representative variable is the integral eddy current power or Joule heat, P. Let's consider aluminium with electrical conductivity $\sigma = 3.8 \cdot 10^7$ S/m as the conductor and set the inductor current $I_{rms} = 1000$ A and frequency $f = 100$ Hz. Quite noticeable differences between $R = 100$ mm and $R = 1$ m can be seen in Joule heat distribution in Fig. 3.6.2. Integral power P is plotted in Fig. 3.6.3. The right graph shows the error relative to the last point, $\frac{P_i - P_{last}}{P_{last}}$, which itself is excluded from the logarithmic plot.

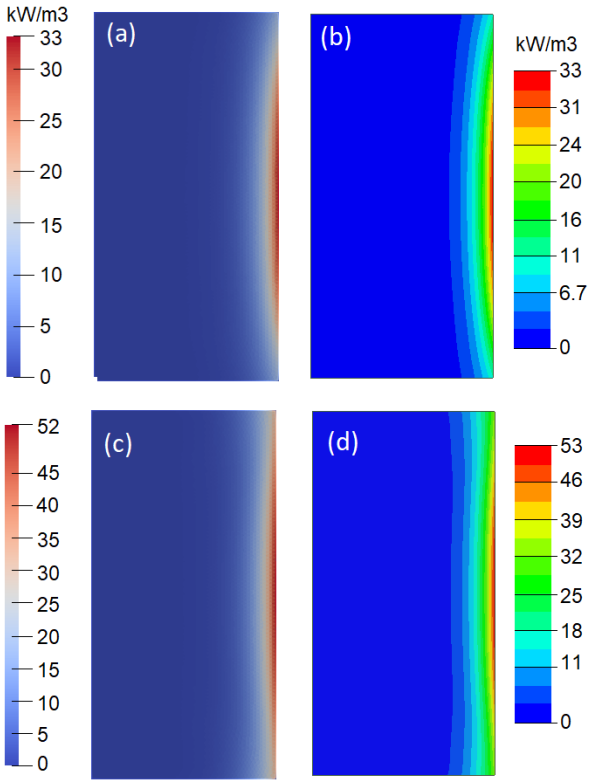

Fig. 3.6.2. Joule heat in the conductor; (a) $R = 100$ mm, Elmer, (b) $R = 100$ mm, Maxwell, (c) $R = 1$ m, Elmer, (d) $R = 1$ m, Maxwell. Mesh element size $\Delta x = 1$ mm.

As expected, the integral power approaches some constant value by increasing the domain size. For reference, the same simulations were also done in ANSYS Maxwell, which gave almost exactly the same results. It can be seen that the error is less than 5% already at $\Delta R = 0.13$ m. It is safe to conclude that $\Delta R = 0.3$ m should be good enough for most applications. Note that this can be different for other sources of magnetic field, for which the field decays at different rate than in this case.

Mesh resolution is important regarding electromagnetic field penetration depth δ. Let's take $R = 0.5$ m and look at how the results change with mesh element size Δx. For the previously set frequency and conductivity, $\delta = 8$ mm. The coarsest mesh in the conductor will have elements of size $\Delta x = 8$ mm and the finest will have $\Delta x = 0.1$ mm, so that δ is resolved by 1 to 80 elements, respectively. Fig. 3.6.1 shows two coarsest meshes. Fig. 3.6.4 shows the integral power depending on the number of elements in the skin layer. The right graph again shows the error relative to the last point (finest mesh). Note that all simulations have converged with residuals below 10^{-10}, so numerical errors should be very small. Surprisingly, the error is less than 2% even with two elements in the layer, which could mean that EM models are not very strict regarding mesh resolution. However, this can not be generalized. In more complex models, such as where the conductor has arbitrary shape, the mesh resolution must be optimised to resolve all the necessary details.

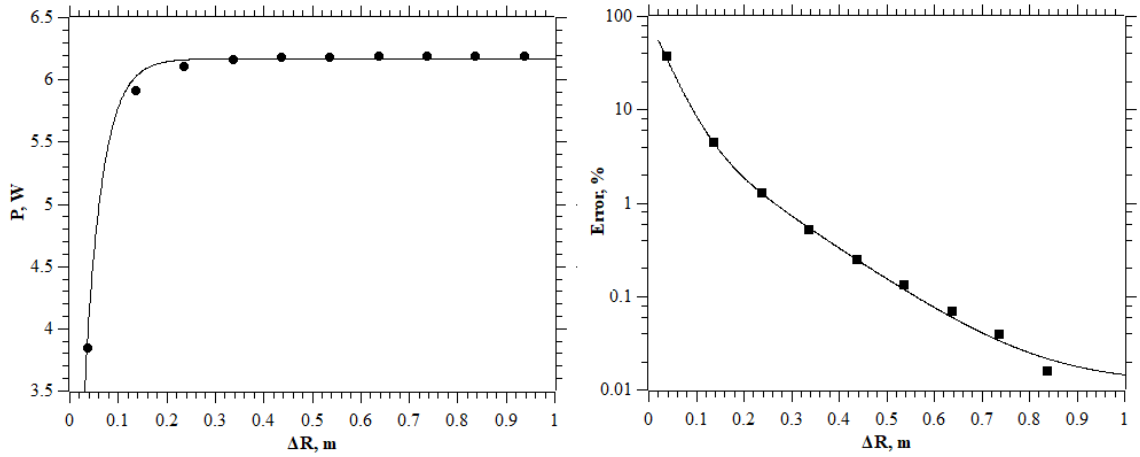

Fig. 3.6.3. Joule heat in the conductor (left) and the error (right) depending on ΔR.

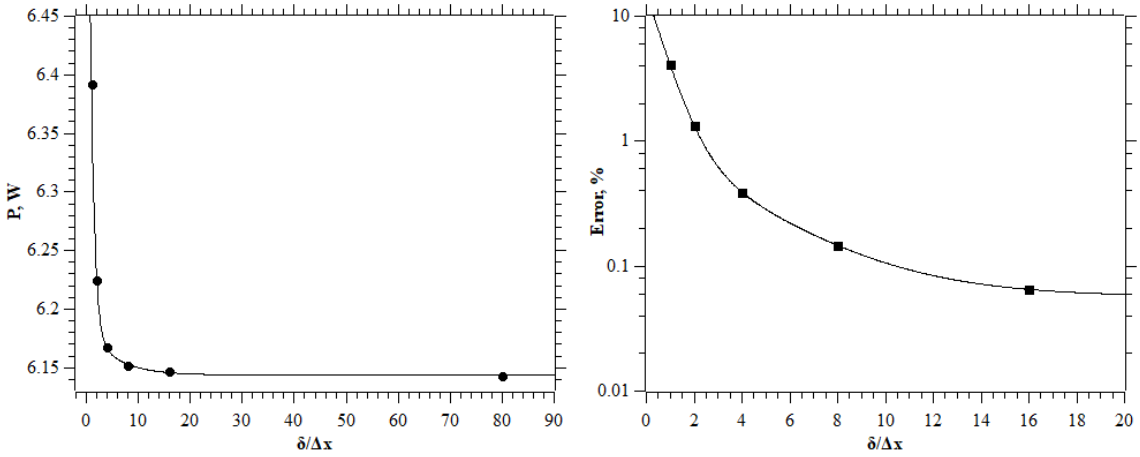

Fig. 3.6.4. Joule heat in the conductor (left) and the error (right) depending on $\delta/\Delta x$.

3.6.2 Coupled MHD simulations

The main simulation tools used in the thesis are Elmer for EM, OpenFOAM for fluid flow and heat transfer, and EOF-Library for coupling. This section presents the

verification of coupled EM-HD models. Verification will be based on various numerical parameters, such as mesh size and coupling frequency (how often EM is recalculated during simulations), as well as comparison of different software, including data from literature. Three simulation frameworks were developed in the thesis, which are summarized as follows (the abbreviations in parentheses will be used throughout this section):

- Elmer + OpenFOAM with EOF-Library (EOF)
- OpenFOAM (MHD/OF)
- ANSYS CFX + Maxwell (ANSYS)

The EOF approach solves EM in Elmer and fluid flow in OpenFOAM. MHD/OF approach solves everything in OpenFOAM alone. ANSYS approach solves EM in Maxwell and fluid flow in CFX.

Let us consider a relatively simple case - electromagnetic levitation of liquid metal. This problem has been studied in the past, literature data is available. Scheme of the model is shown in Fig. 3.6.5. The same configuration was investigated in [66].

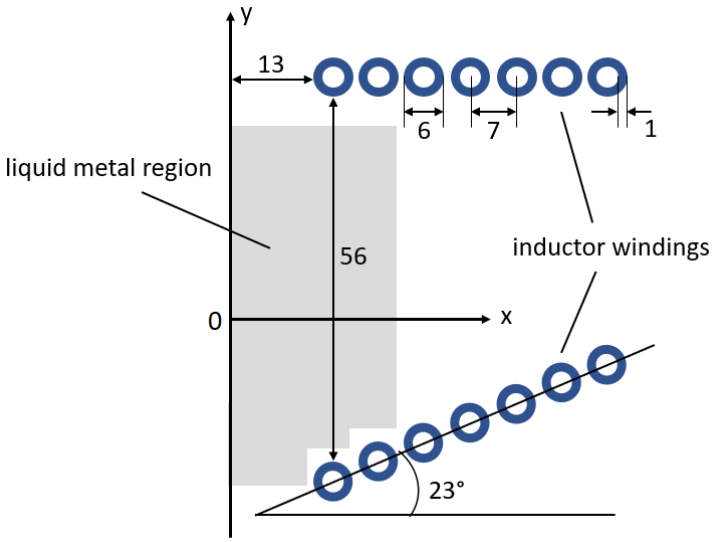

Fig. 3.6.5. Scheme of the EM levitation model with sizes in mm.

The model is axisymmetric. There are two groups of windings - upper and lower, with current flowing in opposite directions (or with phase shift of 180 degrees). The grey melt region in Fig. 3.6.5 is where liquid metal and some air reside. The EM model in Elmer and Maxwell includes the whole domain (windings, melt region and extra surrounding air), but fluid simulation in CFX and OpenFOAM has only the grey region. For simulations using the EOF-Library, it is important to have one overlapping region in Elmer and OpenFOAM where coupling takes place. Here it is the grey region. EM and fluid meshes in this part can be different. For ANSYS coupling, there is no specified coupling region - the liquid metal volume is exported from CFX to Maxwell as a geometrical entity. The MHD/OF model includes the whole domain - inductor windings, liquid metal and surrounding air.

There is a set of "default" system parameters in this levitation case, listed in Table 3.6.1. With these parameters, the levitation is stable, as demonstrated numerically and experimentally in [66].The developed models are verified for these parameters.

Fig. 3.6.6 shows the numerical mesh for Elmer. Mesh for OpenFOAM and CFX fluid flow simulations (the grey region) contain square elements of edge size 0.25 mm. ANSYS Maxwell uses adaptive meshing to reduce simulation errors, so the mesh can be different for each coupling iteration. Maxwell mesh is very similar to the Elmer one and is not shown here. Mesh for the MHD/OF simulations is shown in Fig. 3.6.7. The element size in fluid region is 0.25 mm. All meshes were generated in Salome 8.3.0.

Table 3.6.1: Physical parameters in the levitation model.

Parameter name	**Value**	**Units**
Current, rms	650	A
Frequency	9650	Hz
Melt electrical conductivity	3.85	MS/m
Melt density	2380	kg/m^3
Melt viscosity	2.38	mPa·s
Surface tension	0.94	N/m

Boundary conditions for EM simulations is simply $\vec{A} = 0$ on the external air boundary, which means that magnetic field $\vec{B}$ is parallel to it. For fluid simulation (the mentioned grey region) the boundary is an opening with relative pressure $p_{rel} = 0$. Liquid metal can flow only out, but air can circulate in both directions. Since both OpenFOAM and CFX can only solve 3D problems, the axisymmetric mesh is made as a 2-degree sector with one element thickness and symmetry conditions are applied on front and back faces. Turbulence model is k-ϵ.

The liquid metal is initialized as a sphere of radius $r = 12.3$ mm corresponding to 18.6 g of aluminium. The EM fields in EOF and ANSYS are re-simulated every time volume fraction of liquid metal changes by more than 0.5 in any mesh cell. The whole simulation process goes on until steady liquid metal shape is obtained. EM fields in MHD/OF are solved every time-step.

CFX uses High Resolution space derivative discretization scheme and first order backward Euler scheme for time derivatives. For turbulence variables, first order numerics are used. OpenFOAM uses first order upwind scheme for turbulence variables, second order hybrid central/upwind scheme for divergence terms and also first order backward Euler scheme for time discretization. For volume fraction divergence term, OpenFOAM uses the van Leer scheme (second order). For laplacian (diffusion) terms, central differencing (linear scheme) is used.

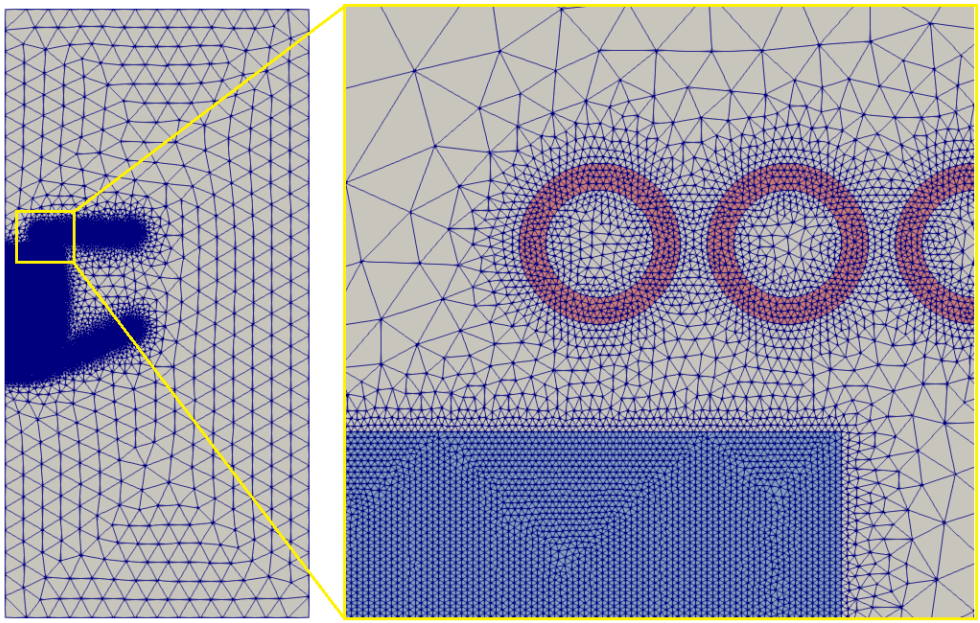

Fig. 3.6.6. Levitation mesh for Elmer.

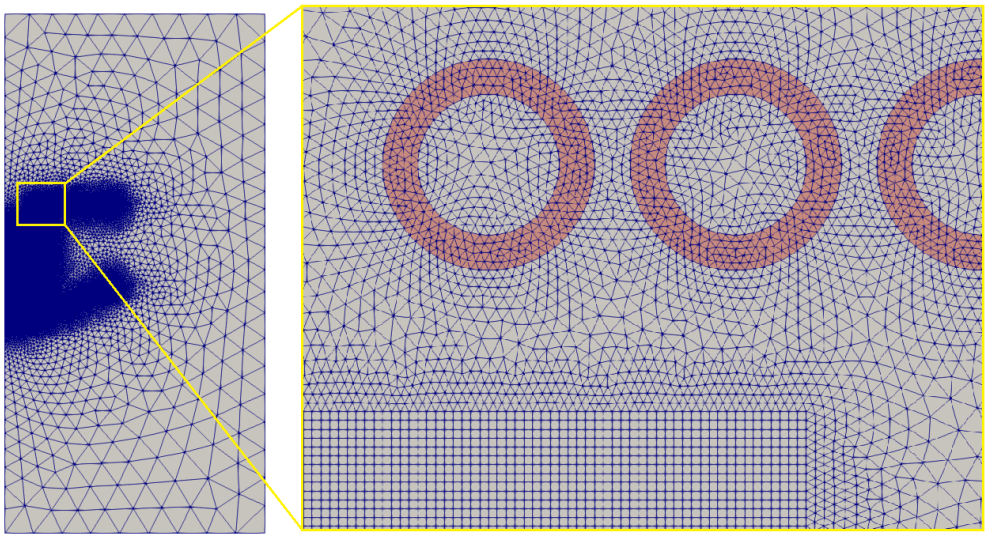

Fig. 3.6.7. Levitation mesh for MHD/OF simulations.

It has been tested that for divergence term in momentum equation, even a first order upwind scheme is good enough (it gives very similar results to higher order schemes, in the considered cases at least). For the volume fraction transport equation, however, it is not the case. Using upwind scheme for volume fraction leads to interface smearing.

The main result for verification is the shape of liquid metal, because it depends on all of the physical and numerical parameters. But first let's look at the EM results. Fig. 3.6.8 (left) shows magnetic flux density magnitude without liquid metal present. Note the opposite direction of magnetic field around the top and bottom windings, which is crucial configuration for stable levitation. Magnetic field magnitude on the symmetry axis is shown in Fig. 3.6.8 (right) simulated in Elmer, Maxwell and the MHD/OF solver.

All three solvers give basically the same result. Elmer curve is not as smooth at the left and right branches due to the mesh being coarser there.

Let us proceed to the main simulations - liquid metal levitation. The developed models will be considered verified if they give the same result regarding melt droplet shape and flow velocity with all three simulation approaches listed above.

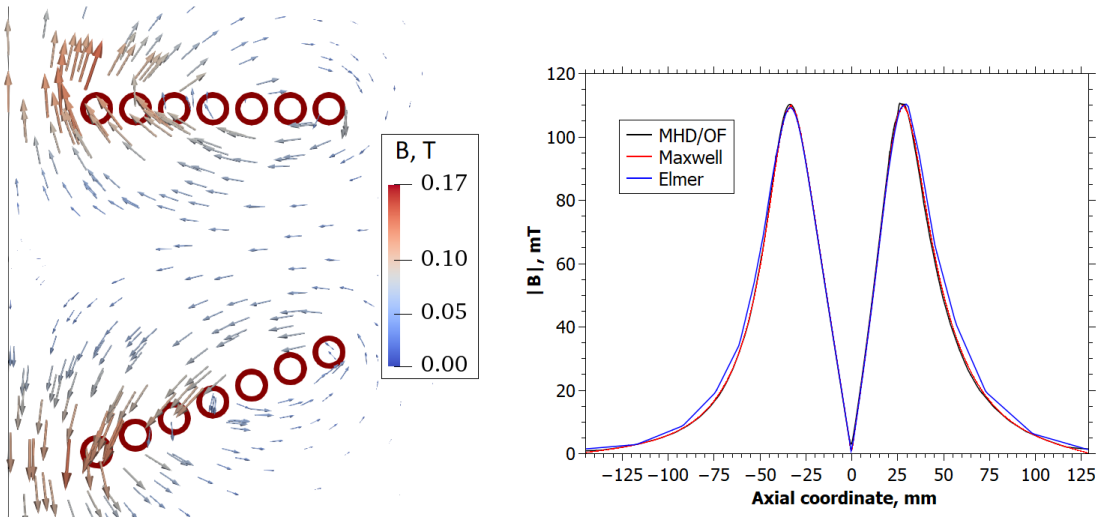

Fig. 3.6.8. Magnetic field magnitude without liquid metal: vectors in Elmer (left) and distribution along the axis (right).

Let's add the liquid metal droplet. Due to the skin effect, magnetic field distribution changes, as can be seen in Fig. 3.6.9. The most important variable here is the Lorentz force. Fig. 3.6.10 shows the time-average force distribution in a spherical droplet on the axis. There is less than 2% difference between Elmer and Maxwell, which can be due to slightly different meshes. Remember that Maxwell always uses adaptive meshing.

The results of levitation depend strongly on initial conditions. The most obvious parameter is the droplet mass or size - if it is too heavy, the Lorentz forces may not support it. If it is too small, induced currents are smaller and again the resulting forces may not be enough. Industrial research in this topic tries to develop a system that can levitated as large mass as possible.

If the spherical droplet is initialized too high, it may accelerate downward to a speed where EM forces may not be able to keep it from spilling out of the inductor. If it is initialized too low, the forces at the bottom of the droplet may already be too low to support it. In both cases, partial levitation may happen - part of the liquid leaves the system and some amount stays due to reduced droplet mass. In experiments, a solid metal piece is inserted in the inductor, where it eventually melts due to Joule heating. In the current numerical model, the droplet is initialized as a sphere of already molten metal.

Physical time to reach steady droplet shape also depends on the initial conditions. If the center of mass of the initial sphere is very close to the one of the final shape, steady condition can be reached in a few seconds. This is, of course, true in any simulation - if

the initial conditions are close to the final results, very few iterations or time-steps are needed.

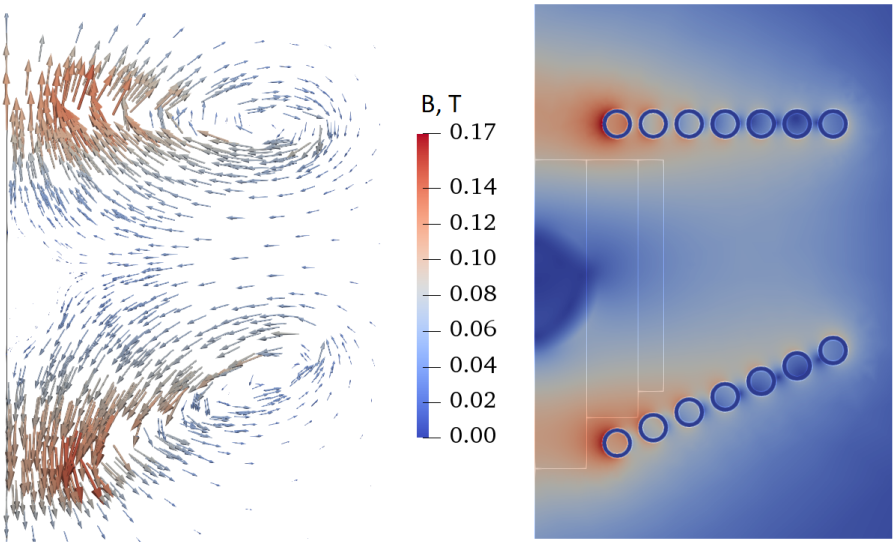

Fig. 3.6.9. Magnetic field with liquid metal droplet (Elmer result).

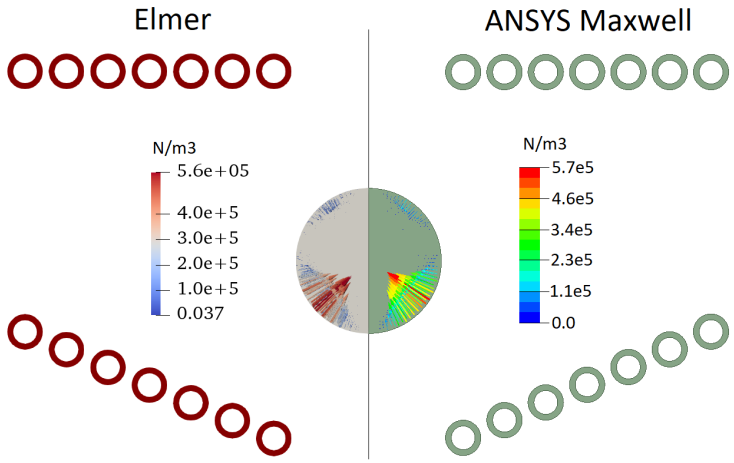

Fig. 3.6.10. Time-average Lorentz force in spherical metal droplet.

Time-development of the liquid metal droplet in EOF simulations is shown in Fig. 3.6.11. The droplet was initialized at $y = 5$ mm (see Fig. 3.6.5) and has reached the steady shape within a second of flow time. Simulation time was about 40 min with EOF and about 80 min with MHD/OF. Simulating 1 s of flow time with the ANSYS coupling takes over 10 hours. The reason for such a slow simulation with ANSYS is the file-based coupling - in every coupling iteration some files are written to disk. Moreover, CFX itself is much slower than OpenFOAM for some reason.

The steady droplet shapes obtained with different tools are shown in Fig. 3.6.12. Literature results are from [66]. Forces and flow velocity inside the steady droplet shape are shown in Fig. 3.6.13. It must be noted here that the free surface in Fig. 3.6.12 is

taken to be at $\alpha = 0.5$. Another important note is that in MHD/OF simulations the frequency is taken 100 times smaller and electrical conductivity 100 times higher, keeping the Lorentz force distribution the same. This approach was described in section 3.2 and has been tested to be completely valid.

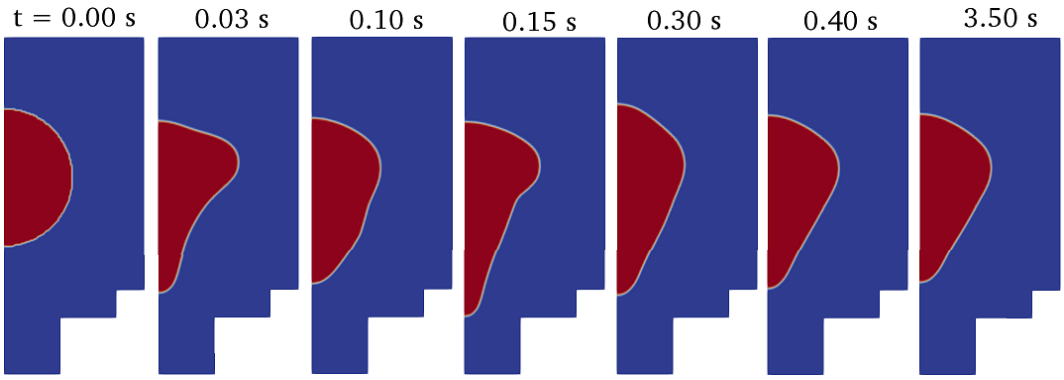

Fig. 3.6.11. Liquid metal droplet shapes, EOF results.

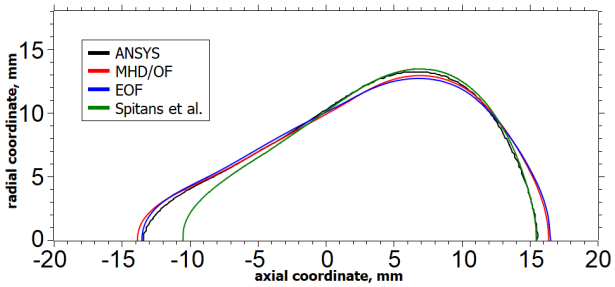

Fig. 3.6.12. Steady liquid metal droplet shape.

The droplet shape with EOF and MHD/OF is virtually the same, with the MHD/OF giving a slightly lower position. The result found in [66] is visibly different. This may be due to different numerical parameters which are not described in that paper. The ANSYS result is very close to EOF and MHD/OF.

The Lorentz force appears to be slightly different among the models. This may be due to a very slight melt shape differences or simply a visualization problem (the number and exact positions of the vectors may be different). Integral force in the vertical direction is the same within 1% in all cases.

The flow velocity distribution is qualitatively very similar in all three models. The velocity magnitude is very strange in the ANSYS results, it is almost ten times smaller, see axial velocity distribution in Fig. 3.6.14. It is actually somewhat surprising that the droplet shape is very close to the other models despite the velocity being much smaller.

The first thing that comes to mind that can decrease velocity is higher viscosity. When using eddy-viscosity turbulence models, the turbulence effects are included as a correction to the molecular viscosity. In many cases, the turbulent or eddy viscosity is said to be overestimated. It indeed seems to be the case here comparing eddy-viscosity distributions in EOF and ANSYS models in Fig. 3.6.15 - the ANSYS result is around three times

higher. It is not yet clear why the eddy-viscosity and velocity are so different in ANSYS, but it must be related to turbulence modelling.

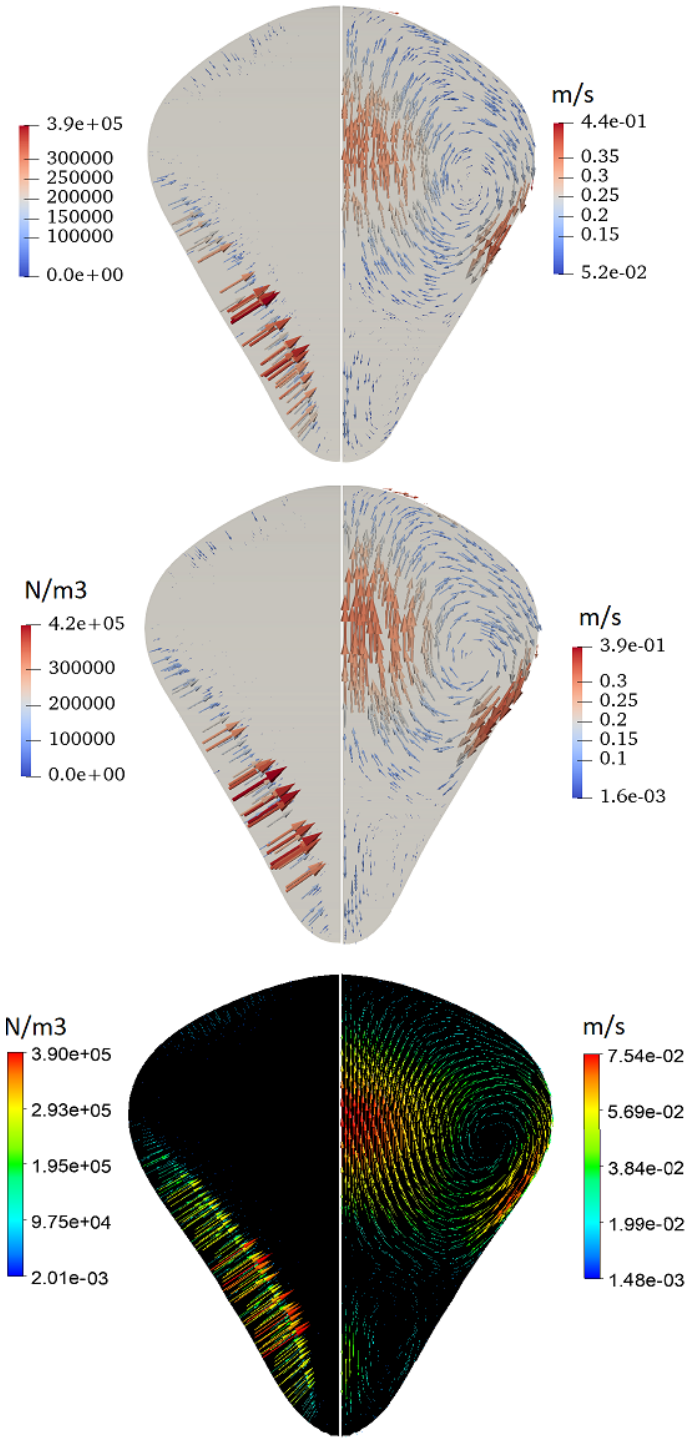

Fig. 3.6.13. Lorentz force and flow velocity in the droplet; from top to bottom: EOF, MHD/OF, ANSYS.

The levitation model can be considered partly verified. The ANSYS CFX/Maxwell model gives very similar force distribution and droplet shape, but it underestimates the flow velocity by an order of magnitude. The initial idea was that the ANSYS solution would serve as a reference, but the ANSYS itself must be verified now. Judging from

other simulations done in CFX (that are not included in the thesis), it can be difficult to obtain stable solutions of free surface problems in CFX. Perhaps it is due to its node-centered finite volume formulation and coupled pressure-velocity approach contrary to the segregated one in OpenFOAM.

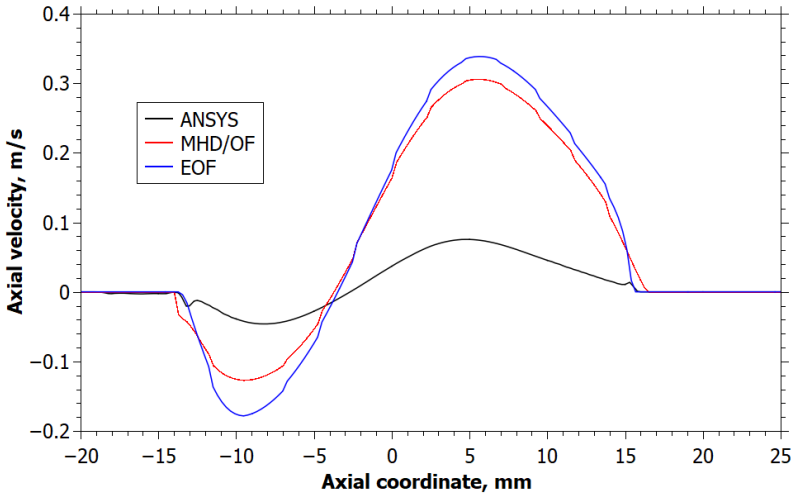

Fig. 3.6.14. Axial velocity on the axis.

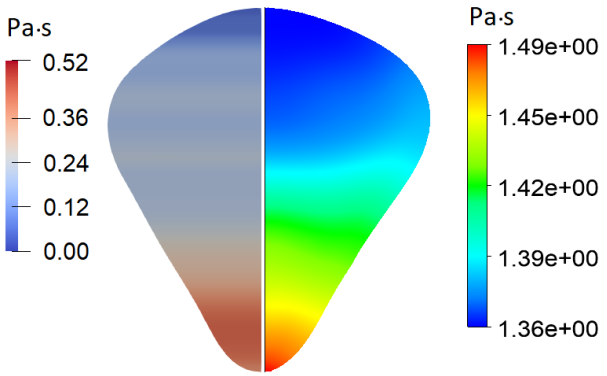

Fig. 3.6.15. Eddy-viscosity distribution, EOF (left) and ANSYS (right).

3.6.3 Induced current approximation

In section 3.4, a way of reducing simulation time with coupled Elmer and OpenFOAM simulations was described. It is relevant for cases where the $\vec{v} \times \vec{B}$ term plays a role, such as with traveling magnetic field or with rotating permanent magnets. In this subsection, the validity of this approach is tested using two models - full model with velocity term in EM equations in Elmer and a simplified model with the velocity term in OpenFOAM (Eq. (3.4.2)). Current density from the full model will be designated as $\vec{j}_{elmer}$ and from the simplified model as $\vec{j}_{openfoam}$. Since one of the studied systems in the thesis is using rotating magnets to induce liquid metal flow, the test model is based on that case.

Scheme of the test model is shown in Fig. 3.6.16. There is a permanent magnet (remanence 1.42 T, diameter 30 mm, length 50 mm) next to a small liquid metal volume

(electrical conductivity $\sigma = 3.17$ MS/m). The magnet is static, with one of its poles pointing towards the liquid metal, as evidenced on the left in Fig. 3.6.18 (this is $\vec{B}_0$, without the secondary field contribution). For simplicity, velocity distribution is constant $\vec{v} = U\vec{e}_y$ in a 1 cm thick layer as shown on the right in Fig. 3.6.18. U will be used to change magnetic Reynolds number $Re_m = \sigma\mu_0 U W_{melt}$.

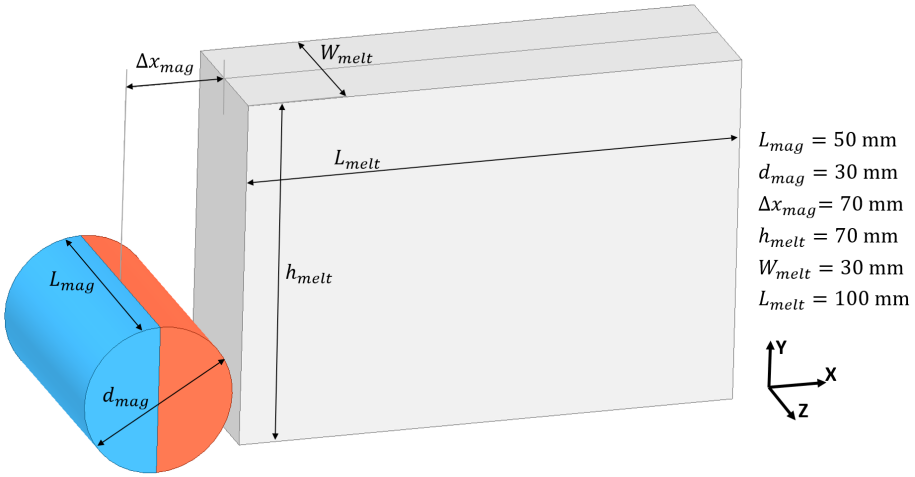

Fig. 3.6.16. Scheme of the model for testing the current correction.

The Elmer model includes the magnet, the melt region and surrounding air. Part of the mesh is shown in Fig. 3.6.17 (left). In case of the full model, Elmer is receiving velocity from OpenFOAM. In the simplified model, Elmer transfers magnetic field to OpenFOAM, where Eq. (3.4.2) is solved to obtain current density. Elmer solves magnetostatics equations using the *BiCGStabl* method, converging to 10^{-9} in 80 iterations on 16 CPU cores.

OpenFOAM model includes only the liquid metal region. The mesh consisting of 1 mm elements (210 000 in total) is shown in Fig. 3.6.17 (right). In case of the full model, OpenFOAM does not solve anything, it only transfers velocity data to Elmer. For the simplified model, a standard `pimpleFoam` solver is modified to solve Eq. (3.4.2) without solving any fluid flow equations (since in the test model velocity is fixed). The laplacian term is discretized using central differencing (`Gauss linear corrected` scheme in OpenFOAM). The system of linear equations after discretization can be solved using different solvers, such as *PCG* or *GAMG*. Using *PCG* with *DIC* preconditioner, the solution of Eq. (3.4.2) converges to tolerance of 10^{-10} in 290 iterations, while with *GAMG* it converges to the same level in 43 iterations. However, it cannot be concluded that *GAMG* is faster than *PCG*, it is only the case for this particular problem and with this particular distribution of velocity and magnetic field.

To test the limits of the simplified model, both cases are simulated for $U = 1$, 10, 100, 1000 m/s, or $Re_m = 0.12$, 1.2, 12, 120. Of course, the higher values are unrealistic for laboratory-scale liquid metal flows, but they are still included for verification purposes. One can expect the simplified model to give incorrect induced current distribution for the higher values of Re_m.

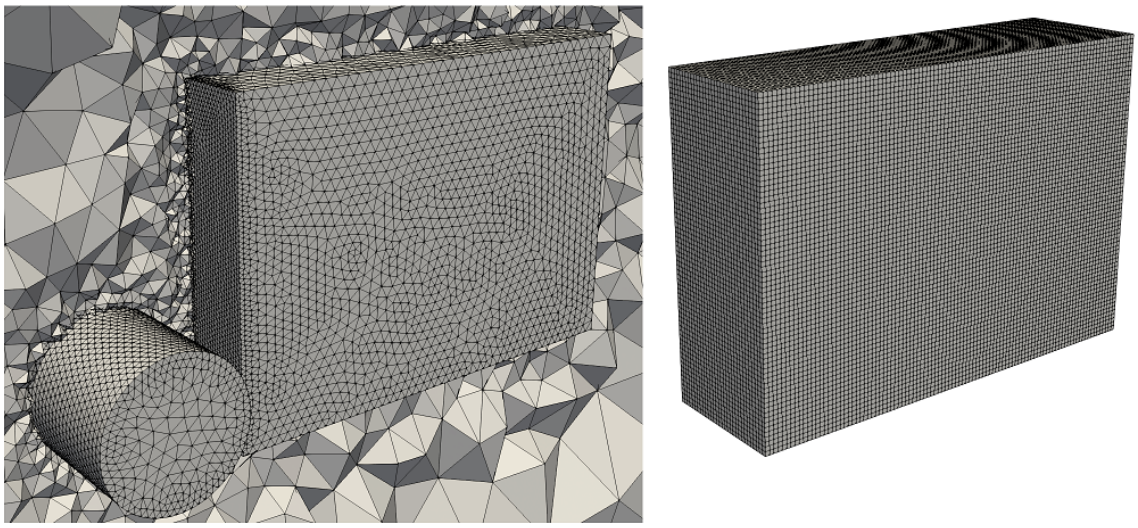

Fig. 3.6.17. Meshes for the test model: (left) Elmer and (right) OpenFOAM.

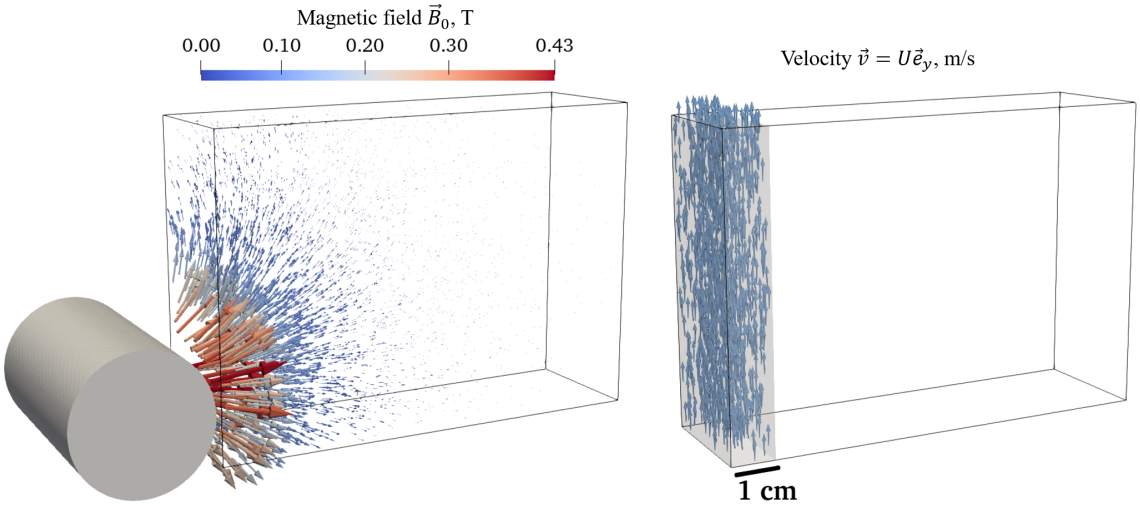

Fig. 3.6.18. Distribution of magnetic field (left) and velocity (right) in the test model.

Fig. 3.6.19 shows $\sigma\vec{v}\times\vec{B}_0$ distribution (simply taking cross product of the fields shown in Fig. 3.6.18), and the induced current calculated by the full and simplified models for $Re_m = 0.12$. The main difference in the distributions is that $\sigma\vec{v} \times \vec{B}_0$ is clearly wrong - this "current" goes into the wall, while the correct behaviour is that the current should form closed loops, which is obtained in both the full and simplified models.

During initial tests, OpenFOAM seemingly produced some artifacts - strange direction of some vectors near corners and some non-zero vectors far from the influence of magnetic field. Upon further investigation, it appeared that the problems arise at the boundaries between sub-domains attributed to different processor cores. It turned out that reference values for the potential were not initialized correctly, therefore the solution was erroneous. After fixing this, the artifacts disappeared.

Current density for all four Re_m values is shown in Fig. 3.6.20. For Re_m up to the order of 10, current densities calculated by both approaches are similar. For large

Re_m, however, they are significantly different. This is due to secondary magnetic field $\vec{B}_v$ opposing the primary $\vec{B}_0$. Total magnetic field distribution $\vec{B} = \vec{B}_0 + \vec{B}_v$ in the full model is shown in Fig. 3.6.21. Remember that in the simplified model, the magnetic field is always only the primary (that is the simplification).

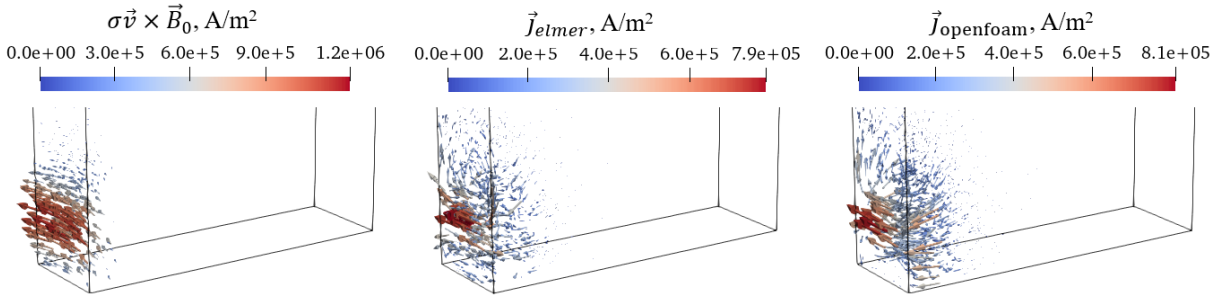

Fig. 3.6.19. Distributions of $\sigma\vec{v} \times \vec{B}_0$ (left), current in the full EM model (center) and current in the simplified model (right).

The result for $Re_m = 120$ in Fig. 3.6.21 might seem a little strange at first. However, it is known that at large Re_m, magnetic field lines tend to be deformed by the movement of the conducting fluid. This effect can be easily seen by looking at magnetic field lines shown in Fig. 3.6.22 - the lines are "pulled" upward by the flow velocity. This directly correlates to field vectors in Fig. 3.6.21, as the vectors are tangent to flux lines.

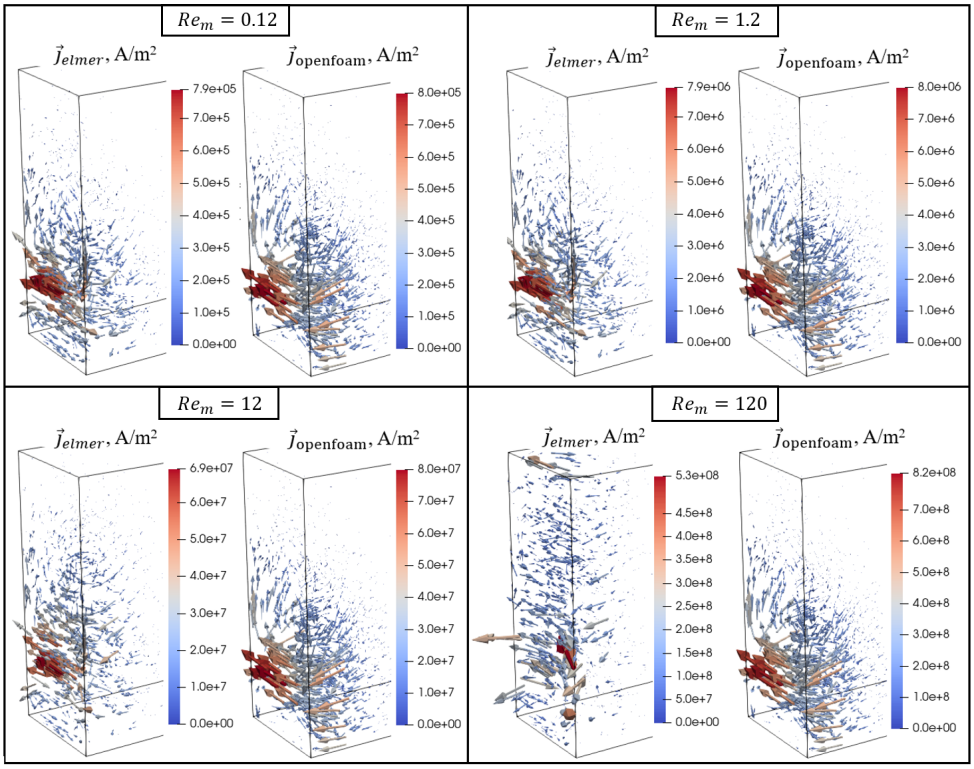

Fig. 3.6.20. Distributions of current density in the full EM model and in the simplified model for a range of Re_m.

Finally, when it comes to fluid flow, the important factor here is not the induced

current or magnetic field separately, but it is the interaction of them in the form of Lorentz force that will affect the fluid flow. Lorentz force in the full model, $\vec{f}_{elmer} = \vec{j}_{elmer} \times \vec{B}$, and the simplified model, $\vec{f}_{openfoam} = \vec{j}_{openfoam} \times \vec{B}_0$, is shown in Fig. 3.6.23. At high Re_m, Lorentz force is larger in the simplified model, in which $\vec{B}_v = 0$. Since $\vec{B}_v$ is mostly opposite to $\vec{B}_0$, the total field $\vec{B}$ is stronger than in the full model where also secondary field is taken into account, i.e., $|\vec{B}_0| < |\vec{B}_0 + \vec{B}_v|$.

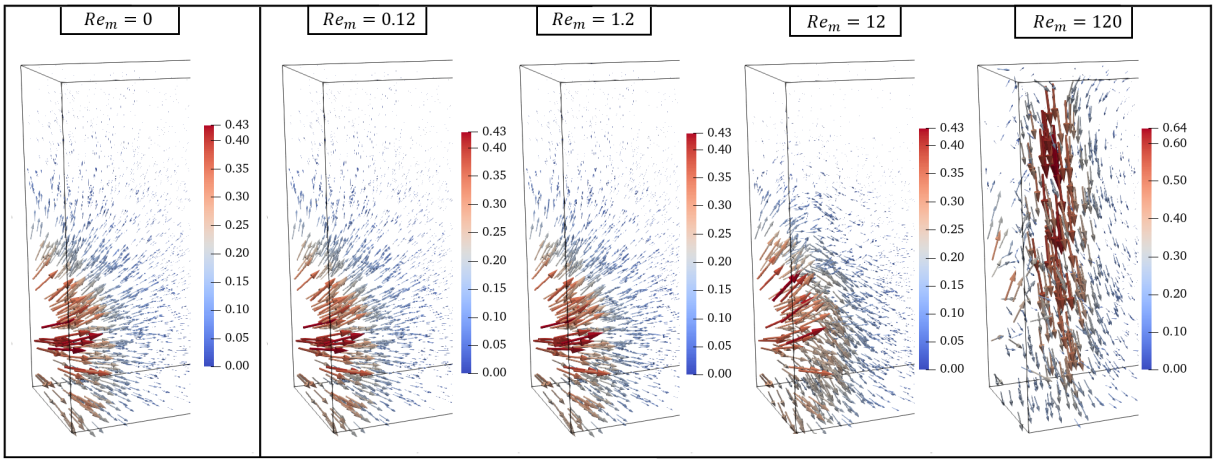

Fig. 3.6.21. Distribution of total magnetic field in the full EM model for a range of Re_m.

The main conclusion from these tests is that the simplification of considering the $\vec{v} \times \vec{B}$ term only in the fluid flow simulation, i.e., neglecting the secondary magnetic field related to this term, is applicable up to $Re_m \sim 1$. This was judged based on the distribution of Lorentz force - it is very close to the full model. However, there was a small difference in magnitude. This may or may not be significant, depending on other forces. In the case of rotating permanent magnets, the fluid flow is driven by the traveling magnetic field. The $\vec{v} \times \vec{B}$ term only leads to some reduction of the forces driving the flow, except near saturation (when $|\vec{B}_v| \to |\vec{B}_0|$), but Re_m rarely even reaches 1 in laboratory-scale cases.

If the motion of the free surface of liquid metal does not influence EM fields much, the simplification examined here can allow significant reduction in simulation time. Aspects related to coupling of EM and fluid flow and free surface are considered in the following section.

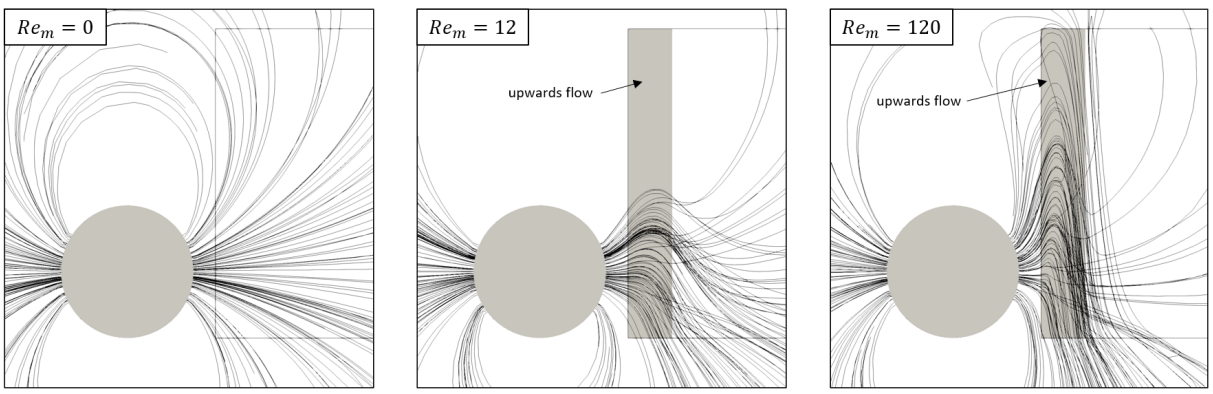

Fig. 3.6.22. Deformation of magnetic field lines depending on Re_m.

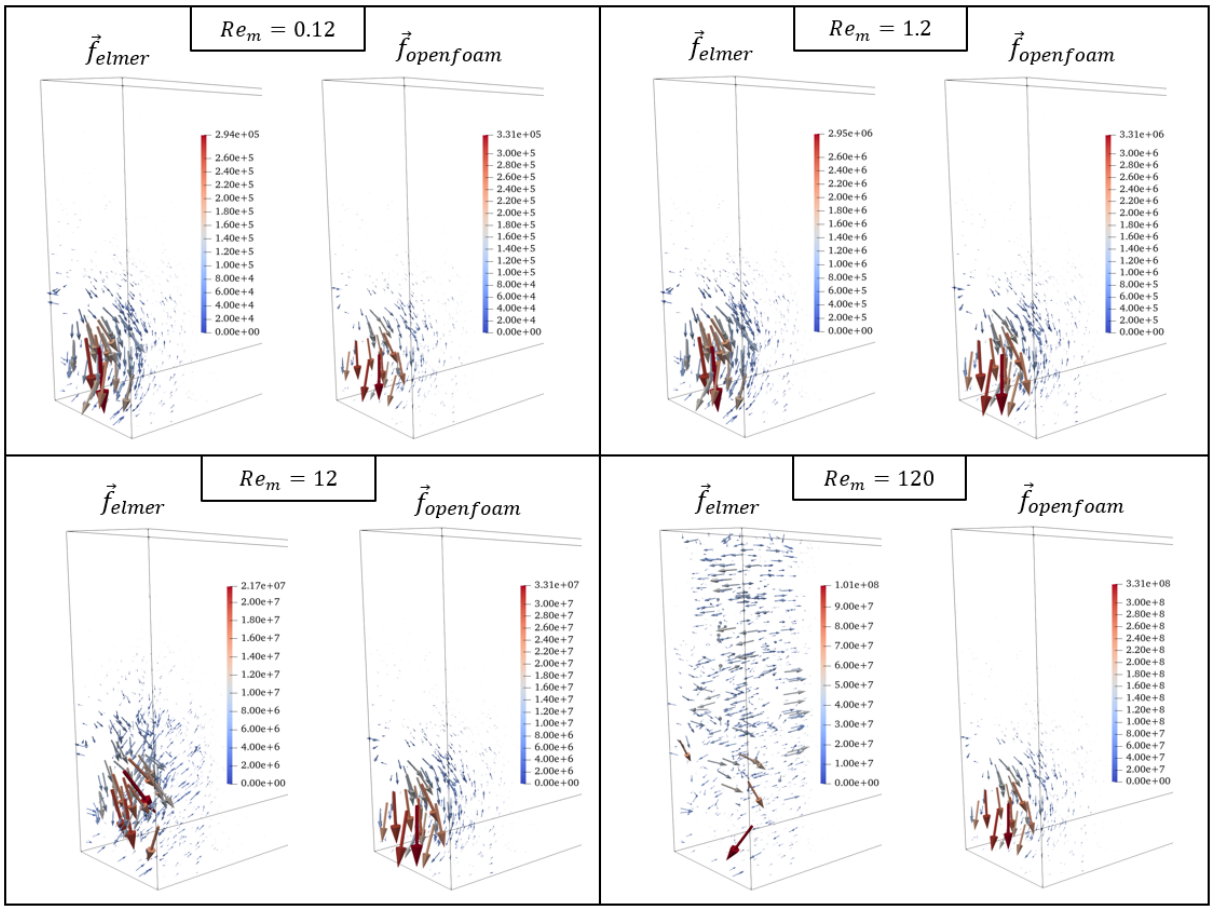

Fig. 3.6.23. Distribution of Lorentz force in the full and simplified models for a range of Re_m.

3.6.4 Coupling algorithms

In this section, different coupling algorithms implemented in Elmer and OpenFOAM simulations using EOF-Library are analyzed. There are three main algorithms:
a) solve EM fields only once at the start of simulation
b) re-calculate EM fields every time the free surface changes shape
c) re-calculate EM fields every time-step during simulations
The third option is used rarely, because if the free surface is not changing, for example, then EM fields will also not change. Let's focus on the a) and b) options.

The option to calculate EM fields only once may be valid for several cases. One is where Lorentz force concentrates reasonably far from the free surface. In such a case, free surface deformation does not affect the force distribution much, and so the force can be calculated only once for the initial free surface shape. This approach will be shown to be valid for a simple test case - flow of liquid gallium induced by a rotating permanent magnet. This case will also be used for experimental validation in section 5.2.

The application of the coupling algorithm where EM forces are updated with free surface changes is obviously necessary for many cases. One good example is the EM levitation shown in the previous section. There, Lorentz force concentrates near the surface and so any free surface changes will affect the force distribution. Even in cases where

most of the force is far from the surface, it may be necessary to check what percentage of it is ignored if the simplest coupling is used.

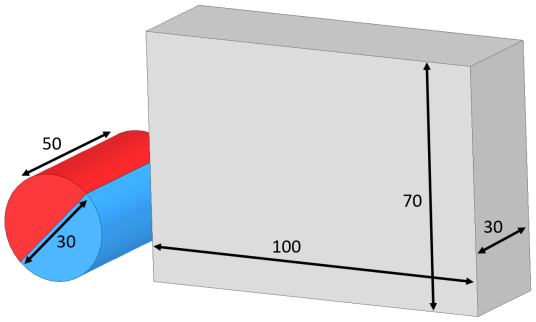

Fig. 3.6.24. Scheme of the test model; sizes in mm.

Let's start with the rotating magnet case. Scheme of the model is shown in Fig. 3.7.3. The configuration is quite simple - one rotating diametrically magnetized cylinder is located next to a rectangular container with liquid gallium. Distance from the magnet edge to gallium is 11 mm. The mesh of the active zone is shown in Fig. 3.7.4. In the model, there is some amount of acid solution on top of the melt for which water properties are used. Physical properties are listed in Table 3.6.2. For simplicity, the contact angle is set to 90 degrees.

The $\vec{v}\times\vec{B}$ term is very important in this model. Magnetic Reynolds number is $Re_m < 1$ so this term is moved to the fluid model in OpenFOAM. As described above, this term needs some correction to account for current path closure in the liquid metal.

Elmer solves electromagnetism in frequency domain for complex amplitudes. It then sends to OpenFOAM real and imaginary parts of current density and magnetic field. OpenFOAM solves time-dependent problem and reconstructs time-dependent functions from the amplitudes. For example, x component of the magnetic field is

$$B_x(t) = \sqrt{B_{x,re}^2 + B_{x,im}^2} cos\left(atan\left(\frac{B_{x,im}}{B_{x,re}}\right) + 2\pi ft\right) \tag{3.6.1}$$

Table 3.6.2: Physical parameters in the rotating magnet model

Magnet remanence	1.45 T
Magnet rotation frequency	15 Hz
Gallium electrical conductivity	3.7 MS/m
Gallium density	6080 kg/m^3
Gallium viscosity	2.0 mPa·s
Gallium surface tension	0.72 N/m
Gallium melting point	30°C
Gallium-wall contact angle	90 deg

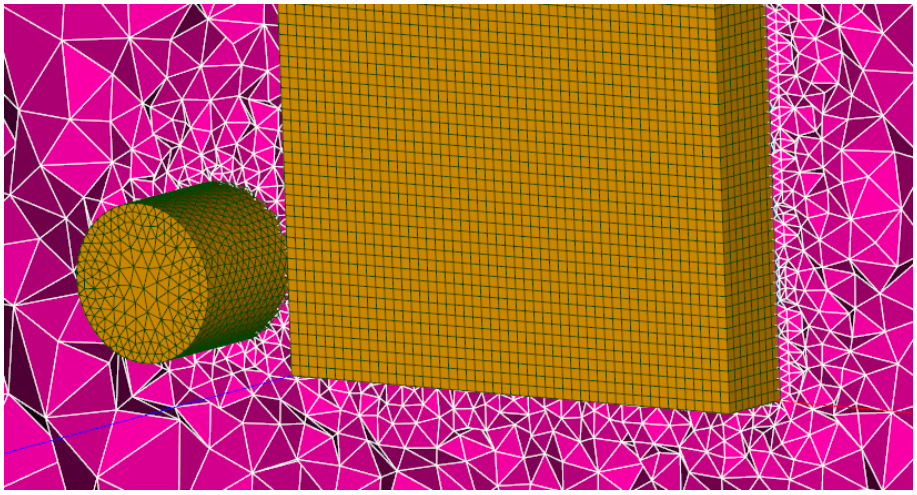

Fig. 3.6.25. Section of the mesh.

Current density is corrected for the $\vec{v}\times\vec{B}$ term as described above and the total current density is

$$\vec{j} = \vec{j}_{elmer} - \sigma\nabla\phi_v + \sigma\vec{v}\times\vec{B} \tag{3.6.2}$$

where subscript *elmer* means that the field is imported from Elmer simulation (that does not include the flow velocity term but includes all other) and ϕ_v is the correcting potential.

Fig. 3.6.26 shows time-average Lorentz force for the initial undeformed liquid metal volume and with $\vec{v} = 0$. In the simplest coupling approach, this force is used throughout the simulation, apart from the $\vec{v}\times\vec{B}$ term which is updated every time-step in the fluid simulation.

From the force graph along a vertical line it can be seen that 1 cm from the surface it is less than 10% of the maximum. This is the argument used to validate the approach of calculating the EM fields only once. When the free surface deforms upwards from this maximum force zone near the left wall, the percentage of the force in the liquid metal above the initial surface level may be negligible. To demonstrate this, Fig. 3.6.27 shows the force distribution without the velocity term for a deformed liquid metal shape.

Integral force in the vertical direction is 0.1546 N for the initial surface shape and 0.1551 N for the deformed shape. This is around 0.3% relative difference, which can be considered negligible, therefore validating the approach of calculating EM fields only once.

This simplified approach may also be valid for some other cases. For example, the electrovortex configuration with current injection in a cylindrical liquid metal volume from the bottom, which is also studied in the thesis. In that case, most of the magnetic field, current density and force is located around the edge of the injection electrode. The force causes a strong upward jet and free surface deformation. Simulations showed that the EM fields change very little with the surface deformations. More details about this setup are presented in the results section.

Let's move the magnet higher, closer to the free surface and see if the single-EM-calculation approach is still valid. In the case above, the top of the magnet was 38 mm from the free surface level. Let's place it 2 mm from the surface. The force results are

shown in Fig. 3.6.28. In this case, the integral force is 0.151 N for the initial surface shape and 0.167 N for the deformed shape. This is over 10% relative difference, which is not acceptable in most applications. In this case, EM simulation must respond to the changes in the conducting region shape and update all relevant fields and forces.

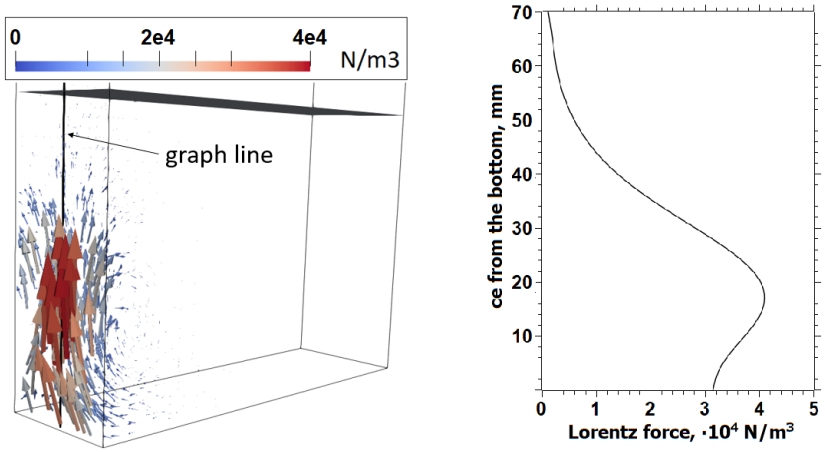

Fig. 3.6.26. Lorentz force in static liquid metal; vectors (left) and magnitude along the line 1 mm from the left wall (right).

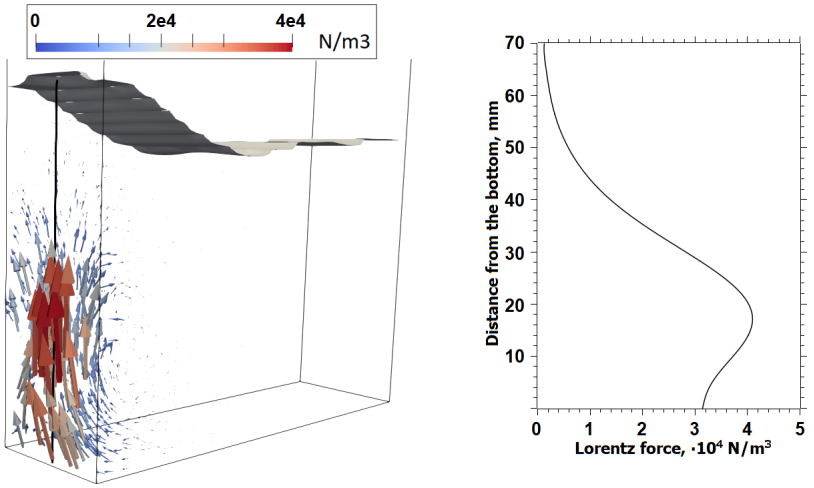

Fig. 3.6.27. Lorentz force in liquid metal with deformed free surface; vectors (left) and magnitude along the line 1 mm from the left wall (right).

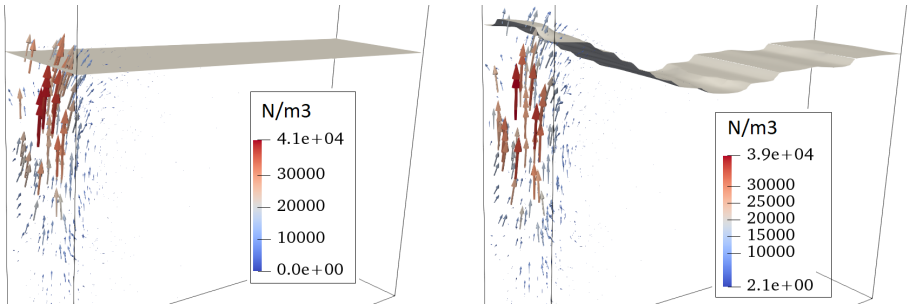

Fig. 3.6.28. Lorentz force vectors in liquid metal: initial surface (left), deformed surface (right).

3.6.5 Liquid metal solidification

A solidification solver was developed in OpenFOAM. The main application of this solver within the thesis is simulation of direct strip casting. This section describes verification and testing of the developed solidification solver.

The solidification solver, which is for now called `solidificationInterFoam` (based on two-phase solver `interFoam`), is based on the enthalpy-porosity method, where the solidified part of material is forced to move with constant velocity $\vec{v}_p$ by introducing liquid fraction function and momentum source

$$\beta = 1 + (0.5 \operatorname{erf}(b_T(\alpha - \alpha_0)) + 0.5)(0.5 \operatorname{erf}(a_T(T - T_s)) + 0.5 - 1) \tag{3.6.3}$$

$$\vec{f}_{solid} = A\frac{(1-\beta)^2}{\beta^3 + \epsilon}(\vec{v}_p - \vec{v}) \tag{3.6.4}$$

where A is the mushy zone constant and ϵ is a small number (like 10^{-3}). More detailed description is given in section 3.5.

The developed approach includes several coefficients which must be adjusted for each solidification case. In the belt casting process, three phases are present - liquid and solid metal, and air. Since the model uses the VOF method, the interface between metal and air is not absolutely sharp but is determined by the change of volume fraction α from 1 (metal) to 0 (air). $\alpha = 1$ includes both liquid and solid metal. Special care must be taken in the zone where $0 < \alpha < 1$ because air is not supposed to be affected by the solidification process. The coefficients b_T and α_0 will determine the fraction of air being affected by the force f_{solid} when $T < T_s$. b_T determines the steepness of the β function around $\alpha = \alpha_0$.

Coefficient a_T controls the steepness of β around melting point T_s. In other words, it determines the interval of temperature where solidification takes place. Another approach would be to rewrite β using liquidus and solidus temperatures, but here the solidification interval is controlled by a_T.

Ideally, the solidified metal preserves its shape during the movement with velocity $\vec{v}_p$. The test case for this is a moving rectangular solid block as shown schematically in Fig. 3.6.29.

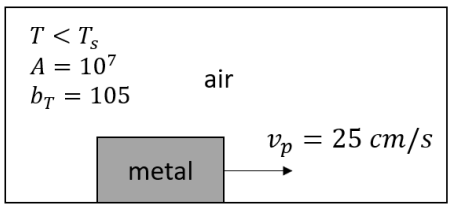

Fig. 3.6.29. Test case for solidification model coefficient α_0.

Fig. 3.6.30 shows shape of the moving block for different values of α_0. The effect of α_0 is very clear - for large values the solid block deforms. All test results will not be shown

here. The main conclusions from this test model is that b_t should be large and α_0 - small. Specific values must be adjusted for each case.

The next test considers a simplified casting simulation, basically testing the whole developed model. Scheme is shown in Fig. 3.6.31. Mesh is uniform with rectangular elements of edge size 1 mm. Optimal model coefficients based on many tests are $b_T = 100$, $a_T = 4$, $\alpha_0 = 0.04$. The metal properties are density 6080 kg/m^3, viscosity 2 mPa·s, surface tension 0.72 N/m, heat conductivity 50 W/m·K, heat capacity 370 J/kg·K and melting point $T_s = 303$ K.

Fig. 3.6.32 shows casting model results with and without latent heat. Qualitatively, the results are physical - liquid metal gradually solidifies on the belt and solid material is constantly pulled away. The effect of latent heat is also captured correctly - with latent heat more energy needs to be removed from liquid metal and the complete solidification process takes longer (point of complete solidification of the layer moves downstream). Almost identical results are obtained using ANSYS Fluent (not shown here).

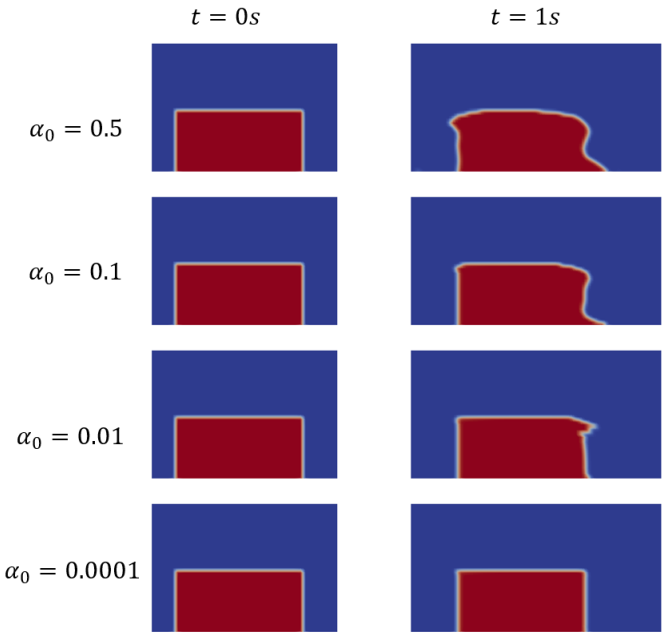

Fig. 3.6.30. Test results for parameter α_0 in the solidification model.

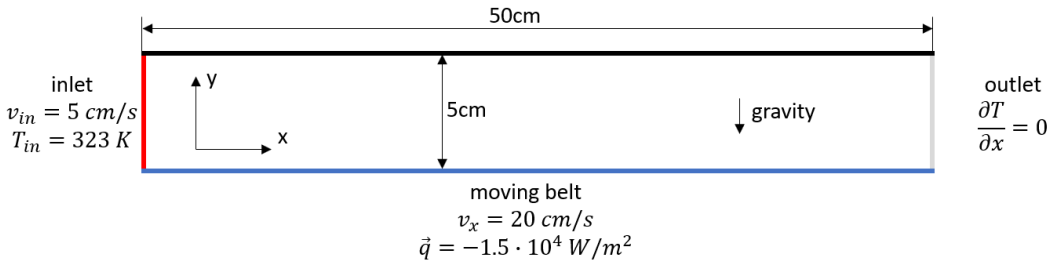

Fig. 3.6.31. Scheme of the test case for metal belt casting.

Fig. 3.6.32. Metal casting test case results: black - solid metal, red - liquid metal, grey - air. The black arrows mark the point from which the layer is completely solid.

3.6.6 Conclusions

In this section, the numerical models developed in the thesis were tested in the range of relevant parameters. Initial tests show promising results and possibilities to reduce simulation time by using different simplifications, such as simulating EM fields only once or moving part of electric current calculation to the fluid simulation.

Agreement between the three MHD simulation approaches ((1) Elmer+OpenFOAM (EOF), (2) OpenFOAM (MHD/OF) and (3) ANSYS Maxwell + CFX (ANSYS)) was partly achieved. In the levitation test case, the steady droplet shape was very similar in all cases. The flow velocity, however, was very different in the ANSYS model. The reason could be related to turbulence models in CFX, although specific issues were not found. Nevertheless, on the basis of most of the results being very close, apart from the velocity in ANSYS, the models can be considered as reasonably verified. Further judgment of the validity of these methods will be provided by comparison to experiments.

The solidification model developed in OpenFOAM performs well. It includes several parameters which must be adjusted for different cases. The casting model will be coupled to Elmer to simulate liquid metal belt casting with electromagnetic flow control.

After the development and verification, several specific numerical models are formulated that, together with experiments, will form the basis of the investigations of various physical processes. These final models are described in the following section.

3.7 Main models

From the fluid dynamics perspective, the first three of the final models (excluding the casting case) are very similar. All three models consider turbulent two-phase flow with free surface capturing using the VOF method. All three models include liquid metal in a solid container with an opening on top. Because of this, many parameters, including boundary conditions, are almost the same. To avoid repeating the same description in each of the subsections, the common parameters and numerical settings are summarized here. The belt casting model is fully described separately.

Table 3.7.1: OpenFOAM boundary conditions for the electrovortex, stirring and thin melt layer models; Names of solution variables and boundary conditions as they are defined in OpenFOAM are given in parentheses.

	walls	opening
$\vec{v}(U)$	$\vec{v} = 0$ (`noSlip`)	$\frac{\partial \vec{v}}{\partial n} = 0$ (for outflow) or $\vec{v} = 0$ (for inflow) (`pressureInletOutletVelocity`)
p (p_rgh)	$\frac{\partial p}{\partial n} = 0$ (`zeroGradient`)	$p_{static} = 0$ (`totalPressure`)
α (alpha.melt)	$\theta = const$ (`constantAlphaContactAngle`)	$\alpha = 0$ (for inflow) or $\frac{\partial \alpha}{\partial n}$ (for outflow) (`inletOutlet`)
k (k)	Wall function (`kqRWallFunction`)	$k = 10^{-3}$ m^2/s^2 (inflow) and $\frac{\partial k}{\partial n} = 0$ (outflow) (`inletOutlet`)
ω (omega)	Wall function (`omegaWallFunction`)	$\omega = 1$ s^{-1} (inflow) and $\frac{\partial \omega}{\partial n} = 0$ (outflow) (`inletOutlet`)
ν_t (nut)	Wall function (`nutkWallFunction`)	calculated from k and ω (`calculated`)

The fluid flow models in OpenFOAM use modified `interFoam` solvers which include coupling to Elmer. The OpenFOAM models are transient, with momentum source received from Elmer. The free surface is captured using the VOF method. Time-step Δt is controlled by the Courant condition $Co = \frac{v\Delta t}{\Delta x} < 1$, which mostly means $\Delta t < 10^{-4}$ s.

Fluid flow boundary conditions are the following. On solid walls: velocity $\vec{v} = 0$; pressure gradient $\frac{\partial p}{\partial n} = 0$; volume fraction has a fixed gradient corresponding to a set contact angle θ (in case of $\theta = 90°$, $\frac{\partial \alpha}{\partial n} = 0$). The top boundary is an opening: $\frac{\partial \vec{v}}{\partial n} = 0$ for outflow and for inflow $\vec{v}$ is determined from the interior cells; pressure condition is $p = p_0 - \frac{1}{2}|\vec{v}|^2$, where total pressure $p_0 = 0$; $\alpha = 0$ for inflow and $\frac{\partial \alpha}{\partial n} = 0$ for outflow. Boundary conditions are summarized in Table 3.7.1.

3.7.1 Electrovortical flow with free surface

Scheme of the model is shown in Fig. 3.7.1. The model includes liquid metal, air, wall and bottom electrodes. Fluid dynamics domain is only the volume inside the cylindrical wall - melt and some air above it. EM model in Elmer includes the whole domain.

We consider axisymmetric and full 3D cases. Due to much shorter simulation time, axisymmetric model is used to obtain free surface deformation height dependence on the injected current up to some threshold current. The axial model is not able to simulate any experimentally observed surface instabilities - there is no swirl and the surface peak always stays on the axis (any deviation of it from the center in axial model would correspond to a ring-shaped surface deformation, which was not observed experimentally). To study the instabilities above the threshold current, a full 3D model was used.

Elmer solves steady EM equations in potential formulation for magnetic vector potential $\vec{A}$ and electric scalar potential ϕ. In the corresponding experiments, due to technical reasons, 50 Hz AC was used instead of DC. For 50 Hz, however, the skin depth is large and the secondary magnetic field is small. The effect of using either AC or DC was tested

numerically, and the results were practically the same. Because of this, the numerical model uses DC. EM boundary conditions are magnetic vector potential $\vec{A} = 0$ on the external boundary and electric scalar potential $\phi = const$ on electrode ends corresponding to a set constant current.

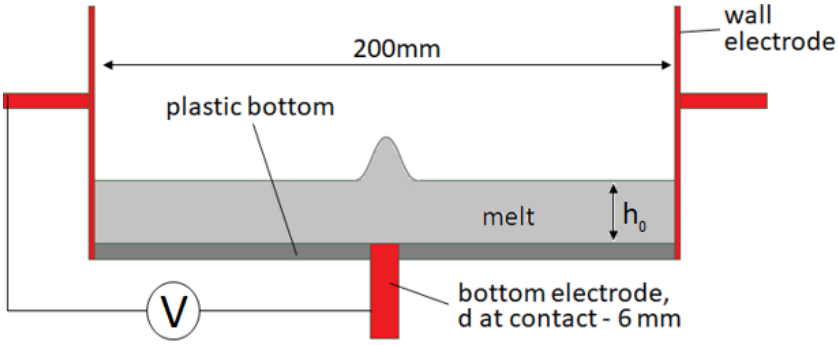

Fig. 3.7.1. Scheme of the numerical model.

Reynolds number in this system is $Re > 10^3$, implying a turbulent flow, which was also evident from the free surface fluctuations in experiments. The axisymmetric case used the k-ω SST turbulence model (`kOmegaSST` in OpenFOAM). Generally, the SST and other RANS eddy-viscosity models overestimate turbulent viscosity, damping the flow and free surface motion. In axisymmetric model, the instabilities are not captured regardless of the turbulence model used. To avoid artificial damping and allow capturing surface dynamics, the 3D model used LES with turbulent kinetic energy k sub-grid model (`kEqn` model in OpenFOAM) or a hybrid DES model based on k-ω SST turbulence model (`kOmegaSSTDES` in OpenFOAM) with wall functions. DES is not as strict as LES regarding mesh resolution, while it still resolves much more oscillations than regular RANS. LES and DES results in this case with the same mesh are very similar.

Axisymmetric model in OpenFOAM is implemented as a few-degree wedge with symmetry boundary conditions on wedge sides (the condition is called `wedge` in OpenFOAM), because OpenFOAM has only 3D capabilities. An axisymmetric EM model in Elmer for this system is a bit tricky to implement. Standard potential-based 2D or axisymmetric EM solvers consider only one component of the vector potential $\vec{A}$ (perpendicular to the solution plane) and the magnetic field is parallel to the this plane. In this case, $\vec{A}$ and current density $\vec{j}$ need to be parallel to the solution plane. This was solved by using quasi-axisymmetric geometry - a few-degree wedge of the whole cylinder with appropriate symmetry boundary conditions.

The EM-HD coupling here is very simple - EM is simulated only at the beginning of the simulation for the initially flat free surface and the Lorentz force stays constant throughout the hydrodynamics simulation, i.e., it is a one-way one-time coupling. This approximation is valid in this system because most of current density, magnetic field and Lorentz force concentrate near the bottom electrode relatively far from the free surface. This approximation may cease to be valid with very strong surface deformations and instabilities. Since the EM is simulated only once at the start, total simulation time is mostly dictated by the fluid flow model.

The geometries and meshes for the fluid model were created for each case separately depending on the initial filling of the container and the expected surface deformation. For example, if the initial level is 10 mm with the maximum deformation 10 mm above the initial level, the geometry inside the container would be a cylinder with at least 30 mm height. The geometry of the bottom electrode, wall electrode and the surrounding air in the EM model was always the same, but the fluid region (coupling zone) was the same as in the fluid model. An example of meshes for Elmer and OpenFOAM are shown in Fig. 3.7.2. Characteristic size of mesh elements in OpenFOAM is 1 mm in the X and Y directions, and 0.7 mm in the Z (vertical) direction.

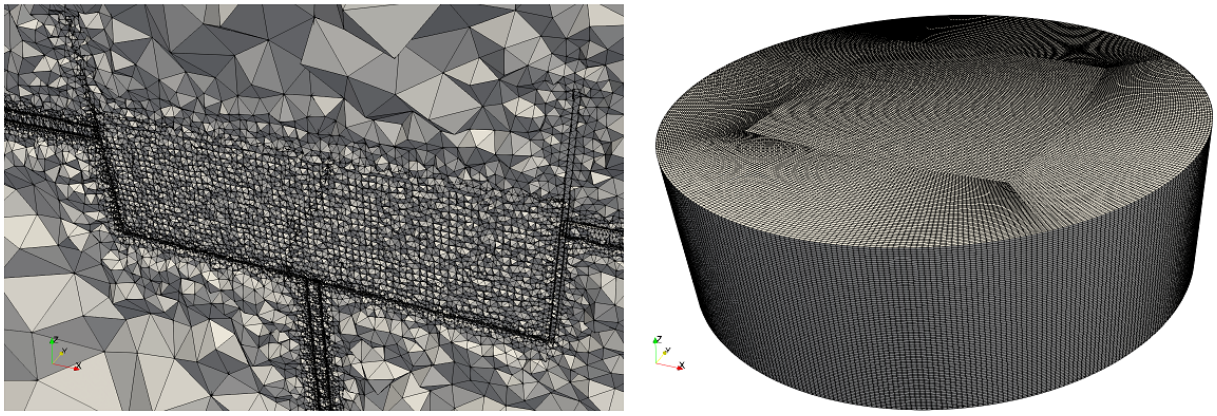

Fig. 3.7.2. Examples of meshes for Elmer (left) and OpenFOAM (right).

3.7.2 Liquid metal stirring

Scheme of the model is shown in Fig. 3.7.3. For simplicity, only one magnet is considered, rotating in such a way as to induce an upwards flow and deformation of the free surface. The initial liquid metal height H is calculated from experiments based on the volume of liquid metal in the container. EM model in Elmer consists of the magnet, liquid metal and surrounding air. Fluid flow model in OpenFOAM contains only the liquid metal with some space above it for the acid solution.

EM problem in Elmer is solved in frequency domain using the `WhitneyAVHarmonicSolver`, which solves EM equations in A-V formulation (A - magnetic vector potential, V - electric scalar potential). The linear system is solved using the BiCGStabl iterative method without matrix preconditioning.

Rotation of the magnet is modelled as a rotating magnetization vector $\vec{M}$ which in complex representation means setting amplitudes of real and imaginary parts. For counter-clockwise rotation around the Z axis time-dependent form is $M_x = \frac{B_r}{\mu_0} cos\left(\omega t\right), M_y = \frac{B_r}{\mu_0} sin\left(\omega t\right)$ and in complex form this is $M_{x,re} = \frac{B_r}{\mu_0}$, $M_{y,im} = \frac{B_r}{\mu_0}$, where B_r is remanence. Elmer then solves the case for the complex amplitude of vector potential $\vec{A}$ from which current density $\vec{j}$ and magnetic field $\vec{B}$ can be calculated. The only EM boundary condition is $\vec{A} = 0$ on the external boundary. A representative EM mesh is shown on the left in Fig. 3.7.4.

The liquid metal in OpenFOAM is initialized as a rectangular block and a simulation

without EM forces is initially run until the shape of the fluid stabilizes and the set contact angle is achieved. After that, the coupled simulation starts.

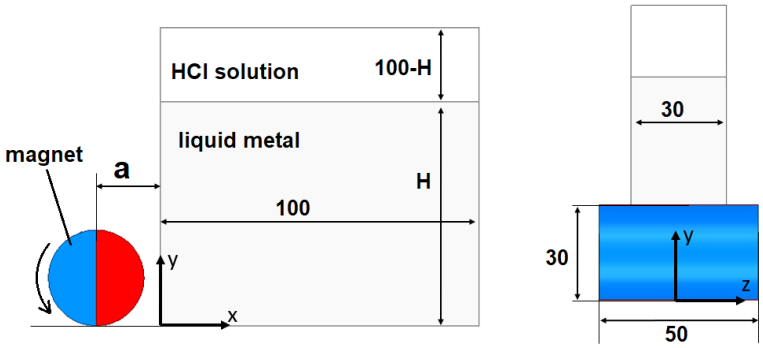

Fig. 3.7.3. Scheme of the rotating permanent magnet stirrer with sizes in mm.

Simulated free surface shape and its dynamics strongly depends on the choice of turbulence models. The main benefit of RANS models is simulation time. While in this case RANS models, such as k-ω SST, can provide reasonable time-averaged free surface deformation shape, they can't resolve all the free surface dynamics observed experimentally. LES models are more time-consuming, but they are more accurate and usually match experiments better. Both approaches were tested for the rotating magnet case - RANS k-ω SST, and LES with the Smagorinsky sub-grid scale model.

An important parameter for turbulence models is the mesh. To get the most out of LES models, a fine mesh must be used, since the resolved part of turbulent fluctuations depends on the mesh element size. RANS results depend weakly on the mesh size. Two meshes were used with both turbulence models - one with 394 thousand elements and one with 1.8 million elements. A qualitative representation of an OpenFOAM mesh with refinement zones is shown on the right in Fig. 3.7.4 (note that this particular mesh was not used, the actual meshes are finer and elements would not be clearly visible in such a picture). Maximum dimensionless wall distance y+ criterion is below 1 for the finest mesh, which means that the hydrodynamic boundary layer is resolved without the use of wall functions. Simulations with the coarsest mesh use wall functions with maximum $y^+ > 17$.

In section 3.6, several EM-HD coupling approaches were tested, each applicable to different cases. The most precise approach in this case would be the one where EM fields are updated every time the free surface changes shape. Using the VOF method, this means that coupling occurs every time the volume fraction changes by, say, 0.5 in any mesh cell. This approach is therefore mesh-dependent - the finer the mesh, the more frequently the free surface will cross mesh cells, and the simulation time will increase significantly. An alternative for finer meshes is to simply choose a fixed coupling time interval related to the magnet rotation period, since small-scale free surface oscillations are related to that. Applying the alternative approach, coupling between Elmer and OpenFOAM was set to trigger 20 times per magnet rotation period, which would resolve force oscillation period with 10 steps. During the field coupling, Elmer receives electrical conductivity

and velocity distributions from OpenFOAM, recalculates EM fields and returns them to OpenFOAM, where time-dependent fields are reconstructed from the complex ones from Elmer.

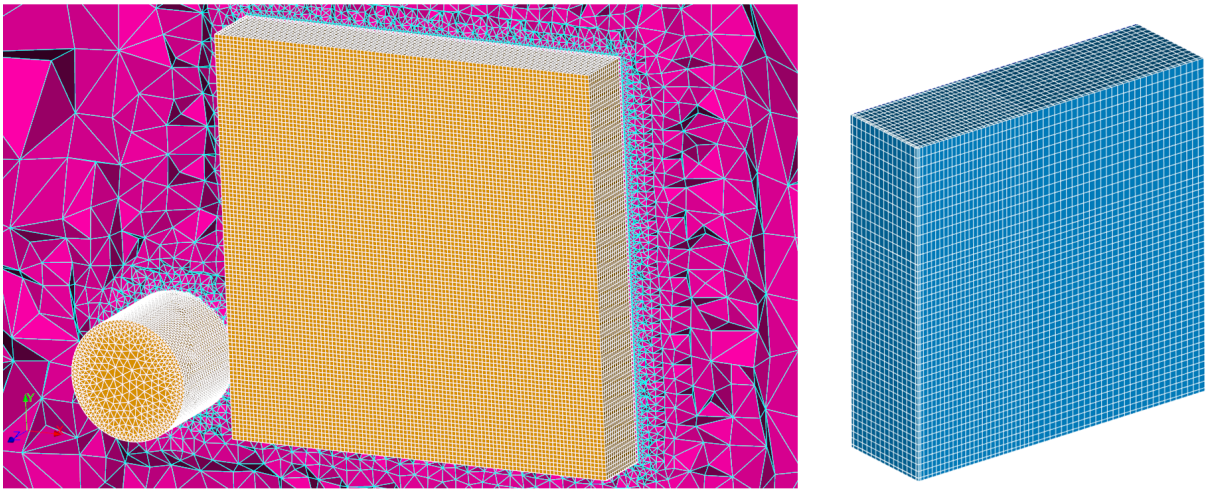

Fig. 3.7.4. Elmer mesh near the magnet and melt (left) and qualitative OpenFOAM mesh (right).

The main simulation results that are compared to experiments are free surface profiles. As noted in section 3.6, there are cases where free surface deformation is directly linked to the bulk flow velocity, such as when the Weber number is small (when surface tension forces are not significant compared to kinetic energy of the fluid). And this is one of the cases - the rotating magnet induces an upward flow which leads to free surface deformation. In other words, the free surface is deformed by the dynamic pressure of the liquid. The free surface deformation indirectly tells us the flow velocity. Therefore, if the free surface shape and deformation in simulations is the same as in experiments, the flow velocity also must be very close.

The free surface is exported from OpenFOAM in VTK format, as shown visually on the left in Fig. 3.7.5. For further processing (time averaging etc.), the VTK data is projected onto a plane and treated as an image (right in Fig. 3.7.5), which is very similar to the projection images obtained in experiments. After some further image processing, these images are processed the same way as the experimental ones.

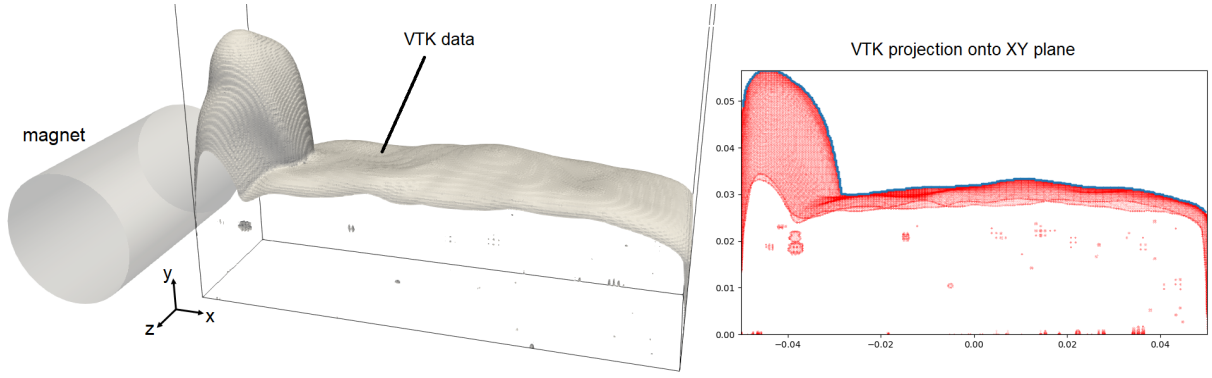

Fig. 3.7.5. Example of free surface from simulations (left) and its projection (right).

3.7.3 Thin melt layers in AC field

Scheme of the model with rectangular melt layer is shown in Fig. 3.7.6. The model includes an inductor, liquid metal and surrounding air or acid solution. Fluid dynamics domain in OpenFOAM is only the inside of the acrylic container with liquid metal and some air or HCl solution on top (the oxidized case includes air, the non-oxidized - water/HCl solution). EM model in Elmer includes the whole domain.

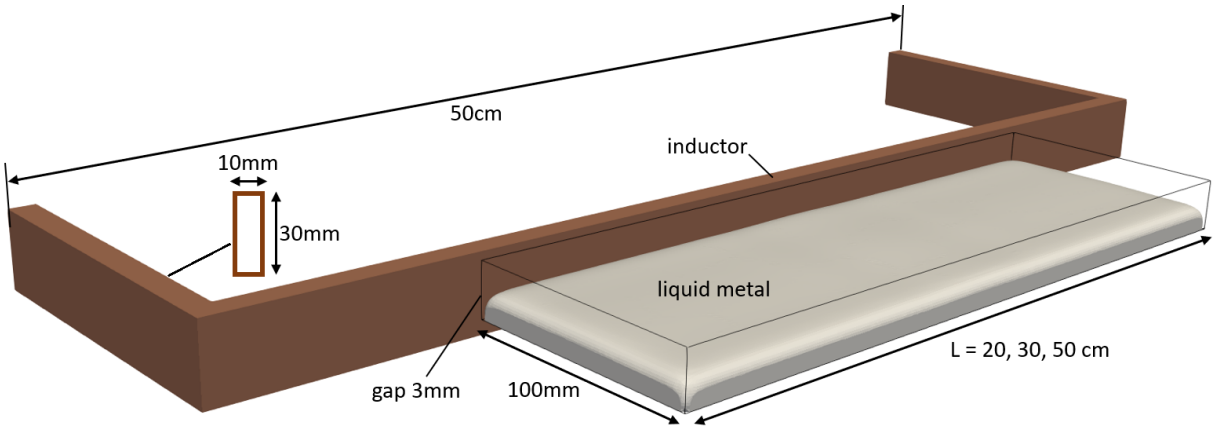

Fig. 3.7.6. Model scheme of melt layer in AC magnetic field with sizes in mm.

EM problem in Elmer is solved in frequency domain using the `WhitneyAVHarmonicSolver`, which solves EM equations in A-V formulation. The linear system is solved using the BiCGStabl iterative method without matrix preconditioning.

Inductor is made as a hollow rectangular tube with 1 mm thickness (approximately equal to the skin depth in copper at 4000 Hz). Current is set as constant voltage across the inductor ends. The boundary conditions in Elmer are constant potential ϕ on inductor ends and magnetic vector potential $\vec{A} = 0$ on the external boundary.

Like in the stirring model, the liquid metal region in OpenFOAM is initialized as a rectangular block and a simulation without EM forces is initially run until the shape of the fluid stabilizes and the set contact angle is achieved. After that, the coupled simulation starts.

For turbulence, the model uses either LES turbulent kinetic energy k sub-grid model (`kEqn` model in OpenFOAM) or a hybrid DES model based on k-ω SST model (`kOmegaSSTDES` in OpenFOAM) with wall functions.

Unlike the previous two models, the coupling between EM and fluid dynamics is more strict in this case. Since the EM force concentrates near the free surface due to skin effect, EM fields must be recalculated based on some criterion that considers the motion of the free surface. The most reasonable criterion was chosen to be the change of volume fraction $\Delta\alpha$ anywhere in the domain between coupling iterations. Setting $\Delta\alpha > 0.5$ will recalculate EM every time the free surface moves over at least half a mesh element anywhere in the domain. The coupling frequency, therefore, depends on the free surface movement and the size of mesh elements. If steady state is reached where free surface

does not move, EM fields are no longer be updated, although completely static state is never the case in this process - the surface always oscillates at least slightly due to the turbulent bulk flow.

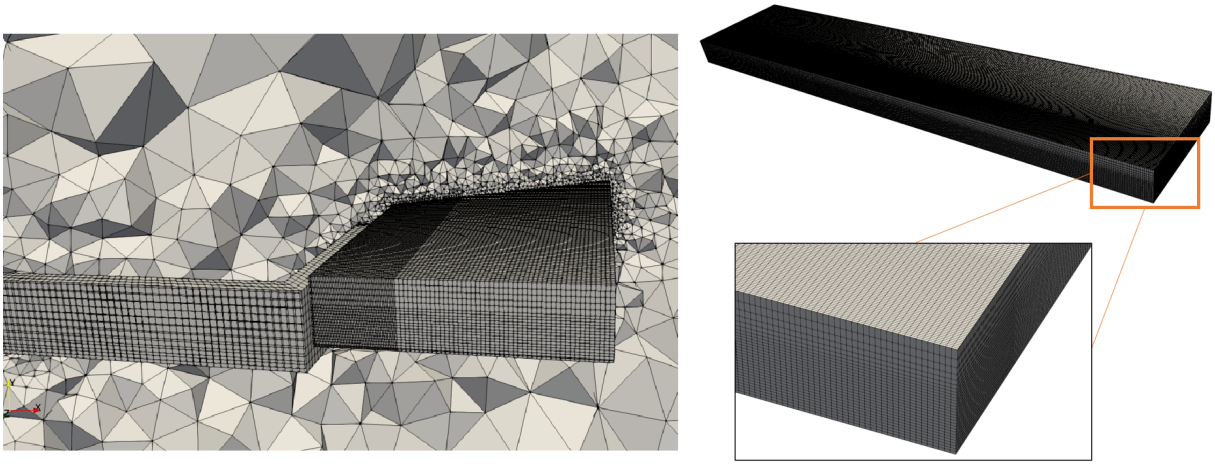

Fig. 3.7.7. Examples of numerical mesh for Elmer (left) and OpenFOAM (right).

The Lorentz force in OpenFOAM is applied gradually from zero to the value received from Elmer over a 3 second period to avoid splashing when the fluid is rapidly accelerated from rest, which improves stability of the simulation. Such splashing is also observed in experiments when switching on the current.

Representative meshes for the rectangular case are shown in Fig. 3.7.7. Characteristic element size in the zone where free surface oscillates is below 1 mm. For $L = 30$ cm, total number of elements in 1 million in Elmer model and 850 thousand in OpenFOAM.

Among different parameters, the effect of surface oxidation was also studied. The experimental observation is that surface oxidation changes the contact angle and adhesive properties. A modified contact angle was used as the parameter in the model separating oxidized and non-oxidized cases. Approximately 40 degrees for oxidized surface was found to work reasonably well. Of course, such approximation of surface oxidation is not completely physically valid, but it leads to reasonable results, at the very least qualitatively.

Most of the simulations were done for the rectangular layer. However, the case with circular liquid metal drops is basically the same, except that the inductor is cylindrical and the container is circular. All numerical settings are identical to those described above for the rectangular layer.

For comparison to experiments, statistical information was extracted from numerical results. In OpenFOAM, the free surface was saved every 10 ms as an iso-surface at $\alpha = 0.5$ in VTK format. These files were opened in ParaView, where the surface shapes (top-down view) were saved as images where liquid metal is black and the background is white. Further processing was done in Wolfram Mathematica 12.1. The goal was to obtain surface oscillations in time at each point along the deformed edge, as well as the mean surface profile and standard deviation that describes the amplitude of oscillations. In Mathematica, the main step was doing edge detection (`EdgeDetect` function) to highlight

the pixels containing the free surface edge. Relative coordinates of the highlighted pixels were obtained with the `PixelValuePositions` function. Using a known scale in the images (e.g., width of the melt layer), the relative coordinates were converted to real ones. The arrays of edge points were interpolated (1st order) to obtain continuous edge profile for each image in the time-series. Using the `Mean` and `StandardDeviation` functions, the mean and standard deviation of the oscillating edge were finally obtained.

Coordinate system and variables used in the results is shown in Fig. 3.7.8. In this coordinate system, the non-deformed edge at rest (with inductor current off) has $y(x,t) =$ 100 mm. The edge dynamics can be characterised by the amplitude A_h, wavelength λ and oscillation frequency f_h, as well as the number N_h of the wave crests or "fingers" in the pattern. Data extracted using the processing described above include the edge coordinates in time $y(x,t)$, the mean edge profile $y(x)$ and standard deviation $\sigma_y(x)$. $y(x,t)$ includes information about oscillation frequency and $\sigma_y(x)$ is related to A_h.

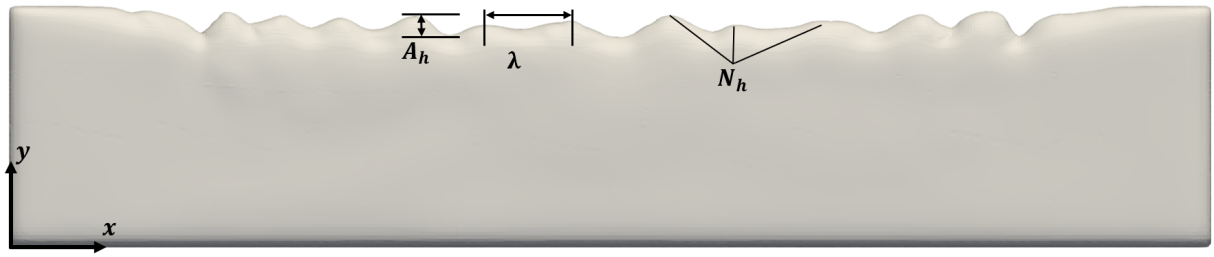

Fig. 3.7.8. Definitions of quantitative parameters for a deformed edge of the free surface (in this example, $N_h = 11$).

3.7.4 Belt casting

A more industrially-oriented case which involves several of the phenomena from the previous three models is the belt casting with EM control. Scheme of the casting model is shown in Fig. 3.7.9. Liquid metal is pouring down from a gap in the refractory, spreads onto the moving belt and gradually solidifies. Two cases are considered - full model with the backflow gap and a simplified model with the backflow gap artificially closed. For stabilisation, two EM systems are considered - straight high-frequency inductor near the backflow area and a static magnetic field system above the belt. The inductor is supposed to keep the liquid metal from entering the gap. The static magnetic field is used to decelerate the fast-flowing liquid metal, spreading the liquid more evenly across the belt and helping achieve a more uniform solid strip a the outlet.

The cast metal is aluminium with a melting point of $T_s = 933$ K. Material properties are assumed constant (independent of temperature and the same for liquid and solid phases for simplicity): density $\rho = 2311$ kg/m^3, viscosity $\mu = 0.8$ mPa·s, electrical conductivity $\sigma = 3.70$ MS/m, surface tension $\gamma = 0.84$ N/m, thermal conductivity $\lambda = 98$ W/(m·K), heat capacity $c_p = 1122$ J/(kg K), latent heat $L_T = 360$ kJ/kg. These are the values for liquid aluminium at 1200 K [127]. Gas phase is air.

The case with the high-frequency inductor in Elmer is solved in frequency domain using the `WhitneyAVHarmonicSolver`, while the case with static magnetic field is using

`WhitneyAVSolver` (magnetostatics). The system of linear equations in both cases is solved using the BiCGStabl iterative method without matrix preconditioning.

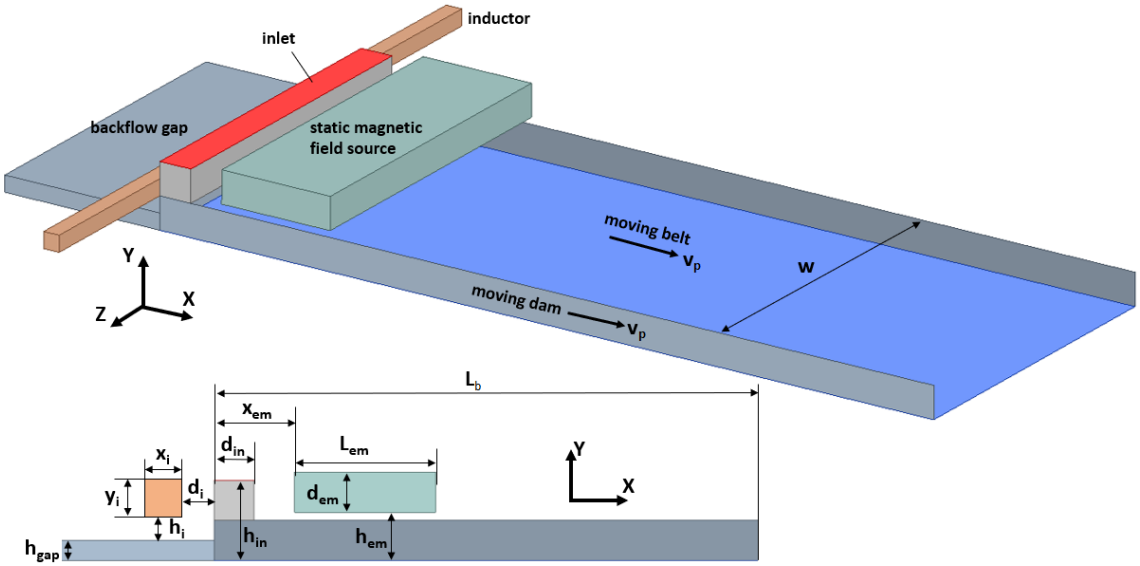

Fig. 3.7.9. Scheme of the casting model.

Inductor is made as a straight rectangular rod with constant current density across its cross-section. In the static field case, magnetic field source (magnetization M) is specified in a box above the melt layer (see Fig. 3.7.9) as $M_y = M_0$. If the static field source is a permanent magnet with remanence B_r, $M_0 = B_r/\mu_0$. To simulate TMF, real and imaginary components of M are set ($M_{y,re} = M_0 cos(2\pi\frac{x}{\tau})$, $M_{y,im} = M_0 sin(2\pi\frac{x}{\tau})$, where τ is pole pitch). The boundary condition in Elmer in both cases is magnetic vector potential $\vec{A} = 0$ on the external air boundary.

Table 3.7.2: OpenFOAM boundary conditions for the casting model.

	belt	dam/walls	inlet	backflow gap and outlet
$\vec{v}$	$\vec{v} = \vec{v}_p$	$\vec{v} = 0$	$\vec{v} = \vec{v}_{in} = const$	$\frac{\partial \vec{v}}{\partial n} = 0$ (for outflow) or $\vec{v} = 0$ (for inflow)
p	$\frac{\partial p}{\partial n} = 0$	$\frac{\partial p}{\partial n} = 0$	$\frac{\partial p}{\partial n} = 0$	$p_{static} = 0$
α	$\theta_b = const$	$\theta_d = 180^o$	$\alpha = 1$	$\alpha = 0$ (for inflow) or $\frac{\partial \alpha}{\partial n}$ (for outflow)
T	$\frac{\partial T}{\partial n} = const$	$\frac{\partial T}{\partial n} = 0$	$T = T_{in}$	$\frac{\partial T}{\partial n} = 0$
k	WF	WF	$k = 10^{-3}$ m^2/s^2	$k = 10^{-3}$ m^2/s^2 (inflow) and $\frac{\partial k}{\partial n} = 0$ (outflow)
ω	WF	WF	$\omega = 1$ s^{-1}	$\omega = 1$ s^{-1} (inflow) and $\frac{\partial \omega}{\partial n} = 0$ (outflow)
ν_t	WF	WF	calculated from k and ω	calculated from k and ω
ϕ_v	$\frac{\partial \phi_v}{\partial n} = 0$	$\frac{\partial \phi_v}{\partial n} = 0$	$\frac{\partial \phi_v}{\partial n} = 0$	$\frac{\partial \phi_v}{\partial n} = 0$

OpenFOAM model contains region above the moving belt with liquid/solid metal, inlet and outlet, and some air. To considerably simplify the model and reduce simulation time, radiation and natural convection are ignored. Typical magnitude of heat flux through the cooled belt is ≈10 MW/m^2 [30]. Assuming emissivity ≈ 1, radiative heat flux from a

surface at 1200 K to the environment at 300 K is on the order of 10^5 W/m^2, which is two orders of magnitude lower than the flux through the cooled belt. Natural convection can be ignored due to relatively small thickness of the melt layer (≈10 mm), and convection of the gas phase has very little influence on the motion of the melt due to density differences.

The k-ω SST DES model was used for turbulence. The OpenFOAM simulation is transient. Time-step Δt is controlled by the Courant number condition $Co = \frac{v\Delta t}{\Delta x} < 1$, where Δx is mesh element size. Typical element size is 1 mm. Boundary conditions in OpenFOAM are summarized in Table 3.7.2 where $\vec{v}_p$ is belt speed, p - pressure, k - turbulent kinetic energy, ω - turbulent eddy frequency, ν_t - eddy viscosity, α - volume fraction, T - temperature, θ - contact angle, ϕ_v - electric scalar potential, WF - wall functions. Using the specified contact angles, OpenFOAM calculates $\frac{\partial \alpha}{\partial n}$ and uses it as boundary conditions for the α equation solved in the VOF method.

For simplicity, the cooling boundary condition on the belt is a constant heat flux $\vec{q}_{belt}$. In OpenFOAM, this must be set using temperature gradient, which is the heat flux divided by the heat conductivity. Based on the geometry, material properties and inlet conditions, the necessary normal heat flux q_{belt} to achieve a fully solid strip by the end of the belt can be estimated as

$$q_{belt} \approx \frac{1}{L_b} \rho h v_p (c_p \Delta T + L_T) \tag{3.7.1}$$

where $h = v_{in} d_{in} / v_p$ and $\Delta T = T_{in} - T_s$. This is a rough estimate as it does not account for convection, heat transfer to atmosphere and other factors. Test simulations need to be performed to obtain an optimal value which ensures fully solid strip by half-way to the outlet. The optimal value in the configurations considered here is usually 2 to 5 times higher than the estimate.

The use of such heat flux condition, which might not be realistic in experiments or industrial processes, requires some comments. Since material properties are assumed independent of temperature, specific values of temperature are irrelevant (for example, fluid at 1000 K and 500 K will behave identically). The important thing is that all aluminium will move with the constant speed of the belt when its temperature falls below the melting point (also considering the latent heat). Therefore, in this model, there is no difference if the solidified part is 10 or 100 degrees below the melting point. A realistic cooling condition would be a Robin boundary condition which basically is a temperature-dependent heat flux that limits the temperature of the boundary to some set value. Such condition would simply require a longer belt to achieve fully solid strip, as the cooling rate would decrease with decreasing temperature. Temperature-dependent properties might be a more important aspect. However, physical properties of liquid aluminium between the melting point and 1200 K (inlet temperature) don't vary significantly, and solid aluminium properties down to some 100 degrees below the melting point differ from liquid ones by less than a magnitude [127]. Since the main purpose of this model in the thesis is to study the concept of EM control of the backflow and free surface dynamics in the belt casting process, it is best to make the model as simple as possible regarding the studied stability aspects. Conclusions drawn from these simulations should be taken qualitatively. The

parameters considered in this study might need tuning for real casting process.

In the model with the inductor, OpenFOAM receives the real part of Lorentz force from Elmer. In the case with static magnetic field, OpenFOAM receives magnetic field distribution from Elmer, and proceeds with the simulation calculating the induced current and Lorentz force as described in section 3.4.

With the high-frequency inductor for backflow control, EM fields are recalculated every time the free surface moves over at least half a mesh element in the zone close to the inductor. With static magnetic field, however, the simplified induced current approach described in section 3.4 was used, and EM model was run only once at the start of the whole simulation, after which the induced current and Lorentz force was computed in OpenFOAM at every time-step. The latter model is significantly faster, since most of the simulation involves only OpenFOAM.

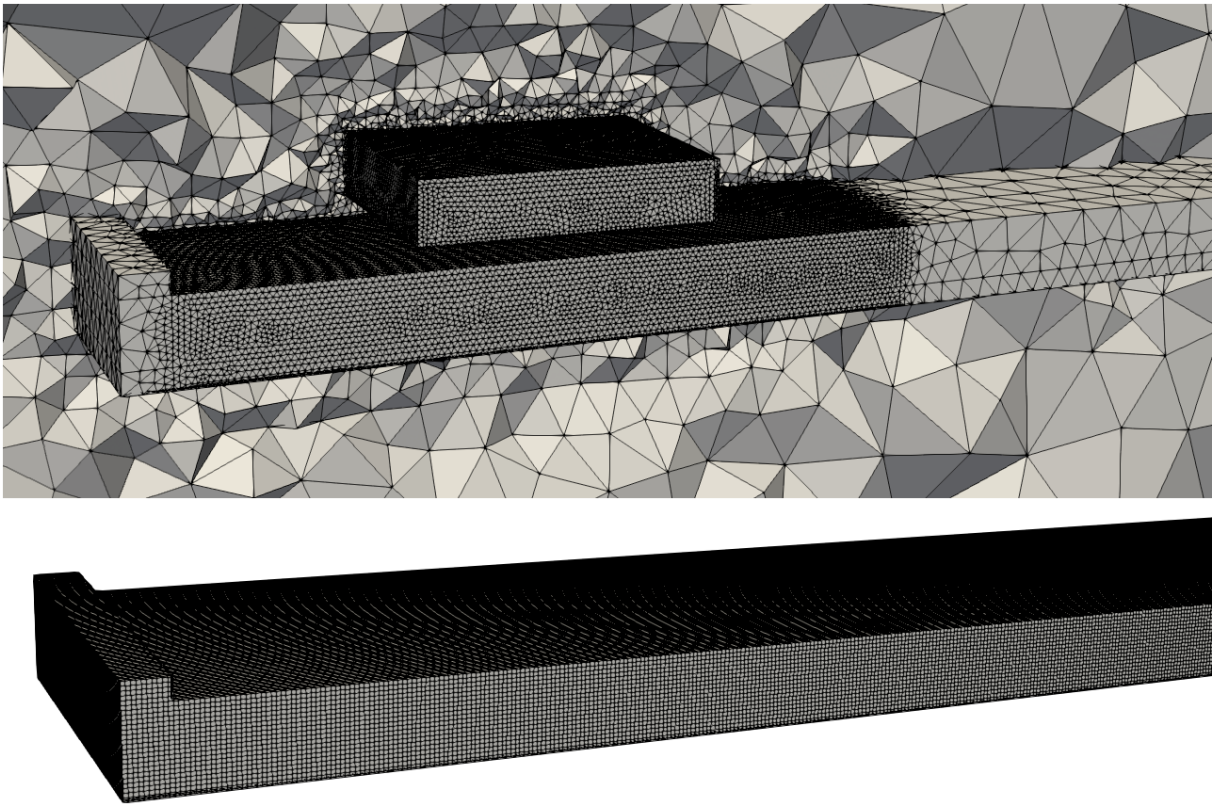

Fig. 3.7.10. Examples of numerical mesh for Elmer (top) and OpenFOAM (bottom) for the case with static magnetic field.

Representative meshes for the belt casting model are shown in Fig. 3.7.10. Characteristic element size in the melt zone is 1 mm.

To summarize the casting model, it consists of geometrical data shown in Fig. 3.7.9 (L_b, w, h_{in}, d_{in}, h_{mag}, d_{mag}, L_{mag}), material properties and boundary data shown in Table 3.7.1. Simulations were done with different dimensions and boundary conditions, such as different belt lengths and widths, different inlet temperatures, belt speeds, contact angles and different levels of EM interaction.

4 Experiments

Several experimental setups have been built to study different processes and validate numerical models - electrovortical flow with free surface, rotating permanent magnet stirrer and thin melt layer in transverse AC magnetic field. Each of the systems is different regarding electromagnetic field frequency and the importance of various physical effects and applicable approximations. For example, in rotating permanent magnet stirring, magnetic field frequency is relatively low (up to 50 Hz) and the interaction between magnetic field $\vec{B}$ and flow velocity $\vec{v}$ in the form of the $\vec{v} \times \vec{B}$ term is crucial. In the case of a thin melt layer in transverse AC magnetic field, the field frequency is much higher (order of 10^3 Hz), leading to strong coupling between electromagnetic fields and the free surface shape (due to electric currents concentrating near the surface in thin skin layer), while the $\vec{v} \times \vec{B}$ can be neglected. The case of electrovortical flow is where the electric currents in the liquid metal are induced not by time-varying magnetic fields but by direct injection via electrodes in contact with the melt. In this case DC can be used. Subsections below describe each experiment in more detail.

4.1 Electrovortical flow

The experimental setup is shown in Fig. 4.1.1 (left). It was built at the Institute of Electrotechnology, Leibniz University of Hannover in Germany. The system is a cylindrical copper wall (diameter 20 cm) with two current connections of the same polarity. The bottom wall is made of plexiglass. In the center of the bottom wall there is a small electrode, which is contacting the liquid metal. The liquid metal is Galinstan, filling the cylindrical container up to a level of 60 mm (the maximum was limited by the available amount of the metal). A 50 Hz electric current in the range of 500 to 2000 A is injected through the bottom electrode and diverges radially through the liquid metal into the copper wall. The resulting Lorentz force was such as to create an upward jet and free surface deformation.

Initially, the bottom electrode was a solid brass cylinder with diameter of either 10 or 21 mm. For high injected currents, the electrode was overheating due to intense Joule heating. This was solved by making an electrode with water cooling, as shown schematically in Fig. 4.1.1 (right). With cooling, the overheating was no longer a problem, and the diameter of the electrode at contact with melt could be made even smaller (6 mm), to increase current density and Lorentz force at the contact between the electrode and liquid metal.

The presence of two current leads on the side wall, of course, introduces some deviation from axial symmetry, which was seen in results - the melt started swirling at around 900 A during the first experiments. To reduce the asymmetry, both current leads were adjusted so that current through each of them was as close as possible. After that, it was more difficult to initiate the swirling, even up to 1500 A, although at such a high current the surface deformation peak was strongly oscillating and moving around the center.

AC was used due to a very small voltage required for DC. For AC, the voltage was

controlled with a transformer. It was tested numerically that DC and 50 Hz AC give virtually identical results for fluid flow and free surface dynamics.

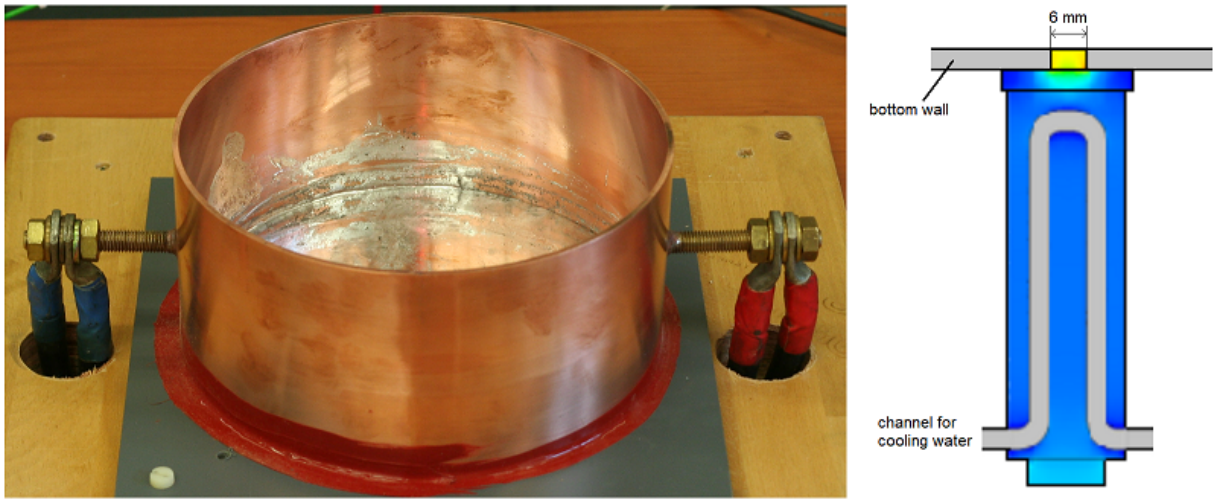

Fig. 4.1.1. Experimental setup of electrovortical flow with free surface (left) and scheme of the bottom electrode (right).

The main experimental results here are video recordings of the free surface, as well as simple measurements of the surface deformation height in the center of the container. The height measurements were reasonable up to some threshold current, at which the surface deformation peak started oscillating and sometimes the whole melt volume started swirling. Velocity measurements using UDV were also attempted, however, this was unreliable due to surface fluctuations and relatively small melt layer thickness. UDV measurements from the side of the container were limited by difficulty of ensuring good contact between the flat surface of the tip of the probe and the curved wall of the container.

4.2 Permanent magnet stirrer

The experiments took place at the Institute of Numerical Modelling, University of Latvia in Riga. The setup is shown in Fig. 4.2.1. It consists of two diametrically magnetized NdFeB cylinders attached independently to two motors providing magnet rotation frequencies up to 50 Hz. Magnets, driveshaft, and motors are held together on aluminium frame and for most parts non-magnetic components are used, to limit possible distortion of magnetic field. The use of two independent motors gives more freedom in changing magnet positions and rotation frequencies. The frequency is varied using a custom script that controls the frequency converters for each motor.

Each magnet has a strength class of N52 which corresponds to remanence of 1.42 to 1.47 T. Since magnetic field of the magnets is the primary source of inducing Lorentz force in the melt, knowing the value of remanence precisely is crucial for an accurate numerical model. To make sure that the model uses the correct remanence, it was determined experimentally by measuring the magnetic field around one of the magnets. Optimization was performed in Comsol Multiphysics by changing remanence, position and orientation of the magnet to match the measured magnetic field data.

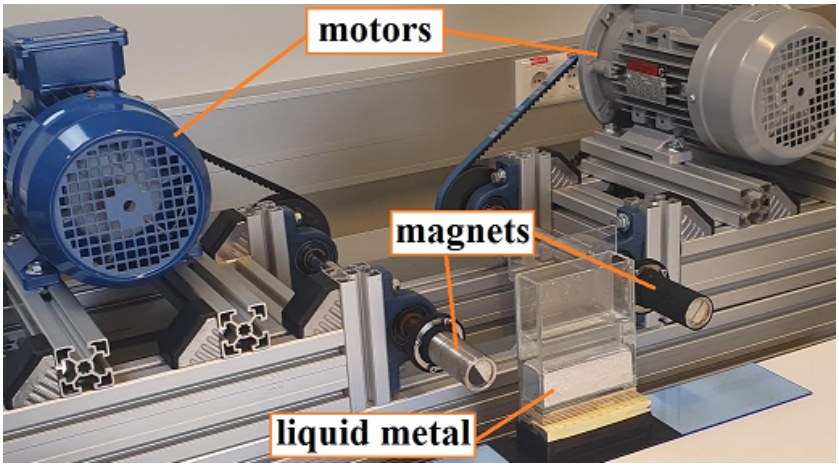

Fig. 4.2.1. Experimental setup of liquid metal stirring by rotating permanent magnets.

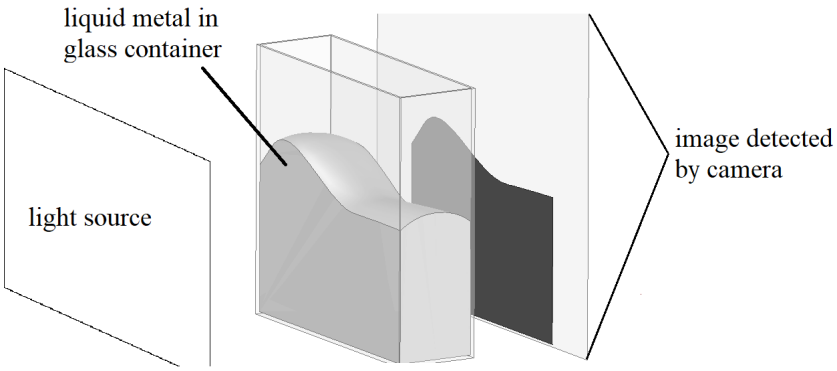

Fig. 4.2.2. Projection of the free surface.

Rectangular acrylic or glass container with liquid Galinstan is placed close to one of the magnets rotating in such a way as to create an upwards liquid metal flow and notable free surface deformation (see the numerical model scheme in Fig. 3.7.3 for the position of the magnet relative to liquid metal). To prevent oxidation and adhesion to walls, Galinstan was covered with HCl solution.

The main result is the shape and dynamics of the free surface. Due to Galinstan's reflectivity, it was decided to capture surface projections by placing the vessel between the camera and a homogeneous light source, as shown in Fig. 4.2.2. Examples of liquid metal in normal light and using the backlight are shown in Fig. 4.2.3. The light source is an array of light diodes with a diffuser. The Basler acA2000-340km (2MP 350 fps, gray-scale) camera with Euresys Grablink Full card was used for image capturing. Recorded sequences last for 20 sec and consist of 7000 images, requiring around 14 GB of RAM. Due to loss of depth information when capturing projections, an additional recording angle is used. Two perpendicular angles were filmed as separate events (from the front and from the side), which should be acceptable for gathering statistical data (mean and standard deviation).

Experimental images are processed using the ImageJ application (cropping the images and calculating mean and standard deviation) and OpenCV library in Python environ-

ment (binarizing the images and removing static artifacts). An example of mean and standard deviation of a series of experimental images is shown in Fig. 4.2.4. The standard deviation basically describes how often the free surface crosses a certain location. In this case, the standard deviation correlates to free surface movement - the higher the standard deviation (the brighter the color in the standard deviation image), the more often the free surface crosses that location, and the width of the standard deviation band relates to the amplitude of surface oscillations.

Fig. 4.2.3. Examples of experimental images: left - normal light, right - using backlight.

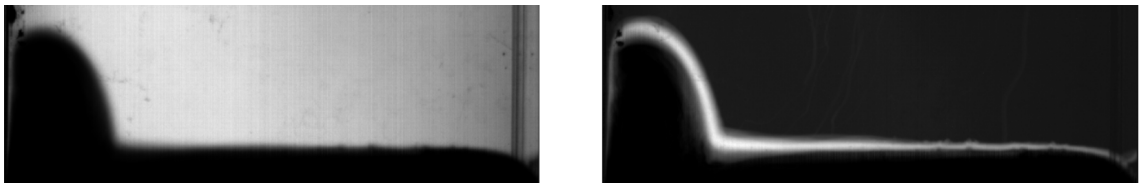

Fig. 4.2.4. Examples of processed experimental images: left - mean, right - standard deviation.

Processing of numerical results is marginally different. 3D surface is extracted from OpenFOAM as an iso-surface (at $\alpha = 0.5$). The surfaces consist of triangular elements, and their vertices can be treated as a list of points. Using a custom Python script, the clouds of points are interpolated and projected onto a surface, after which the liquid metal projection can be separated, resulting in images which can be processed in a similar fashion to the experimental ones.

4.3 Thin layers in AC field

Two configurations are considered - a rectangular liquid metal layer next to a straight single-winding inductor (from here on referred to as linear inductor) shown in Fig. 4.3.1 and a circular drop or pool in a helical or circular inductor shown in Fig. 4.3.2. Both setups were built at the Institute of Electrotechnology, Leibniz University of Hannover in Germany.

Both inductors are water-cooled copper tubes. For the linear inductor, RMS current is in the range of 700 A to 3 kA and frequency is 3 to 8 kHz. For the circular case, the current was from 50 A to 500 A with frequency of 22 kHz (different generator was used in this case). Liquid metal is gallium or Galinstan (both have very similar physical properties in liquid state). Containers are made of acrylic and for the circular setup the bottom of the vessel was made 1° conical to help center the liquid metal.

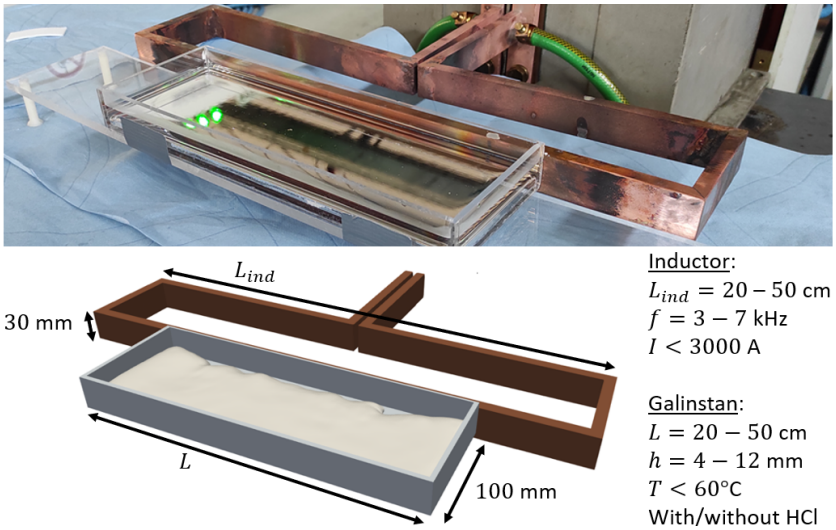

Fig. 4.3.1. Experimental setup of rectangular liquid metal pool in AC magnetic field.

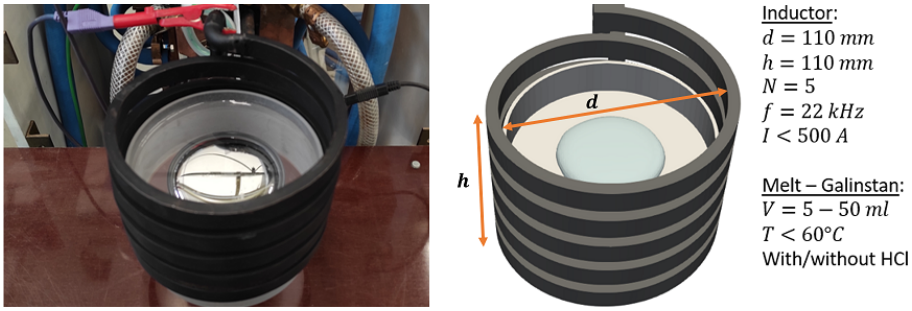

Fig. 4.3.2. Experimental setup of circular liquid metal pool in AC magnetic field.

Temperature of the liquid metal was monitored during experiments to keep it between room temperature and 60°C. In addition to keeping material properties as constant as possible, the rectangular container was made of glued acrylic pieces, and the glue could melt at higher temperatures. In the circular case, the container was made of a single piece. However, the circular drop was overheating quickly due to smaller surface area for cooling compared to the rectangular case, limiting each run to 10 - 30 seconds.

An important parameter in this process is liquid metal free surface oxidation. Two states were considered - oxidized (liquid metal is in contact with air) and non-oxidized (HCl solution is added on the free surface). The most notable effect of oxidation is on the liquid metal contact with the bottom of the container. When surface is oxidized, the melt tends to stick to the bottom which significantly reduces the dynamic behaviour of the contact line. It also makes the contact angle effectively smaller than 90 degrees, in this case somewhere around 40 degrees. When acid solution is added, the oxides are dissolved and the free surface becomes clear. The wetting conditions change considerably - the contact angle between the melt and walls is now larger than 90 degrees and the contact line can move more freely.

The main experimental instrument is a video camera (Xiaomi Redmi Note 9 Pro, 1080p, 60fps) which is set up above the liquid metal container and records the free surface

shapes during experiments. Due to small layer thickness, flow velocity measurements were not feasible. However, sometimes, there were small bubbles on the free surface. Motion of the bubbles indicate some correlation to the bulk flow. The flow pattern for undeformed or slightly deformed surface of the rectangular layer consists of two large counter-rotating eddies. Multiple larger or smaller vortices can develop for a deformed surface according to local Lorentz force distribution. The small bubbles on the surface actually trace out such flow patterns. However, it is unknown if the bubbles move with the bulk velocity, as they can in principle slide or get stuck to some residual oxides etc.

Series of experiments were conducted, varying inductor current, frequency, thickness/volume of the liquid metal layer and oxidation. Experimental images were processed using ImageJ and Wolfram Mathematica. All frames were extracted from experimental videos using `ffmpeg`, after which they were cropped in ImageJ to contain only the liquid metal region. The frames were imported in Wolfram Mathematica, where several steps were taken to obtain image masks (liquid metal as black, the uncovered bottom of the container as white). First, dominant colours were extracted and analyzed. Second, two colours containing most of the relevant information were selected. Third, numerous mathematical operations were performed on the series of images to finally separate the liquid metal region from the background. The black and white masks were then processed in exactly the same way as numerical results - doing edge detection, associating the edge points to coordinates using known scale in the images, interpolating the points to obtain continuous curve, and then extracting statistical data.

Coordinate system and variables used in the results is shown in Fig. 4.3.3. The edge at rest has $y(x) = 100$ mm. Just like defined for numerical model in section 3.7.3, the edge dynamics can be characterised by the amplitude A_h, wavelength λ and oscillation frequency f_h, as well as the number N_h of the wave crests or "fingers" in the pattern. Data obtained by image processing include the edge coordinates in time $y(x,t)$, the mean edge profile $y(x)$ and standard deviation $\sigma_y(x)$. $y(x,t)$ includes information about oscillation frequency and $\sigma_y(x)$ is related to A_h.

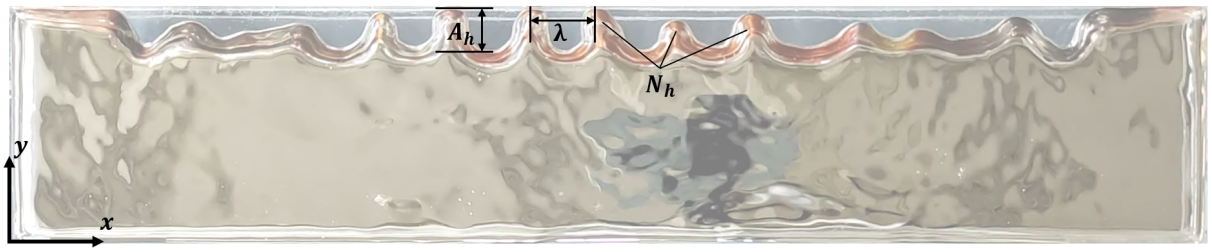

Fig. 4.3.3. Definitions of quantitative parameters for a deformed edge of the free surface (in this example, $N_h = 11$).

5 Results

The following subsections consider each of the MHD systems separately, presenting the main experimental and numerical results, discussing validation and applicability of the numerical models, as well as identifying potential relevance of various physical effects in real applications. Three experimental setups were built to study liquid metal flows and free surface dynamics excited by different configurations of electromagnetic forces. Each system is different regarding how EM forces are generated inside the liquid metal. In electrovortical flow (section 5.1), the force is generated by directly passing electric current through the liquid metal, which then interacts with its own magnetic field, creating EM force. In stirring by rotating permanent magnets (section 5.2), electric currents are induced by low-frequency magnetic field of the rotating magnets, which then leads to oscillating EM force. Section 5.3 presents the results of thin liquid metal pools in medium or high frequency magnetic field, which enables qualitatively different free surface dynamics compared to the previous cases. Section 5.4 is devoted to studying numerically a relatively new metallurgical process - the direct strip casting (DSC) or horizontal single belt casting (HSBC), exploring possible solutions to some stability issues in the casting process using static or time-varying magnetic field. With EM field, this process involves several characteristics of the previous setups.

5.1 Electrovortical flow

This section presents the results of free surface dynamics in a special configuration of electrically-induced vortical flow. Some results were reported in conferences [C.8][C.9] and were published in [A.4][A.7]. The most important results are given here.

Before considering the setup with free surface, electrovortical flow was simulated in a closed cylindrical container with small top and large bottom electrode, results of which were reported in [A.7]. The axial velocity depending on the injected current I was found to agree well to experiments of [128]. Moreover, the dependence is linear, which agrees to analytical estimate for turbulent flow [8]. This can also be estimated simply by considering that, for steady flow at high Reynolds number, from Navier-Stokes equation follows $(\vec{v} \cdot \nabla)\vec{v} \sim \vec{f_L}$. Considering this in magnitudes, $|\vec{f_L}| \sim I^2$ and so $v \sim I$.

Now, let's move to the setup with free surface. Experimental setup was shown in Fig. 4.1.1 and scheme of the model in Fig. 3.7.1. Two parameters were varied - amount of liquid metal in the container or the initial free surface height $h_0 = 5 - 60$ mm and the injected current $I < 1500$ A. In addition, differences between using gallium or Galinstan were tested. Both of the metals gave very similar results due to similar physical properties in liquid state, although experiments with gallium were more consistent and stable.

In this setup, the injected current diverges radially from the small bottom electrode through the liquid metal into the side wall. The resulting Lorentz force induces an upwards jet in the center of the container. Fig. 5.1.1 shows some examples of Galinstan surface shapes in experiments. At low currents, the shape of the deformation is quite smooth, similar to the shape of Gaussian distribution. At higher currents, the peak of the

deformation is higher and oscillates, assuming different irregular shapes. The unsteady behaviour at higher currents is also indicated by surface waves radiating from the peak. Note that the free surface was exposed to air, meaning it was oxidized. After each run, the film was manually removed. It is known that oxide film on Galinstan has a lower surface tension coefficient than pure surface [129]. This might affect the surface deformation at lower currents, when inertial effects (bulk flow, dynamic pressure) are smaller. At high currents, however, when the deformation is much more pronounced and unsteady, inertial effects dominate, and changes of surface tension due to oxidation are less important.

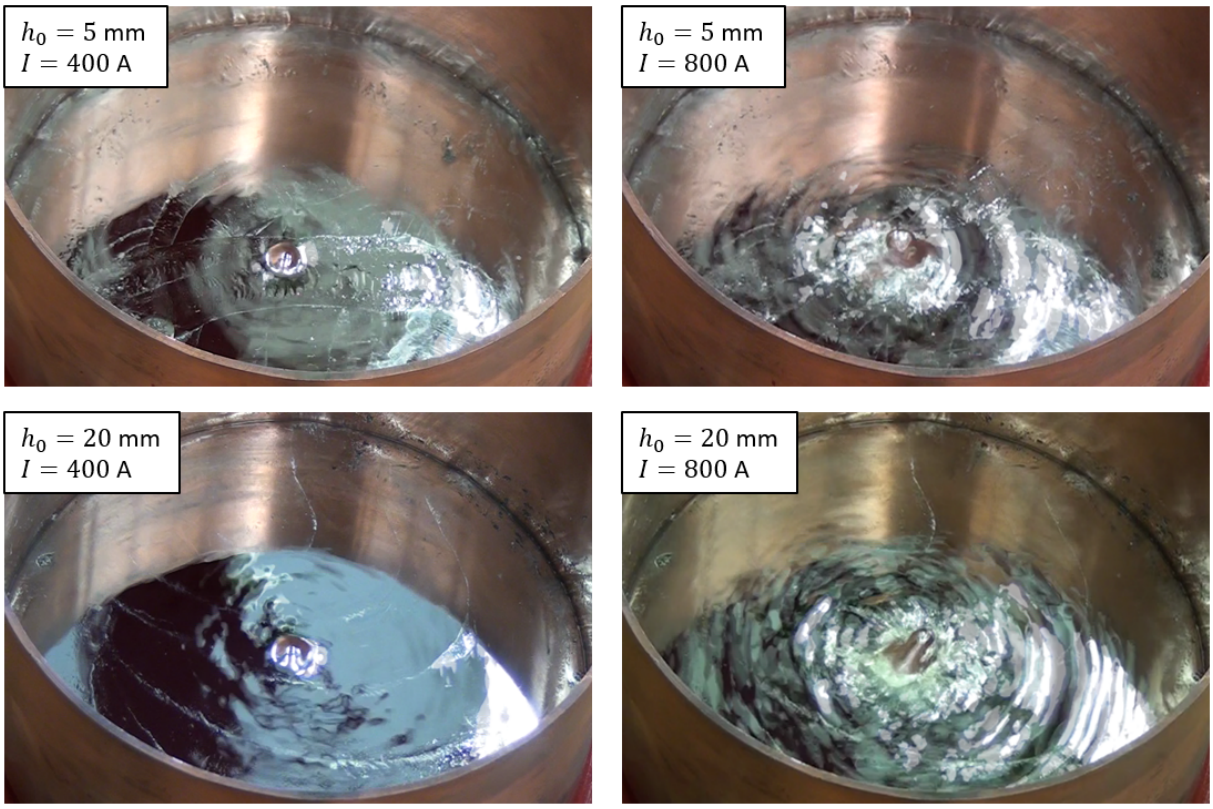

Fig. 5.1.1. Free surface shape in experiments with Galinstan depending on the injected current I for different initial levels h_0.

Up to 800 A or so, the surface jet was fluctuating but overall stable. Increasing the current further, the fluctuations became stronger, sometimes leading to sloshing and even swirling of the whole melt volume, especially at larger melt levels. If the liquid metal layer is small ($h \leq 5$mm) the sloshing can cause the liquid to move away from the bottom electrode so that the current is interrupted for a brief moment. When the liquid moves back over the electrode, contact is immediately restored and some of the liquid metal can shoot out of the container.

The cause of swirling can be due to the injected current interacting with some stray magnetic fields, but most probably it is due to the asymmetry of the setup - imbalance between the two current terminals on the cylindrical wall. Indeed, during initial test experiments, the swirling almost always occurred for high currents. After careful adjustment of the current leads on the side wall to balance the currents, the swirling was much more

difficult to achieve. Also, sloshing and swirling was observed more often for Galinstan than for gallium, perhaps due to higher oxide contents in Galinstan, which can disturb the current flow from the bottom electrode.

The numerical model utilized the fact that most of the EM fields concentrate far from the free surface, which allowed us to calculate EM only once at the start of simulation. Fig. 5.1.2 shows examples of injected current lines, magnetic field, Lorentz force and velocity distributions near the bottom electrode. Quantitative data for comparison between experiments and simulations is the height of the free surface jet, h, above the initial level h_0. Since 3D simulations can take quite a long time (order of days or even weeks for high current cases), to gather more quantitative data, series of axisymmetric simulations were performed. Fig. 5.1.3 shows experimental and simulated h depending on current. For low currents or when there is no swirling and sloshing, axisymmetric model gives very good results. However, axysimmetric model couldn't predict any instabilities and hence the deformation simply keeps growing when increasing the current, as evidenced in Fig. 5.1.4. Interestingly, the slope of the linear proportionality changes at around 1000 A. Analysing the reason for this might not be reasonable, since axisymmetric approximation in the high current range is inappropriate.

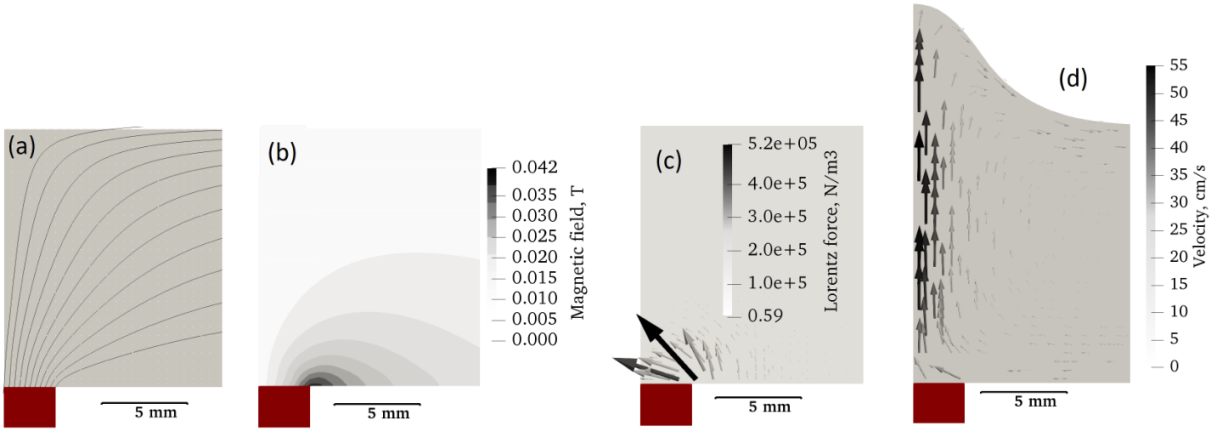

Fig. 5.1.2. Examples of (a) injected current lines, (b) magnetic field, (c) Lorentz force and (d) flow velocity near the axis; $I = 700$ A, $h_0 = 15$ mm, results of axisymmetric model.

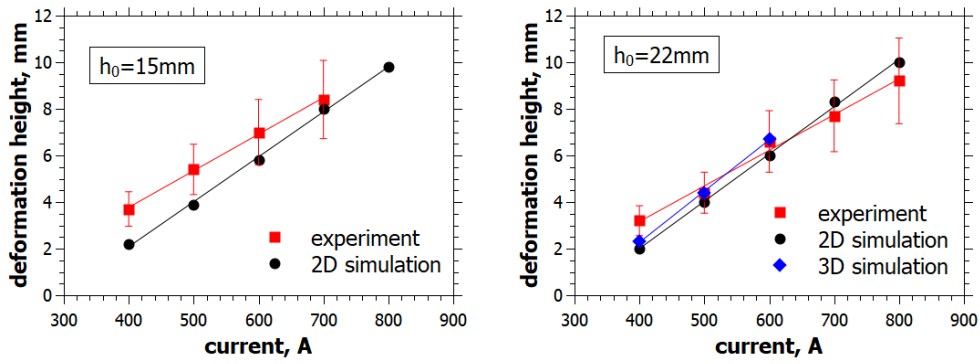

Fig. 5.1.3. Free surface deformation height depending on the injected current.

Agreement between experiments and simulations is good but not ideal. There is a

linear tendency of $h(I)$ in the considered range of currents, but the experiments give slightly higher deformation in the lower range. Error bars for experimental data are estimated from the fluctuation of the free surface at the point of measurements. Reasons for some quantitative disagreement can be due to some factors that are difficult to consider in the model, such as imperfections in the setup, possible deviations of material properties, etc. Moreover, some inconsistencies in experiments have been observed. Sometimes, when repeating the experiments, the deformation height was much smaller, with no swirling even above 1000 A. The most probable cause is that some oxides stick to the surface of the bottom electrode, because removing the melt and cleaning the surface of the electrode solves this problem.

Unlike in the axisymmetric model, surface deformation in a realistic 3D model becomes increasingly unstable for higher currents. Comparison of instantaneous free surface shapes in experiments and 3D simulations is shown in Fig. 5.1.5. Similar tendencies are observed - at smaller currents the surface is quite stable. At higher currents, the surface jet is asymmetric, assuming different shapes. Example of time series of simulated free surface shapes is shown in Fig. 5.1.6. Similar dynamics can be observed in experiments, although they are not as clear in still images due to oxides and reflections.

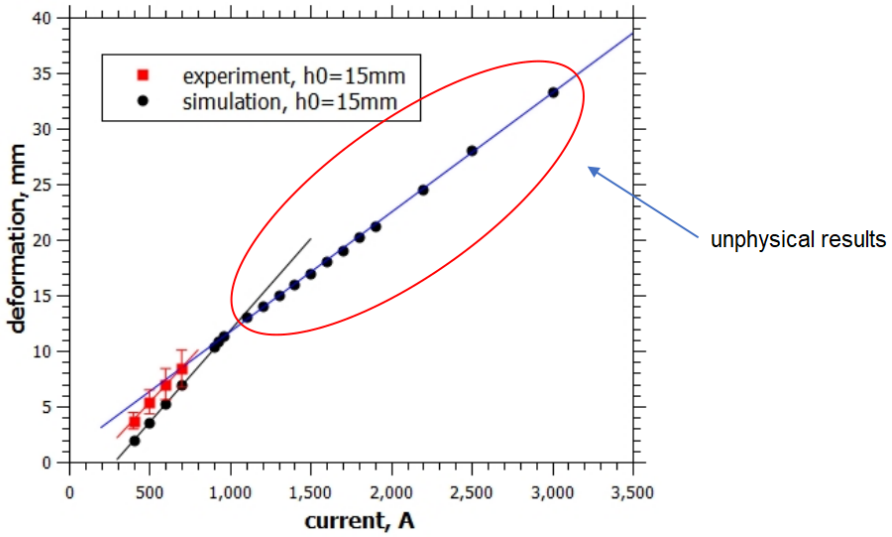

Fig. 5.1.4. Unphysical deformation height in the axisymmetric model for high currents.

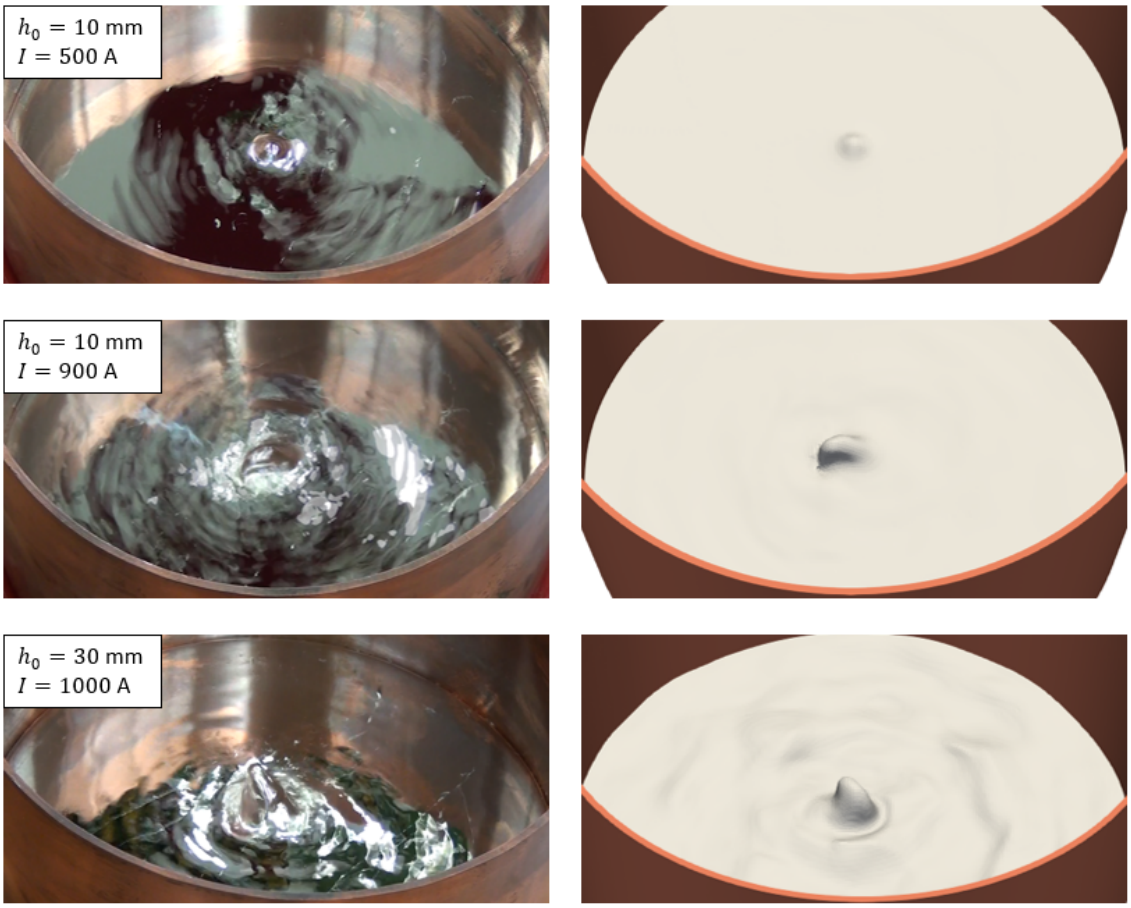

Fig. 5.1.5. Free surface of liquid gallium: experiments (left) and simulations (right).

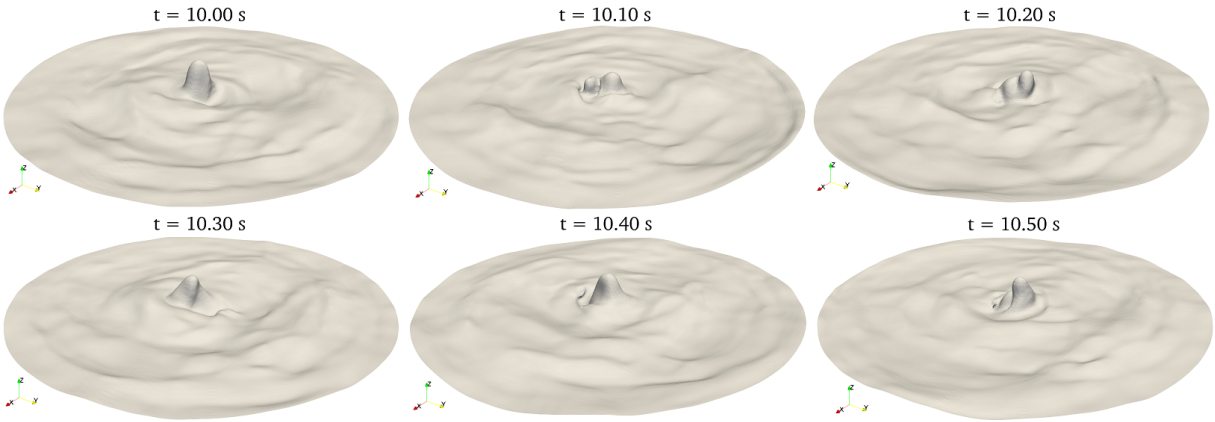

Fig. 5.1.6. Time series of simulated free surface shapes, $h_0 = 30$ mm, $I = 900$ A.

Comparing shape of the surface deformation between different initial levels h_0, we can observe that, at low currents, they are slightly different. The main tendency is that the shape of the surface peak is lower and wider for higher h_0. At higher currents, this effect is less visible due to fluctuations of the peak. It is difficult to see this in still images from experiments due to reflections, hence it is demonstrated in simulation results in Fig. 5.1.7. This difference is probably due to bulk flow distribution - for higher depth,

the flow has more time to redistribute due to viscous damping. This can be seen in the velocity distribution in Fig. 5.1.8, where the graph on the bottom right is vertical velocity component on the line overlayed in the vector images. Naturally, the free surface deformation takes more time to develop for larger h_0.

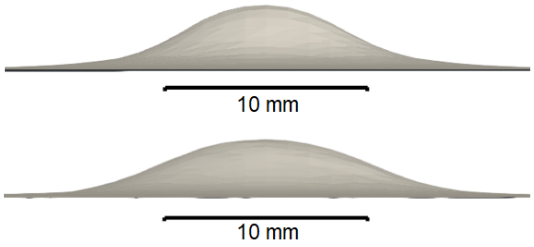

Fig. 5.1.7. Shape of the surface peak, $h_0 = 10$ mm (top) and $h_0 = 60$ mm (bottom), $I = 500$ A.

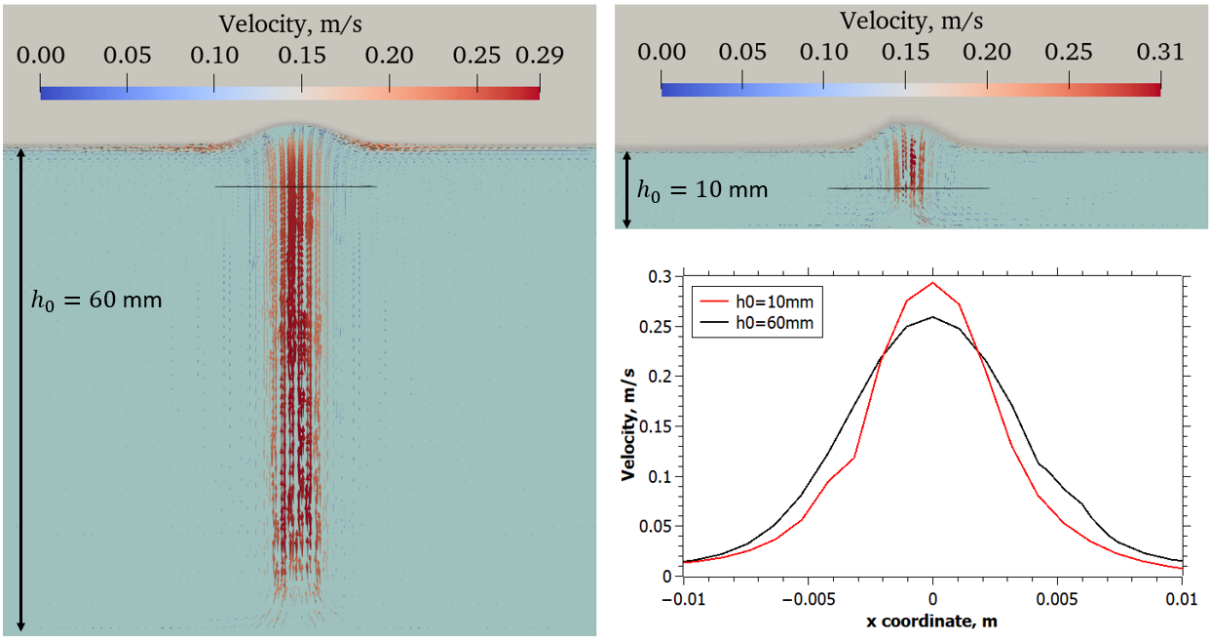

Fig. 5.1.8. Velocity on a vertical slice in the center of 3D model for $h_0 = 10$ mm and $h_0 = 60$ mm, the graph on the bottom right is vertical velocity component on a line 5 mm below the initial level.

5.1.1 Conclusions

Simple one-way coupling between EM and fluid dynamics, where EM is calculated only once, is justified by the fact that EM fields concentrate far from the free surface. The axisymmetric model gives good qualitative and quantitative results for low injected currents, above which only 3D model can provide agreement to experimental observations regarding free surface shape and dynamics. In experiments, strong sloshing and swirl can be observed for high injected currents. 3D numerical model is capable of predicting that.

5.2 Permanent magnet stirrer

This section continues experimental validation of coupled Elmer and OpenFOAM numerical models for a slightly more complex system - stirring of liquid metal by rotating permanent magnets. Some results were reported in conference [C.3] and were published in [A.1][A.3]. A related study with four counter-rotating magnets was published in [A.6][A.9] and reported in [C.11][C.12][C.13], where disagreement between single-phase (liquid metal in closed container) simulations and neutron radiography experiments was shown. As part of seeking reasons for disagreement and for validation of the models, new experiments were conducted where strong free surface deformation was induced by a single rotating magnet, allowing us to validate the model based on the free surface dynamics.

Before doing simulations, it was important to make sure that the remanence of the magnet used in experiments is what the manufacturer's data sheet provides. This was solved by measuring magnetic field around the magnet using a teslameter and doing an optimization in Comsol Multiphysics, varying remanence B_r and orientation of the magnet to match resulting magnetic field distribution to experimental data. The magnet is manufactured as having the N52 class, which has $B_r = 1.42 - 1.47$ T. The optimized value is $B_r = 1.394$ T, which is slightly lower. This value is used in simulations.

Many experiments with the rotating permanent magnet setup were done. Results for one of the most representative cases, where strong free surface deformation and oscillations are observed, are presented here. This is a case with initial liquid metal level $H = 30$ mm and the distance of magnet center to the liquid metal $a = 21$ mm (see the scheme in Fig. 3.7.3). $H = 30$ mm melt level is low enough that the simplification of calculating EM fields only one for undeformed surface is not valid - EM fields in simulations must be updated with changing free surface shape. The magnet is rotating at 20 Hz. The influence of mesh element size was tested by considering two different meshes for the fluid dynamics model - a coarse one with 394 thousand elements and a fine one with 1.8 million elements. In addition, two turbulence models were considered - k-ω SST and LES with Smagorinsky sub-grid model. The LES model can be expected to match better with experiments.

Strong free surface oscillations were observed experimentally. Fig. 5.2.1 shows some experimental images at different time instances during the same run. The main goal is to simulate this process and achieve agreement to experiments regarding both the time-averaged surface profile and the oscillations which are described by the standard deviation.

Fig. 5.2.2 shows the main results for two perpendicular liquid metal projections (XY and ZY like shown in Fig. 3.7.3) - simulations with RANS and LES models with coarse and fine mesh, as well as the experimental results. In experiments, there is a wide deviation band around the mean profile near the deformation peak. Moving further away from the influence of Lorentz force, the free surface is quite static and the deviation band is narrow.

Simulations with the coarse mesh are very similar between RANS and LES. For the fine mesh, however, LES is able to resolve more free surface oscillations, shown by the wider deviation band around the mean profile. RANS model does predict some oscillations, but not as strong as LES. The mean surface profiles are different. With fine LES the mean surface profile is flatter matching closely to the experimental one. The mean profile is

flattened due to sideways oscillations in the ZY plane. RANS model does not predict the variety of oscillations present in experiments. Due to this, LES models are strongly recommended in cases of dynamic free surface oscillations.

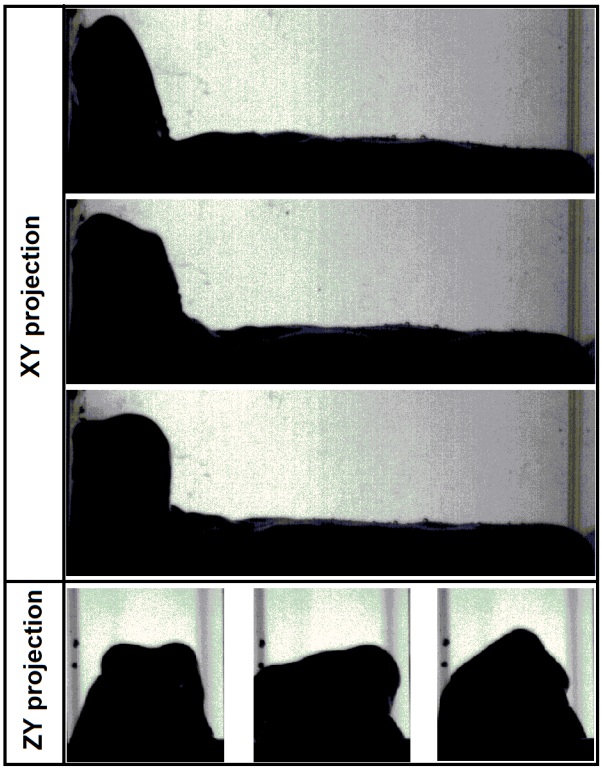

Fig. 5.2.1. Experimental images of different instantaneous free surface shapes.

Regarding quantitative comparison, the maximum deformation height is slightly higher in LES simulations than in experiments. Fig. 5.2.3 shows the mean profiles around the deformation peak in experiments and with LES model with the estimated experimental distance from the magnet center to melt $a = 21$ mm, as well as $a = 22$ mm. Since the Lorentz force depends on magnet rotation frequency, magnetization and distance to metal, and the first two are known well, the distance is suspected to be inaccurate, which indeed is a known source of uncertainty. Minimal distance between the magnet and liquid metal is limited by physical contact between the shell holding magnet and the glass vessel. Since the magnet is held in place on a prolonged axis, due to machining faults, some magnet precession takes place. Because of this, the vessel had to be moved very slightly away from the magnet to avoid direct contact. The "very slightly" is not an exactly known distance, but it should be below 1 mm. Fig. 5.2.3 shows that moving the magnet only 1 mm further, the free surface deformation changes noticeably, which is due to magnetic field decaying rapidly with distance from the magnet and Lorentz force being proportional to the square of magnetic field.

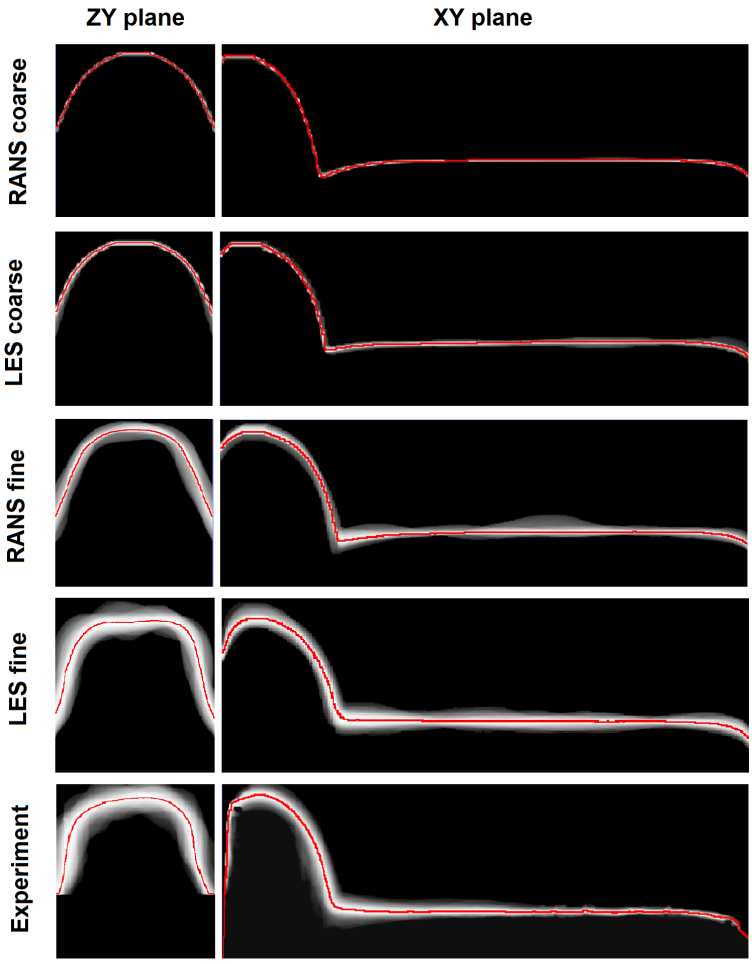

Fig. 5.2.2. Mean surface profiles and standard deviation distributions.

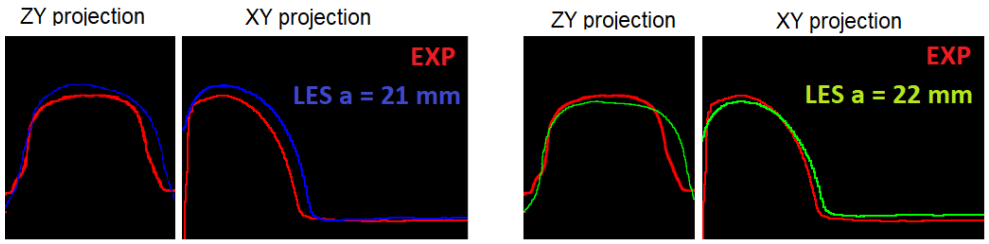

Fig. 5.2.3. Time-averaged free surface profile around the deformation peak in experiment and LES model; left - LES with $a = 21$ mm, right - LES with $a = 22$ mm.

Agreement between LES simulations and experiments is good. In addition to mean profile, agreement for standard deviation means that surface also oscillates similarly and that instantaneous surface shapes must also be similar. To demonstrate this, Fig. 5.2.4 shows examples of instantaneous free surface and velocity distribution in simulations and similar surface shapes in experiments for $H = 70$ mm. The simulations in these examples calculated EM fields only once, since the magnet was located near the bottom of the container and free surface motion did not influence EM force distribution. Note that the images from experiments in these examples are captured in normal light, and the side angle was captured at the same time using a mirror.

The flow velocity in this system was not measured due to difficulties with UDV to obtain reliable signal, perhaps due to the magnetic field affecting the probe. The main point of experimental validation is the free surface shape and deformation height. However, the deformation can be linked to flow velocity. Unlike high-frequency systems, such as the one presented in the next section, potential part of Lorentz force in this stirrer is negligible. This means that rotational part dominates, which drives bulk flow. Hence the surface is deformed only by the upwards bulk flow. Surface tension and gravity oppose the deformation. A relevant dimensionless number here is the Weber number, $We = \frac{\rho U^2 L}{\gamma}$, where U is characteristic flow velocity and L is size (e.g., deformation height). For slowly rotating magnet, surface deformation is small and surface tension forces dominate over fluid's inertia, i.e. $We \leq 1$. At high rotation speed, inertia dominates, $We \gg 1$, and surface tension plays a minor role in surface deformation. In such a case, it can be said that surface deformation directly correlates with flow velocity. The results presented above correspond to the latter case. Therefore, if the simulated surface shape and deformation height is close to the experiments, the flow velocity must also be similar. Of course, surface tension can not be neglected in the model even if $We \gg 1$. Surface tension and contact angles still play a role in keeping the surface locally smooth without sharp spikes. All of this actually also relates to the electrovortical case of the previous section, where strong upwards flow was deforming the free surface.

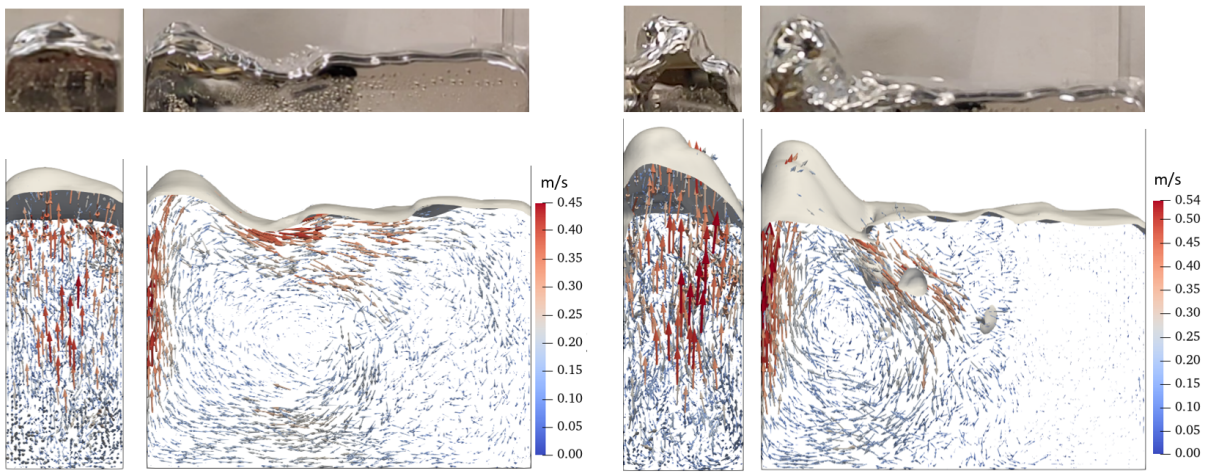

Fig. 5.2.4. Simulated free surface shapes and flow velocity, and similar surfaces in experiments for $H = 70$ mm: (left) $f = 10$ Hz, (right) $f = 15$ Hz.

If the free surface does not deform too much, the numerical model can be simplified by assuming the surface to be flat. In that case, only the liquid metal is simulated, with free slip condition on the top boundary where the free surface would be. This considerably simplifies the model and reduces simulation time, since the VOF equations are not solved and recalculation of EM fields (even if the magnet is close to the free surface) due to motion of the surface is not needed.

Characteristic velocity distribution with fixed and moving surface is shown in Fig. 5.2.5. The results are quite close in magnitude. Flow structures are slightly different because free surface shape has some influence. Due to surface motion, the velocity dis-

tribution in the full model is also more unsteady. However, the unsteadiness of flow structures is not just due to surface dynamics. As was shown in [A.6][A.9] for a case with multiple rotating magnets, transitions between different flow structures can occur even if the surface is fixed and even if the driving Lorentz force is constant. Such flow transitions and instabilities are characteristic to turbulent recirculating flows in closed containers [130]. This can actually contribute to discrepancies between experimental measurements and simulations (especially steady state), because of possibly different residence times of different flow configurations.

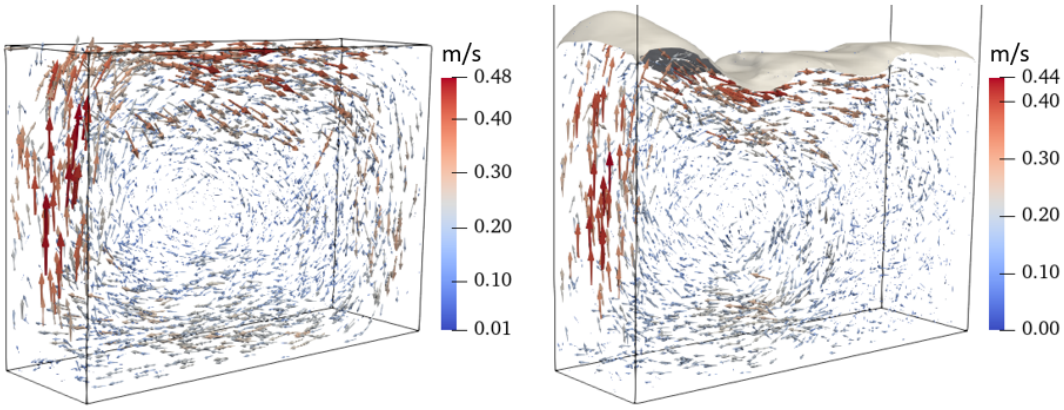

Fig. 5.2.5. Simulated flow velocity for $f = 10$ Hz, $H = 70$ mm: (left) fixed flat surface, (right) moving surface.

5.2.1 Conclusions

A slightly more complicated setup compared to the electrovortical flow was considered in this section. Rotating permanent magnet induces strong upwards flow in liquid metal, which in turn deforms the free surface. To simulate this, $\vec{v} \times \vec{B}$ has to be considered, otherwise the Lorentz force is overestimated. If $Re_m \ll 1$, the $\vec{v} \times \vec{B}$ term can be neglected in the EM model, and considered in the fluid dynamics model as a correction to the current density. The results with such a simplification is justified by comparison to experiments.

For a relatively high rotation speed of the magnet, the deformed free surface was highly oscillating. RANS model failed to predict the amplitude of the oscillations, whereas a LES model matched closely to experiments. Refining the mesh showed some improvement in the RANS results, although the oscillations were still considerably damped. On a coarse mesh, both RANS and LES performed poorly.

Without measuring flow velocity, because simulated surface deformation agrees well to experiments, we can trust that the velocity distribution must also be close due to high Weber number (which means that bulk flow is the main reason for surface deformation, with surface tension having secondary role).

5.3 Thin layers in AC field

A case with more diverse free surface dynamics and instabilities is considered in this section. It is a case of relatively thin (4-12 mm) liquid metal layers in transverse AC

magnetic field. Initially, a rectangular layer was considered, as shown in Fig. 4.3.1. For completeness and to gather additional data, a circular liquid metal layer was also studied, as shown in Fig. 4.3.2. Fundamentally, both systems have the same underlying physical processes - AC magnetic field induces electric currents along the edge of the melt layer and the resulting Lorentz force deforms it. Free surface dynamics and instabilities, however, are different mostly due to geometrical differences. The rectangular layer in experiments always spanned the whole container (the melt was in contact with all side walls), whereas the circular drop was studied with different sizes, ranging from small $V = 5$ ml droplets to large drops filling the whole container. The main results for both setups are discussed below.

5.3.1 Rectangular layer

Series of experiments were done varying length of the layer L, initial thickness h_0 and inductor current I, with and without HCl solution on the surface. Frequency of the current was varied in a range from 3 to 8 kHz. The main experimental and numerical results with $L = 20$ cm were presented at conferences [C.4][C.6][C.7], as well as were published in [A.2]. Some preliminary results with $L = 30$ and $L = 50$ cm were presented in [C.1]. More results will be shown here and will be published after the thesis.

Let's start with the $L = 20$ cm case. Note that the inductor length along the container was also 20 cm (for $L = 30$ and 50 cm the inductor was 50 cm long). The most representative results with and without HCl are shown in Fig. 5.3.1 (the figure shows only the deformed edge of the melt). The simplest case in terms of very little oscillations and stability of simulations is the thinnest layer with HCl. $h_0 = 7$ mm was the minimum thickness at which the melt spanned the whole container. Smaller melt volumes were contracted by surface tension away from the corners. For the thinnest layer, Lorentz force caused a relatively smooth deflection of the edge due to strong dominance of surface tension. It was qualitatively the same for all inductor currents in the considered range, with the edge deflection simply being larger for higher current.

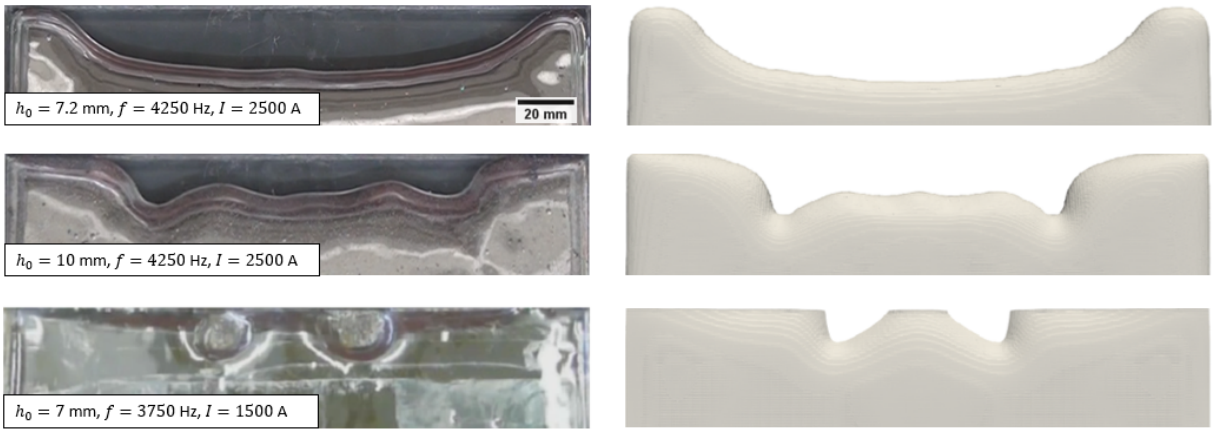

Fig. 5.3.1. Characteristic edge shapes in experiments (left column) and simulations (right column), $L = 20$ cm. View from above, gravity is directed into the page.

For larger h_0, the edge deformation was not smooth anymore. Instead, notable oscil-

lating patterns developed. For thicker layer, hydrostatic and inertial forces oppose surface tension. This can be characterised by the Bond number $Bo = \frac{\Delta\rho g D^2}{\gamma}$, where $\Delta\rho$ - density difference between liquid metal and HCl solution, D - length scale. Typically, low Bo means that surface tension dominates, while high Bo means that surface tension cannot hold the shape of the surface and the liquid front can move more easily. What is low or high Bo is not clearly defined, as it depends on what is chosen as the length scale, and other factors. For Galinstan in HCl solution (mostly water), taking $D = h_0$, $Bo \approx 10^5 h_0^2$. For the smoothly deformed edge with $h_0 = 7$ mm, $Bo \approx 5$. For $h_0 = 10$ mm, $Bo \approx 10$. The typical assumption of 1 as the value separating different behaviours characterised by dimensionless numbers is clearly not exactly true here. However, taking $D = h_0$ might not be appropriate, since skin depth and other dimensions directly or indirectly influence the dynamics, as will be evident below in the results with larger length of the layer.

In principle, if there were no local perturbations of the edge, it could be possible to obtain smooth deflection also for higher h_0. In reality, there are imperfections in the setup, some residual oxides on the surface etc., which can initiate local deviations. Small local perturbations can then grow due to redistribution of the induced current and magnetic field, according to the mechanism explained in [61]. Higher Bo means that these perturbations or waves along the edge are not completely stabilised by surface tension, and the edge pattern and oscillations are determined by the interaction of hydrostatics (gravity), inertia of the fluid and Lorentz force. The edge pattern is also affected by the turbulent bulk flow.

Simulating the thinnest layer was relatively easy. Remember that the numerical model is based on coupling between OpenFOAM and Elmer, where Elmer recalculates EM fields whenever the free surface in OpenFOAM model moves over some small distance (half a mesh element). If the free surface is not changing or oscillating much, the number of recalculations during simulations are not many. Moreover, lack of oscillations and waves means that the mesh can be coarser. For thicker layer, where oscillations take place, simulations can take much longer due to many more EM recalculations and finer meshes. Smaller mesh elements actually not only make the simulations longer due to larger systems of linear equations, but also increase the number of EM recalculations because they are triggered by a criterion based on mesh element size. As can be seen in Fig. 5.3.1, simulations agree very well to experiments with HCl. In the model, HCl solution had the properties of water. Presence of HCl required no special treatment, since the dynamics were determined by surface tension coefficient and contact angles with solid surfaces.

Quite different edge patterns develop without HCl. Oxide film forms on the surface, which sticks to solid surfaces, making the contact line less mobile. Deformation of the oxidized layer was always almost completely static. Unlike with HCl, the minimal melt thickness was not 7 mm. With oxide film adhering to solid surfaces, including side walls of the container, it was possible to spread even smaller melt volumes across the container. In other words, while thinner layers were contracted by surface tension in cases with HCl, the oxide film without HCl helped melt stick to the side walls, maintaining a rectangular shape of the layer. Adhesion of the oxides was so strong, that in some cases the deformed

edge shape remained so even after turning off the inductor current.

The oxidized case with two troughs or pinch zones in the edge pattern shown at the bottom in Fig. 5.3.1 was one of the few cases where simulations reasonably matched with experiments. While with HCl the surface was pure and did not require any special treatment in the model, the oxidized case proved to be much more complex. In the model, the oxidation was taken into account in a very simplified manner as a modified contact angle. Setting contact angle to 40 degrees to somehow simulate wetting behaviour of the oxide film, provided reasonably good qualitative agreement to experiments. Of course, such a simple approach is not physically completely valid, since surface oxide film introduces much more complexity than just modified contact angle. Nevertheless, qualitatively the results are good - shapes of the pinch zones are similar and the pattern is virtually static both in simulations and experiments. More complicated edge patterns from experiments with oxidized layer, which were not simulated successfully, are shown in Fig. 5.3.2. At $h_0 = 4$ mm hydrostatic forces were so small compared to the adhesion of the oxide film, that this deformation pattern remained supported by the oxides after turning off the current.

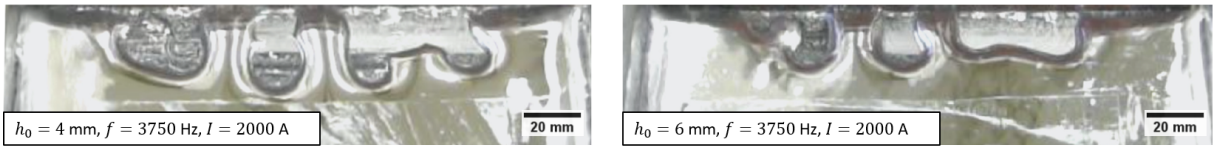

Fig. 5.3.2. Various oxidized liquid metal surface shapes in experiments with $L = 20$ cm.

In the results with $L = 20$ cm, notable influence of the finite width of the layer can be seen - significant portion of the free surface is not pushed away from the wall near the inductor. This is why a longer inductor and containers were built later. A longer system would not only be closer to idealized cases of infinite conducting sheets, but would also better correspond to potential practical applications, for example, direct strip casting where the melt layer would be contained on the moving belt or deflected from critical zones using AC magnetic field.

Fig. 5.3.3 shows the most representative experimental images for $L = 30$ cm with HCl. Note that the inductor along the melt layer in this case is 50 cm long. Since the layer (and inductor) is wider, end effects of induced current paths are less pronounced, and the zone with oscillatory pattern is wider. Again, stronger oscillations are observed for higher h_0. Dependency on current I is a bit more complex. When h_0 is small, such as $h_0 < 8$ mm, low I makes a relatively smooth deflection of the free surface edge. At higher I, the deflection is larger, but it is accompanied by small waves along the edge.

Comparison of instantaneous edge shapes between experiments and simulations for $L = 30$ cm with HCl is shown in Fig. 5.3.4. Note that it was difficult to perfectly match all parameters, especially the inductor current, which may be due to slight inaccuracy of distance between the inductor and container in experiments. Nevertheless, very similar shapes and oscillations can be found by slightly adjusting the current in the model.

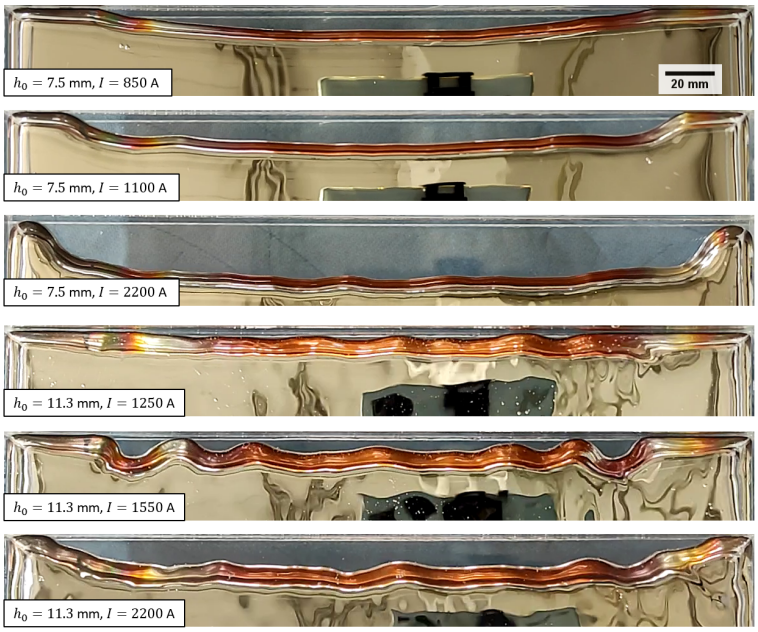

Fig. 5.3.3. Instantaneous edge shapes with HCl in experiments, $L = 30$ cm.

One important aspect in simulations must be mentioned. It is the spatial resolution or mesh size. During development and testing phase, it was found that sometimes the free surface in simulations is much more stable than in experiments, even with LES turbulence models. Unsurprisingly, the main reason turned out to be the mesh resolution (although this was not as critical for $L = 20$ cm due to less oscillations). Since these coupled simulations can take a lot of time, mainly due to recalculation of EM fields, a comprehensive mesh dependence study was not conducted. However, some mesh sensitivity was performed to find the mesh that gives results close to the experiments. For this, several meshes with different element sizes in the zone where edge oscillations take place were created for a case with $L = 30$ cm, $h_0 = 11.3$ mm, $I = 1430$ A. Size of the elements was not uniform, different sizes were used in X (direction away from the inductor), Y (vertical direction) and Z (along the edge) directions, Δx, Δy and Δz, respectively. In these tests, Lorentz force was increased from zero to maximum over 3 s and the total flow time was 4 s. The main test results are summarized in Fig. 5.3.5 for $t = 4$ s. Total simulation time with mesh 1 was approximately 40 hours on 48 cores of Intel Xeon Gold 5218 CPU 2.30GHz. During this time, OpenFOAM solved 5617 time-steps and Elmer recalculated EM fields 406 times. On average, it means that we could obtain around 1 s of flow time in 10 hours of calculating. With mesh 2, the same simulation took 1.6 hours, OpenFOAM solved 5611 time-steps and Elmer recalculated EM fields 43 times. Smaller amount of EM recalculations with a coarser mesh are due to the criterion of recalculation based on free surface moving over half a mesh element (larger element means the surface can move larger distance for recalculation to be triggered) and also due to damped oscillations (if surface does not move, EM fields are not recalculated).

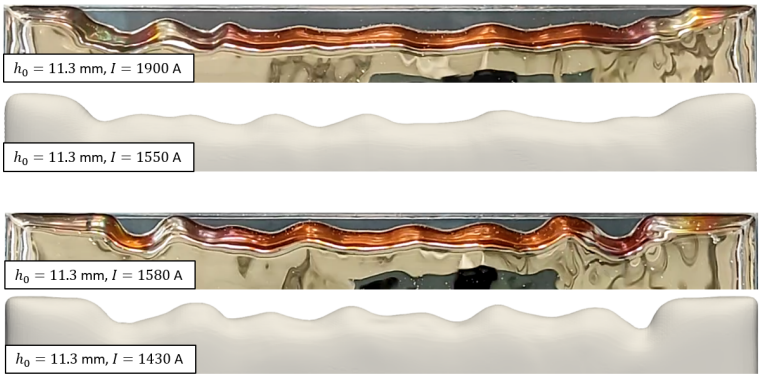

Fig. 5.3.4. Comparison of edge patterns for $L = 30$ cm in experiments and simulations.

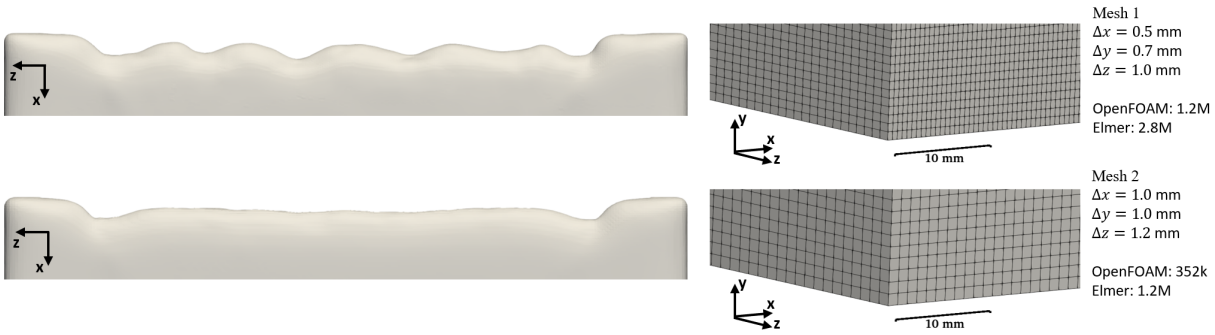

Fig. 5.3.5. Mesh dependence results, $L = 30$ cm, $h_0 = 11.3$ mm, $I = 1430$ A.

More diverse patterns and stronger oscillations can be observed for melt in the longest container due to even more reduced influence of the finite length of the layer. Fig. 5.3.6 shows some experimental results with $L = 50$ cm for three different h_0. Again, surface tension prevents oscillations for thinner layer. If the inductor current is switched on immediately to the set value, instead of increasing it gradually from a small value, there are edge waves and oscillations initially, but they subside within some 10 seconds, depending on the current. In case of higher h_0, very strong edge oscillations are observed, which don't subside even if the current is increased slowly to the specified value. The tendency of stronger oscillations for thicker melt layer is similar as in the shorter containers. However, now very strong edge deformations occur for thicker layer at high currents, with "fingers" in the pattern that oscillate and move laterally back and forth. This must be due to not only the competition between EM, surface tension, inertial and hydrostatic forces, but also due to interaction of the free surface with the front wall of the container. At very strong currents, the gaps between the "fingers" are pushed even deeper when the peaks come into contact with the wall. This is probably due to a decreased surface tension force when the peaks are flattened against the wall, which gives opportunity for Lorentz forces to promote the troughs. This is in line with [61], where such "pinching" instability is attributed to redistribution of magnetic field and induced current in the crests and troughs of a wavy edge pattern. This is demonstrated numerically below.

Fig. 5.3.7 shows examples of deformed free surface with and without HCl solution on the melt for $L = 50$ cm. The contrast between the melt and the bottom of the container

is not as good for the oxidized case due to the reflective oxide film covering the bottom. Again, the oxidized surface was mostly static. Similar quantitative characteristics can be seen between the two cases - the amplitudes and number of the peaks are similar.

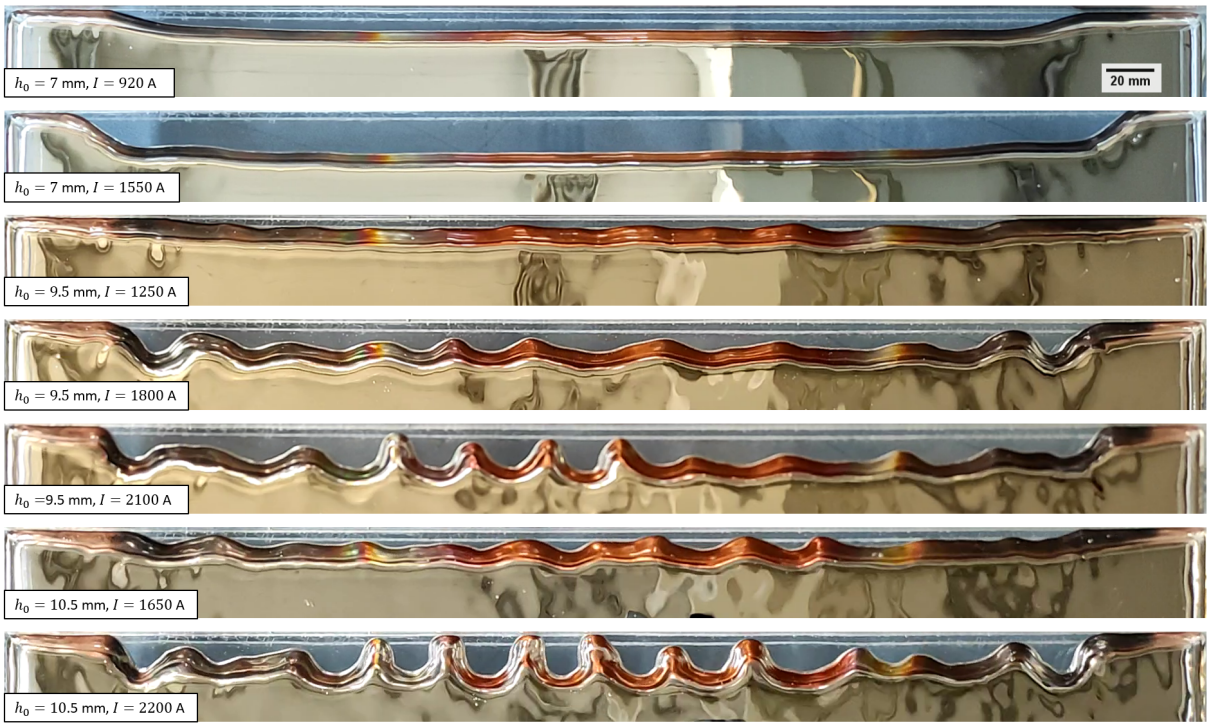

Fig. 5.3.6. Instantaneous edge shapes with HCl in experiments, $L = 50$ cm.

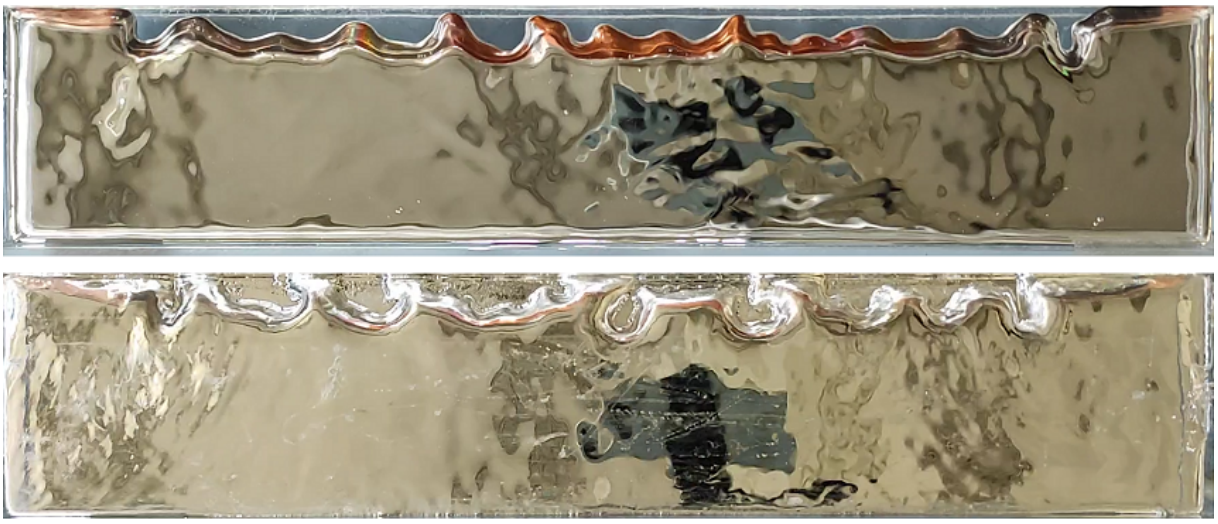

Fig. 5.3.7. Melt in $L = 50$ cm container with (top) and without HCl (bottom), $h_0 = 10.5$ mm, $I = 2.2$ kA, $f = 4$ kHz. Note that the whole surface is shown here.

An example of instantaneous edge pattern in experiments and simulations for $L = 50$ cm, $h_0 = 10.5$ mm, $I = 1650$ A (non-oxidized) is shown in Fig. 5.3.8. As defined in section 4.3, in this example, the average number of peaks, distance between them and their amplitude in experiments is, respectively, $N_{exp} = 11 \pm 2$, $\lambda_{exp} = 32.8 \pm 8.4$

mm, $A_{\lambda,exp} = 5.5 \pm 1.4$ mm. Simulations give $N_{sim} = 11 \pm 2$, $\lambda_{sim} = 32.2 \pm 7.0$ mm, $A_{\lambda,sim} = 7.7 \pm 2.4$ mm. The values are averages of 100 measurements and the errors are standard deviations. λ and A_λ don't take into account the first peaks on both sides which are largely influenced by the layer ends. Agreement is quite good. Some disagreement for A_λ can be related to mismatch of inductor currents, which is similar as was shown for $L = 30$ cm. Up to some critical current when the edge oscillations become very large and push against the front wall, N and λ are independent of the current, as evidenced in Fig. 5.3.18 (left).

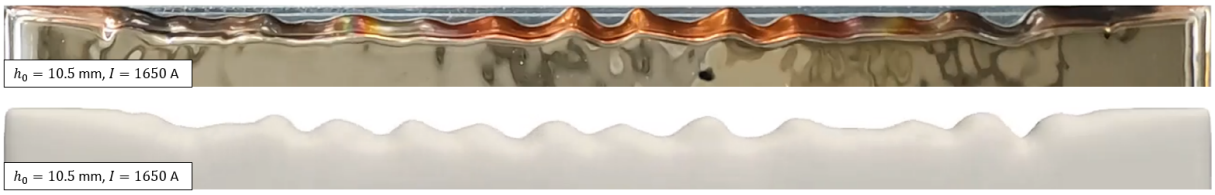

Fig. 5.3.8. Instantaneous edge patterns for $L = 50$ cm, $h_0 = 10.5$ mm, $I = 1650$ A (non-oxidized) in experiment (top) and simulation (bottom).

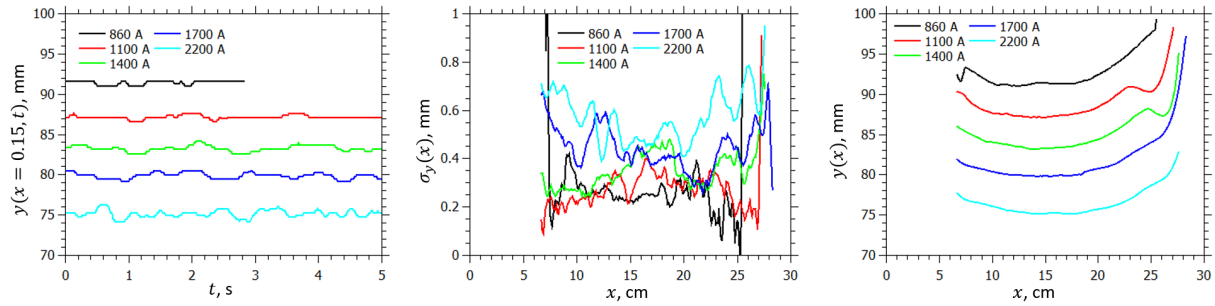

Fig. 5.3.9. Edge position in time in the middle of the edge ($x = 15$ cm) (left), the standard deviation $\sigma_y(x)$ (center) and the mean position $y(x)$ (right); $L = 30$ cm, $h_0 = 7.5$ mm.

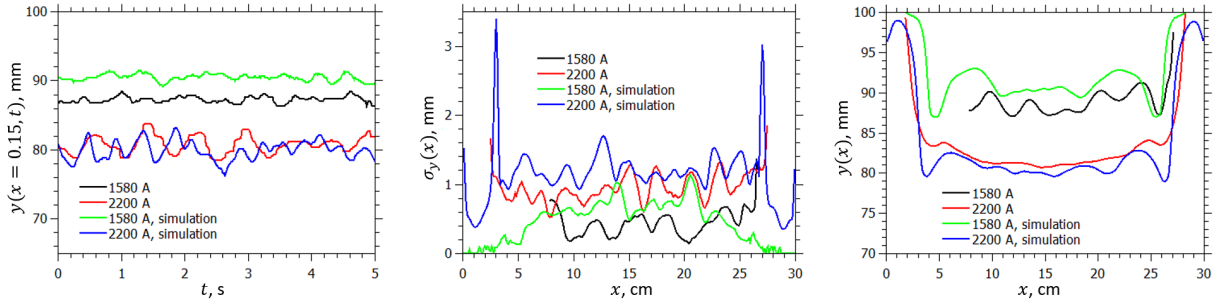

Fig. 5.3.10. Edge position in time in the middle of the edge ($x = 15$ cm) (left), the standard deviation $\sigma_y(x)$ (center) and the mean position $y(x)$ (right); $L = 30$ cm, $h_0 = 9.3$ mm.

Free surface images from experiments were processed as described in section 4.3. The best series of images were selected for different inductor currents and layer thicknesses for further analysis. The processing allowed extracting edge position in time, $y(x, t)$, standard deviation describing oscillations at each point along the edge over some time period, $\sigma_y(x)$, as well as the time-average or mean edge profile, $y(x)$. These results for

$L = 30$ cm and $L = 50$ cm are summarized in Figs. 5.3.9 to 5.3.14. The $\sigma_y(x)$ and $y(x)$ graphs cover the whole range of x, from 0 to L, however, some graphs have missing sections due to difficulties of extracting the edge coordinates in parts of the surface where lighting and reflections were considerably different than most of the surface, which caused problems for the image processing algorithm.

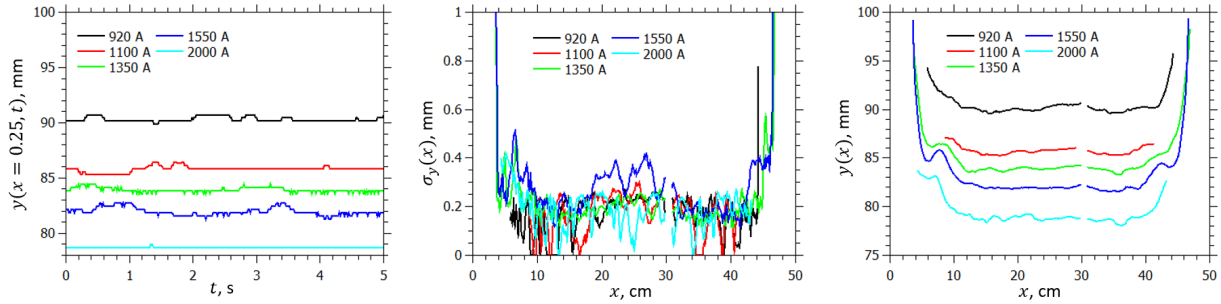

Fig. 5.3.11. Edge position in time in the middle of the edge ($x = 25$ cm) (left), the standard deviation $\sigma_y(x)$ (center) and the mean position $y(x)$ (right); $L = 50$ cm, $h_0 = 7.0$ mm.

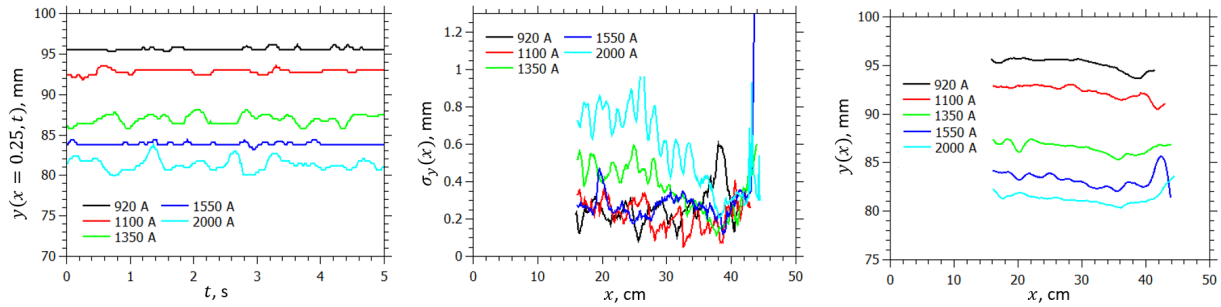

Fig. 5.3.12. Edge position in time in the middle of the edge ($x = 25$ cm) (left), the standard deviation $\sigma_y(x)$ (center) and the mean position $y(x)$ (right); $L = 50$ cm, $h_0 = 8.7$ mm.

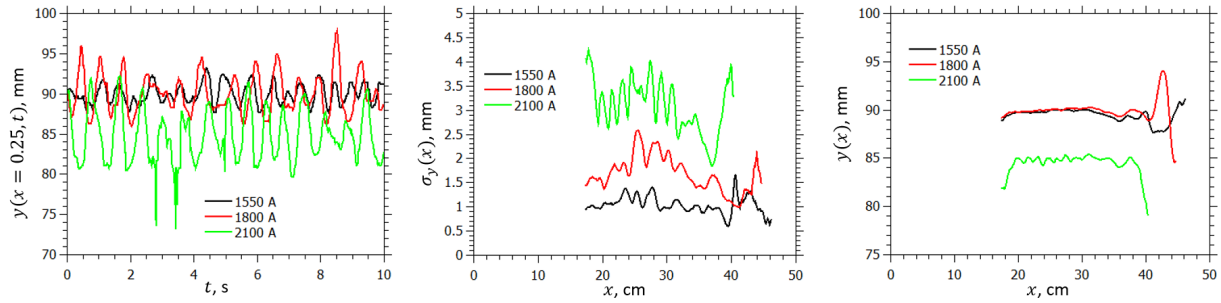

Fig. 5.3.13. Edge position in time in the middle of the edge ($x = 25$ cm) (left), the standard deviation $\sigma_y(x)$ (center) and the mean position $y(x)$ (right); $L = 50$ cm, $h_0 = 9.5$ mm.

Characteristic dependency of $y(x)$ on I can be found from the fact that, in the first approximation neglecting oscillations, the volume of displaced fluid is proportional to the change in the hydrostatic pressure, Δp. Considering a 2D case corresponding to a vertical cross-section of the real system, shown schematically in Fig. 5.3.15, the change in layer thickness is $\Delta h = \frac{h_0 l_0}{l_0 - \Delta y} - h_0$. Since the increase of hydrostatic pressure is proportional to the applied force, $\Delta p \sim |\vec{f}_L| = jB \sim I^2$, we get $\Delta y \sim \frac{I^2}{c + I^2}$, where c is a constant.

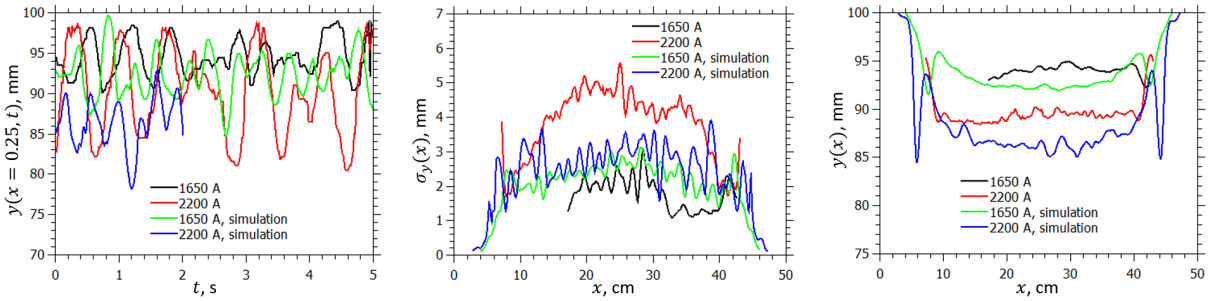

Fig. 5.3.14. Edge position in time in the middle of the edge ($x = 25$ cm) (left), the standard deviation $\sigma_y(x)$ (center) and the mean position $y(x)$ (right); $L = 50$ cm, $h_0 = 10.5$ mm.

Let's summarize the results shown in Figs. 5.3.9 to 5.3.14. The mean edge deflection, $\Delta y = 100$ mm$-y$, and σ_y depending on I are shown in Figs. 5.3.16 and 5.3.17, respectively. Error bars for Δy are the standard deviations shown in the right graph. Both variables in these graphs are spatially averaged over $x \in$[10 cm, 20 cm] for $L = 30$ cm and $x \in$[15 cm, 35 cm] for $L = 50$ cm. This was done to even out slight asymmetries in the edge pattern. However, these values are very close to those obtained in the middle of the edge without spatial averaging.

Logical tendency of larger deflection for higher I is obtained for all cases. The proportionality $\Delta y \sim \frac{I^2}{c+I^2}$ holds well for smallest h_0 when oscillations are small. For higher h_0 the relation does not hold because force distribution is strongly affected by local edge curvatures, and so the overall change in pressure is not proportional to force. Moreover, there are fewer data points for higher h_0 due to relatively high minimum current at which the layer is detached from the front wall and due to limited maximum current, which makes it inappropriate to fit non-linear functions.

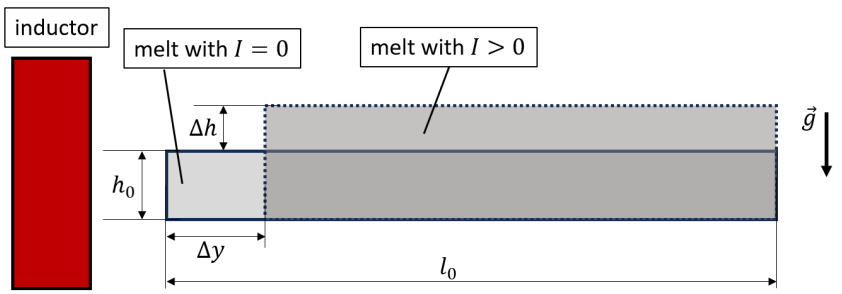

Fig. 5.3.15. Displacement of fluid by magnetic pressure.

Similar increasing tendency is also observed for σ_y. However, values below 0.5 mm should be viewed with caution. Typical spatial resolution in experimental images was around 0.25 mm per pixel. This means that any fluctuations of similar amplitude could be inaccurately captured by the image processing.

Dependence of λ on h_0 is shown in Fig. 5.3.18 (right), with the results for each h_0 averaged over different currents. A tendency of λ decreasing with increasing h_0 can be related to Bo. As shortly mentioned above, higher Bo means that the surface or contact line can move more freely. This means that Lorentz force can more easily induce surface

oscillations. Skin depth certainly can also play a role - for thinner layer EM field penetrates deeper into the melt, which makes the surface less sensitive to redistribution of EM fields. However, since skin depth in Galinstan at $f = 4$ kHz is approximately $\delta \approx 4$ mm, which is only slightly smaller than h_0, δ relative to h_0 can have only marginal effect in this case.

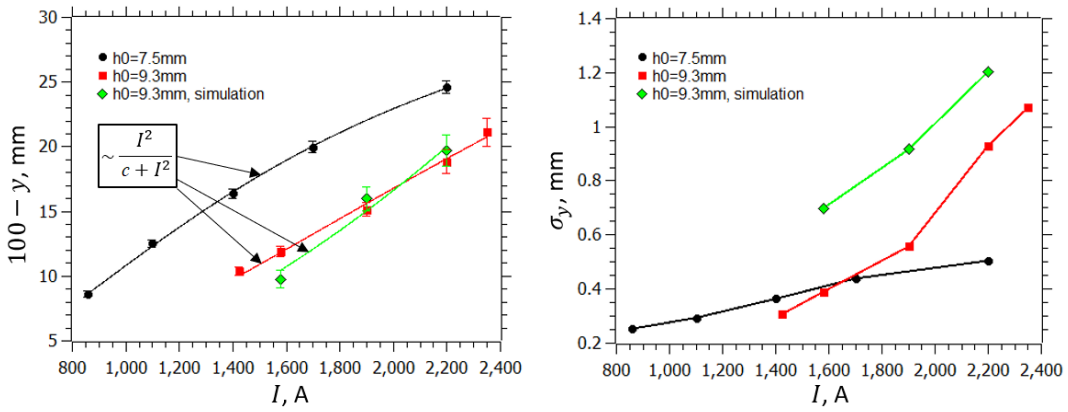

Fig. 5.3.16. Mean edge deflection Δy (left) and standard deviation σ_y (right) depending on inductor current I for $L = 30$ cm. The values are averaged over interval $x = 10 - 20$ cm.

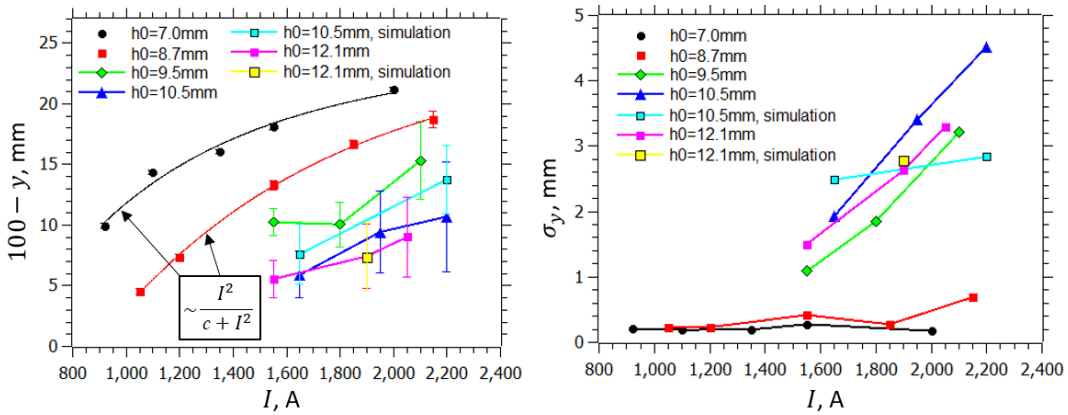

Fig. 5.3.17. Mean edge deflection Δy (left) and standard deviation σ_y (right) depending on inductor current I for $L = 50$ cm. The values are averaged over interval $x = 15 - 35$ cm.

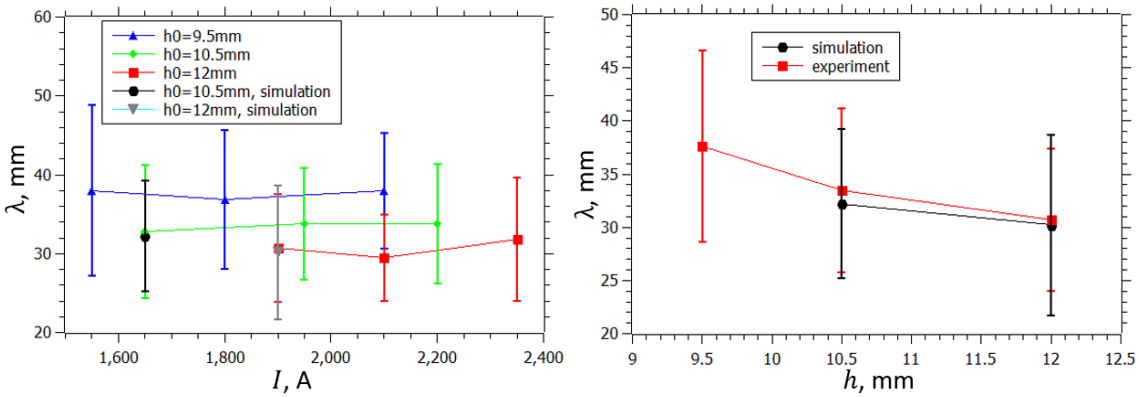

Fig. 5.3.18. Peak spacing λ for $L = 50$ cm depending on current (left) and layer thickness (right).

Overall, the numerical model is representing the experiment well. However, it is not the case for higher currents. Increasing the current in experiments makes the amplitude of the waves grow until they even reach the front wall. Such behaviour was not captured by the model. Higher current in the model does make the amplitudes slightly larger, but shapes of the peaks become more irregular. There is a large number of parameters in the numerical model that can affect the results, ranging from purely numerical (discretization schemes, linear solvers etc.) to physical (inaccurate material properties). Judging from many tests, the disagreement is either related to some coupling parameters (coupling between Elmer and OpenFOAM models) or simply due to spatial and temporal resolution. The spatial resolution was already mentioned above, noting that the mesh elements must be quite small to capture the surface dynamics. Based on experience, under-resolved model in this case should damp the oscillations, not make the peaks irregular. However, the necessary mesh resolution in such a complex model can be very difficult to reach, mainly due to very long simulation times. Doing mesh independence study is unfeasible. At this stage, the application of the model is limited to cases where the oscillations are not the strongest.

Simulations show similar results regarding edge pattern characteristics and oscillations, at least in the low to medium current range. However, somewhat different initiation of these patterns were observed. Initially, the edge is straight. When the inductor current is turned on, melt is deflected away from the inductor, and eventually some perturbations along the edge grow due the mechanism described above, until the final oscillating patterns are fully developed, i.e., quasi-steady state is reached. It is worth looking into how these patterns form. Fig. 5.3.19 shows the edge deformation in time from the moment the current is turned on. The final oscillatory pattern takes a few seconds to form. In experiment, the edge is slightly wavy during the initial deflection, which act as seed perturbations. In simulations, however, the initial deflection does not have any waves. Because of the end effect, where Lorentz force decreases near the sides of the layer, the free surface edge is bending. As the initial deflection grows, these bends near the sides increase, until fluid in the middle of the edge starts pushing back, which initiates small waves traveling from the sides to the center. The waves meet at the center, and the oscillations then continue in a similar fashion like in experiments.

The main reason for such disagreement is not difficult to explain. In experiments, the conditions are not ideal - walls of the container may not be perfectly smooth, especially where acrylic pieces are glued together, there may be some residual oxides on the surface, etc. This can cause the initial edge perturbations. Simulations are an idealization without any imperfections in the setup. However, the tendency of waves traveling from the sides to the center can be observed in some experiments, so the numerical model is adequate. Moreover, if the force in simulations is increased slowly over a few seconds, the perturbations do appear everywhere along the edge simultaneously.

Finally, let's have a closer look at the mechanism that drives these edge instabilities. As derived theoretically in [61], the phenomenon of edge oscillations of a thin liquid conductor can be attributed to redistribution of induced current and magnetic field around edge perturbations. The theoretical model considers a semi-infinite conducting sheet and

infinite magnetic field frequency (zero skin depth), however, the physical principles must also hold for more realistic cases.

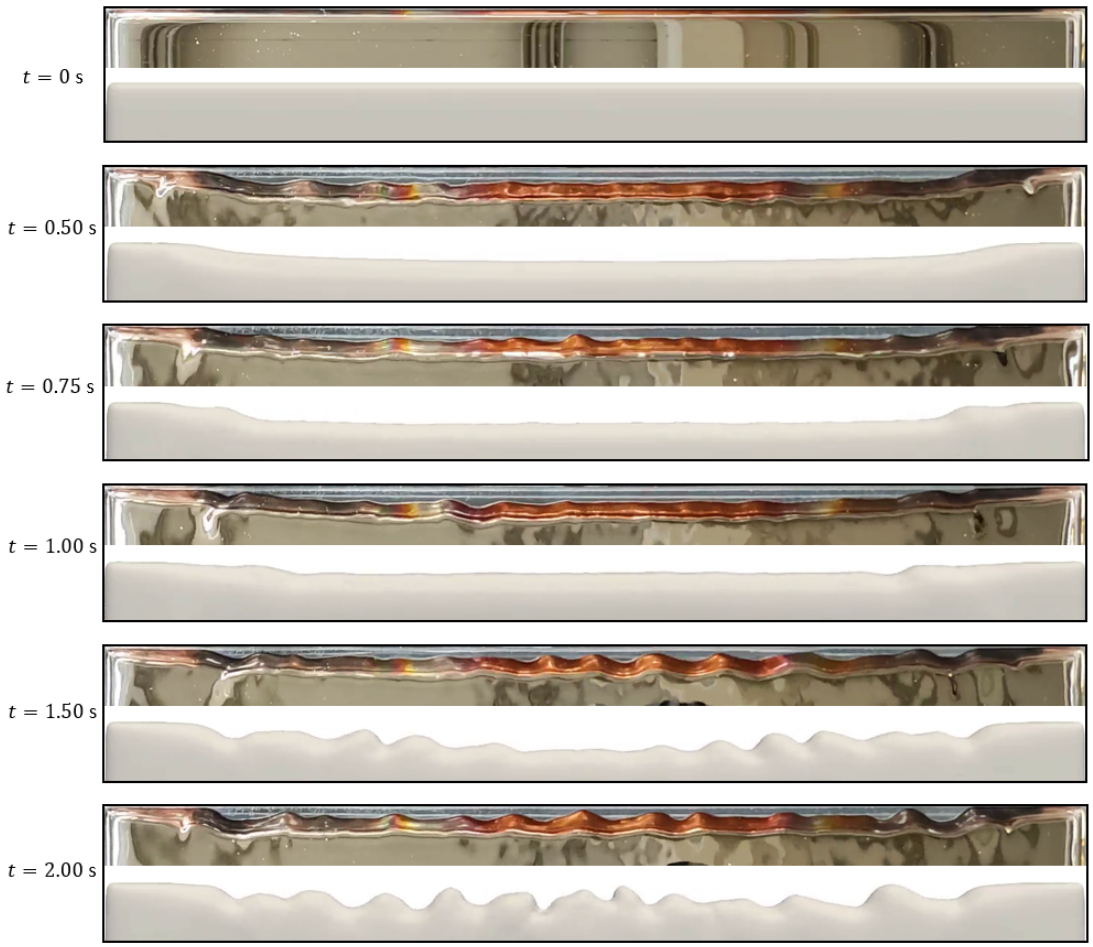

Fig. 5.3.19. Initiation of the oscillatory pattern, $L = 50$ cm, $h_0 = 10.5$ mm, $I = 1650$ A.

When the edge is straight, induced current, magnetic field, Lorentz force and surface tension force is as shown in Fig. 5.3.20. Note that the EM fields shown here are amplitudes that were obtained from a supplementary model where time-dependent quantities were reconstructed from the real and imaginary parts. The maximum of surface tension force is at the corners where curvature is highest. End effect of finite length of the layer is evident here - current paths change direction near the corners and the Lorentz force magnitude decreases. Logically, the initial surface deflection relates to the uneven distribution of the Lorentz force.

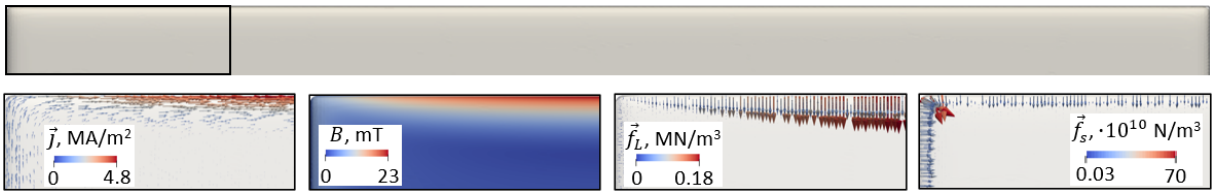

Fig. 5.3.20. Amplitudes of induced current, magnetic field, Lorentz force and surface tension force for initial melt shape, $L = 50$ cm, $h_0 = 10.5$ mm, $I = 1650$ A.

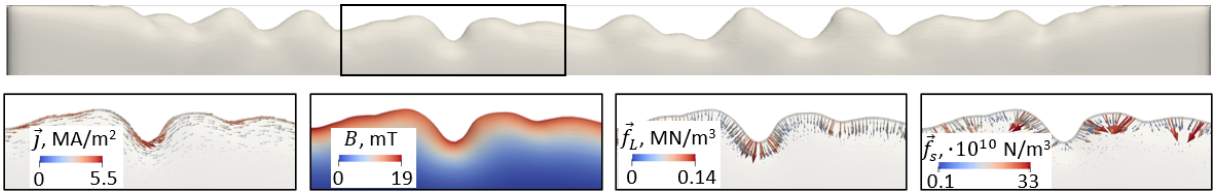

Fig. 5.3.21. Amplitudes of induced current, magnetic field, Lorentz force and surface tension force for deformed melt shape, $L = 50$ cm, $h_0 = 10.5$ mm, $I = 1650$ A.

Upon development of some edge perturbations or waves, the EM fields redistribute accordingly, as exemplified in Fig. 5.3.21. The Lorentz force now has a localized character with maxima in the troughs of the wavy pattern, therefore tending to promote the growth of the perturbations. Surface tension has maximums at the crests or peaks, therefore opposing the effects of EM fields. The competition between the forces leads to a parametric instability where the changing shape of the surface modulates the forces.

In experiments with $L = 20$ cm, the current frequency was varied in a small range of 3 to 8 kHz. In this range, frequency had very little effect on surface dynamics. A marginal tendency was that the peaks in the edge pattern appeared narrower at higher frequency. This makes sense, since skin depth is smaller at higher frequency, which would support development of smaller surface structures.

Thus far, only the interaction of EM fields and surface tension was considered as the main aspect of the parametric edge instabilities. Bulk flow velocity can also play a role. For undisturbed or flat edge, the Lorentz force would drive bulk flow in the form of two symmetrical eddies in the plane of the layer as sketched on the left in Fig. 5.3.22. This is similar to the double vortex in the meridional plane of melt in induction crucible furnace. This flow pattern was detected in some experiments at low currents (so that the edge deformation is negligible) by observing the motion of small bubbles on the surface of the melt. The bubbles were not introduced on purpose, they sometimes simply appeared as a product of some chemical reactions between oxides and the acid solution. When the edge deforms, Lorentz force distribution changes, with local maxima appearing at some places. This also modifies the flow pattern accordingly. An example flow pattern for deformed surface is sketched on the right in Fig. 5.3.22, which was also observed experimentally. Interestingly, edge deformations can cause the reversal of the two dominant vortices. The flow directly towards the deformed edge therefore enhances the oscillations. Another example of bulk flow modifications is the merging of the two dominant vortices forming a single eddy spanning the whole melt volume, which was observed to reduce or smoothen the wavy pattern. This could be observed experimentally by introducing some asymmetry, e.g. by shifting the container slightly left or right.

These flow characteristics were mostly observed for $L = 20$ cm. In longer containers, the edge contained more crests and troughs, and the corresponding Lorentz force distribution drove much more complicated flow patterns that were difficult to distinguish. Nevertheless, it is clear that bulk flow can influence the surface dynamics. This could be very crucial in applications, such as DSC, where AC field would be used to control the free surface of flowing liquid metal layers.

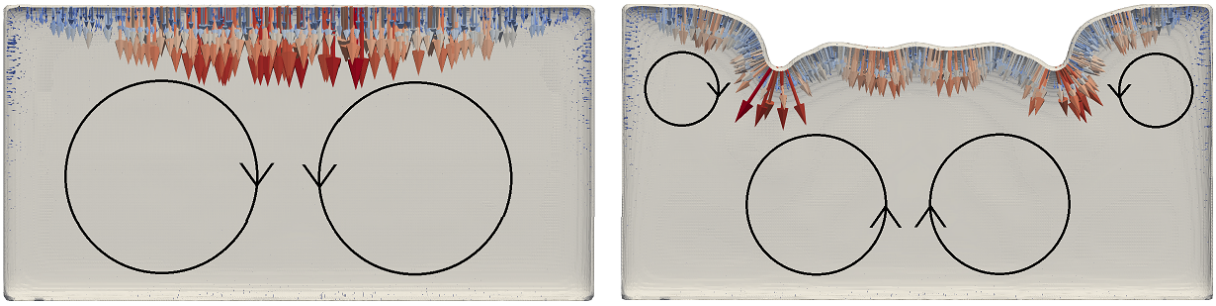

Fig. 5.3.22. Schematic representation of Lorentz force (coloured vectors) and bulk flow patterns (black circular arrows) for undisturbed melt shape (left) and with edge deformations (right).

5.3.2 Circular layer

There are several studies reported in literature of circular drops in AC magnetic field. Most studies consider either oxidized or pure (with HCl) drops. We built an experimental setup to study both pure and oxidized drops in similar conditions, extending the range of studied parameters and observing various interesting instabilities. Note that dimensionless parameters can differ among different studies depending on how characteristic sizes and other factors are considered in their calculation. Characteristic size is often taken as $L = V^{1/3}$, where V - drop volume, instead of just the radius.

Inductor current frequency in this case was 22 kHz, which is up to 5 times higher than in experiments with the rectangular layer. Skin depth difference is therefore up to 2.3 times. This can mean that electromagnetic field and Lorentz force are slightly more sensitive to free surface deformations.

Series of experiments were done with drop volumes $V = 5 - 60$ ml and inductor currents $I = 60-500$ A. Magnetic field in the center of the inductor is $B_I = 42$ μT/A (from numerical model). The considered cases cover $Bo = 27-125$ and $B_m = \frac{\sigma f B_I^2 V}{\gamma} = 5-3000$.

Depending on Bond and magnetic Bond numbers, different circular drop shapes and dynamics can be observed experimentally. Typically, at small Bo, axisymmetric squeezing is observed, such as shown in the middle of Fig. 5.3.23 for $Bo = 27$ and $B_m = 20$. Increasing inductor current, some azimuthal disturbances start accompanying the axisymmetric squeezing, as shown on the right in Fig. 5.3.23. At some critical current, the axial symmetry completely breaks down into azimuthal oscillations of different modes. For $Bo = 27$, the first excited oscillations are with mode number $m = 3$ (triangular oscillations), shown on the left in Fig. 5.3.24 (note that the lighting conditions are not the same in all experiments, in some runs a light from the bottom of the container was used to improve contrast, which may be useful should we want to do some automated image processing in the future). With further increase of B_m, higher modes appear, such as $m = 4$ shown in the middle and right in Fig. 5.3.24.

For higher Bo (larger drops), the first excited mode, after the onset of azimuthal perturbations, is higher. For example, for $Bo = 42.9$ ($V = 10$ ml), $m = 3$ was not observed and the first excited mode was $m = 4$. Since at higher Bo surface tension forces are less dominant, various free surface deformations can occur, instead of only regular

oscillations. For larger drops, topologically different oscillating shapes were observed. For example, a "C" or "H", or even more complex shapes, shown in Fig. 5.3.25. Transitions between different shapes also occurred, e.g. the "C" shape could turn into an "H" etc.

Fig. 5.3.23. Axisymmetric squeezing and the onset of edge perturbations for $Bo = 27$ ($V = 5$ ml): $B_m = 0$ (left), $B_m = 20$ ($I = 135$ A, $B = 5.7$ mT) (middle), $B_m = 50$ (right).

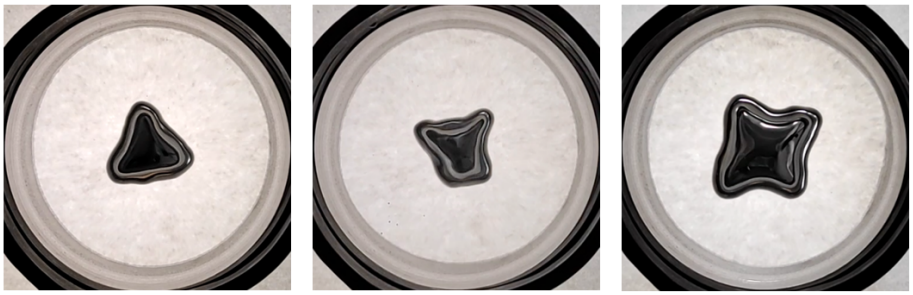

Fig. 5.3.24. Surface oscillation modes: (left) $m = 3$, $Bo = 27$, $B_m = 83$; (middle) $m = 4$, $Bo = 27$, $B_m = 123$; (right) $m = 4$, $Bo = 42.9$, $B_m = 131$.

Intriguing instabilities were captured for larger drops. It was clear also for smaller drops that surface dynamics are sensitive to how fast the inductor current is increased from 0 to a specific value. Ideally, if current was increased slowly over a very long period, significant edge perturbations would not develop and the threshold for the onset of oscillations could be larger, i.e. axisymmetric squeezing could be observed for larger Bo and B_m. This sensitivity to the rate of application of EM force proved to be very strong for large drops. Although the rate was not controlled exactly, a number of different behaviours could be distinguished. For intermediate Bo and B_m, when the current was turned on instantly, regular oscillating modes initially developed, which subsided in a few seconds into small oscillating edge perturbations, as shown in Fig. 5.3.26. For larger B_m, the initial modes turned into relatively stable irregular deformations, as seen in Figs. 5.3.27 and 5.3.28. If the current was increased gradually, the initial regular modes did not appear, but the drop was squeezed until some edge perturbations allowed the irregular shapes to form.

Largest drops, which nearly covered the whole bottom of the container, were very sensitive, to the point where it was almost impossible to achieve a stable shape. Note that due to technical solutions, minimum inductor current was $I_{min} \approx 60$ A. For $V = 50$ ml ($Bo = 125.4$), the surface was very unstable even at I_{min}. While it possessed similar

characteristics as slightly smaller drops - initial regular perturbations turned into irregular patterns, the irregular shapes were highly oscillating. One of the most intriguing instabilities were observed when a stable circular shape was achieved at I_{min}, which allowed to slowly increase the current. At some point during the increase of current, axisymmetric squeezing turned into strong spontaneous oscillations with distinct azimuthal modes. Time-dependent behaviour of one such case is shown in Fig. 5.3.29. The inductor current was fixed when the oscillations started at around $t = 25$ s. Slight variations of current later are related to changing impedance due to changing shape of the drop.

Fig. 5.3.25. Irregular surface shapes: (left) $Bo = 68$, $B_m = 263$; (middle) $Bo = 108$, $B_m = 406$; (right) $Bo = 125$, $B_m = 215$.

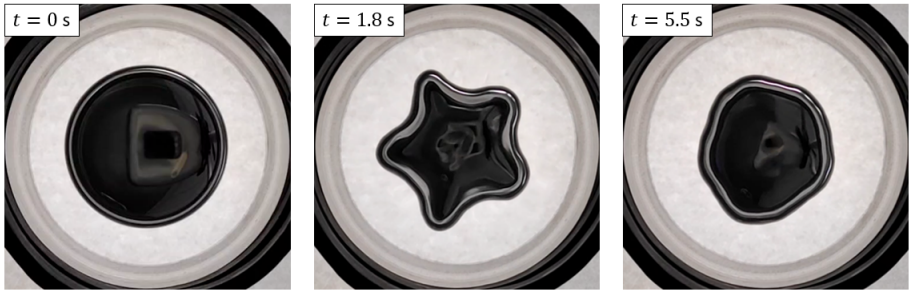

Fig. 5.3.26. Stabilisation of edge oscillations, $Bo = 68$, $B_m = 134$. Time shown is from turning on the current.

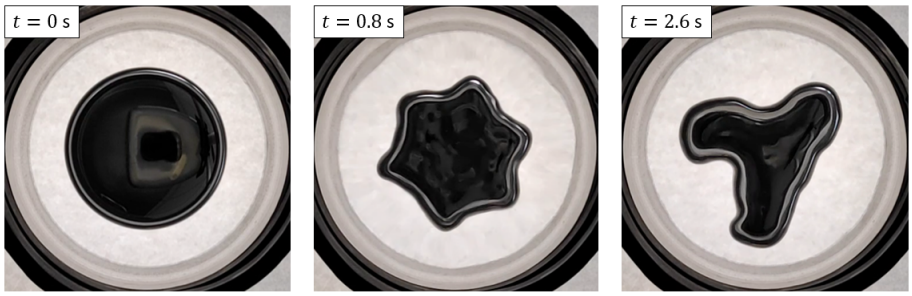

Fig. 5.3.27. Stabilisation of edge oscillations, $Bo = 68$, $B_m = 193$. Time shown is from turning on the current.

Before the spontaneous oscillations, the drop was slowly deforming into an irregular shape. It could be that this deformation is related to the shape of the inductor, since it

seems that the drop is squeezed in the area closest to where inductor leads connect to the generator (near bottom in the images).

Fig. 5.3.28. Stabilisation of edge oscillations, $Bo = 68$, $B_m = 263$. Time shown is from turning on the current.

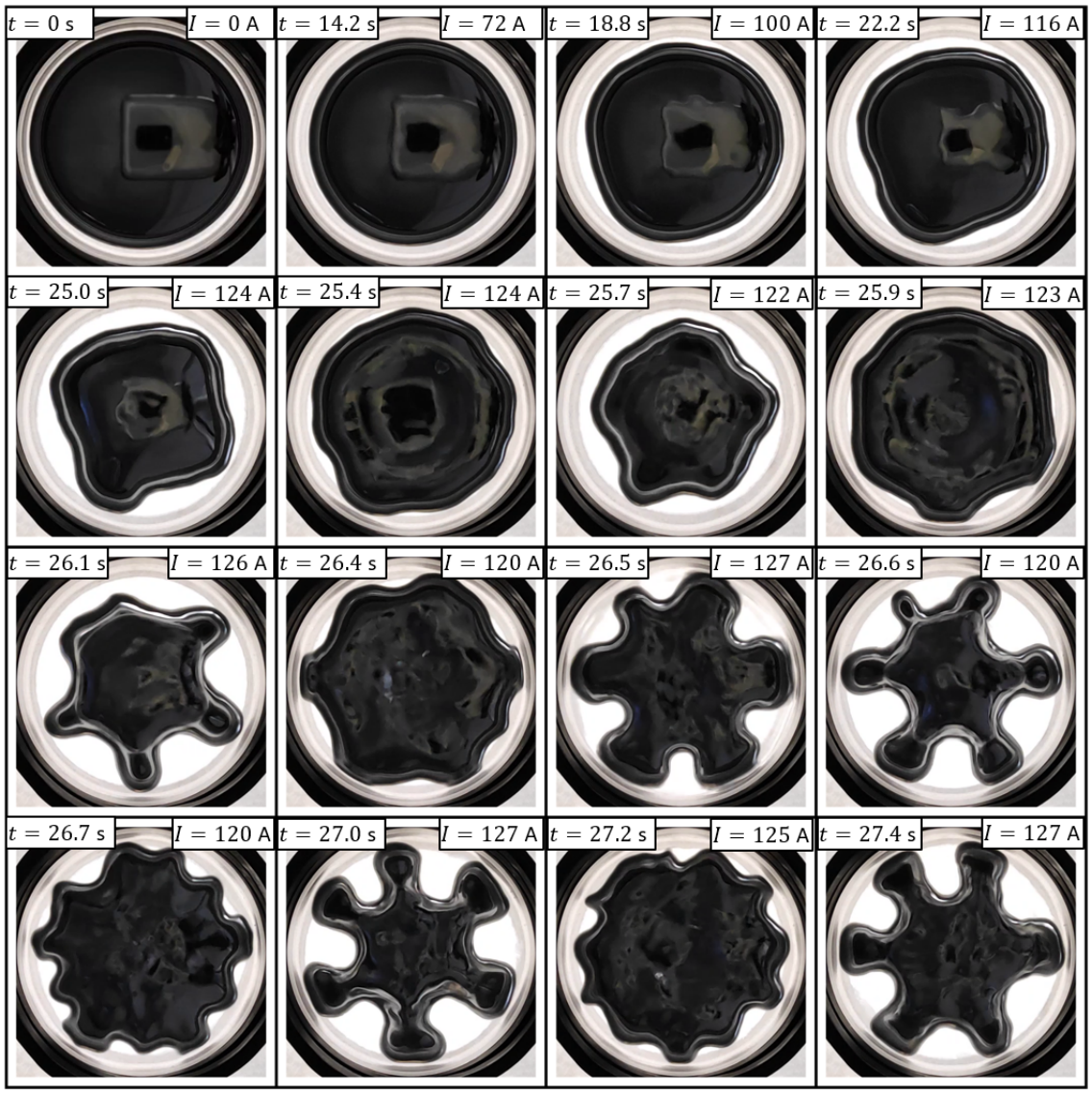

Fig. 5.3.29. Oscillatory instability of a large drop, $Bo = 125$ ($V = 50$ ml). $I = 120$ A is equivalent to $B = 5$ mT and $B_m = 158$.

Similarly to the rectangular layer, surface oxidation leads to static free surface shapes. Examples of two different drop sizes are shown in Fig. 5.3.30. Working with oxidized drops is tricky. Since the contact line sticks to the bottom of the container, it is more difficult to make circular shape before turning on the inductor current. This means that there are initial edge perturbations, which can determine the final shape with current on. Nevertheless, the shapes shown in Fig. 5.3.30 are characteristic for oxidized surface.

The physical mechanism for formation of the wavy edge patterns and oscillations described in the previous section for the rectangular layer also holds for circular drops. This mechanism was demonstrated using numerical results, attributing it to the redistribution of the induced current, magnetic field and Lorentz force. The effect of this field redistribution is clearly evident in experimental results with large oxidized circular drop. Let's look at the initialization and development of the static labyrinth structures. Fig. 5.3.31 shows the time-series of the drop shape from the moment of turning on the inductor current until the pattern is stabilized (current is turned on instantly instead of increasing it slowly). Initially circular drop is squeezed, and immediately some azimuthal perturbations are forming. As the EM force increases in the perturbations, they grow until gravity is able to spread the drop radially. When the azimuthal peaks of the edge reach the wall, they are squeezed against the wall. EM force increases in the cavities or troughs around the perimeter of the drop, and they are enhanced until all forces are in balance.

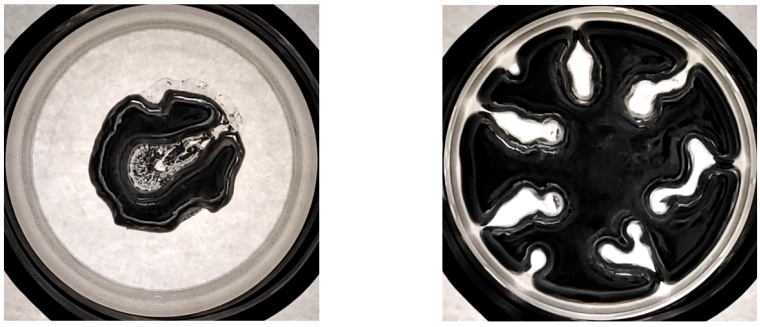

Fig. 5.3.30. Static oxidized drop shapes: (left) $Bo = 43$, $B_m = 126$; (right) $Bo = 125$, $B_m = 215$.

Numerical modelling of circular drops proved to be much more difficult. While the rectangular melt pool was in contact with side walls of the container, the circular drops are positioned in the center of the cylindrical container. Problems with this arise due to spurious currents or parasitic flows at the interface, characteristic to the VOF method in surface tension dominated cases. Spurious currents are due to inaccuracies calculating interface curvature and normals, leading to inaccurate surface tension forces which cause the spurious currents. The effect of this can be best seen when simulating a simple static drop without any external forces. The spurious currents start unphysically deforming the free surface and can even cause strong motion and breakup of the liquid drop. There are methods to reduce spurious currents, such as volume fraction smoothing, but none of the options completely eliminates spurious currents. The smoothing does indeed reduce these errors significantly, however, simulation of static drops was still not possible.

Spurious currents are less pronounced when other forces, such as Lorentz force, are

dominating over surface tension. However, at some intermediate B_m, when surface tension and EM forces are comparable, it can be impossible to distinguish free surface oscillations caused by spurious currents and those due to EM forces. This is further complicated by the fact that sometimes purely numerical effects can lead to physical results. In this case, it means that the droplet can respond to different free surface excitations (numerical inaccuracies or EM forces) similarly. It is indeed so, as it was found that in some cases simulating a static droplet (which is strongly affected by spurious currents) shows very similar surface oscillations as with EM forces. Due to the problems with the VOF method, simulation of circular drops in AC magnetic field is left for future work.

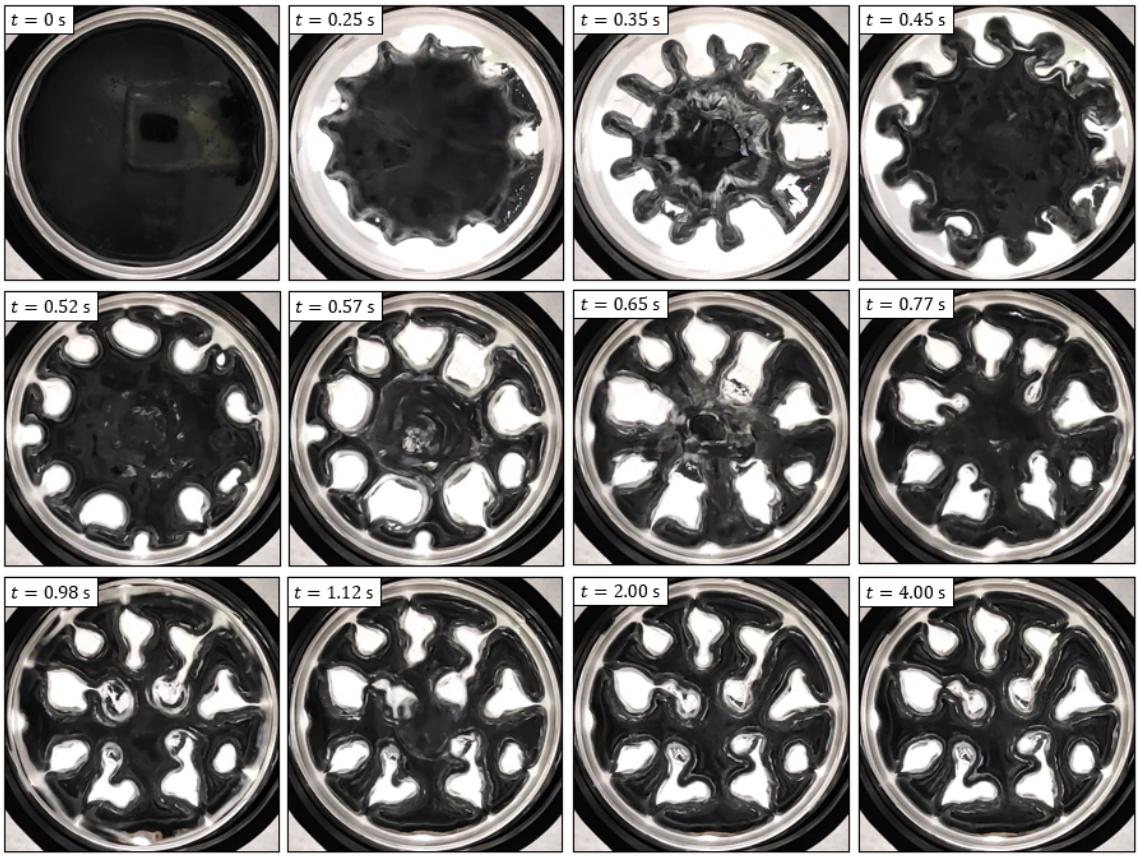

Fig. 5.3.31. Formation of static irregular patterns for a large oxidized drop, $Bo = 125$ ($V = 50$ ml), $B_m = 507$ ($I = 215$ A, $B = 16.9$ mT).

5.3.3 Conclusions

This part of the thesis was concerned with thin liquid metal layers subjected to transverse AC magnetic field with high frequency - rectangular pools close to a straight inductor and circular melt drops in a cylindrical inductor. Fundamentally, both cases are similar, involving high-frequency EM induction and two-phase flow with free surface. Dynamics of the free surface are different due to topological or geometrical differences. In rectangular cases, qualitatively different edge deformations of the liquid metal layer can be observed depending on the layer thickness, inductor current and surface oxidation. Longer edge (along the inductor) allows more diverse oscillations and instabilities due to reduced influence of paths of the induced currents.

To gain more insight into the mechanisms of surface dynamics and instabilities, this complex process was simulated using coupled open-source software. The numerical model considers dynamic two-way coupling between free surface motion and EM fields. For the rectangular layer, simulations show good agreement to experiments for low to medium inductor currents. For high currents, strong oscillations are observed experimentally, which proved to be difficult to reproduce numerically, mainly due to limited spatial resolution. The coupled simulations are very time-consuming, therefore conducting mesh independence study was unfeasible.

Interesting dynamics were observed for circular drops. Typically, regular azimuthal modes developed for small drops, while larger drops assumed irregular shapes. For largest drops almost covering the bottom of the container were quite unstable, with spontaneous azimuthal pulsations occurring even when the inductor current is increased very slowly. Simulation of circular drops is left for future work due to problems with the spurious currents in the VOF method (this was not an issue for the rectangular case).

Practical implications of such EM-driven instabilities are obvious. In some processes, AC magnetic field can be used to control liquid metal flow and free surface dynamics. However, as the experiments and simulations show, AC magnetic field can also enhance instabilities, which can be detrimental to the stability of the process, compromising the quality of the final product. One industrial application where this could be relevant is investigated in the next section.

5.4 Direct strip casting

This section is concerned with a novel industrial application - direct strip casting (DSC), where EM field can be used to control the stability of the process. Some preliminary results were reported in conferences [C.2][C.5]. Most of the results are presented here. To establish the basics of DSC, the process is first simulated without EM in section 5.4.1. When the main issues are identified, the application of static magnetic field is considered in section 5.4.2 and electromagnetic backflow control in section 5.4.3.

5.4.1 Without EM field

Aluminium is considered as a representative alloy, with all physical properties at 1200 K, which were given in section 3.7.4. Contact angle between liquid and solid depends on materials, surface characteristics (roughness etc.), temperature and other factors. The belt is typically made of either steel or copper [27]. On copper substrate, liquid aluminium has a dynamic contact angle from 105 to 140 degrees [40]. For simplicity, constant contact angle is set on the belt, θ_{belt}. The influence of contact angle in this range is tested for the casting process without EM. Contact angle to the moving side dam is set to $\theta_{dam} = 180°$, and to other surfaces (refractory) to 135 degrees.

The cooling condition on the belt is constant normal heat flux q_b, as estimated in section 3.7.4. In real casting process, the correct condition would be the mixed boundary condition (Robin condition), but the simulation with constant temperature or constant

heat flux converges better and it is a reasonably good approximation if the material and other properties are independent of temperature (which is assumed here).

Two cases are considered here - with backflow gap closed and open. The former case basically would correspond to a stable meniscus at a very small gap, while the latter is with a larger gap allowing backflow. Let's first consider closed gap. Geometrical parameters are (see Fig. 3.7.9): $L_b = 50$ cm, $w = 10$ cm, $h_{in} = 2.5$ cm, $d_{in} = 1$ cm. Casting conditions are $v_{in} = 20$ cm/s, $T_{in} = 1200$ K, $v_p = 20$ cm/s. With these conditions, the cast strip should have $h = 10$ mm average thickness. The estimated cooling heat flux is $q_{belt} = 2.27\frac{\rho h v_p}{L_b}(c_p(T_{in} - T_s) + L_T) = -13.8$ MW/m^2, which is close to typical values in belt casting [30]. Transient simulation in OpenFOAM is run until $t = 5L_b/v_p = 12.5$ s.

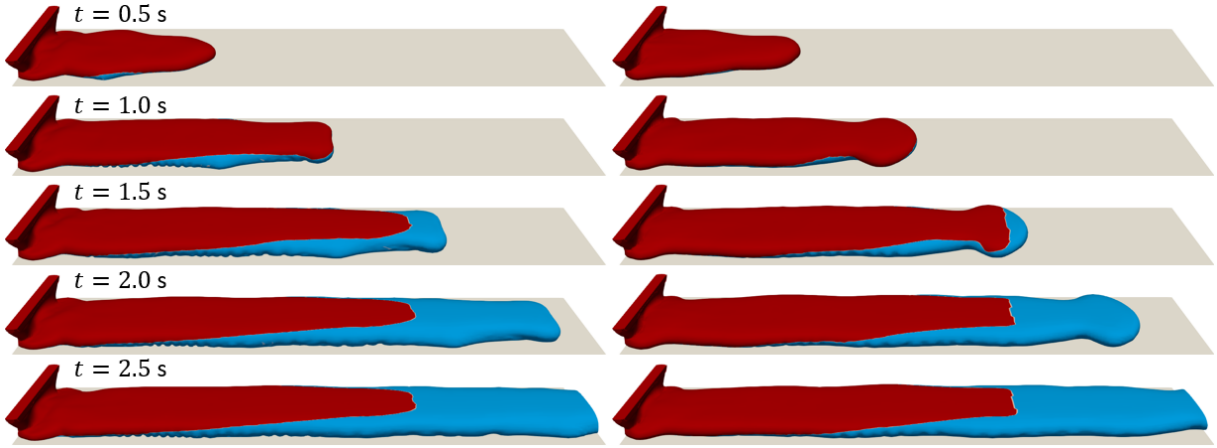

Fig. 5.4.1. Phases during the first 2.5 s with $\theta_{belt} = 105^o$ (left) and 140^o (right) without magnetic field; red - liquid, blue - solid.

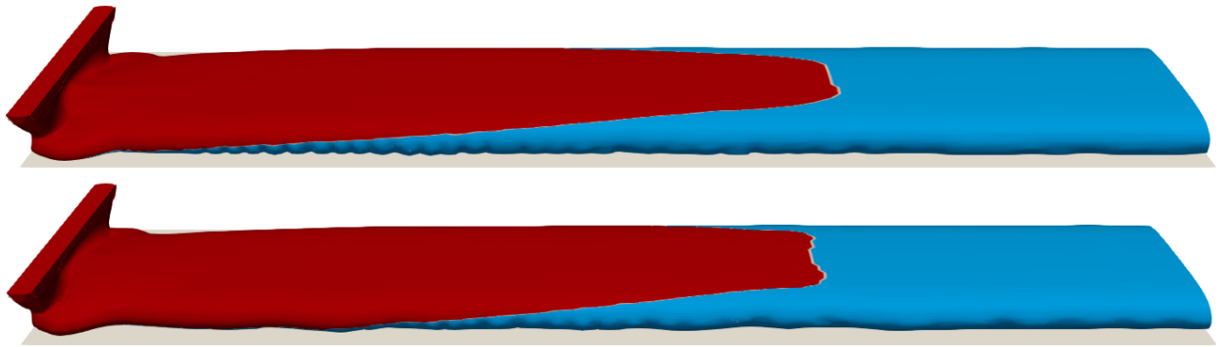

Fig. 5.4.2. Phases at $t = 12.5$ s with $\theta_{belt} = 105^o$ (top) and 140^o (bottom) without magnetic field; red - liquid, blue - solid.

Fig. 5.4.1 shows phase distribution during the first 2.5 s of casting. Figs. 5.4.2 and 5.4.3 show metal phase distribution and layer thickness with $\theta_{belt} = 105^o$ and 140^o. Clearly, the melt does not cover the whole width of the belt with both contact angles. With higher θ_{belt} the strip profile in the belt direction is slightly more wavy. Similar waviness has also been observed numerically and experimentally in laboratory-scale casting of aluminium [30]. Static or traveling magnetic field can be used to help spread the melt across the belt and stabilize the free surface to achieve more uniform strip shape.

The sizes of real casting equipment would be considerably larger. Phase and thickness distributions with 2 times wider belt, $w = 20$ cm, are shown below. The result is qualitatively very similar to the narrower case, but the sides are even wavier. Of course, this is with the simplest feeding system - a slit in refractory with the same width as the belt. The feeding system can be optimized to achieve better results. A way to stabilize the casting process using magnetic field is investigated in the next section.

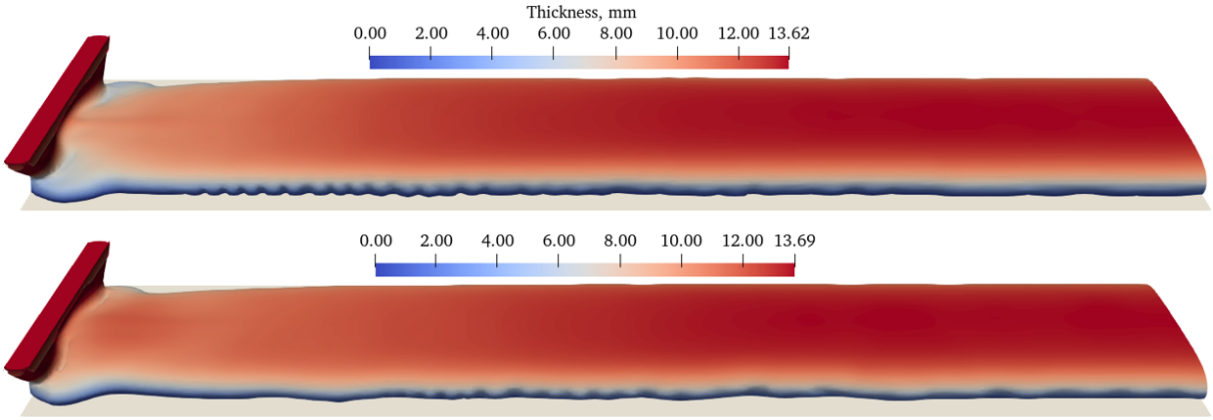

Fig. 5.4.3. Layer thickness at $t = 12.5$ s with $\theta_{belt} = 105^o$ (top) and 140^o (bottom) without magnetic field.

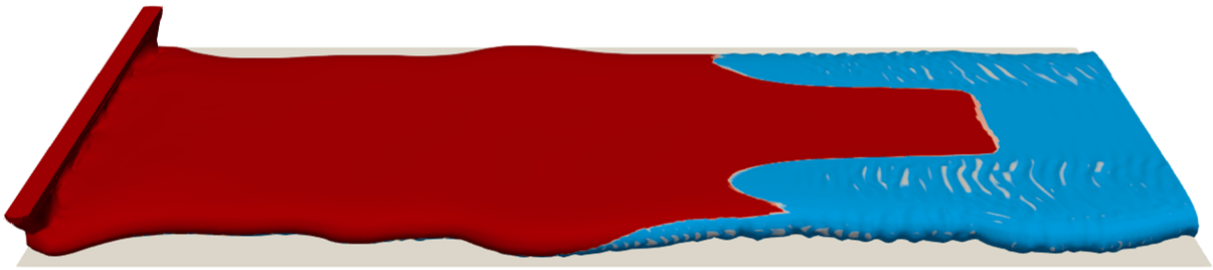

Fig. 5.4.4. Phases at $t = 12.5$ s without magnetic field, $\theta_{belt} = 140^o$, $w = 20$ cm; red - liquid, blue - solid.

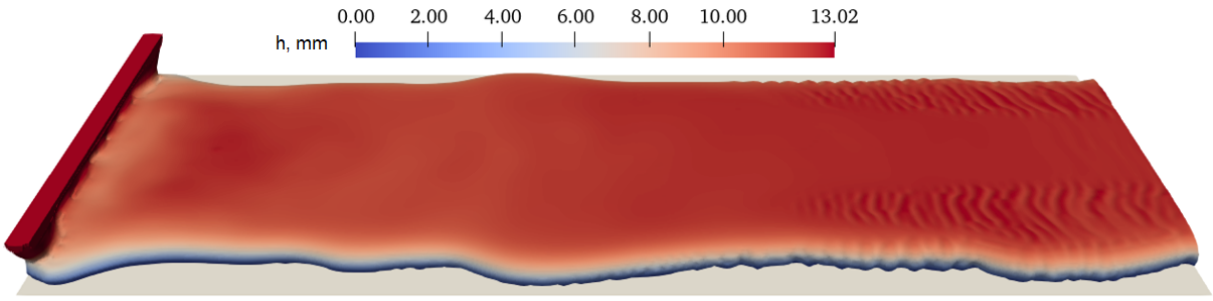

Fig. 5.4.5. Layer thickness at $t = 12.5$ s without magnetic field, $\theta_{belt} = 140^o$, $w = 20$ cm; red - liquid, blue - solid.

The backflow gap between refractory and the moving belt so far was assumed to be very small. If the gap is larger, the meniscus at the triple point can become unstable and

the melt can flow into the gap opposite to the belt movement. Let's see what happens during the casting with gap height $h_{gap} = 5$ mm. Metal phase distribution during the first moments of casting is shown in Fig. 5.4.6.

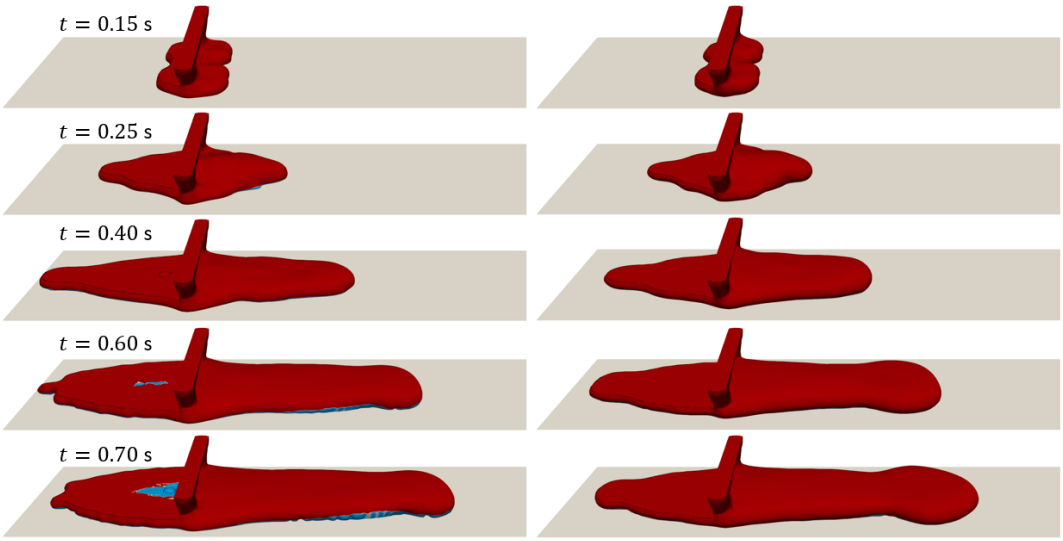

Fig. 5.4.6. Phases during the first 0.7 s with $\theta_{belt} = 105^{o}$ (left) and 140^{o} (right) without magnetic field, $h_{gap} = 5$ mm, $w = 10$ cm; red - liquid, blue - solid.

$h_{gap} = 5$ mm is more than enough for the melt to flow into the gap opposite to the belt movement. In the model, cooling is applied equally throughout the belt, even under the gap, therefore melt can solidify there. This is clearly evident for $\theta_{belt} = 105^{o}$ where the metal has solidified through the entire gap height behind the inlet. Since all solidified material is set to move with the belt (from left to right in the figures), at some point in time all of the metal, liquid together with solid, is pulled out of the gap until it reaches the area directly below the inlet, after which fresh liquid metal is allowed to again flow into the gap. Fig. 5.4.7 demonstrates this effect more clearly by showing vertical middle cross-section of the metal. This effect of melt being periodically pulled forward modulates the width of the solid strip, making the quality of cast material unacceptable. Possible solutions to the backflow problem are investigated in section 5.4.3.

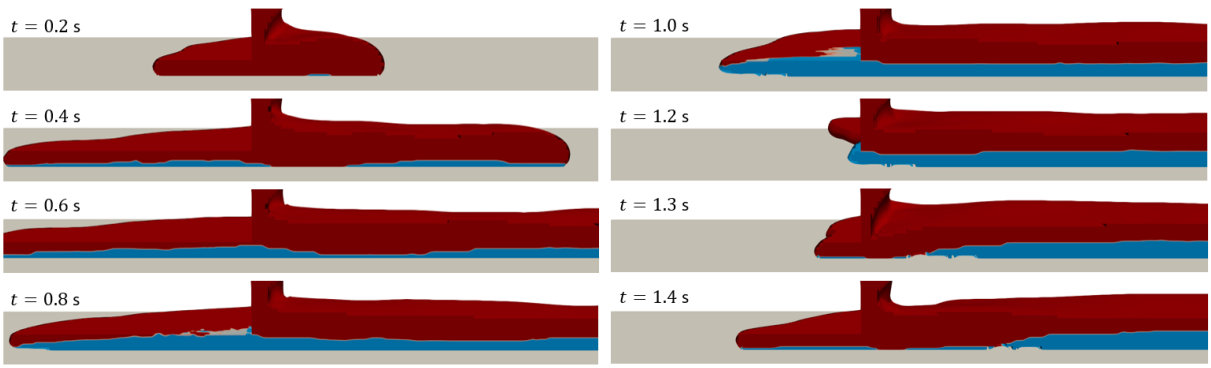

Fig. 5.4.7. Phases in middle cross-section during the first 1.4 s with $\theta_{belt} = 140^{o}$ without magnetic field, $h_{gap} = 5$ mm, $w = 10$ cm; red - liquid, blue - solid.

5.4.2 Static magnetic field

Static magnetic field is applied near the inlet where most of the metal is liquid. Geometrical parameters are (see Fig. 3.7.9): $L_b = 50$ cm, $w = 10$ cm, $h_{in} = 2.5$ cm, $d_{in} = 1$ cm, $h_{em} = 2.5$ cm, $x_{em} = 6$ cm, $d_{em} = 1.5$ cm, $L_{em} = 7$ cm. Casting conditions are $v_{in} = 20$ cm/s, $T_{in} = 1200$ K, $v_p = 20$ cm/s. The cooling heat flux is $q_{belt} = -13.8$ MW/m^2. Contact angle in this section is $\theta_{belt} = 140^o$. EM field calculation in Elmer is run only once at the start of simulation to obtain magnetic field distribution, which is then used in OpenFOAM to calculate induced current and Lorentz force. Transient simulation in OpenFOAM is run until $t = 5L_b/v_p = 12.5$ s.

Magnetic field distribution with $M_0 = 1$ T is shown in Fig. 5.4.8. Phases and thickness during the first 2 s are shown in Fig. 5.4.9, and induced current and Lorentz force in Fig. 5.4.10. Figs. 5.4.11 and 5.4.12 show final phases and thickness at steady state ($t = 12.5$ s). The melt is slowed down below the magnetic field source, and at some point in time the braking force causes the melt to spread across the belt width. This leads to more efficient cooling and more uniform layer thickness. Flow velocity with and without magnetic field is shown in Fig. 5.4.13. Flow is obviously homogenized by magnetic field.

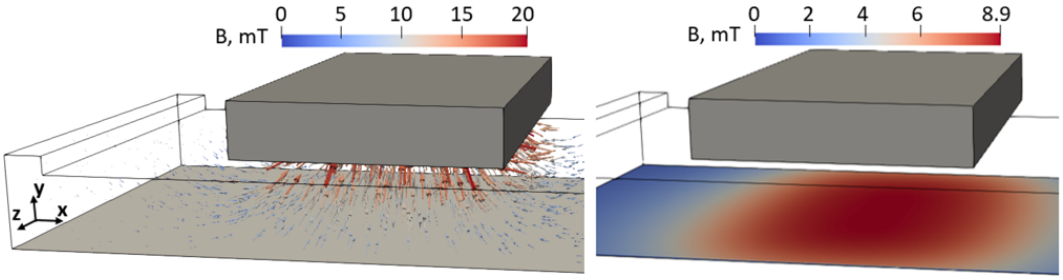

Fig. 5.4.8. Static magnetic field, $M_0 = 1$ T: vectors (left) and magnitude on the belt (right).

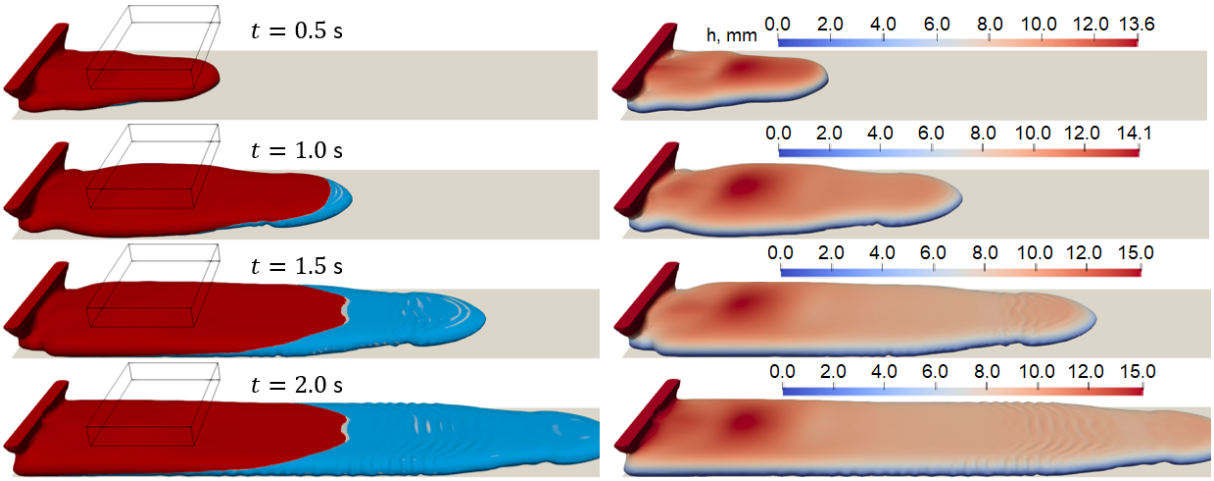

Fig. 5.4.9. Phases (left) and thickness (right) during the first 2 s, $M_0 = 0.5$ T; red - liquid, blue - solid.

There might be some disadvantages of magnetic field in this case. The intensive braking force with $M_0 = 0.5$ T also causes the melt level before to increase near the inlet.

This increases pressure at the triple point at the backflow gap, increasing the probability of melt entering the gap even if the gap is very small. One could find an optimal value of M_0 to prevent build-up of melt near the inlet while at the same time stabilising free surface downstream. Fig. 5.4.14 shows phase distribution with $M_0 = 0.2$ T and 0.3 T. Interestingly, weaker field can actually introduce instabilities. $M_0 = 0.3$ T appears to eliminate melt build-up and spread the melt evenly across the belt further downstream.

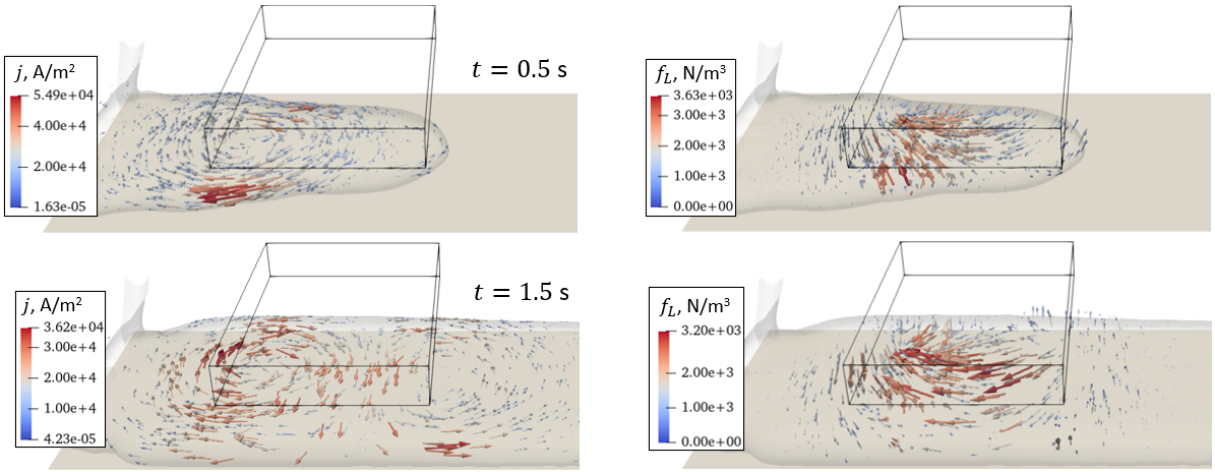

Fig. 5.4.10. Examples of induced current (left) and Lorentz force (right), $M_0 = 0.5$ T.

The influence of TMF instead of static field is similar - fast moving liquid metal is slowed down. But with TMF the effect is weaker - since the field is traveling with the belt speed, the braking force in the melt is weaker. Static magnetic field is more efficient in cases where most of the liquid metal is moving faster than the belt. However, static field can not accelerate parts of the fluid moving slower, in which case traveling field would be more appropriate. In addition, TMF would not cause melt build-up near the inlet. However, simulations with TMF are much more time-consuming, since the simple approach of considering the $\sigma\vec{v} \times \vec{B}$ term in OpenFOAM would not work for induction by time-dependent field.

Fig. 5.4.11. Phases at steady state ($t = 12.5$ s), $M_0 = 0.5$ T; red - liquid, blue - solid.

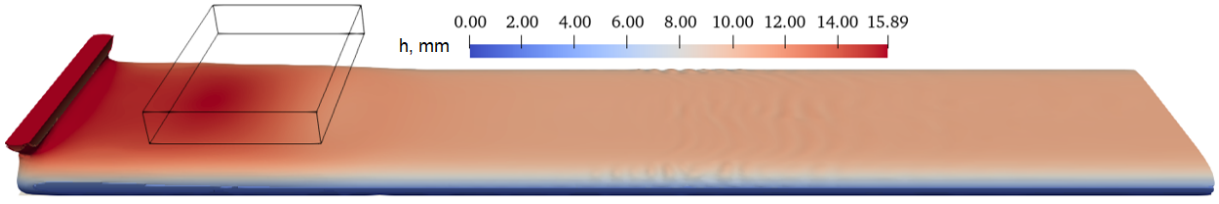

Fig. 5.4.12. Layer thickness at steady state ($t = 12.5$ s), $M_0 = 0.5$ T.

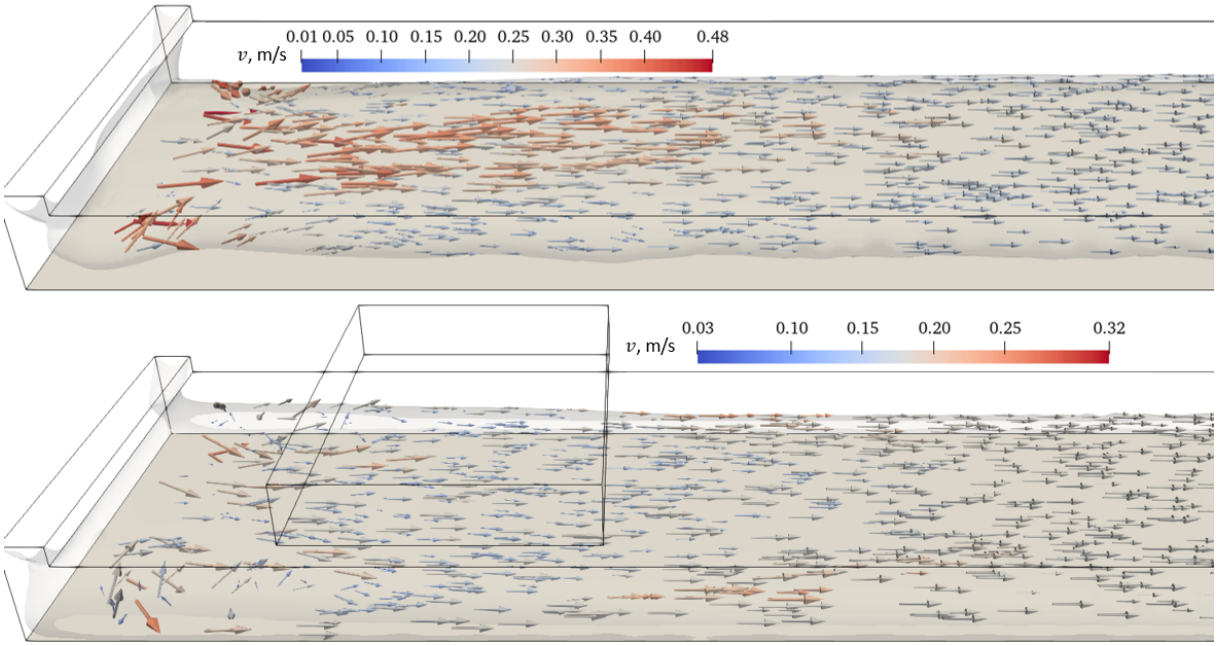

Fig. 5.4.13. Flow velocity without magnetic field (top) and with $M_0 = 0.5$ T (bottom).

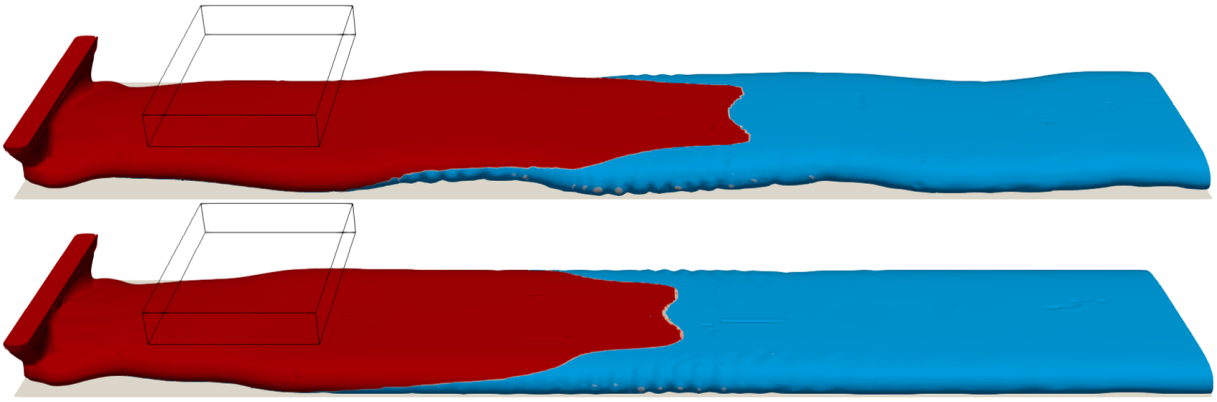

Fig. 5.4.14. Phases with $M_0 = 0.2$ T (top) and $M_0 = 0.3$ T (bottom); red - liquid, blue - solid.

Application of magnetic field to moving conductor not only induces force but also generates Joule heat, q_{em}, due to induced currents. In this case, Joule heat was ignored. This is easily justified by checking the magnitude of Joule heat. Integrating $q_{em} = j^2/\sigma$ over the volume directly below the field source results in approximately 10 mW, which is very small compared to the cooling rate. This, however, is not necessarily the case with AC field investigated in the next section.

5.4.3 Backflow control

Flow of liquid metal opposite to the belt motion is one of the problems in DSC. As demonstrated above, even a few millimeter gap height can make the whole process unstable. There are several possible solutions reported in literature, such as using inclined refractory and optimizing the feeding system. It could be possible control the backflow using EM technologies. The main idea here is to use AC magnetic field of a straight

inductor placed near the gap behind the inlet to repel the liquid metal from that area. In essence, the physical effects are then related to section 5.3.1, where EM force was used to deflect a thin liquid metal layer. Of course, it was shown for the thin layers that AC field can actually induce free surface instabilities, however, it all depends on various parameters, such as layer thickness (gap height in the casting case), field frequency and material properties.

Geometrical parameters in this section are (see Fig. 3.7.9): $h_{gap} = 5$ mm, $L_b = 50$ cm, $w = 10$ cm, $h_{in} = 2.5$ cm, $d_{in} = 1$ cm, $x_i = y_i = 5$ mm, $h_i = 2$ mm, $d_i = 10$ mm. Casting conditions are $v_{in} = 20$ cm/s, $T_{in} = 1200$ K, $v_p = 20$ cm/s. The cooling heat flux is $q_{belt} = -13.8$ MW/m^2. Contact angle is $\theta_{belt} = 140^o$. Frequency of the inductor current is $f = 4$ kHz. EM field calculation in Elmer is repeated every time melt moves over at least half a mesh element, which is very often considering the dynamics of casting. Transient simulation in OpenFOAM uses Lorentz force calculated by Elmer. In addition, Joule heat is also applied in this case.

Considering the properties of liquid aluminium and the results of section 5.3.1, one can expect relatively stable deflection of melt layer with thickness $h_0 = h_{gap} = 5$ mm. However, since now the melt layer is not initially static, i.e., melt is constantly flowing down from the inlet, flow velocity could play a more important role in determining stability of the free surface near the inductor.

For the cases shown in Figs. 5.4.6 and 5.4.7, quite stable repulsion of the melt was achieved with $I = 1$ kA. Transient behavior in the first moments of casting with AC inductor is shown in Fig. 5.4.15. The AC field keeps the melt from entering the gap. Some free surface oscillations can be observed there, but no instabilities occur. However, the small perturbations travel downstream where they disturb the solidification process. A representative phase distribution at a later time is shown in Fig. 5.4.16.

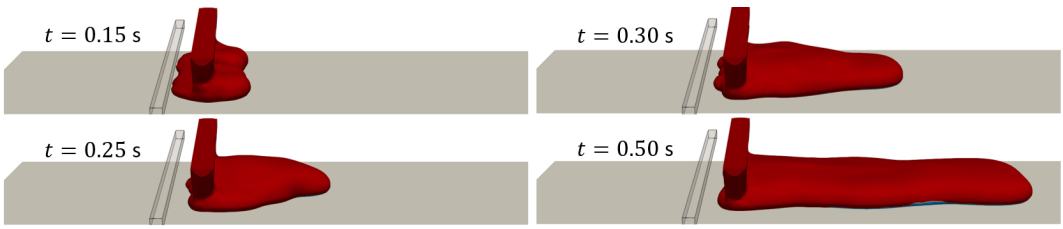

Fig. 5.4.15. Phases during the first 0.5 s with AC field, $I = 1$ kA; red - liquid, blue - solid.

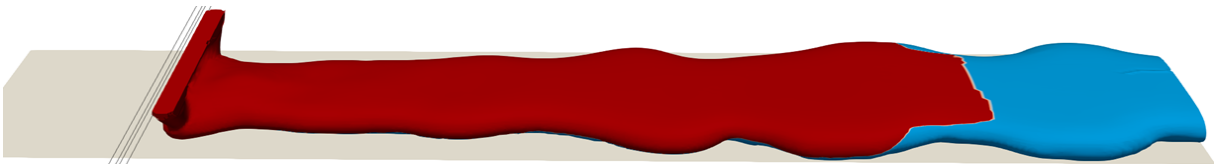

Fig. 5.4.16. Phases at $t = 2$ s with AC field, $I = 1$ kA; red - liquid, blue - solid.

The AC field solves the backflow problem, but overall makes the layer more non-uniform downstream. As was shown in the previous section, the surface shape can be

controlled by static magnetic field. If the AC field for backflow control is combined with static field for flow homogenization downstream, a fully stable casting process can be achieved. Figs. 5.4.17 and 5.4.18 show phases and layer thickness during stable casting with combined AC ($I = 1$ kA) and static magnetic field ($M_0 = 1$ T). Melt is abruptly slowed down by the static field forcing it to spread across the belt. $M_0 = 0.5$ T was not enough in this case because the melt was flowing faster than in the case where the backflow gap was assumed completely closed as evidenced by narrower melt channel (e.g., Fig. 5.4.2).

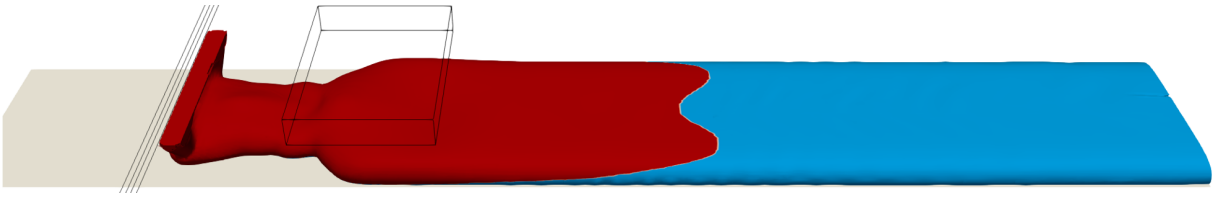

Fig. 5.4.17. Phases at steady state with combined AC and static magnetic field, $I = 1$ kA, $M_0 = 1$ T; red - liquid, blue - solid.

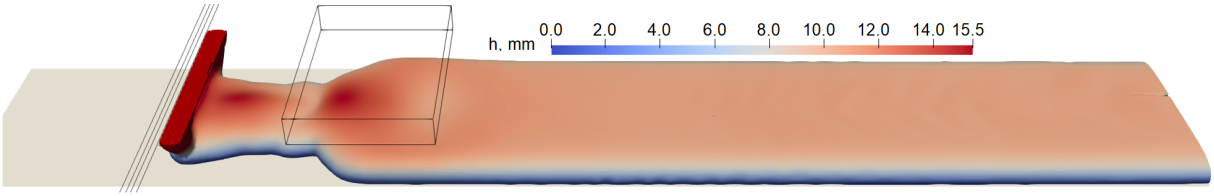

Fig. 5.4.18. Layer thickness at steady state with combined AC and static magnetic field, $I = 1$ kA, $M_0 = 1$ T.

With the intensive cooling considered here, small amount of melt immediately solidifies when it comes into contact with the belt. Fig. 5.4.19 shows phase distribution in different cross-sections through the computational domain with the combined AC and static magnetic field. The figure actually shows the field $(1 - \alpha + \beta)$, which has a value of 0 for solid, 1 for liquid and 2 for gas. Since the model is based on continuous phase fields, phase boundaries are not absolutely sharp and fractional values also exist, e.g., values between 0 and 1 correspond to the mushy zone. The part of melt that solidifies right at the contact to the belt is constantly remelted by incoming fresh melt and by recirculation in this zone.

Gas bubble entrapment between the melt and the belt is also observed here, as indicated by the two streaks of brighter spots on the bottom in Fig. 5.4.19. This is characteristic to the belt casting process, as reported in [40][30] and attributed to free surface oscillations at the triple point [29]. In the results shown here, the bubble entrapment occurs at the zones where melt suddenly expands across the belt due to electromagnetic braking by the static magnetic field. In a real casting processes, the gas entrapment decreases heat fluxes at those spots, compromising the quality of the cast strip. In the numerical model used here, the heat flux is constant, therefore the bubbles don't have much influence.

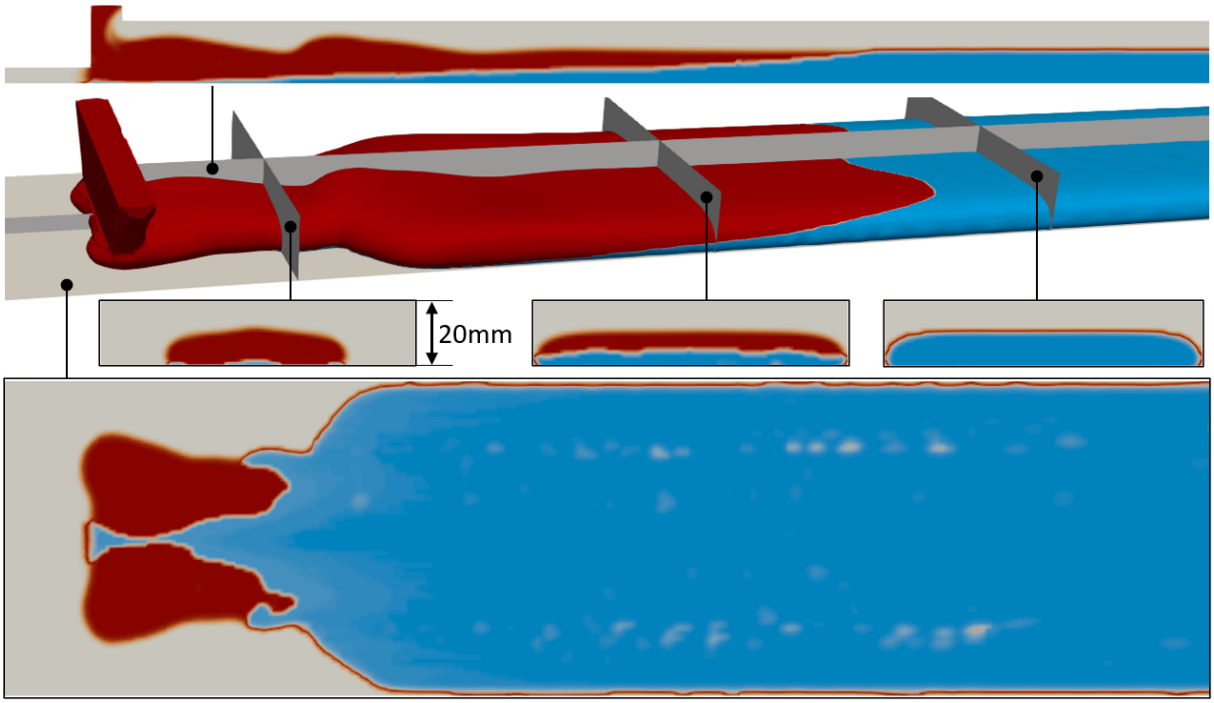

Fig. 5.4.19. Phases in different cross-sections with combined AC and static magnetic field, $I = 1$ kA, $M_0 = 1$ T; red - liquid, blue - solid, grey - air.

5.4.4 Conclusions

This section presented the main results of simulation of the belt casting process with electromagnetic flow control, investigating the influence of contact angle between liquid metal and the moving belt, system size and various strengths and configurations of magnetic field on the process stability and quality of the final product.

For free surface stabilisation, traveling magnetic field, moving with the belt speed, was found to be less efficient in stabilising the flow and spreading the liquid metal across the belt width than static magnetic field. This is probably due to the fact that most of the liquid metal was moving faster than the belt in the zone below the EM system, and so more efficient deceleration was achieved with static field. While efficient stabilisation was achieved with static field, it may have a detrimental effect regarding the backflow - flow braking force causes some buildup of melt near the inlet, which increases pressure at the backflow gap.

To prevent backflow, AC magnetic field of a straight inductor placed near the gap was found to efficiently deflect melt from this area. Edge instabilities that were studied previously don't appear to have much influence on keeping the melt from entering the gap. However, some surface oscillations do take place, which causes non-uniformities of the solidified material downstream. A combination of AC field for backflow control and static or traveling field for surface stabilisation downstream can be used to achieve fully stable casting process.

Conclusions

In the thesis, different electromagnetically-induced liquid metal flows were studied, with special focus on cases with notable free surface deformation. Numerical models were developed and tested using different approaches to simulating coupled electromagnetics and hydrodynamics problems. Three laboratory-scale systems with different complexity of EM interaction were considered, ranging from DC to low-frequency AC, to high-frequency AC. Different numerical approximations are applicable in each of the cases, and simulations were validated by laboratory experiments. A more practical application of the developed models were in simulation of the belt casting process, investigating the feasibility of applying EM technologies to control the flow and free surface motion of the cast alloy. The main conclusions are summarized below.

1. There are configurations where very simple one-way coupling between EM and fluid flow is applicable even with strong free surface dynamics. These are cases where most of the induced Lorentz concentrates relatively far from the free surface. This considerably simplifies the models and dramatically reduces simulation time. In more complex cases, where Lorentz force is mostly at the surface, a full two-way coupling must be employed, where the recalculation of EM fields is triggered by changes in free surface shape. When using the VOF method, the recalculation can be controlled by the maximum change of volume fraction α in any mesh cell. $max(\Delta\alpha) > 0.5$, which means that the free surface crosses at least a half of any mesh cell, usually is enough, while $max(\Delta\alpha) > 0.9$ produces non-physical oscillations. This criterion can be very restrictive regarding simulation time, since smaller value means more EM recalculations. A more general approach would be to combine this criterion with the specifics of Lorentz force distribution to avoid recalculations if free surface changes shape only where it would not have influence on force distribution.

2. Experiments with electrovortical flow showed stable free surface deformation at low currents and notable oscillations, sloshing and swirling at higher currents. Using simple one-way coupling where EM fields are calculated only once, experimental observations were successfully captured by 3D numerical model, while the 2D axisymmetric model failed to predict any instabilities. In the considered range, depth of the melt pool had only a marginal effect on the shape and height of free surface deformation.

3. The simplest one-way one-time coupling was generally not appropriate for the permanent magnet stirrer due to strong influence of fluid flow and surface motion on EM field distribution. Simulations with LES turbulence model agree well to experiments, while RANS models give somewhat damped oscillations. If $Re_m < 1$ and the surface motion does not influence EM fields much, the one-way one-time coupling was still appropriate by including the $\vec{v} \times \vec{B}$ term in the fluid flow model, which significantly reduced simulation time. Validity of this was confirmed by comparison to the full model and by experiments.

4. The most complex laboratory-scale system was thin rectangular and circular liquid metal pools in transverse AC magnetic field. At smaller thickness, the edge deflection

of the rectangular layer was relatively smooth and stable, with clear proportionality to inductor current. At larger thickness, distinct wavy patterns and oscillations along the edge developed. This is difficult to characterize by simple arguments of the amount of displaced fluid being proportional to Lorentz force, since Lorentz force strongly depends on local edge curvatures. According to a physical mechanism reported in literature, if some perturbations along the edge develop, induced current, magnetic field and consequently Lorentz force redistribute in such a way as to try to enhance the perturbations. This was confirmed by the 3D numerical simulations, which employed dynamic two-way coupling. The oscillations can be seen as a parametric instability, where changing surface shape alters the EM force distribution, and the different forces (surface tension, gravity and Lorentz force) push the surface back and forth, maintaining the oscillations.

5. Circular drops in AC field exhibit deformations ranging from axisymmetric squeezing for low Bo and low currents, to regular oscillation modes at higher Bo. Very large drops that nearly spanned the whole container were quite unstable. If the inductor current was turned on immediately, the drops assumed irregular oscillating shapes. However, if the current was increased slowly, initial squeezing of the drop turned into spontaneous pulsations with regular azimuthal modes. This instability could be triggered by a combination of factors, such as asymmetric inductor shape, small variations of inductor current due to noise or changing impedance/load, etc.

6. Oxidation drastically changes the dynamics of the free surface. Oxides form as a thin film on the surface, which tends to adhere to solid surfaces. In the case of rectangular and circular liquid metal layers in AC field, oxidation changed the dynamic oscillations into nearly static surface deformation patterns. In case of large circular drops, the dynamic irregular shapes in case without oxides turned into static labyrinth structures with oxides. Simulation of oxidized cases proved to be difficult. Considering the effect of oxidation as a modified contact angle allowed simulating some cases of rectangular layer, giving qualitatively reasonable agreement to experiments. Better agreement requires a more detailed representation of the effects of oxidation on surface tension, contact angles and friction.

7. There are several numerical parameters in the developed solidification solver determining the behaviour of the phase boundaries. Optimal parameters must be found for each case individually. In the thesis, the solidification model model was applied for simulation of the belt casting process.

8. Application of static magnetic field in the direct strip casting process can help stabilize the free surface and spread the liquid metal evenly across the belt, although an optimal field strength must be used to prevent melt build-up near the backflow gap. The backflow can be efficiently controlled by AC magnetic field. The edge instabilities studied in the laboratory setup don't appear to have a significant effect on keeping the melt from fully entering the gap. However, some oscillations do occur, which introduces non-uniformities of the solidified material further downstream. To achieve fully stable casting process, the AC field for backflow control can be applied in combination with

static or traveling field for surface stabilisation downstream. Note that the belt casting results must be viewed only qualitatively due to several assumptions used in the model, such as constant physical properties, constant cooling heat flux, ignored radiation and natural convection, etc.

Outlook

Several aspects remained either unsolved, requiring further improvements or simply requiring more data. Some of this forms the basis of further work, as outlined below.

1. During verification of coupled EM/HD models, some differences of bulk flow velocity were identified between the results of ANSYS CFX/Maxwell and Elmer/OpenFOAM models. A more detailed verification procedure should be considered in order to rule out possible differences in implementations of hydrodynamics, turbulence, electromagnetics models or parameters related to coupling.
2. To increase the dataset and allow better quantification of the instabilities observed for the thin layers in transverse AC field, new experiments are planned covering a wider range of parameters, including the field frequency. The new experiments will also use improved lighting conditions to simplify the image processing.
3. Further efforts are needed to improve the numerical model for thin layers in AC field. For the rectangular case, the model was not applicable to cases with strongest oscillations that were observed experimentally. This could be either due to limited spatial resolution or due to some parameters related to coupling and interpolation between Elmer and OpenFOAM. For the circular case, even though the model was essentially the same as for the rectangular case, it was strongly limited by spurious currents, which is characteristic to the VOF method. It was impossible to initialize a stable circular drop in the center of the container. Even without EM forces, spurious currents started to deform the drop. Interestingly, physically realistic oscillation modes can develop due to the spurious currents, which makes it virtually impossible to distinguish them from oscillations induced by EM forces. Volume fraction smoothing does reduce this numerical effect considerably, however, it does not prevent it.
4. The solidification model performed well. At this stage, however, the obtained results must be viewed only qualitatively. Several assumptions and approximations were used in the model. Further improvements of the model should consider more realistic conditions. That would make the model considerably more complicated, which would then require a lot of additional verification and validation.
5. In addition to the above-mentioned simplifications, the belt casting process was investigated for a relatively small system. Industrial scale is usually larger, which could make the process more unstable. To further test the applicability of AC and DC field for industrial scale casting process, large-scale simulations are required.

References

[1] S. C. Hardy. The surface tension of liquid gallium. *Journal of Crystal Growth*, vol. 71 (1985), pp. 602–606. DOI: https://doi.org/10.1016/0022-0248(85)90367-7.

[2] S. Chirattananon and Z. Gao. A model for the performance evaluation of the operation of electric arc furnace. *Energy Conversion and Management*, vol. 37 (1996), pp. 161–166. DOI: https://doi.org/10.1016/0196-8904(95)00173-B.

[3] H. J. Odenthal, et al. Review on modeling and simulation of the electric arc furnace. *Steel research international*, vol. 89 (2018), p. 1700098. DOI: https://doi.org/10.1002/srin.201700098.

[4] B. Silwal and M. Santangelo. Effect of vibration and hot-wire gas tungsten arc (gta) on the geometric shape. *Journal of Materials Processing Technology*, vol. 251 (2018), pp. 138–145. DOI: https://doi.org/10.1016/j.jmatprotec.2017.08.010.

[5] G. M. Oreper and J. Szekely. Heat- and fluid-flow phenomena in weld pools. *Journal of Fluid Mechanics*, vol. 147 (1984), pp. 53–79. DOI: https://doi.org/10.1017/S0022112084001981.

[6] H. Barati, et al. Mhd instability at the cathode spot as the origin of the vortex formation in high-intensity plasma arcs. *Journal of Physics Communications*, vol. 6 (2022), p. 015008. DOI: https://doi.org/10.1088/2399-6528/ac4b49.

[7] V. Bojarevics, J. A. Freibergs, E. I. Shilova, and E. V. Scherbinin. *Electrically Induced Vortical Flows* (Kluwer Academic Publishers, 1989).

[8] P. A. Davidson. *An Introduction to Magnetohydrodynamics* (Cambridge University Press, 2001).

[9] I. Kaldre, C. Wang, and R. Baranovskis. Experimental investigation of weld pool flow under external dc magnetic field. *Magnetohydrodynamics*, vol. 55 (2019), pp. 469–474.

[10] H. K. Moffatt. Electromagnetic stirring. *Physics of Fluids A: Fluid Dynamics*, vol. 3 (1991). DOI: https://doi.org/10.1063/1.858062.

[11] V. G. Zhilin, Y. P. Ivochkin, and I. O. Teplyakov. The problem of swirling of axisymmetric electrovortex flows. *High Temperature*, vol. 49 (2011), pp. 927–929. DOI: https://doi.org/10.1134/S0018151X11060241.

[12] A. Kharicha, et al. Experimental and numerical analysis of free surface deformation in an electrically driven flow. *Experimental Thermal and Fluid Science*, vol. 62 (2015), pp. 192–201. DOI: https://doi.org/10.1016/j.expthermflusci.2014.11.014.

[13] O. Lucía, P. Maussion, E. J. Dede, and J. M. Burdío. Induction heating technology and its applications: Past developments, current technology, and future challenges. *IEEE Transactions on Industrial Electronics*, vol. 61 (2014), pp. 2509–2520. DOI: https://doi.org/10.1109/TIE.2013.2281162.

[14] A. Umbrasko, E. Baake, B. Nacke, and A. Jakovičs. Numerical studies of the melting process in the induction furnace with cold crucible. *COMPEL - The international journal for computation and mathematics in electrical and electronic engineering*, vol. 27 (2008), pp. 359–368. DOI: https://doi.org/10.1108/03321640810847643.

[15] V. Bojarevics, K. Pericleous, R. A. Harding, and M. Wickins. The development and experimental validation of a numerical model of an induction skull melting furnace. *Metallurgical and Materials Transactions B*, vol. 35 (2004), pp. 785–803. DOI: https://doi.org/10.1007/s11663-004-0019-3.

[16] D. Coupard, et al. Residual stresses in surface induction hardening of steels: Comparison between experiment and simulation. *Materials Science and Engineering: A*, vol. 487 (2008), pp. 328–339. DOI: https://doi.org/10.1016/j.msea.2007.10.047.

[17] K. Gao, et al. Numerical and experimental analysis of 3d spot induction hardening of aisi 1045 steel. *Journal of Materials Processing Technology*, vol. 214 (2014), pp. 2425–2433. DOI: https://doi.org/10.1016/j.jmatprotec.2014.05.010.

[18] M. Ščepanskis, A. Jakovičs, E. Baake, and B. Nacke. Analysis of the oscillating behaviour of solid inclusions in induction crucible furnaces. *Magnetohydrodynamics*, vol. 48 (2012), pp. 677–686.

[19] T. Campanella, C. Charbon, and M. Rappaz. Grain refinement induced by electromagnetic stirring: A dendrite fragmentation criterion. *Metallurgical and Materials Transactions A*, vol. 35 (2004), pp. 3201–3210. DOI: https://doi.org/10.1007/s11661-004-0064-1.

[20] E. Shvydkiy, E. Baake, and D. Köppen. Liquid metal flow under traveling magnetic field—solidification simulation and pulsating flow analysis. *Metals*, vol. 10 (2020), p. 532. DOI: https://doi.org/10.3390/met10040532.

[21] Y. Peng, et al. Experimental study on alternating magnetic field magnetohydrodynamic pump. *Journal of Hydrodynamics*, vol. 20 (2008), pp. 591–595. DOI: https://doi.org/10.1016/S1001-6058(08)60099-2.

[22] E. Koroteeva, M. Ščepanskis, I. Bucenieks, and E. Platacis. Numerical modeling and design of a disk-type rotating permanent magnet induction pump. *Fusion Engineering and Design*, vol. 106 (2016), pp. 85–92. DOI: https://doi.org/10.1016/j.fusengdes.2016.03.030.

[23] I. Bucenieks. High pressure and high flowrate induction pumps with permanent magnets. *Magnetohydrodynamics*, vol. 39 (2003), pp. 411–418.

[24] K. Timmel, S. Eckert, and G. Gerbeth. Experimental investigation of the flow in a continuous-casting mold under the influence of a transverse, direct current magnetic field. *Metallurgical and Materials Transactions B*, vol. 42 (2011), pp. 68–80. DOI: https://doi.org/10.1007/s11663-010-9458-1.

[25] R. Chaudhary, B. G. Thomas, and S. P. Vanka. Effect of electromagnetic ruler braking (embr) on transient turbulent flow in continuous slab casting using large eddy simulations. *Metallurgical and Materials Transactions B*, vol. 43 (2012), pp. 532–553. DOI: https://doi.org/10.1007/s11663-012-9634-6.

[26] K. Cukierski and B. G. Thomas. Flow control with local electromagnetic braking in continuous casting of steel slabs. *Metallurgical and Materials Transactions B*, vol. 39 (2008), pp. 94–107. DOI: https://doi.org/10.1007/s11663-007-9109-3.

[27] K. H. Spitzer, et al. Direct strip casting (dsc) - an option for the production of new steel grades. *Steel Research International*, vol. 74 (2003), pp. 724–731. DOI: https://doi.org/10.1002/srin.200300256.

[28] R. I. L. Guthrie, I. L. Roderick, and M. Isac. Horizontal single belt casting of aluminum and steel. *Steel Research International*, vol. 85 (2014), pp. 1291–1302. DOI: https://doi.org/10.1002/srin.201300105.

[29] U. Niaz. Numerical modeling & experimental casting of aa6111 aluminium alloy and advanced high strength steels (ahss) produced through horizontal single belt casting (hsbc) process. Ph.D. thesis, McGill University, Canada, 2020.

[30] S. Ge. Numerical and physical modeling of the horizontal single belt casting (hsbc) process. Ph.D. thesis, McGill University, Canada, 2015.

[31] U. Niaz, M. M. Isac, and R. I. L. Guthrie. Numerical modeling of transport phenomena in the horizontal single belt casting (hsbc) process for the production of aa6111 aluminum alloy strip. *Processes*, vol. 8 (2020), p. 529. DOI: https://doi.org/10.3390/pr8050529.

[32] H. Palkowski and L. Wondraczek. Direct strip casting of magnesium. *International Journal of Materials Research*, vol. 95 (2004), pp. 1080–1086. DOI: https://doi.org/10.1515/ijmr-2004-0198.

[33] M. McBrien, J. M. Allwood, and N. S. Barekar. Tailor blank casting - control of sheet width using an electromagnetic edge dam in aluminium twin roll casting. *Journal of Materials Processing Technology*, vol. 224 (2015), pp. 60–72. DOI: https://doi.org/10.1016/j.jmatprotec.2015.03.034.

[34] J. S. Kim, M. Isac, and R. I. L. Guthrie. Metal-mold heat transfer and solidification of magnesium alloys in belt casting processes. In *TMS Annual Meeting* (2004), pp. 247–255.

[35] J. Wans, et al. Belt casting technology - experiences based on the worldwide first bct caster. In *46º Seminário de Aciaria - Internacional* (2015). DOI: https://doi.org/10.5151/1982-9345-26265.

[36] R. I. L. Guthrie and M. Isac. Continuous casting practices for steel: Past, present and future. *Metals*, vol. 12 (2022), p. 862. DOI: https://doi.org/10.3390/met12050862.

[37] C. Klinkenberg, B. Kintscher, K. Hoen, and M. Reifferscheid. More than 25 years of experience in thin slab casting and rolling current state of the art and future developments. *Steel Research International*, vol. 88 (2017), p. 1700272. DOI: https://doi.org/10.1002/srin.201700272.

[38] S. Ge, M. Isac, and R. I. L. Guthrie. Progress in strip casting technologies for steel; technical developments. *ISIJ International*, vol. 53 (2013), pp. 729–742. DOI: https://doi.org/10.2355/isijinternational.53.729.

[39] J. Kroos, et al. Development of the direct strip casting process. (2003). EC Report 20598: https://op.europa.eu/en/publication-detail/-/publication/f737caf3-4071-49fc-b616-2d45e6f46df8.

[40] S. Ge, M. Isac, and R. I. L. Guthrie. The computational fluid dynamic (cfd) modeling of the horizontal single belt casting (hsbc) processing of al-mg-sc-zr alloy strips. *Metallurgical and Materials Transactions B*, vol. 46 (2015), p. 2264–2277. DOI: https://doi.org/10.1007/s11663-015-0375-1.

[41] Direct Strip Casting, TU Clausthal, http://www2imet.rz-housing.tu-clausthal.de/mp/main/research/projekte/dsc/dsc.shtml.

[42] M. Milgrāvis, A. Bojarevičs, A. Gaile, and V. Geža. Application of ac and dc magnetic field for surface wave excitation to enhance mass transfer. *Journal of Crystal Growth*, vol. 534 (2020), p. 125409. DOI: https://doi.org/10.1016/j.jcrysgro.2019.125409.

[43] J. M. Galpin and Y. Fautrelle. Liquid-metal flows induced by low-frequency alternating magnetic fields. *Journal of Fluid Mechanics*, vol. 239 (1992), p. 383–408. DOI: https://doi.org/10.1017/S0022112092004452.

[44] X. Wu, et al. Analysis on the characteristics of pulsed electromagneticforce and the fluctuation behavior of molten metal free surface under pulsed magnetic field. *Materials Research Express*, vol. 7 (2020), p. 056514. DOI: https://doi.org/10.1088/2053-1591/ab8df2.

[45] J. M. Galpin, Y. Fautrelle, and A. D. Sneyd. Parametric resonance in low-frequency magnetic stirring. *Journal of Fluid Mechanics*, vol. 239 (1992), p. 409–427. DOI: https://doi.org/10.1017/S0022112092004464.

[46] Y. Fautrelle, J. Etay, and S. Daugan. Free-surface horizontal waves generated by low-frequency alternating magnetic fields. *Journal of Fluid Mechanics*, vol. 527 (2005), p. 285–301. DOI: https://doi.org/10.1017/S002211200400312X.

[47] V. Geža, J. Venčels, . Zāģeris, and S. Pavlovs. Numerical study of surface waves generated by low frequency em field for silicon refinement. *IOP Conf. Series: Materials Science and Engineering*, vol. 424 (2018), p. 012049. DOI: https://doi.org/10.1088/1757-899X/424/1/012049.

[48] A. Sneyd, J. Etay, and Y. Fautrelle. The starfish experiment: a lagrangian approach. *Magnetohydrodynamics*, vol. 39 (2003), pp. 277–282. Http://www.mhd.sal.lv/contents/2003/3/MG.39.3.8.R.html.

[49] Z. Lei, et al. Parametric instability of a liquid metal sessile drop under the action of low-frequency alternating magnetic fields. *Journal of Hydrodynamics*, vol. 25 (2013), pp. 300–308. DOI: https://doi.org/10.1016/S1001-6058(13)60367-4.

[50] P. Brunet and J. H. Snoeijer. Star-drops formed by periodic excitation and on an air cushion – a short review. *The European Physical Journal Special Topics*, vol. 192 (2011), pp. 207–226. DOI: https://doi.org/10.1140/epjst/e2011-01375-5.

[51] V. Palero, et al. 3d characterization of the inner flow in an oscillating drop. *Experiments in Fluids*, vol. 54 (2013), p. 1568. DOI: https://doi.org/10.1016/S1001-6058(13)60367-4.

[52] S. Spitans, E. Baake, A. Jakovičs, and H. Franz. Numerical simulation of electromagnetic levitation in a cold crucible furnace. *Magnetohydrodynamics*, vol. 51 (2015), pp. 567–578. DOI: http://mhd.sal.lv/contents/2015/3/MG.51.3.17.R.html.

[53] Deepak and J. W. Evans. The stability of an interface between viscous fluids subjected to a high-frequency magnetic field and consequences for electromagnetic casting. *Journal of Fluid Mechanics*, vol. 287 (1995), pp. 133–150. DOI: https://doi.org/10.1017/S0022112095000899.

[54] E. J. McHale and J. R. Melcher. Instability of a planar liquid layer in an alternating magnetic field. *Journal of Fluid Mechanics*, vol. 114 (1982), pp. 27–40. DOI: https://doi.org/10.1017/S0022112082000020.

[55] D. Perrier, Y. Fautrelle, and J. Etay. Free surface deformations of a liquid metal drop submitted to a middle-frequency ac magnetic field. In *Proceedings of the 4th International Symposium on Electromagnetic Processing of Materials* (2003), p. 279–282.

[56] Y. Boussant-Roux. Ph.D. thesis, Institut National Polytechnique de Grenoble, 1990.

[57] M. Hinaje, G. Vinsard, and S. Dufour. Analytical modelling of a thin liquid metal layer submitted to an ac magnetic field. *Journal of Physics D: Applied Physics*, vol. 39 (2006), pp. 2641–2646. DOI: http://dx.doi.org/10.1088/0022-3727/39/13/001.

[58] M. Hinaje, G. Vinsard, and S. Dufour. Determination of stable shapes of a thin liquid metal layer using a boundary integral method. *Journal of Physics D: Applied Physics*, vol. 39 (2006), pp. 1244–1248. DOI: http://dx.doi.org/10.1088/0022-3727/39/6/035.

[59] V. Kocourek, C. Karcher, M. Conrath, and D. Schulze. Stability of liquid metal drops affected by a high-frequency magnetic field. *Physical Review E*, vol. 74 (2006), p. 026303. DOI: https://doi.org/10.1103/PhysRevE.74.026303.

[60] K. Spragg, et al. Instabilities in electromagnetic quasilevitation. *Physical Review E*, vol. 89 (2014), p. 053014. DOI: http://dx.doi.org/10.1103/PhysRevE.89.053014.

[61] J. Priede, J. Etay, and Y. Fautrelle. Edge pinch instability of liquid metal sheet in a transverse high-frequency ac magnetic field. *Physical Review E*, vol. 73 (2006), p. 066303. DOI: https://doi.org/10.1103/PhysRevE.73.066303.

[62] J. Priede. Edge pinch instability of oblate liquid metal drops in a transverse ac magnetic field. *Journal of Fluid Mechanics*, vol. 676 (2011), pp. 218–236. DOI: https://doi.org/10.1017/jfm.2011.40.

[63] S. Spitans, H. Franz, and E. Baake. Numerical modeling and optimization of electrode induction melting for inert gas atomization (eiga). *Metallurgical and Materials Transactions B*, vol. 51 (2020), pp. 1918–1927. DOI: https://doi.org/10.1007/s11663-020-01934-5.

[64] J. Mohring, C. Karcher, and D. Schulze. Dynamic behavior of a liquid metal interface under the influence of a high-frequency magnetic field. *Physical Review E*, vol. 71 (2005), p. 047301. DOI: http://dx.doi.org/10.1103/PhysRevE.71.047301.

[65] V. Bojarevics, et al. Investigation of the cold crucible melting process: experimental and numerical study. *Magnetohydrodynamics*, vol. 39 (2003), pp. 395–402. DOI: http://mhd.sal.lv/contents/2003/4/MG.39.4.2.R.html.

[66] S. Spitans, E. Baake, B. Nacke, and A. Jakovičs. Numerical modeling of free surface dynamics of melt in an alternate electromagnetic field. part ii: Conventional electromagnetic levitation. *Metallurgical and Materials Transactions B*, vol. 47 (2016), pp. 522–536. DOI: https://doi.org/10.1007/s11663-015-0515-7.

[67] J. H. Ferziger and M. Peric. *Computational Methods for Fluid Dynamics* (Springer, 2002).

[68] E. M. de les Valls. Ph.D. thesis, Universitat Politecnica de Catalunya, 2011.

[69] B. E. Launder and D. B. Spalding. The numerical computation of turbulent flows. *Computer methods in applied mechanics and engineering*, vol. 3 (1974), pp. 269–289. DOI: https://doi.org/10.1016/0045-7825(74)90029-2.

[70] J. R. Mooney and A. N. Stokes. Time-varying mhd flows with free surfaces. *Applied Mathematical Modelling*, vol. 22 (1998), pp. 949–962. DOI: https://doi.org/10.1016/S0307-904X(98)10039-2.

[71] F. Harlow, J. Welch, J. Shannon, and B. Daly. The mac method. *Report LA-3425*, (1965).

[72] C. W. Hirt and B. D. Nichols. Volume of fluid (vof) method for the dynamics of free boundaries. vol. 39 (1981), p. 201–225. DOI: https://doi.org/10.1016/0021-9991(81)90145-5.

[73] J. U. Brackbill, D. B. Kothe, and C. Zemach. A continuum method for modeling surface tension. *Journal of Computational Physics*, vol. 100 (1992). DOI: https://doi.org/10.1016/0021-9991(92)90240-Y.

[74] D. J. E. Harvie, M. R. Davidson, and M. Rudman. An analysis of parasitic current generation in volume of fluid simulations. *Applied Mathematical Modelling*, vol. 30 (2006), pp. 1056–1066. DOI: https://doi.org/10.1016/j.apm.2005.08.015.

[75] M. Sussman and E. G. Puckett. A coupled level set and volume-of-fluid method for computing 3d and axisymmetric incompressible two-phase flows. *Journal of Computational Physics*, vol. 162 (2000), pp. 301–337. DOI: https://doi.org/10.1006/jcph.2000.6537.

[76] K. J. Vachaparambil and K. E. Einarsrud. Comparison of surface tension models for the volume of fluid method. *Processes*, vol. 7 (2019). DOI: https://doi.org/10.3390/pr7080542.

[77] B. Lafaurie, et al. Modelling merging and fragmentation in multiphase flows with surfer. *Journal of Computational Physics*, vol. 113 (1994), p. 134–147. DOI: https://doi.org/10.1006/jcph.1994.1123.

[78] B. Lafaurie, et al. Benchmark numerical simulations of segmented two-phase flows in microchannels using the volume of fluid method. *Computers & Fluids*, vol. 86 (2013), pp. 28–36. DOI: https://doi.org/10.1016/j.compfluid.2013.06.024.

[79] VOF Smoothing in OpenFOAM, https://github.com/floquation/OF-kva_interfaceProperties.

[80] R. Scardovelli and S. Zaleski. Direct numerical simulation of free-surface and interfacial flow. *Annual Review of Fluid Mechanics*, vol. 31 (1999), pp. 567–603. DOI: https://doi.org/10.1146/annurev.fluid.31.1.567.

[81] H. Rusche. Computational fluid dynamics of dispersed two-phase flows at 675 high phase fractions. Ph.D. thesis, Imperial College London, 2003.

[82] Y. Okagaki, T. Yonomoto, M. Ishigaki, and Y. Hirose. Numerical study on an interface compression method for the volume of fluid approach. *Fluids*, vol. 6 (2021), p. 80. DOI: https://doi.org/10.3390/fluids6020080.

[83] P. Cifani, et al. A comparison between the surface compression method and an interface reconstruction method for the vof approach. *Computers & Fluids*, vol. 136 (2016), pp. 421–435. DOI: https://doi.org/10.1016/j.compfluid.2016.06.026.

[84] J. Klostermann, K. Schaake, and R. Schwarze. Numerical simulation of a single rising bubble by vof with surface compression. *International Journal for Numerical Methods in Fluids*, vol. 71 (2013), pp. 960–982. DOI: https://doi.org/10.1002/fld.3692.

[85] J. Venčels, A. Jakovičs, and V. Geža. Simulation of 3d mhd with free surface using open-source eof-library: levitating liquid metal in an alternating electromagnetic field. *Magnetohydrodynamics*, vol. 53 (2017), pp. 643–652.

[86] J. Zhang and M.-J. Ni. Direct simulation of single bubble motion under vertical magnetic field: Paths and wakes. *Physics of Fluids*, vol. 26 (2014), p. 102102. DOI: https://doi.org/10.1063/1.4896775.

[87] K. Takatani. Mathematical modeling of incompressible mhd flows with free surface. *ISIJ International*, vol. 47 (2007), pp. 545–551. DOI: https://doi.org/10.2355/isijinternational.47.545.

[88] H. Yamasaki and H. Yamaguchi. Numerical simulation of bubble deformation in magnetic fluids by finite volume method. *Journal of Magnetism and Magnetic Materials*, vol. 431 (2017), pp. 164–168. DOI: https://doi.org/10.1016/j.jmmm.2016.10.012.

[89] Y. Li, A. Deng, B. Yang, and E. Wang. Inhibiting bulging deformation of liquid metal free surface by magnetic pressure. *Journal of Iron and Steel Research International*, vol. 28 (2020), pp. 818–829. DOI: https://doi.org/10.1007/s42243-020-00468-z.

[90] X. R. Zhu, R. A. Harding, and J. Campbell. Calculation of the free surface shape in the electromagnetic processing of liquid metals. *Applied Mathematical Modelling*, vol. 21 (1997), pp. 207–214. DOI: https://doi.org/10.1016/S0307-904X(97)00008-5.

[91] X. Wang and Y. Li. A comprehensive 3d mathematical model of the electroslag remelting process. *Metallurgical and Materials Transactions B*, vol. 46 (2015), pp. 1837–1849. DOI: https://doi.org/10.1007/s11663-015-0342-x.

[92] EOF-Library, https://github.com/jvencels/EOF-Library.

[93] J. Venčels, P. Raback, and V. Geža. Eof-library: Open-source elmer fem and openfoam coupler for electromagnetics and fluid dynamics. *SoftwareX*, vol. 9 (2019), pp. 68–72. DOI: https://doi.org/10.1016/j.softx.2019.01.007.

[94] OpenFOAM, https://openfoam.org.

[95] Elmer FEM, https://www.csc.fi/web/elmer.

[96] R. Baranovskis, et al. Contactless aluminum degassing system - gainsn model experiments and numerical study. *Journal of Sustainable Metallurgy*, vol. 7 (2021), pp. 1899–1909. DOI: https://doi.org/10.1007/s40831-021-00459-8.

[97] N. Sizganov and M. Khatsayuk. Free metal surface resonance under alternating magnetic field low-frequency oscillations. *IOP Conf. Series: Materials Science and Engineering*, vol. 950 (2020), p. 012010. DOI: https://doi.org/10.1088/1757-899X/950/1/012010.

[98] R. J. Adrian. Twenty years of particle image velocimetry. *Experiments in Fluids*, vol. 39 (2005), pp. 159–169. DOI: https://doi.org/10.1007/s00348-005-0991-7.

[99] Y. Takeda. Velocity profile measurement by ultrasound doppler shift method. *International Journal of Heat and Fluid Flow*, vol. 7 (1986), pp. 313–318. Https://doi.org/10.1016/0142-727X(86)90011-1.

[100] R. Ricou and C. Vives. Local velocity and mass transfer measurements in molten metals using an incorporated magnet probe. *International Journal of Heat and Mass Transfer*, vol. 25 (1982), pp. 1579–1588. DOI: https://doi.org/10.1016/0017-9310(82)90036-9.

[101] S. Eckert, A. Cramer, and G. Gerbeth. *Velocity Measurement Techniques for Liquid Metal Flows* (Springer Netherlands, 2007) pp. 275–294. DOI: https://doi.org/10.1007/978-1-4020-4833-3_17.

[102] A. Cramer, S. Eckert, and G. Gerbeth. Flow measurements in liquid metals by means of the ultrasonic doppler method and local potential probes. *The European Physical Journal Special Topics*, vol. 220 (2013), pp. 25–41. DOI: https://doi.org/10.1140/epjst/e2013-01794-2.

[103] S. Franke, et al. Ultrasound doppler system for two-dimensional flow mapping in liquid metals. *Flow Measurement and Instrumentation*, vol. 21 (2010), pp. 402–409. DOI: https://doi.org/10.1016/j.flowmeasinst.2010.05.001.

[104] A. Thess, E. Votyakov, and Y. Kolesnikov. Lorentz force velocimetry. *Physical Review Letters*, vol. 96 (2006), p. 164501. DOI: https://doi.org/10.1103/PhysRevLett.96.164501.

[105] J. Priede, D. Buchenau, and G. Gerbeth. Single-magnet rotary flowmeter for liquid metals. *Journal of Applied Physics*, vol. 110 (2011), p. 034512. DOI: https://doi.org/10.1063/1.3610440.

[106] I. Sokolov. Lorentz force velocimetry at high magnetic reynolds numbers. Ph.D. thesis, Ilmenau Techinal University, Germany, 2015.

[107] X. Dai, X. Yang, J. Campbell, and J. Wood. Effects of runner system design on the mechanical strength of al–7si–mg alloy castings. *Materials Science and Engineering: A*, vol. 354 (2003), pp. 315–325. DOI: https://doi.org/10.1016/S0921-5093(03)00021-2.

[108] M. Birjukovs, et al. Particle tracking velocimetry in liquid gallium flow around a cylindrical obstacle. *Experiments in Fluids*, vol. 63 (2022), p. 99. DOI: https://doi.org/10.1007/s00348-022-03445-2.

[109] M. Ščepanskis, et al. Assessment of electromagnetic stirrer agitated liquid metal flows by dynamic neutron radiography. *Metallurgical and Materials Transactions B*, vol. 48 (2017), p. 1045. DOI: https://doi.org/10.1007/s11663-016-0902-8.

[110] M. Sarma, et al. Neutron radiography visualization of solid particles in stirring liquid metal. *Physics Procedia*, vol. 69 (2015), pp. 457–463. DOI: https://doi.org/10.1016/j.phpro.2015.07.064.

[111] T. Lappan, et al. Neutron radiography of particle-laden liquid metal flow driven by an electromagnetic induction pump. *Magnetohydrodynamics*, vol. 56 (2020), pp. 167–176. Http://www.mhd.sal.lv/contents/2020/2/MG.56.2.8.R.html.

[112] M. Narula, A. Ying, and M. A. Abdou. A study of liquid metal film flow, under fusion relevant magnetic fields. *Fusion Science and Technology*, vol. 47 (2005), pp. 564–568. DOI: http://dx.doi.org/10.13182/FST05-A745.

[113] J. Smagorinsky. General circulation experiments with the primitive equations: I. the basic experiment. *Monthly Weather Review*, vol. 91 (1963), pp. 99–164. DOI: https://doi.org/10.1175/1520-0493(1963)091<0099:GCEWTP>2.3.CO;2.

[114] B. E. Launder and D. B. Spalding. The numerical computation of turbulent flows. *Computer Methods in Applied Mechanics and Engineering*, vol. 3 (1974), pp. 269–289. DOI: https://doi.org/10.1016/0045-7825(74)90029-2.

[115] F. R. Menter, M. Kuntz, and R. Langtry. *Proceedings of the 4th international symposium on turbulence, heat and mass transfer*, (2003).

[116] C. D. Argyropoulos and N. C. Markatos. Recent advances on the numerical modelling of turbulent flows. *Applied Mathematical Modelling*, vol. 39 (2015), pp. 693–732. DOI: https://doi.org/10.1016/j.apm.2014.07.001.

[117] M. Strelets. Detached eddy simulation of massively separated flows (2001). DOI: https://doi.org/10.2514/6.2001-879.

[118] P. R. Spalart, et al. A new version of detached-eddy simulation, resistant to ambiguous grid densities. *Theoretical and Computational Fluid Dynamics*, vol. 20 (2006), pp. 181–195. DOI: https://doi.org/10.1007/s00162-006-0015-0.

[119] J. Hart. Comparison of turbulence modeling approaches to the simulation of a dimpled sphere. *Procedia Engineering*, vol. 147 (2016), pp. 68–73. DOI: https://doi.org/10.1016/j.proeng.2016.06.191.

[120] S. B. Pope. *Turbulent Flows* (Cambridge University Press, 2000) .

[121] F. Rosler and D. Bruggemann. Shell-and-tube type latent heat thermal energy storage: numerical analysis and comparison with experiments. *Heat and Mass Transfer*, vol. 47 (2011). DOI: https://doi.org/10.1007/s00231-011-0866-9.

[122] Elmer Models Manual, CSC - IT Center for Science, Finland. Available online: http://www.nic.funet.fi/pub/sci/physics/elmer/doc/ElmerModelsManual.pdf.

[123] J. R. Hull, T. Wiencek, and D. M. Rote. Magnetohydrodynamic stability in the electromagnetic levitation of horizontal molten-metal sheets. *Physics of Fluids A*, vol. 1 (1989), pp. 1069–1076. DOI: https://doi.org/10.1063/1.857398.

[124] Y. Fautrelle and A. Sneyd. vol. 80, chap. Liquid Metal Magnetohydrodynamics for Fusion Blankets (Springer, 2007).

[125] Y. Méheust, G. Løvoll, K. J. Måløy, and J. Schmittbuhl. Interface scaling in a two-dimensional porous medium under combined viscous, gravity, and capillary effects. *Physical Review E*, vol. 66 (2002), p. 051603. DOI: https://doi.org/10.1103/PhysRevE.66.051603.

[126] A. Cramer, V. Galindo, and M. Zennaro. Frequency dependence of an alternating magnetic field driven flow. *Magnetohydrodynamics*, vol. 51 (2015), pp. 133–148. Http://mhd.sal.lv/contents/2015/1/MG.51.1.13.R.html.

[127] M. Leitner, et al. Thermophysical properties of liquid aluminum. *Metallurgical and Materials Transactions A*, vol. 48 (2017), pp. 3036–3045. Https://link.springer.com/article/10.1007/s11661-017-4053-6.

[128] V. G. Zhilin, et al. An experimental investigation of the velocity field in an axisymmetric electrovortical flow in a cylindrical container. *Magnetohydrodynamics*, vol. 22 (1986), pp. 110–116.

[129] S. Handschuh-Wang, et al. Surface tension of the oxide skin of gallium-based liquid metals. *Langmuir*, vol. 37 (2021), pp. 9017–9025. DOI: https://doi.org/10.1021/acs.langmuir.1c00966.

[130] D. Berenis and I. Grants. Experimental and numerical investigation of bistability in rotating permanent magnet-generated electrolyte flow in a ring-shaped container. *Physics of Fluids*, vol. 34 (2022). DOI: https://doi.org/10.1063/5.0128454.

Acknowledgements

I express my gratitude to the advisor of the thesis, Dr. Phys. Andris Jakovičs. I thank him for giving me the opportunity to work in this field, for guiding me throughout the develompent of the thesis and for motivating me in difficult times.

Thanks to my colleagues at the Institute of Numerical Modelling for friendly atmosphere and valuable discussions, and for supporting me with experimental work.

I thank Prof. Egbert Baake for the opportunities of doing experimental work at the Institute of Electrotechnology, Leibniz University Hannover in Germany. I also thank other colleagues at the Institute for always welcoming me and for preparing and assisting during experiments.

I acknowledge financial support from the ERDF project No. 1.1.1.1/18/A/108 "Development of numerical modelling approaches to study complex multiphysical interactions in electromagnetic liquid metal technologies" and project No. 8.2.2.0/20/I/006 "Strengthening the LU doctoral capacity within the framework of the new doctoral model".